GEOLOGIC SETTING, NATURE, AND STRUCTURAL EVOLUTION OF INTRUSION-HOSTED AU-BEARING QUARTZ VEINS AT THE LONGLINE OCCURRENCE, MOOSEHORN RANGE AREA, WEST-CENTRAL YUKON TERRITORY

by

NANCY L. JOYCE (née M^{ac}DONALD)

B.Sc. Honours, Carleton University – Ottawa, Ontario, 1999

A THESIS SUBMITTED IN PARTIAL FULFILMENT OF
THE REQUIREMENTS FOR THE DEGREE OF

MASTER OF SCIENCE

in

THE FACULTY OF GRADUATE STUDIES

(Department of Earth and Ocean Sciences)

We accept this thesis as conforming
to the required standard

…….

…….

…….

…….

……

THE UNIVERSITY OF BRITISH COLUMBIA

March 2002

Abstract

The Longline gold occurrence is located within the Tintina Gold Belt, in the Moosehorn Range area of west-central Yukon Territory. Gold occurs in sheeted, high-grade (~30 g/t), shallowly dipping mesothermal quartz veins hosted within mid-Cretaceous intrusions of the Dawson Range batholith.

Felsic to intermediate intrusions in the Moosehorn Range area are probably closely related; they were emplaced at ~96-100 Ma, and have similar geochemical and lead isotopic compositions. Geochemistry of the intrusive phases suggests the magmas were mantle-derived, subduction-related, and extensively contaminated by continental crust. The gold-bearing quartz veins post-date all of these intrusions and are cut by younger mafic dykes.

Metallic minerals inside the veins include galena, sphalerite, arsenopyrite, pyrite, boulangerite, tetrahedrite, native gold, and scheelite. The alteration assemblage includes muscovite, sericite, iron carbonate, pyrite, arsenopyrite, minor clay, quartz, and tourmaline. Vein minerals precipitated from moderately saline fluids, containing H_2O-CO_2-CH_4-NaCl ± N_2, at temperatures of ~260º-300ºC, pressure of ~1.3 – 1.9 kbar, and depth of 5-7 km, assuming near-lithostatic fluid pressures. Lead isotopic studies indicate the Moosehorn Range area intrusions are not the source of the metals in the veins and the ultimate source remains uncertain.

The veins were emplaced between 92 and 93 Ma along NNW-striking, shallowly ENE-dipping brittle reverse fault structures during a WSW-verging contractional event. The veins are 1cm to 1m thick, sheeted, lens-shaped, banded, and locally connected by sub-horizontal dilational oreshoots, creating a ramp-flat geometry. The long axis of the oreshoots is NNW and slip along the reverse faults was up-dip towards the WSW.

Regional structural context for the formation of the veins is unclear. Prominent NNW-trending topographic and magnetic lineaments in the area may be dextral strike-slip faults along which there may be contractional and dilational jogs. Contraction at a jog in the vicinity of the Longline property may have generated the structures that host the veins. If so, dextral strike-slip faults and associated contractional and/or dilational jogs may be an important exploration guide to finding other shallowly dipping auriferous quartz vein systems in the region.

Table of Contents

List of Tables

List of Figures

Acknowledgments

This has been a long and rewarding journey, the successful culmination of which could not have been possible without the support of many people and organizations.

I am truly grateful to the Mineral Deposit Research Unit and the Department of Earth and Ocean Sciences at the University of British Columbia, Barramundi Gold Limited, and Newmont Exploration Limited for financial and logistical support throughout the course of my research. Additional funds were gratefully received from a Thomas and Marguerite MacKay Memorial Scholarship, a Society of Economic Geologists Hugh E. McKinstry research grant, and a Natural Science and Engineering Research Council PGS-A scholarship. I sincerely thank my advisor, Dr. Jim Mortensen, for his undying energy, encouragement, open-door policy, and wisdom. And for getting me addicted to coffee. In addition, Drs. Dick Tosdal and Shane Ebert taught me a great deal about mesothermal gold-bearing vein systems and are thanked for their advice and support. Drs. Lori Kennedy, Ken Hickey, and Steve Rowins also contributed greatly to ideas and concepts presented in this thesis.

I thank Sandy Sears, David Ritcey, and Mike Johnson of Barramundi Gold Limited, John Read (Newmont Exploration Limited), and Craig Hart (Yukon Geology Program) for their insight and many enlightening conversations both in and out of the field. Many thanks to Heather Douglas, who assisted me in the field during the summer of 2000.

Janet Gabites and Richard Friedman were instrumental in assisting with geochronology and lead isotopic sample preparation, analyses, and data interpretation. Thanks also to Mike Villeneuve (Geological Survey of Canada, Ottawa) for carrying out my Ar-Ar analyses, and to Dr. David Selby (University of Alberta) for Re-Os isotope analyses.

Rob Shives of the Geological Survey of Canada (Ottawa) is thanked for allowing me to examine and utilize radiometric survey data prior to its publication.

I owe a great deal to Arne Toma for his ability to solve almost every software and hardware problem I ever had, and to Alex Allen for helping me keep afloat on the ocean of UBC bureaucratic red tape.

The encouragement, companionship, and advice of my fellow grad students helped me to achieve my goals and I sincerely thank them all. I particularly thank Scott Heffernan for tolerating my messy corner of the office, my singing to myself, and for being a great friend; I also thank Kate Bone for always being there, always lending an ear, and ironically introducing *me* to playing hockey! Many thanks to a very special circle of friends that I wish could be together always; there are many but in particular Lawrence Winter, Angie Carter, Steve Israel, Olwyn Bruce, Keith Patterson, Kathi Dilworth, Simon Haynes, Steve Piercey, Steve Quane, Martin Stewart, Geoff Bradshaw, Kim Welford, Cari Deyell, Fionnuala Devine, Tina Roth, and Kellie Emon.

I am truly grateful to my parents, my family and all of my in-laws whose support has been absolutely indispensable. I am so fortunate to be surrounded by incredibly supportive family and friends.

Most importantly I owe everything to my husband Steve Joyce. I could never have done this without him; I sincerely thank him for believing in me and for all the sacrifices he has made in letting me pursue my dreams. I did it!

CHAPTER 1

Introduction

The Longline gold occurrence is located in the Moosehorn Range area of west-central Yukon Territory, within the Tintina Gold Belt, which forms an arcuate belt of gold-rich mineral deposits and occurrences extending from southeastern Yukon into central and southwestern Alaska (Fig. 1). High-grade gold-bearing mesothermal quartz veins (~30 g/t) in the Moosehorn Range area formed along brittle reverse shear zones within the mid-Cretaceous Dawson Range batholith. The geology of the area is not well understood due to poor exposure and thus any new information about the nature and origin of the mineralization will help refine exploration strategies.

A field- and laboratory-based project was undertaken to constrain the setting of the gold-bearing quartz veins in the context of Moosehorn Range area geology. A structural model was developed from known veins to delineate extensions of currently recognized oreshoots and predict the orientation of other potentially mineralized structures in the region.

This research was carried out as part of a regional study of intrusion-related gold deposits within the Tintina Gold Belt, supported by the Mineral Deposit Research Unit at the University of British Columbia and a consortium of eight companies, with matching funds from the Natural Sciences and Engineering Research Council (NSERC Cooperative Research and Development Program). Logistical work in the field was supported by Barramundi Gold Ltd. and Newmont Mining Corporation. Additional funding was provided by an NSERC PGS-A scholarship and a Hugh E. McKinstry research grant from the Society of Economic Geologists.

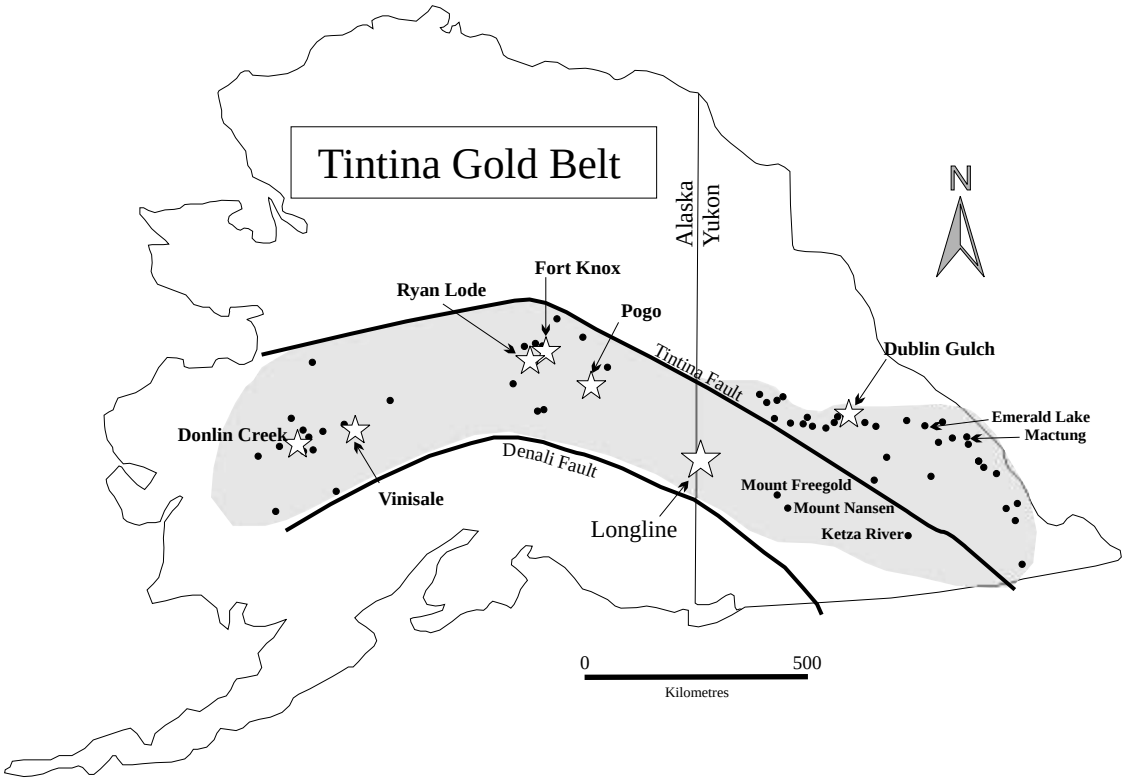

Figure 1 Map of Alaska and Yukon Territory showing the general trend of the Tintina Gold Belt and the locations of various gold deposits and showings within it (black dots). Selected deposits are highlighted with stars, including Longline, located immediately east of the Yukon-Alaska border (after Mortensen et al., 2000).

Methodology and Objectives

Integrated field and laboratory studies were undertaken to understand the geology and gold-bearing veins of the Moosehorn Range area.

Field Work

Field work was carried out by the author over the course of two partial field seasons. Detailed mapping of excavated vein exposures provided structural data crucial for development of a model for vein geometry and formation. Fresh and altered wallrock and vein material were sampled both from surface exposures and drill core for petrographic, geochronological, lithogeochemical, fluid inclusion, and isotopic studies. Bedrock mapping in the main study area and in relatively well exposed areas along the crest of the Moosehorn Range provided geological context for the samples collected and the trench-scale structural mapping.

Geochronology

U-Pb

Earlier mapping (e.g., Tempelman-Kluit, 1974) suggested a Triassic to Jurassic crystallization age for the intrusions in the Moosehorn Range area whereas more recent work (e.g., Godwin, 1975; Hart and Langdon, 1998; Mortensen et al., 2000) suggests they are related to the mid-Cretaceous Dawson Range batholith. Systematic U-Pb dating was undertaken to resolve this discrepancy and to better understand the magmatic history of the area. Mid-Cretaceous intrusions are commonly associated with economic gold, silver, tin, and tungsten mineralization elsewhere in the Tintina Gold Belt (Lang et al., 2000, and

references therein); thus, confirming a mid-Cretaceous crystallization age for the Moosehorn Range area intrusions was extremely important. U-Pb zircon and titanite ages obtained in this study provide a temporal context for magmatism in the Moosehorn Range area. All U-Pb geochronology was completed in the Geochronology Laboratory at the University of British Columbia.

K-Ar

Two fine-grained mafic dyke samples were dated using K-Ar methods. The dykes are the only phases that post-date gold-bearing veins, and the composition of the dykes precluded dating via U-Pb methods. The ages obtained for the dykes provide a minimum age for the mineralization and constrain the timing of the youngest recognized magmatic event in the area. All K-Ar sample preparation and analysis were carried out by Activation Laboratories Ltd. in Ancaster, Ontario.

$^{40}Ar/^{39}Ar$

$^{40}Ar/^{39}Ar$ ages were obtained for selected samples of biotite, hornblende, and muscovite from the property. This provided age constraints on magmatic cooling, metamorphic cooling of mylonitized granodiorite, and on formation of alteration muscovite adjacent to the gold-bearing veins. The latter was important for assigning a relatively specific age to the vein formation. Mineral separates were prepared by the author and all $^{40}Ar/^{39}Ar$ analyses were carried out by the Geological Survey of Canada in Ottawa.

Re-Os

A Re-Os age for molybdenite from within an aplite dyke on the Moosehorn Range was obtained to determine whether molybdenum mineralization was temporally related to the gold mineralization. The ^{187}Re and ^{187}Os concentrations in molybdenite were determined by isotope dilution thermal ionization mass spectrometry at the University of Alberta Radiogenic Isotope Facility.

Lithogeochemistry

A representative suite of samples from all the recognized intrusive phases in the Moosehorn Range area were analyzed for major, trace, and rare earth element geochemical compositions. These geochemical compositions, together with the results from geochronological and isotopic studies, help constrain the paleotectonic setting in which the magmatism occurred. All samples were prepared by the author and geochemical analyses were carried out by ALS Chemex Laboratories in North Vancouver, British Columbia, using a combination of X-ray fluorescence and inductively coupled plasma mass spectrometry.

Reconnaissance Fluid Inclusion Study

A reconnaissance-level study of fluid inclusions in quartz from the main gold-bearing veins in the Mooshorn Range area was conducted to determine the composition and temperature of the mineralizing fluids. Sample chips were analyzed by the author using a FLUID INC.-adapted USGS gas-flow heating-freezing stage at the University of British Columbia.

Pb Isotopic Study

Lead isotope compositions of sulphide minerals and spatially associated wallrocks in ore deposits are commonly used to identify metal sources and to assess the degree of fluid-wallrock interaction. The Pb isotopic compositions of vein minerals and wallrocks in the Moosehorn Range were determined to evaluate possible genetic relationships between gold mineralization and the magmas of the host batholith. Preparation and analyses of whole rock, feldspar, sulphide, and sulphosalt samples were carried out by the author and by J. Gabites employing thermal ionization mass spectrometry at the Geochronology Laboratory at the University of British Columbia.

Presentation

Results of this project are presented as two research papers (Chapters 2 and 3) that will be submitted for publication in refereed international journals. Chapter 2 focuses on Moosehorn Range geology and regional geologic setting, and on the ages and petrochemistry of intrusive phases of the Dawson Range batholith in the area. Some regional samples were incorporated in this study but the majority of samples were collected by the author from the Longline property from both surface and drill core. Chapter 3 comprises the results of a detailed property-scale study of gold mineralization in the Moosehorn Range area. The structural and hydrothermal evolution of the auriferous quartz veins was constrained by detailed trench mapping, and petrographic, geochronological, fluid inclusion, and lead isotopic investigations. A shear model for vein formation was developed which delineates the geometry of the Moosehorn Range veins and oreshoots in the subsurface. Examples of analogous styles of mineralization from elsewhere in the world are briefly discussed.

Chapter 4 presents a brief summary of the conclusions drawn in Chapters 2 and 3, identifies outstanding questions raised during the course of this study, and makes recommendations for further work in the area.

References

Godwin, C.I. 1975. Alternative interpretations for the Casino complex and Klotassin batholith in the Yukon Crystalline terrane. Canadian Journal of Earth Sciences, **12**: 1910-1916.

Hart, C.J.R., and Langdon, M. 1998. Geology and mineral deposits of the Mount Nansen camp, Yukon. *In* Yukon Exploration and Geology 1997, Exploration and Geological Services Division, Yukon, Indian and Northern Affairs Canada. *Edited by* C.F. Roots and D.S. Emond, pp. 129-138.

Lang, R.L., Baker, T., Hart, C.J.R., and Mortensen, J.K. 2000. An exploration model for intrusion-related gold systems. Society of Economic Geologists Newsletter, no. 40.

Mortensen, J.K., Hart, C.J.R., Murphy, D.C., and Heffernan, S. 2000. Temporal evolution of Early and Mid-Cretaceous magmatism in the Tintina Gold Belt. *In* The Tintina Gold Belt: Concepts, exploration, and discoveries, British Columbia and Yukon Chamber of Mines Cordilleran Roundup Special Volume 2, Vancouver, British Columbia, pp. 49-57.

Newberry, R.J., Layer, P.W., Burleigh, R.E., and Solie, D.N. 1998b. New $^{40}Ar/^{39}Ar$ dates for intrusions and mineral prospects in the eastern Yukon-Tanana terrane, Alaska – regional patterns and significance. *In* Geologic studies in Alaska by the U.S. Geological Survey, 1996: U.S. Geological Survey Bulletin. *Edited by* J.E. Gray, and J.R. Riehle. pp. 131-159.

Chapter 2

Age and Geologic Setting of the Moosehorn Range Area Intrusions, West-Central Yukon Territory; Constraints from Isotopic and Geochemical Studies

Introduction

A recognized genetic relationship between voluminous Cretaceous intrusions in west-central Yukon Territory and east-central Alaska and several porphyry Cu, mesothermal Au, and epithermal Au deposits within the Tintina Gold Belt (e.g., Casino, Pogo, and Mt. Nansen deposits; Fig. 2) has generated significant exploration interest in the region (McCoy et al., 1997; Hart and Langdon, 1998; Selby et al., 1999). The Longline high-grade gold-bearing mesothermal quartz vein system, located in the Moosehorn Range area about 140 km south-southwest of Dawson City, Yukon Territory, is hosted by felsic to intermediate mid-Cretaceous intrusions of the Dawson Range batholith. However, in contrast to most deposits in the Tintina Gold Belt, the wallrock intrusions in the Moosehorn Range area are not genetically related to the mineralization at Longline. This paper summarizes the geology, geochronology, geochemical characteristics, and deformation history of these intrusions. Interpretations have been made regarding the origin of the magmas and the mid-Cretaceous tectonic setting in which the intrusions formed based on these various lines of evidence.

Regional Geologic Setting

Intrusions in the Moosehorn Range area were emplaced entirely within the Yukon-Tanana Terrane (YTT), which underlies central and western Yukon Territory and east central Alaska (Mortensen, 1992). The YTT consists of mainly mid-Paleozoic to mid-

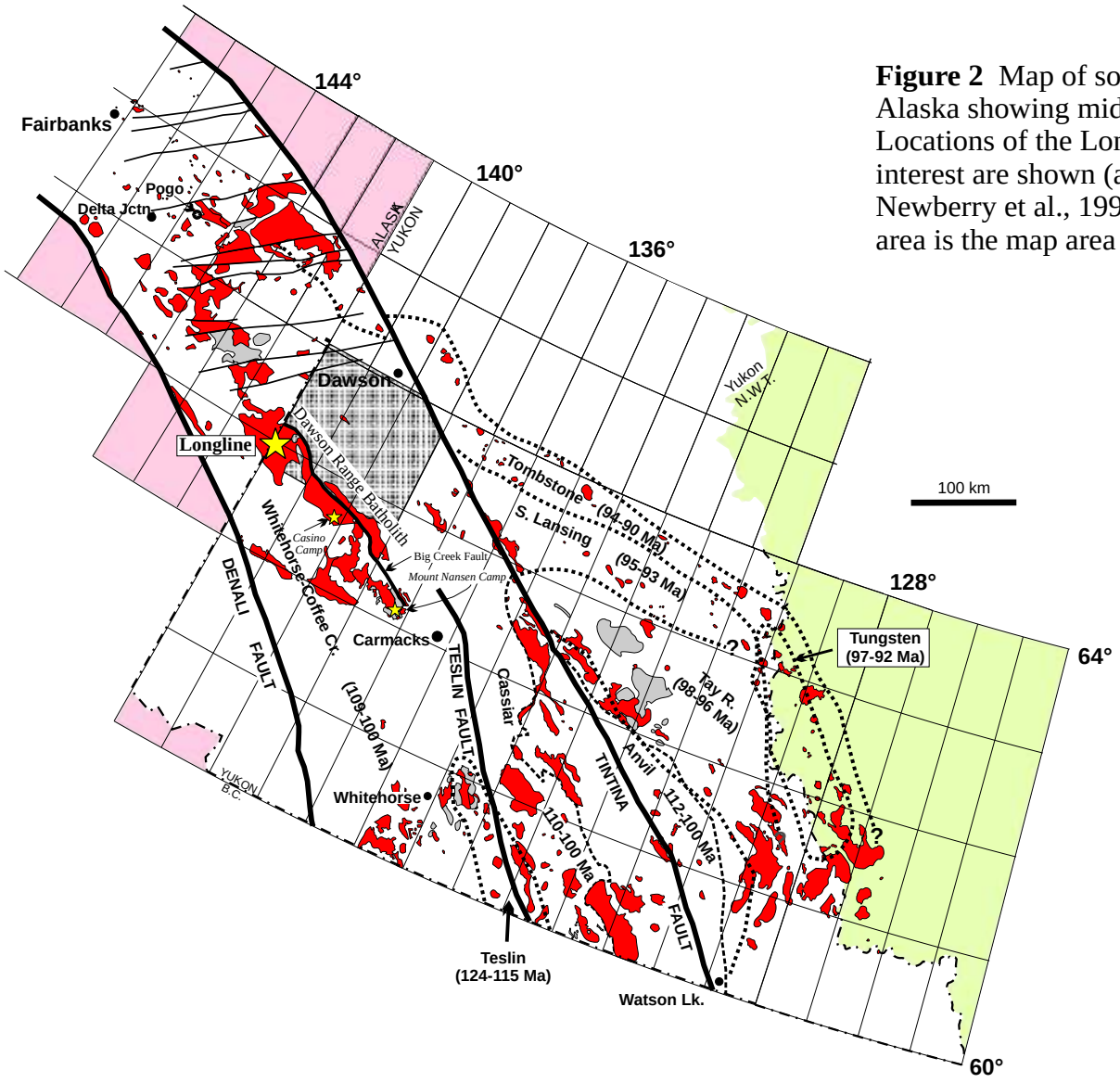

Figure 2 Map of southern Yukon Territory and east-central Alaska showing mid-Cretaceous intrusions and volcanic rocks. Locations of the Longline property and other deposits of interest are shown (adapted from Tempelman-Kluit et al., 1991; Newberry et al., 1998b; Mortensen et al., 2000). Stippled area is the map area shown in Figure 3.

Mesozoic continental arc assemblages built on Lower Paleozoic and possibly older continental basement (e.g., Mortensen, 1992; Selby et al., 1999). This pericratonic terrane exhibits laterally variable stratigraphy and records a complex tectonic history, many aspects of which are still controversial (e.g., Mortensen, 1992; Mihalynuk et al., 1999; Colpron and Yukon-Tanana Working Group, 2001).

Most of the YTT is composed of variably deformed metamorphic rocks, including pelitic and quartzofeldspathic schist and paragneiss, felsic orthogneiss, and mafic to felsic metavolcanic and metaplutonic rocks (Tempelman-Kluit, 1974; Mortensen, 1992; Hart and Langdon, 1998). These metamorphic rocks are intruded by several mafic to felsic volcanic and plutonic suites that range in age from Late Triassic to Neogene (Mortensen, 1992; Francis et al. 1999; Mortensen et al., 2000; this study). Late Triassic to Early Jurassic (~220-185 Ma) volcanic arc magmatism in western Yukon and eastern Alaska followed mid-Permian to Late Triassic accretion of YTT onto the North American craton (Mortensen et al., 1999). It has been suggested that the voluminous mid-Cretaceous Whitehorse-Coffee Creek intrusive suite (WCCS), which includes the Whitehorse batholith and Dawson Range batholith, may also be arc-related; however, extensive crustal contamination of the magmas has prevented a definite understanding of the tectonic setting in which the WCCS was formed (Mortensen et al., 1999; Selby et al., 1999; Aleinikoff et al., 2000; Mortensen et al., 2000). Dominant rock types of this suite include metaluminous and calc-alkaline biotite-hornblende granodiorite and quartz monzonite, syenite, and minor biotite-muscovite quartz monzonite and granite (Carlson, 1987; Mortensen et al., 2000). These and other plutonic units were subsequently intruded and/or overlain by mid-Cretaceous to Eocene rhyolitic to basaltic suites such as the Mount Nansen Group (~105-108 Ma), Prospector Mountain plutonic suite (~70 Ma), and the Carmacks Group (~70 Ma) (Grond et al., 1984;

Tempelman-Kluit, 1984; Carlson, 1987; Hunt and Roddick, 1991; Johnston et al., 1996; Hart and Langdon, 1998; Selby et al., 1999). Crystallization ages and geochemical compositions of the Mount Nansen Group are similar to those of WCCS intrusions and the volcanics are considered to be extrusive equivalents of the intrusive suite (Mortensen et al., 2000).

Dawson Range Batholith

The Dawson Range batholith (DRB), formerly referred to as the Klotassin batholith (e.g., Godwin, 1975; Tempelman-Kluit and Wanless, 1980), is an elongate, orogen-parallel, sill-like body of Cretaceous granite and granodiorite that extends northwest from Carmacks into eastern Alaska (Johnston, 1999) (Fig. 2). The DRB was emplaced entirely within the YTT during mid-Cretaceous northeastward subduction of the Farallon plate (Johnston, 1995; Johnston et al., 1995; Hart and Langdon, 1998; Selby et al., 1999; Mortensen et al., 2000). The age of WCCS intrusive rocks of the DRB has been somewhat controversial. The DRB was originally considered to be Late Triassic in age (Le Couteur and Tempelman-Kluit, 1976). As isotopic dating methods improved and the available age database in the area expanded, the interpreted age of the batholith was revised to Early Jurassic (Tempelman-Kluit and Wanless, 1980), and finally to mid-Cretaceous (Godwin, 1975; Hart and Langdon, 1998; Mortensen et al., 2000). The mid-Cretaceous age assignment for the batholith is based on a substantial number of U-Pb zircon and titanite ages (J.K. Mortensen and C.J.R. Hart, unpublished data, 2001). The DRB has been interpreted to have formed in a continental magmatic arc environment (Mortensen et al., 2000).

The geology of the northwestern Dawson Range (Fig.3), has been described by Cockfield (1921), Tempelman-Kluit (1974), and Morin (1977), and the southeastern portion

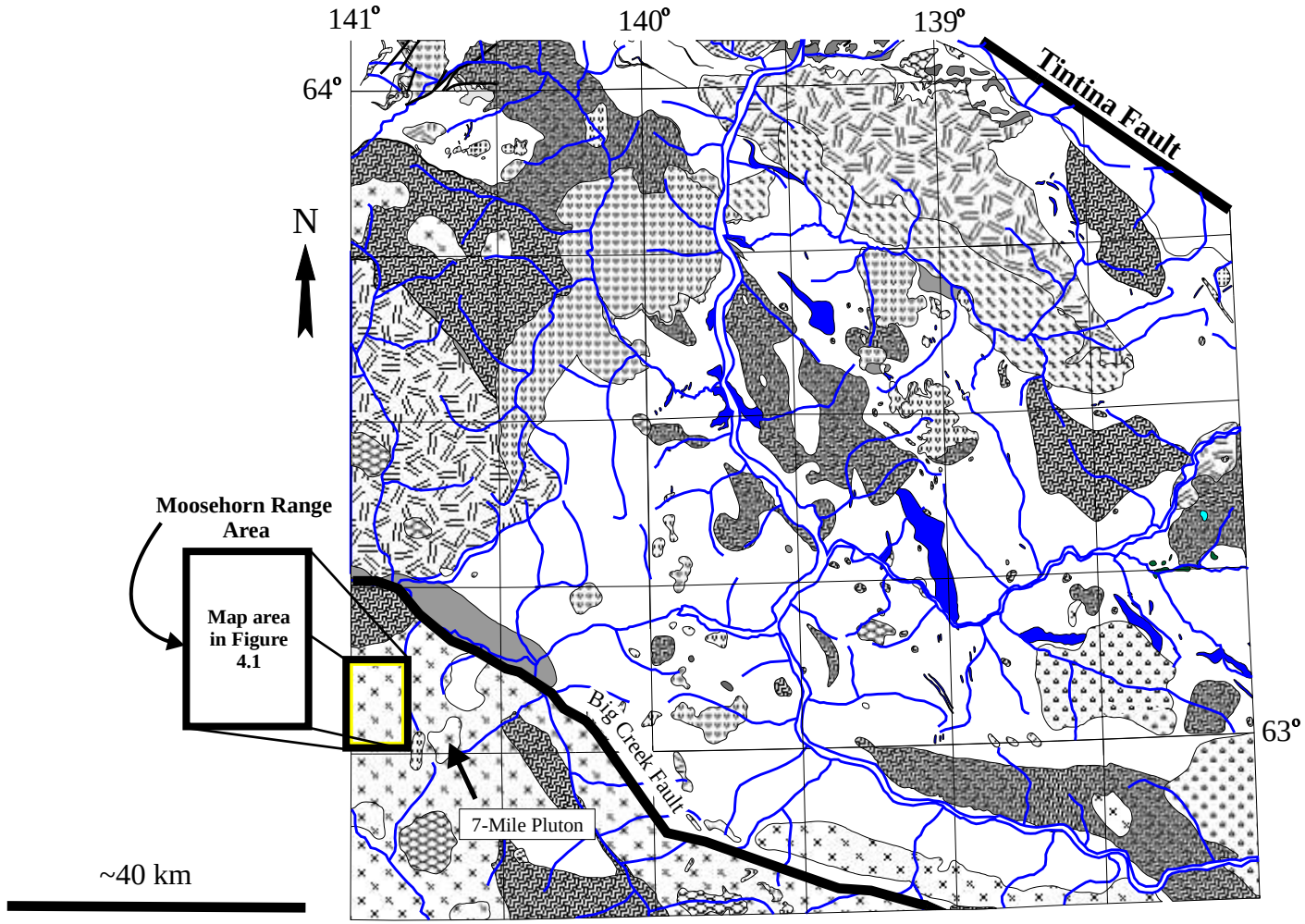

Figure 3 Regional geology of west-central Yukon Territory. The area is underlain predominantly by mid-Paleozoic metamorphic rocks of the pericratonic Yukon-Tanana terrane. Geology modified after Tempelman-Kluit (1974). Legend for map is on the following page.

Legend


Eocene felsic volcanic rocks and high level intrusions


Paleocene sedimentary rocks within the Tintina fault zone


Late Cretaceous volcanic rocks (Carmacks Gp.) and associated sedimentary rocks (Tantalus Fm)


Permian Klondike Schist - metavolcanic and metasedimentary rocks


Paleozoic marble


mainly mid-Paleozoic undifferentiated metasedimentary and metavolcanic rocks of the Yukon-Tanana Terrane

Intrusive Rocks


Late Cretaceous intermediate to felsic intrusions


Early to mid-Cretaceous intermediate to felsic intrusions


Late Triassic-Early Jurassic mafic to felsic intrusions


Permian granite and quartz monzonitic gneiss


Devonian-Mississippian intermediate to felsic composition metaplutonic rocks


Paleozoic(?) greenstone and serpentinized ultramafic rocks


Fault


Rivers/Creeks

by Cairnes (1917), Bostock (1936), Tempelman-Kluit (1984), and Carlson (1987). The batholith consists of equigranular to porphyritic hornblende-biotite quartz diorite, and granodiorite (Johnston, 1995; Johnston et al., 1995; Selby et al., 1999). Other associated phases, such as those of the mid-Cretaceous Casino Plutonic Suite, comprise leucocratic granite, quartz monzonite, alaskite, and aplite (Carlson, 1987; Selby et al., 1999).

Geology of the Moosehorn Range Area

The southeastern Moosehorn Range area immediately east of the Yukon-Alaska border is predominantly underlain by intrusive rocks, including the main Moosehorn Range granodiorite, as well as granodioritic and granitic dykes and plugs, and aplite, felsite, and mafic dykes, and scattered occurrences of gneissic wallrock. The most voluminous intrusive phases are granodioritic in composition; these units are hornblende- and/or biotite-bearing, massive to variably foliated, and commonly porphyritic. These and other lithologies in the area are described below.

Metamorphic Country Rock

The contact between the DRB and metamorphic country rocks is oriented approximately northwest-southeast, parallel to the long axis of the elongate batholith (Tempelman-Kluit, 1974) (Figs. 2 and 3). The metamorphic country rock occurs in the northeast portion of the Moosehorn Range area (Fig. 4.1). This contact is poorly exposed and it is unclear whether the contact in this vicinity represents the margin of the batholith or simply one side of a large raft of country rocks. The country rocks are fine- to medium-grained biotite-quartz ± feldspar ± muscovite gneiss and schist, locally containing feldspar augen. They are correlated with Schist Gneiss unit of Tempelman-Kluit (1974), which

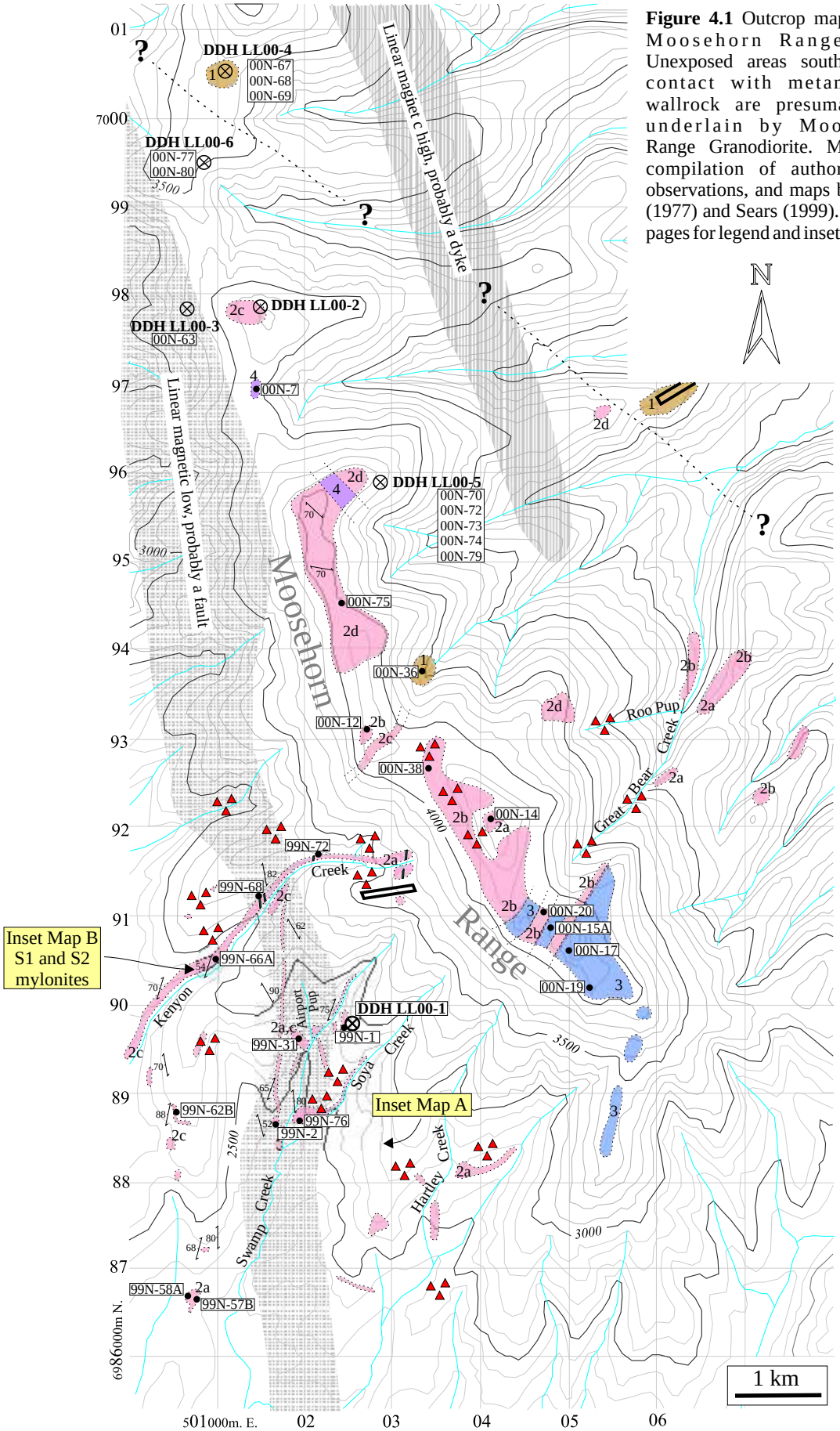

Figure 4.1 Outcrop map for the Moosehorn Range area. Unexposed areas south of the contact with metamorphic wallrock are presumably all underlain by Moosehorn Range Granodiorite. Map is a compilation of author's field observations, and maps by Morin (1977) and Sears (1999). See next pages for legend and inset maps.

Legend for Moosehorn Range Area Outcrop Map

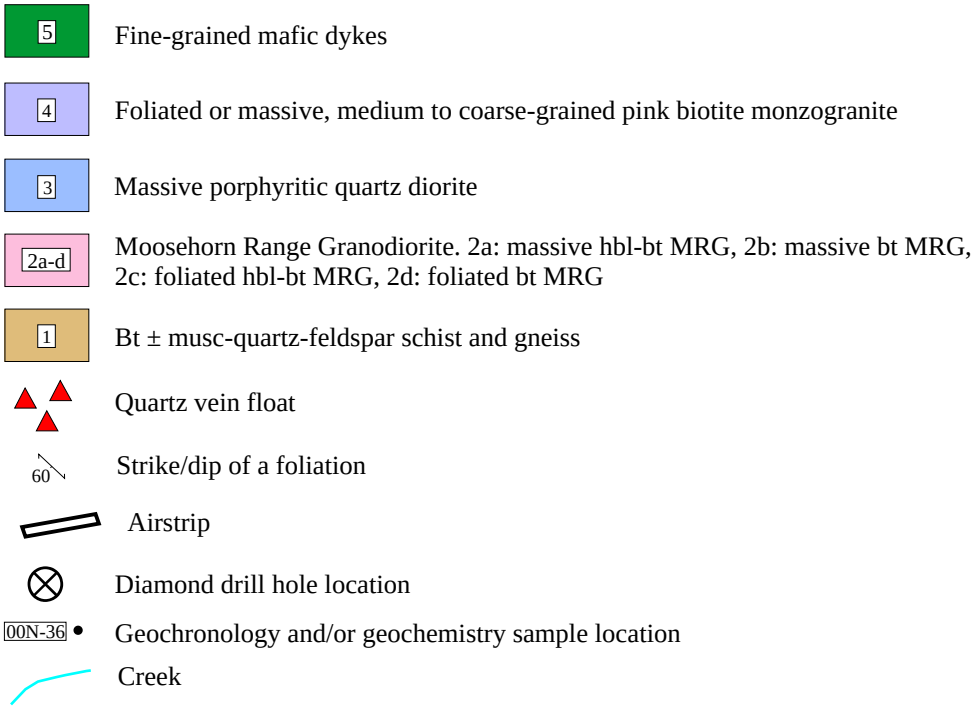

Inset Map A

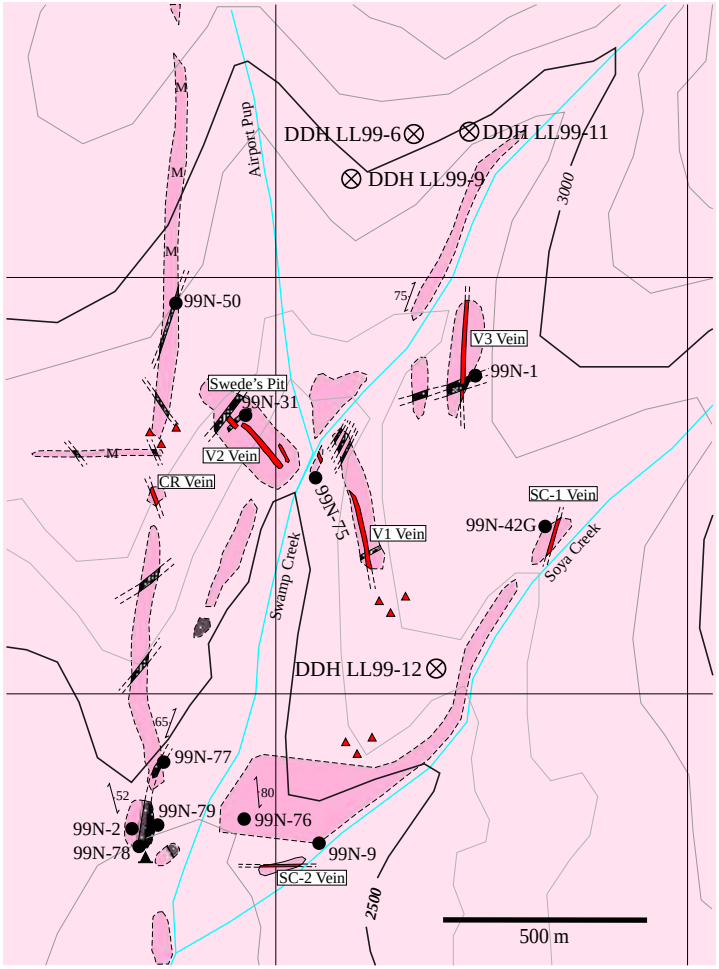

Figure 4.2 Inset map A, showing the geology of the main study area. All the quartz veins, except for the SC-1 vein, occupy shallowly east-northeast-dipping contractional fault structures.

Legend for Inset Maps

N

- Fine-grained mafic dykes
- Massive tan to grey felsite dykes
- Massive porphyritic quartz diorite
- Foliated to mylonitic porphyritic hornblende-biotite granodiorite dykes
- Massive to weakly foliated Moosehorn Range Granodiorite
- M — Outcrop of fine-grained mafic dykes 10cm to 1m thick
- Quartz vein
- Quartz vein float
- 60 — Strike/dip of a foliation
- 00N-36 • Geochronology and/or geochemistry sample location
- Diamond drill hole location
- Camp
- Creek

Inset Map B

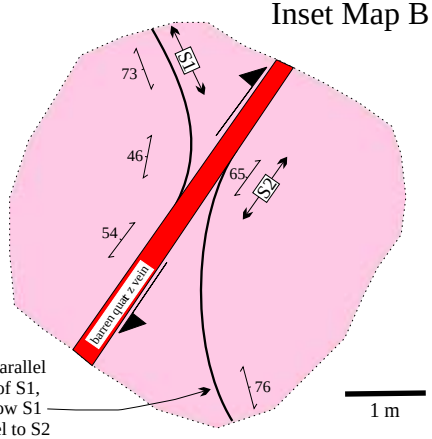

This line is parallel to the strike of S1, and shows how S1 bends parallel to S2

Figure 4.3 Schematic diagram of an outcrop showing the relationship between S1 and S2 foliations. S1 is strongly foliated in the southeast end of the outcrop, and mylonitic at the northwest end. S2 is predominantly ultramylonitic; the dextral strike-slip fault offset S1 by about 3-4 m.

consists mainly of quartz mica schist and amphibolite, as well as undifferentiated metaplutonic rocks assigned to the Pelly Gneiss (Tempelman-Kluit, 1974). Thin, undeformed, tan to white pegmatite veins composed of potassium feldspar, quartz, and muscovite locally crosscut foliation. Minor foliation-parallel, lens-like, barren quartz veins, 10-40 cm thick, are also present. Foliation strikes northwest and dips moderately towards the northeast. In thin section, feldspars are poikilitic, unzoned, and the presence of subgrains within the crystals indicates that the metamorphic rocks experienced high-temperature (500°-550°C) deformation (Tullis, 1983; Passchier and Trouw, 1996). Microcline twinning and granophyric textures are also present. Quartz in the groundmass is variably annealed and foam-textured.

Migmatitic gneiss intersected in DDH LL00-4 (see Fig. 4.1) in the northwestern Moosehorn Range area is interpreted to be metaplutonic in origin, and is correlated with the Pelly Gneiss, which Tempelman-Kluit (1974) mapped about 3 km north of the drill collar. The gneiss, which contains quartz, potassium feldspar, biotite, plagioclase, muscovite, and pyrite, is intensely deformed with distinct leucosomes and melanosomes.

Moosehorn Range Granodiorite

The term Moosehorn Range Granodiorite (MRG) is used to describe the main granodiorite phase in the Moosehorn Range area. The MRG underlies most of the study area and is the main host rock for the gold-bearing quartz veins. It is a composite intrusion, consisting predominantly of massive hornblende-biotite granodiorite similar to the rest of the DRB, but also includes phases of massive and foliated biotite ± hornblende granodiorite and granite. Crosscutting field relationships indicate this unit is the oldest intrusive phase in the area. Partially resorbed, oval-shaped, porphyritic mafic enclaves are ubiquitous

throughout the intrusion and range from approximately 1 cm to 2 m in size. Grain size in all phases of the MRG generally coarsens towards contacts with pegmatite veins, xenoliths, and enclaves.

The average modal mineralogy for the undeformed hornblende-biotite granodiorite was estimated from thin section to be 20-35% quartz, 25-45% plagioclase, 10-20% potassium feldspar, 10-15% biotite, 10% hornblende, and minor titanite, pyrite, magnetite, allanite, epidote, and chlorite. More granitic varieties that lack hornblende are composed of 25-40% quartz, 25-35% plagioclase, 20-30% potassium feldspar, 5-15% biotite, and minor titanite, magnetite, chlorite, and epidote. Quartz, which in hand sample is typically pale brown in granitic varieties and grey in the granodiorite phases, is commonly deformed or annealed in thin section. Most feldspar crystals are concentrically zoned and intergrown with quartz to form myrmekitic and granophyric textures. Potassium feldspars locally exhibit crosshatched microcline twins and/or perthitic textures. Partial replacement of hornblende by biotite, biotite by chlorite ± epidote, and weak to moderate sercitization of feldspars indicates minor retrograde reactions took place. Figures 5.1, 5.2, and 5.3 show the typical mineral assemblages and textures of MRG seen in thin section.

The MRG along the crest of the Moosehorn Range contains larger and more numerous xenoliths and enclaves than the MRG immediately southwest of the range. Mafic porphyritic enclaves or xenoliths of amphibolite, metapelite, and biotite-quartz-feldspar gneiss of up to two metres in size are common in this area. Fine-grained mafic and felsic dykes, aplite, white leucogranite, and abundant quartz-potassium feldspar pegmatite veinlets and dykes that crosscut the MRG are also more abundant. The abundance of xenoliths and pegmatite veining in this area could be an indication that the rocks along the crest of the Moosehorn Range formed near the roof of the pluton.

Figure 5.1 Hand sample of massive MRG.

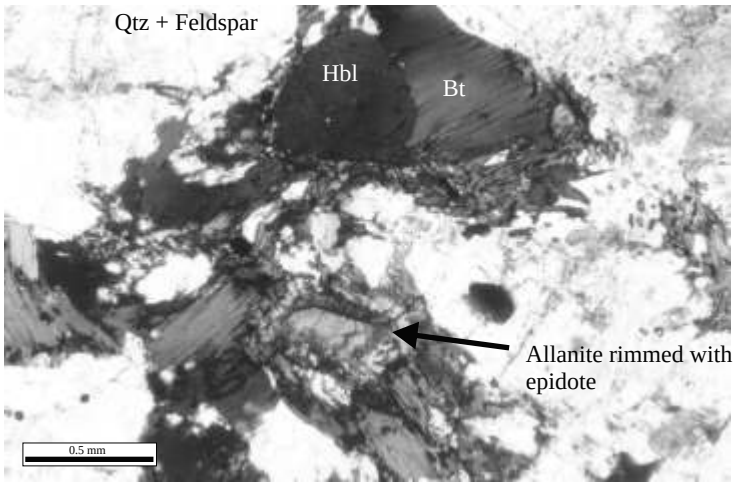

Figure 5.2 Photomicrograph of MRG sample 99N-2.

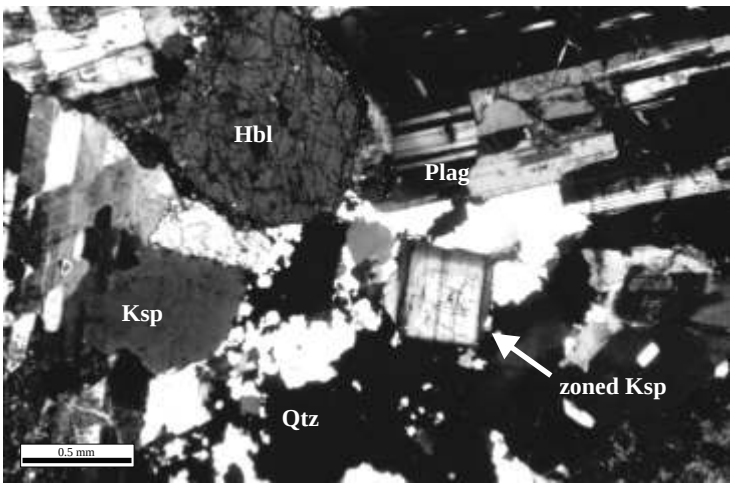

Figure 5.3 Photomicrograph of MRG sample 99N-75 with crossed polars. Subgrains in quartz have irregular grain boundaries. Feldspars are undeformed and commonly zoned.

Foliated MRG

The granodiorite is dominantly massive; however, weakly to moderately developed tectonic foliation within shear zones of variable width and near contacts with foliated porphyritic dykes are common. This foliation predominantly strikes north-northwest (330º-360º) and dips moderately to steeply (50º-90º) to the east-northeast. Similarly oriented flow foliations in the MRG, defined by aligned feldspar, biotite, and hornblende phenocrysts, were also observed. The Big Creek Fault (Figs. 2 and 3), which is a west-northwest-striking dextral strike-slip fault, forms the northern contact of the DRB against metamorphic rocks of the YTT (Johnston, 1999). The DRB may have intruded during displacement along this fault, producing the foliations observed in the MRG.

In the western and northwestern parts of the Longline property, the granodiorite gradationally becomes weakly to intensely foliated and locally mylonitic. Two generations of mylonitic fabrics (S1 and S2; see Fig. 6.1) were observed on the northwestern flank of Kenyon Creek (Fig. 4.1). An early strong gneissic to mylonitic S1 foliation oriented at approximately 150/75 (strike/dip, employing right hand rule) is dextrally offset by a later steeply west-northwest dipping mylonitic D2 shear zone (see Fig. 4.3). Two barren bull quartz veins (12 and 60 cm thick) parallel to D2 within the D2 shear zone were found. Locally the D2 mylonites are L-S tectonites with very strong sub-horizontal stretching lineations. The MRG in the northwestern portion of the Moosehorn Range has a moderately developed foliation oriented approximately 145/70 (Morin, 1977) which is parallel to the D1 fabrics to the south.

Foliations in the MRG are defined by quartz, quartzofeldspathic, and hornblende- and biotite-rich bands or ribbons (Fig. 7.1). Shear bands, quartz ribbons, and rotated quartz,

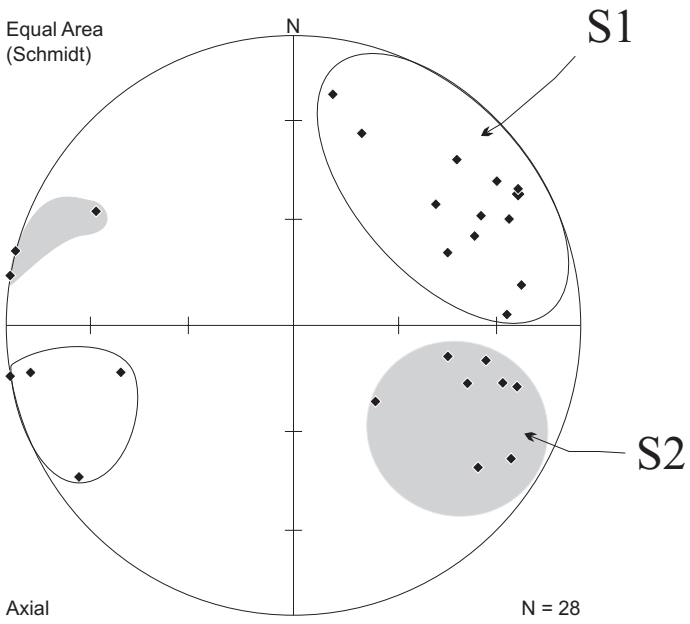

Figure 6.1 Stereonet showing poles to planes of S1 (white fields) and S2 (grey fields) foliations. S1 is dextrally offset across S2.

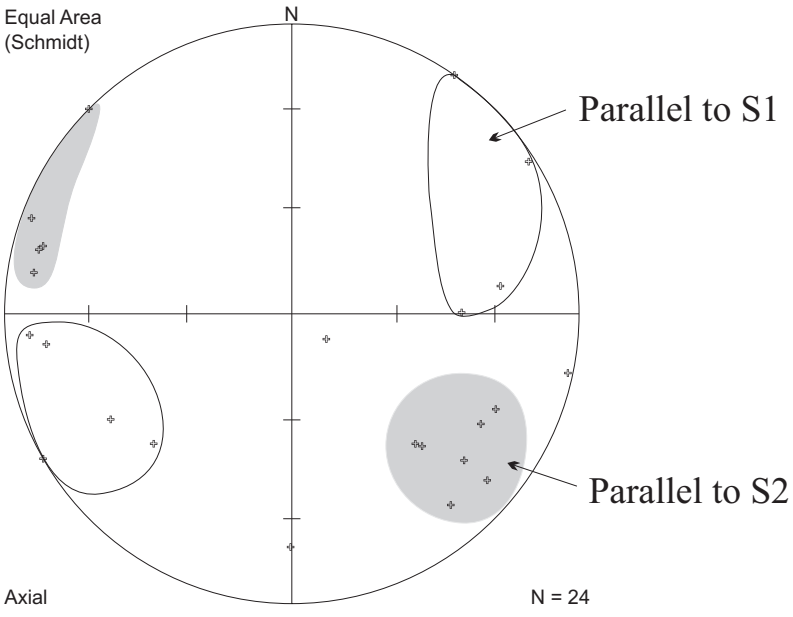

Figure 6.2 Stereonet showing poles to planes of foliations within porphyritic granodiorite and quartz diorite dykes. White fields are foliations parallel to S1, grey fields are parallel to S2. Most of the foliations are parallel to S2.

feldspar, hornblende, and biotite porphyroclasts are common. Most quartz ribbons exhibit an annealed granoblastic or foam texture with grain sizes coarser (100–200 μm) than those of the quartzofeldspathic bands (less than 10-20 μm). Microstructures observed in quartz, including undulatory extinction, deformation bands, subgrains, core and mantle structures, and serrated and sutured grain boundaries indicate that the quartz deformed ductilely (Hobbs et al., 1976; Poirier and Guillope, 1979; Urai et al., 1986). Development of deformation twins, subgrains, and serrated and sutured grain boundaries in feldspar indicates that the temperature of deformation may have reached about 500°-550°C (Tullis, 1983, Passchier and Trouw, 1996). Hornblende and mica grains are fractured, rotated, kinked, and bent.

Shear sense indicators in thin sections are rare but σ- and δ-porphyroclasts, shear bands, and mica fish observed in oriented sections all indicate the sense of shear for the D2 mylonites was *dextral* (Figs. 7.2, 7.3, and 7.4). This sense of shear is consistent with the dextral offset of D1 fabrics, and the macroscopic shear bands and σ- and δ-porphyroclasts seen in outcrop. Shear sense was not constrained for the D1 mylonites.

The mylonitic granodiorite west of Kenyon Creek has approximately the same modal mineralogy as the undeformed MRG equivalents, except that there is significantly more abundant epidote, chlorite, allanite, and sericite. Scattered grains of coarse-grained muscovite were also locally present. Titanite is *not* present in the mylonites, whereas in the undeformed phases it is ubiquitous and abundant. The absence of titanite suggests the possibility that the mylonitic rocks and the main MRG are different phases. No contact with the less deformed MRG was identified, however, perhaps due to lack of exposure in the area. Although much of the epidote, chlorite, and sericite can be attributed to retrograde metamorphism during and/or after the deformation, the assemblage may reflect syn-tectonic

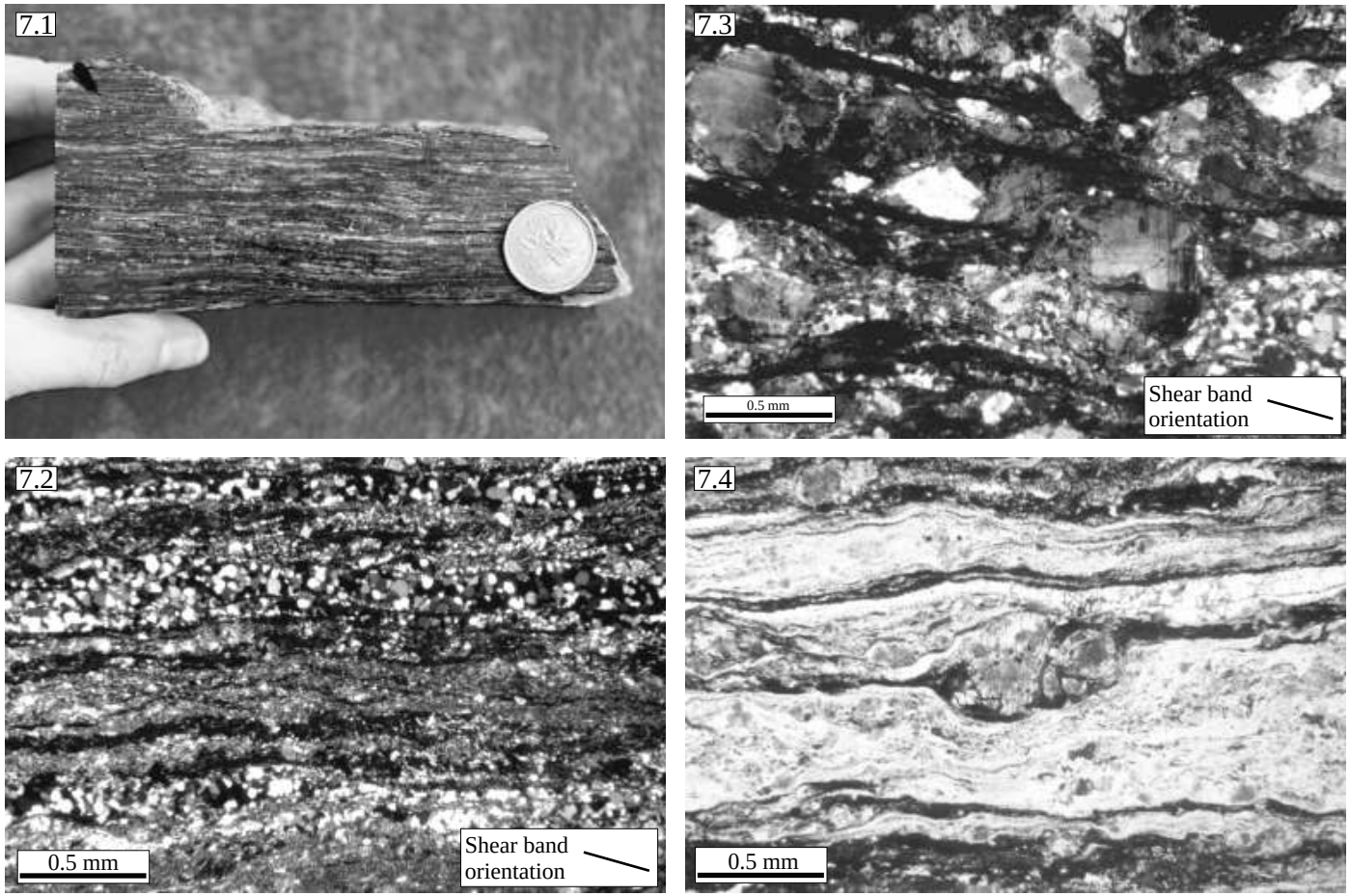

Figure 7 Mylonitic granodiorite. **7.1.** Hand sample (99N-66B) of ultramylonitic MRG from the D2 shear zone west of Kenyon Creek. **7.2.** The same sample in an oriented thin section, cut perpendicular to F2 and parallel to stretching lineation,under crossed polars; annealed quartz ribbons, microcrystalline quartzo-feldspathic bands, and dark bands of biotite-chlorite-hornblende. Subtle shear bands suggest a dextral sense of shear. **7.3.** Sample 99N-66A taken from same shear zone as sample 99N-66B but not as strongly deformed. Section is oriented as in Fig. 7.2 (also under crossed polars). Relict porphyroclasts of feldspar and quartz are mantled by recrystallized feldspar and quartz grains. Shear bands defined by biotite and chlorite indicate a dextral sense of shear. **7.4.** Sample 99N-66B under plane light showing a rotated feldspar porphyroclast with alpha-asymmetry. Shear sense is dextral.

greenschist-facies metamorphism. If this is the case, the temperature of deformation did not reach 450˚-500˚ (Yardley, 1989) and hydrolytic weakening probably facilitated ductile feldspar deformation under greenschist-facies (350º-400ºC) conditions (Etheridge et al., 1984; Brodie and Rutter, 1985; Tullis and Yund, 1985). Late carbonate veinlets (< 1mm) crosscut the foliations.

Porphyritic Dykes

Mafic and felsic porphyritic dykes cut MRG in numerous locations throughout the study area. Strongly foliated, porphyritic biotite granodiorite dykes are common southwest of the Moosehorn Range. Massive to strongly foliated mafic and felsic porphyritic quartz diorite dykes are most voluminous in the southeastern portion of the Moosehorn Range (Fig. 4.1). Although they are texturally variable, all the porphyritic dykes have similar rare earth element compositions and may all have been comagmatic.

Orientations of the dykes and foliations contained within them are variable but they generally strike southwest and dip moderately to steeply towards the northwest, parallel to S2 (Fig. 6.2). Some dykes contain a foliation that is not parallel to the dyke margins and the immediate wallrock MRG is undeformed. This phenomenon may be consistent with the hypothesis proposed by Poulsen (1989) that a shear zone may be confined within dyke rocks that are finer-grained and weaker than the surrounding coarse-grained plutonic wallrock. If a shear zone obliquely intersects with a rheologically weak dyke, shearing can be localized and propagated within the dyke rocks. Poulsen et al. (1986a) suggest that a mylonitic foliation oriented obliquely to a shear zone margin (in this case, a dyke margin) indicates that an inclined component of shear displacement may have taken place during the

deformation. The lack of outcrop in the Moosehorn Range area precludes a thorough analysis of the geometry of these discrete shear zones.

Foliated Porphyritic Granodiorite Dykes

Foliated porphyritic granodiorite dykes are typically less than 15 m thick. They are weakly foliated to mylonitic, and are generally finer grained and more felsic in composition than other porphyritic intrusions. Quartz and feldspar phenocrysts (0.2-1.5 cm in diameter) comprise 10-30% of the rock volume and the matrix is composed of microcrystalline foam-textured quartz ± feldspar, peppered with aligned fine-grained biotite ± hornblende grains. Modal mineralogy of this unit, estimated visually from thin section, is 35-50% quartz, 20-30% plagioclase, 5-20% potassium feldspar, 10-15% biotite, 0-10% hornblende, and minor titanite, epidote, and allanite. The majority of hornblende grains are rimmed by biotite and epidote. As with much of the MRG, feldspars are zoned and moderately to strongly sericitized. Deformation was accommodated by the fine-grained quartz-rich matrix. Abundant quartz phenocrysts, which exhibit deformation bands, subgrains, and irregular grain boundaries, are commonly ribboned parallel to the foliations.

Porphyritic Quartz Diorite Dykes

These dykes range in thickness from several metres to over 300 m. They share most of the features observed in the foliated granodioritic porphyry dykes but they are generally more mafic in composition. Those intruding the MRG southwest of the Moosehorn Range are melanocratic and variably foliated. Varieties encountered along the crest of the Moosehorn Range are generally massive (Fig. 8.1) with a variable colour index. Melanocratic varieties have finer-grained matrices than the more leucocratic ones.

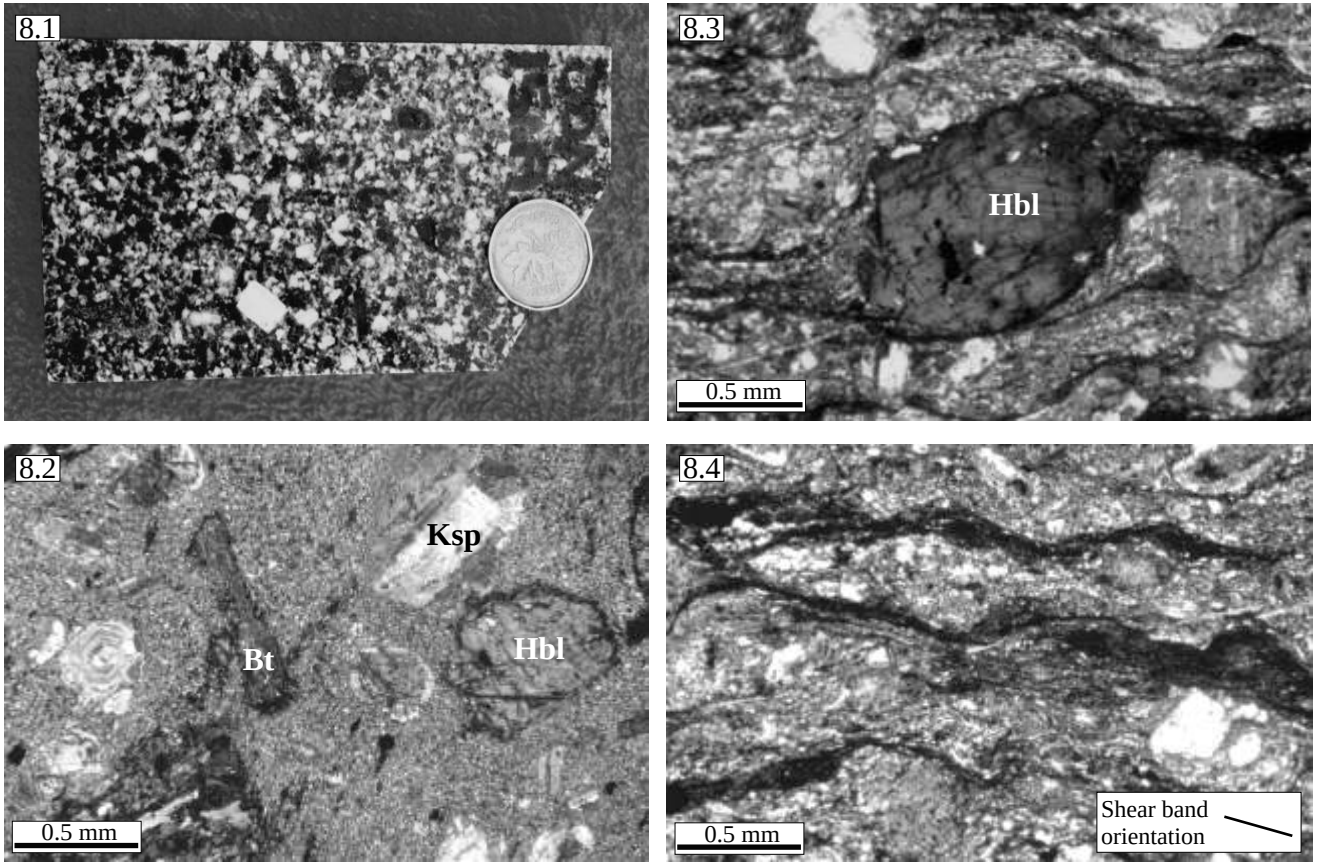

Figure 8 Porphyritic quartz diorite dyke samples. **8.1.** Hand sample 00N-15A of massive quartz diorite collected from the southeastern area of the Moosehorn Range. **8.2.** Photomicrograph of sample 00N-15A in crossed polars. Hornblende, biotite, and variably zoned feldspar phenocrysts within an aphanitic quartzofeldspathic matrix.**8.3.** Foliated sample of quartz diorite (sample 99N-71B), collected near the campsite. Section is cut perpendicular to foliation (F2) and parallel to the lineation, and is shown under crossed polars. Asymmetric rotated hornblende porphyroclast suggests a dextral sense of shear, consistent with shear sense interpreted from foliated MRG at the D2 shear zone west of Kenyon Creek. Recrystallized quartz and feldspar in the groundmass indicates that solid state deformation took place. **8.4.** Same sample as in Fig. 8.3 showing recrystallized quartz and feldspar groundmass, a relict quartz porphyroclast to the lower right, and shear bands defined by biotite and minor chlorite. The orientation of these shear bands is also consistent with a dextral sense of shear.

Phenocrysts of plagioclase, hornblende, biotite, and locally quartz make up 20-30% of the rock volume and are up to 1 cm in size (Figs. 8.2, 8.3). Locally developed shear bands in foliated varieties suggest a dextral sense of displacement (Fig. 8.4), consistent with fault kinematics in the mylonitic MRG near Kenyon Creek. Modal mineralogy for these dykes is as follows: 30-50% plagioclase, 20-40% quartz, 5-20% potassium feldspar, 0-15% hornblende, 10% biotite, and minor titanite, pyrite, and epidote.

Felsite Dykes

Siliceous felsite dykes up to about 5m thick generally strike east, northeast, and north and are steeply dipping. They are fine-grained, light grey to brownish grey in colour, and contain up to 10% phenocrysts (0.2–0.5 cm in diameter) of quartz, unzoned potassium feldspar, and biotite (Fig. 9.1 and 9.2). Hydrothermally altered phases are cream to tan coloured and pervasively sericitized and pyritized, and locally contain abundant carbonate and minor muscovite. The modal mineralogy for relatively unaltered varieties is 50% potassium feldspar, 20-30% quartz, 5-10% plagioclase, and 5-10% biotite. Microcline twins and granophyric and perthitic textures are common. All dykes are undeformed except for one in which the foliation is defined in thin section by aligned biotites and elongate deformed quartz ribbons. This fabric is imperceptible in hand specimen. Parallel felsite and porphyry dykes are commonly closely associated in the field; however, cross cutting relationships between the two phases have not been observed.

Aplites, Pegmatites, and Leucogranites

Variably oriented aplite dykes cross cut all granodiorite and porphyry units as well as the metamorphic wallrock. Contacts between aplite and felsite dykes were not observed.

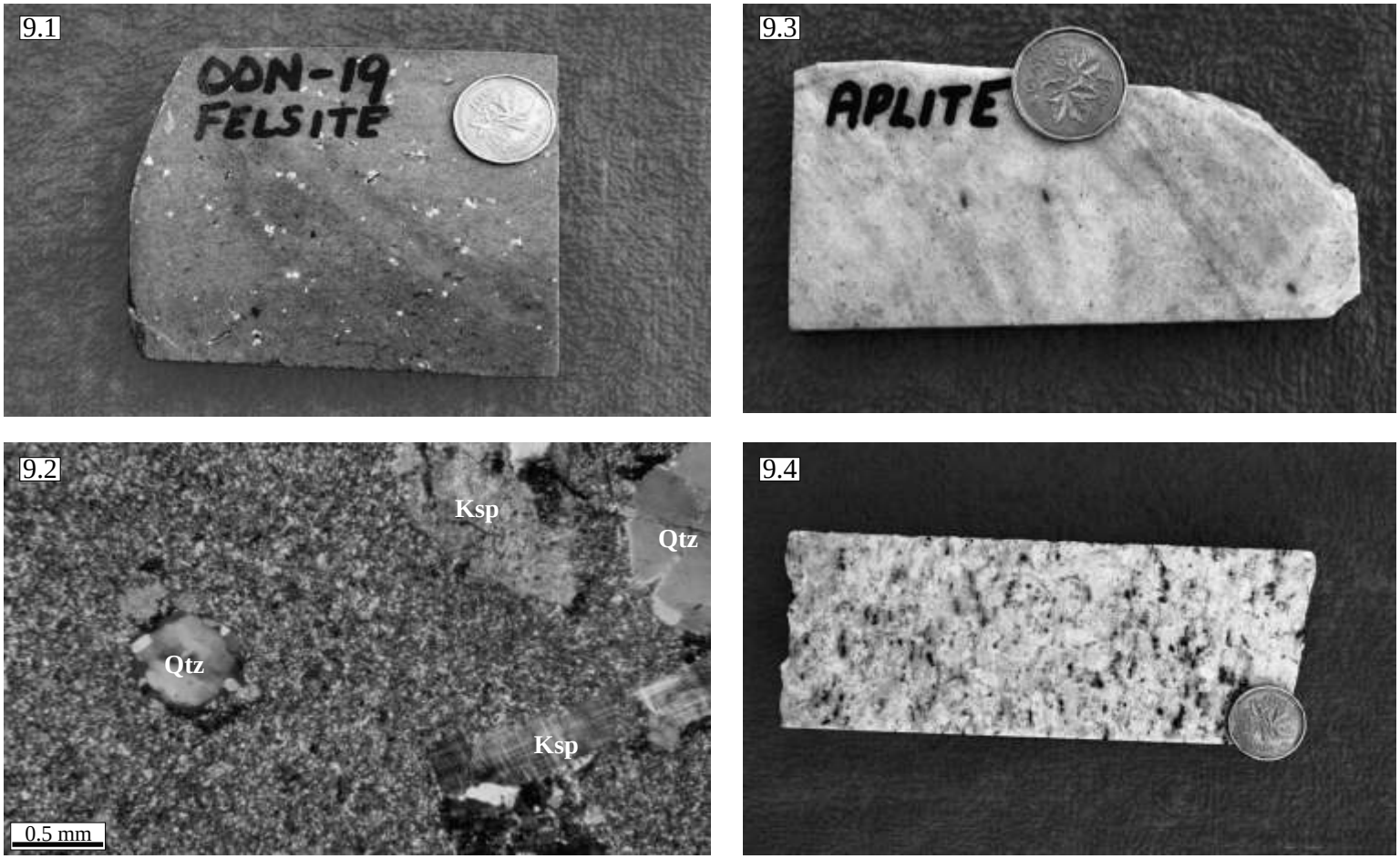

Figure 9 Felsite, aplite, and leucogranite samples. **9.1.** Hand sample of massive felsite dyke material. Phenocrysts of quartz, feldspar, and biotite are visible in the aphanitic groundmass. **9.2.** Photomicrograph of the felsite under crossed polars. **9.3.** Hand sample of foliated aplite with small phenocrysts of biotite and magnetite. **9.4.** Hand sample (00N-74) of leucogranite (alaskite?) with 5-10% biotite phenocrysts.

The aplite dykes, which are typically 2 cm to several metres thick, commonly include pegmatitic zones, particularly at their margins where individual feldspar crystals reach 5 cm in diameter. The aplites are composed predominantly of potassium feldspar and quartz. They are cream to pink in colour, fine- to medium-grained, and exhibit textures ranging from massive to moderately foliated (Fig. 9.3). Highly fractionated varieties are composed almost entirely of quartz. The main accessory mineral phases in the aplites include magnetite, pyrite, biotite, muscovite, and locally garnet, molybdenite, and secondary carbonate. Potassium feldspars are unzoned in thin section and display microcline twins and perthitic intergrowths.

White and pink leucogranitic dykes or plugs of alaskite and quartz monzonite (Fig. 9.4) are common in the northwestern portion of the Moosehorn Range, and may be related to the aplites and pegmatites elsewhere in the study area but contain significantly more plagioclase. Biotite comprises less than 10% of these intrusions. Both massive and weakly foliated varieties have been identified. Siliceous chilled margins in the pink quartz monzonite were observed at contacts with the granodiorite, but contacts between alaskite and the MRG are indistinct and possibly gradational.

Mafic Dykes

Mafic dykes are the youngest intrusive phase in the area. They range from 1 cm to tens of metres in width, are undeformed to locally foliated, and commonly have extremely irregular geometry. The thicker dykes are more consistently planar and generally strike south-southwest and dip moderately to steeply to the west-northwest. Varieties of mafic dykes encountered in outcrop and drill core include fine- to medium-grained black or grey-green basalt or andesite that locally contain amygdules and phenocrysts, coarse-grained

diorite, and lamprophyric minettes. Spatial association between mafic and felsite dykes indicates that the two phases were locally intruded along the same fracture sets. Most of the mafic dykes are cut by late quartz-carbonate veinlets.

The massive fine- to medium-grained dykes are composed dominantly of intergranular-textured plagioclase and clinopyroxene (Fig. 10.1). Abundant amorphous ferromagnesian material is distributed interstitially between the clinopyroxene and plagioclase crystals, and randomly oriented needle-shaped opaque minerals (possibly ilmenite) are ubiquitous. Amphibole, biotite, and chlorite have partially or entirely replaced clinopyroxene and rare primary hornblende. Amphibole, calcite, quartz, and amphibole-filled vesicles up to 3 mm in diameter, phenocrysts of feldspar and chloritized hornblende up to 3 mm in diameter, and disseminated pyrite occur in many dykes.

Shallowly east-dipping undeformed lamprophyric minette dykes about 1 m thick were intersected in two drill holes (DDH LL00-3 and DDH LL00-5; Fig. 4.1). The dykes display chilled margins 2 cm wide, and envelopes of chlorite-sericite-pyrite alteration up to 20 cm wide are developed in adjacent MRG wallrock. Zoned biotite phenocrysts up to 1 cm are evenly distributed within the finer-grained plagioclase-clinopyroxene-biotite-calcite-quartz-potassium feldspar matrix (Fig. 10.2). Round plagioclase-, quartz-, and calcite-filled vesicles up to 5 mm in diameter occur throughout the dykes.

An undeformed coarse-grained diorite was intersected in DDH LL00-6. This phase is compositionally distinguished from the other mafic dykes by the presence of relatively abundant potassium feldspar and blebs of pyrrhotite and chalcopyrite up to about 15 mm in diameter. The geometry of the body is uncertain.

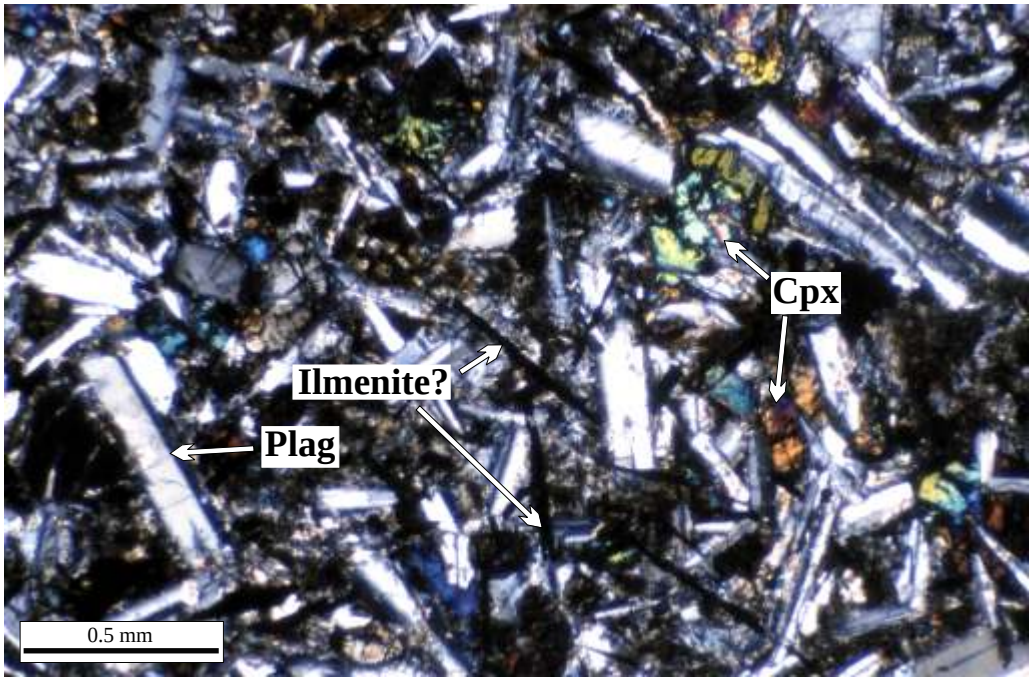

Figure 10.1 Photomicrograph of the massive fine-grained mafic dyke sample 99N-50, under crossed polars.

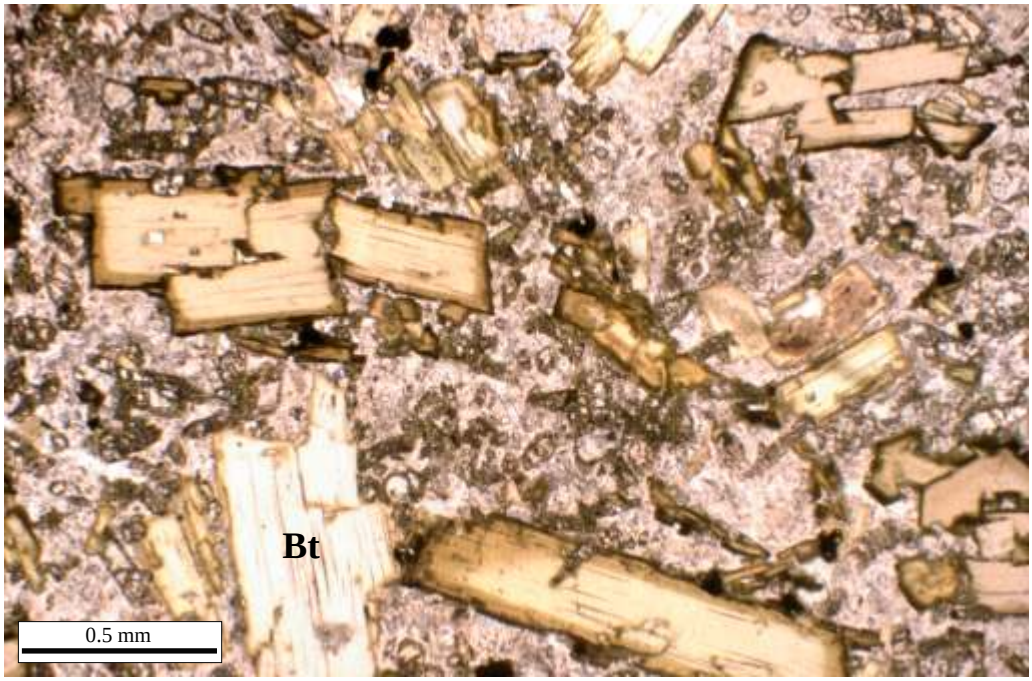

Figure 10.2 Photomicrograph of lamprophyre sample 00N-72 in plane light.

Structural Setting

Understanding the regional structural setting in the Moosehorn Range area is complicated by scarcity of outcrop in the area. Brittle faults in the region can be interpreted from limited field evidence, and from lineaments on satellite images, air photos, and aeromagnetic and radiometric survey maps.

Topographic lineaments recognized from a satellite image of the Moosehorn Range area are defined predominantly by aligned and/or offset creeks, rivers, and ridges. The valleys, which are probably surface expressions of fault structures, create a ladder-like geometry with prominent 10-20 km long north-northwest-trending features interconnected by several northeast-trending ones (Fig. 11). In east-central Alaska, the landscape is dominated by very prominent > 100 km long northeast-striking, steeply-dipping, oblique sinistral faults (Page et al., 1995; McCoy et al., 1997; Newberry et al., 1998a). The northwest- and northeast-trending faults may represent conjugate sets (Newberry, 2000), but temporal relationships between these structures are poorly understood. If the north-northwest-oriented structures in the Moosehorn Range area are dextral strike-slip faults, the northeast structures may be conjugate Riedel sinistral shear faults (R') or normal faults (Twiss and Moores, 1992). The northeast-striking structures in the Moosehorn Range area may be related to the sinistral and/or oblique normal northeast-striking faults in eastern Alaska, which became active in Early Tertiary time and throughout the Cenozoic (Wilson et al., 1985; Page et al., 1995; Newberry et al., 1998a; Smith et al., 1999). Slip along these faults was probably contemporaneous with dextral strike-slip movement along the Tintina and Denali faults (e.g., Jackson and Mortensen, 2000).

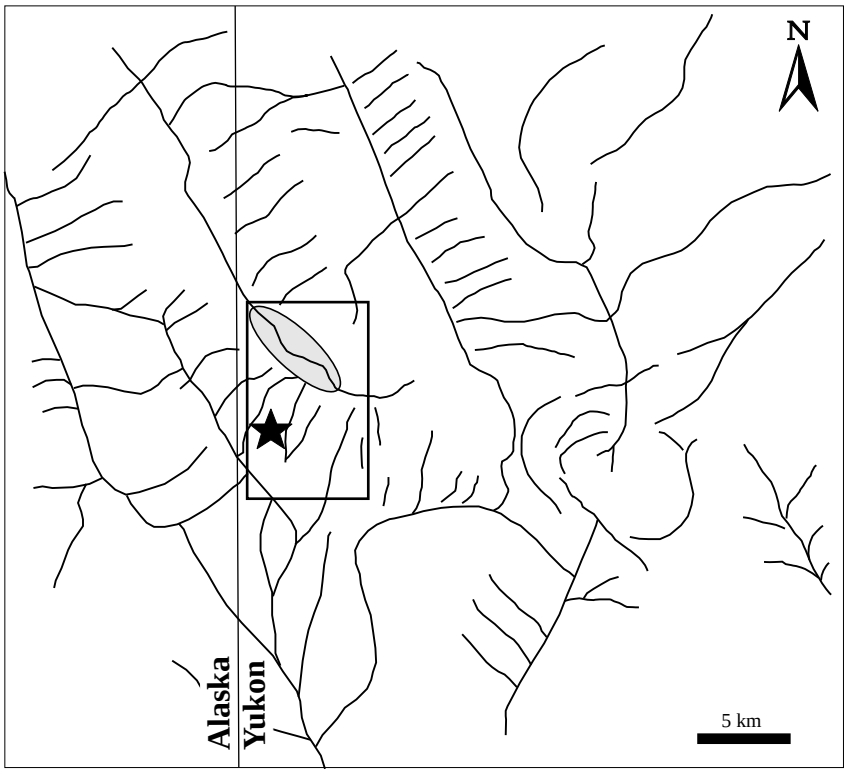

Figure 11 Lineaments in the Moosehorn Range area, traced from a satellite image of the region. The rectangle outlines the main study area and the shaded oval outlines the Moosehorn Range. The star represents the location of gold-bearing veins. Below are two possible scenarios for possible fault geometry based on the lineament orientations. If the NNW-oriented lineaments are dextral strike-slip faults, then the interconnecting NE-striking structures could be (A) conjugate Riedel (R') shear fractures with sinistral displacement *or* (B) sets of normal faults (after Twiss and Moores, 1992). In (A), the dextral Riedel shears (R) are essentially parallel to the mylonites near Kenyon Creek, which also exhibit dextral kinematics. Alternatively, if the NNW-oriented structures are sinistral faults, the NE-striking structures may be sinistral conjugate Riedel shears (R') or thrust faults.

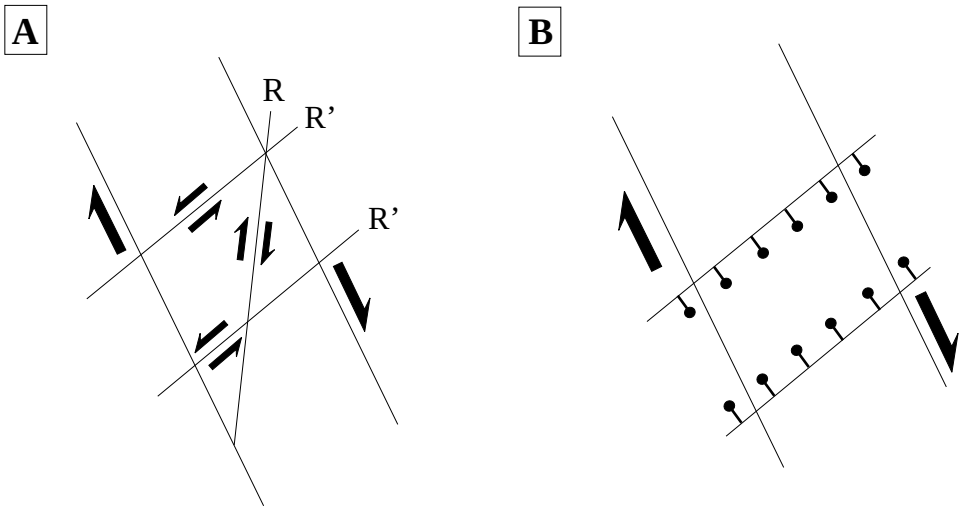

On a magnetic first vertical derivative map of the Stewart River map area (115 N/2) (Shives et al., 2001) the northeast and north-northwest-oriented "faults" manifest as magnetic lows. Distinct north-northwest-trending linear magnetic highs coincide with ridges, including the northwest extension of the Moosehorn Range, but they also cut across topography. These features are probably steeply-dipping mafic to intermediate intrusions with relatively high magnetic susceptibilities, perhaps emplaced along planes of weakness parallel to the fault structures.

The S1 foliations observed in the MRG are probably the oldest deformational fabric in the Moosehorn Range area of the batholith. They formed during or very soon after intrusion. Subsequent dextral deformation generated steeply northwest-dipping D2 mylonites. Porphyritic granodiorite and quartz diorite dykes with margins and foliations approximately parallel to the D2 fabrics probably also formed at this time (see subsequent discussion of absolute timing of intrusion). Brittle fault reactivation along these steeply dipping southwest- and southeast-striking planes of weakness may have generated the regional-scale lineaments recognized on the satellite image. Morin (1977) described a narrow (10 m) zone of mylonite oriented approximately north-south within the composite Seven Mile pluton, which is about 6 km southeast of the Moosehorn Range (Fig. 3). North-south oriented faults are not widely recognized in west-central Yukon Territory; however, faults at this orientation have been recognized in eastern Alaska by Werdon et al. (2001). The relationship of this structural element to D1 and/or D2 in the study area is unknown.

Brittle west-southwest verging compressional faulting postdates all ductile deformation in the Moosehorn Range area. This event is related to the formation of shallowly east-northeast dipping brittle shear zones that contain sheets of high-grade auriferous quartz veins.

Most of the late crosscutting mafic dykes in the area dip moderately to steeply to the west-northwest. They may have been emplaced along S2 planes of weakness that were brittlely reactivated.

Age Constraints on Intrusions

U-Pb, K-Ar, and $^{40}Ar/^{39}Ar$ dating techniques were employed to constrain the timing of crystallization and cooling of various intrusions in the Moosehorn Range area.

Samples and Methods

U-Pb Geochronology

Zircon (Zr) and/or titanite (Ti) were separated from eight samples from surface exposures on the Longline property. The dated units include the MRG (sample 99N-2), mylonitic MRG from the D2 shear zone near Kenyon Creek (sample 99N-66A), MRG (sample 00N-14), foliated granodiorite porphyry (sample 99N-31), quartz diorite porphyry (sample 99N-77), felsite (samples 99N-1 and 99N-58), and aplite (sample 00N-36). Sample locations are shown in Figures 4.1 and 4.2.

Zircon and titanite were separated from 10 to 20 kilogram samples using conventional crushing, grinding, and Wilfley table techniques, followed by heavy liquid and magnetic separation. Mineral fractions for analysis were selected based on grain size, quality, morphology, and magnetic susceptibility. Most titanite fractions were not abraded but most zircon fractions were abraded prior to dissolution using the technique of Krogh (1982) in order to minimize the effects of post-crystallization lead loss. Fraction A from the felsite sample 99N-1 was not abraded due to the small amount of mainly fine-grained zircon recovered. All geochemical separations and mass spectrometry were done in the

Geochronology Laboratory at the University of British Columbia. Samples were dissolved in concentrated HF and HNO_3 in the presence of a mixed $^{233-235}U$-^{205}Pb tracer. Separation and purification of Pb and U employed ion exchange column techniques modified slightly from those of Parrish et al. (1987). Pb and U were eluted separately and loaded together on a single Re filament using a phosphoric acid silica-gel emitter. Isotopic ratios were measured using a modified single collector VG-54R thermal ionization mass spectrometer equipped with a Daly photomultiplier. Most measurements were done in peak switching mode on the Daly detector. U and Pb analytical blanks throughout the course of this study were in the range of 1-4 pg and 3-25 pg, respectively. Uranium fractionation was determined directly on individual runs using $^{233-235}U$ tracer, and Pb isotopic ratios were corrected for a fractionation of 0.12%/amu and 0.43%/amu for Faraday and Daly runs, respectively, based on replicate analyses of the NBS-981 Pb standard and values recommended by Thirlwall (2000). All analytical uncertainties were propagated through the age calculations using the numerical technique of Roddick (1987). Analytical results, with errors presented at the 2σ level, are presented in Table 1.

$^{40}Ar/^{39}Ar$ Geochronology

Four samples of hornblende and biotite from various intrusions on the property were dated using $^{40}Ar/^{39}Ar$ techniques. The $^{40}Ar/^{39}Ar$ age of biotite from the main massive MRG unit (sample 99N-2) gives a cooling age for the intrusion. For the mylonitized MRG sample 99N-62B, which was collected from the same D2 shear zone as sample 99N-66A, the biotite $^{40}Ar/^{39}Ar$ systematics would likely have been reset because the estimated temperature of the greenschist-facies deformation (~350º-400ºC) probably exceeds the $^{40}Ar/^{39}Ar$ closure temperature of biotite (300º-350ºC; McDougall and Harrison, 1999). The hornblende

$^{40}Ar/^{39}Ar$ systematics were most likely not reset during ductile deformation because the 500ºC closure temperature for hornblende (McDougall and Harrison, 1999) exceeds the estimated temperature of deformation. Biotite and hornblende $^{40}Ar/^{39}Ar$ ages for this sample were obtained to constrain the cooling and/or metamorphic history of the mylonites. Finally, biotite from the minette dyke sample 00N-72 was analyzed to constrain the age of this phase of mafic magmatism.

Fresh grains of hornblende and biotite (uniform sizes of about 150-300 μm diameter) were picked under a binocular microscope. The mineral separates were sent to the Geological Survey of Ottawa and were loaded into aluminum foil packets and arranged in an aluminum can 40 mm x 19 mm in diameter, along with flux monitor Fish Canyon Tuff Sanidine (apparent age of 28.03 Ma; Renne et al., 1994). The samples were irradiated in the research reactor at McMaster University in Hamilton, Ontario. The J factors for the samples were as follows: 99N-2 (J = 0.00318840), 99N-62B (J = 0.00272080, same for both hornblende and biotite), and 00N-72 (J = 0.00316870). Upon return from the reactor, samples were divided into aliquots, loaded into individual holes in a copper planchet, and heated and analyzed separately. Data were collected using a VG3600 gas source mass spectrometer at the Geological Survey of Canada in Ottawa. Data collection protocols follow those outlined by Villeneuve and MacIntyre (1997) and data reduction procedures follow Roddick (1988). The data were compiled and the corresponding spectra are presented in Figures 13.1-13.4. Analytical results are presented in Table 2.

K-Ar

Two whole-rock samples (00N-78 and 00N-79) of the fine-grained mafic volcanic rocks collected from drill core were dated by conventional K-Ar methods at Activation

Laboratories in Ancaster, Ontario. Altered and weathered surfaces were removed where possible. Sample 00N-78 was treated with dilute nitric acid to remove intergranular carbonate material. The samples were fused and potassium concentrations were analyzed using inductively coupled plasma optical emission spectroscopy (ICP-OES) (a Thermo Jarrell Ash Enviro II spectrometer) with a minimum of three international standards of varying levels of K on each run. The argon analyses were performed using isotope (^{38}Ar) dilution techniques on a noble gas mass spectrometer. Analytical data are presented in Table 3.

Results

U-Pb

U-Pb analyses of zircon and titanite for the eight analyzed samples are presented in conventional concordia plots in Figures 13.1 to 13.8.

1: Moosehorn Range Hbl-Bt Granodiorite (99N-2): This sample of massive unaltered granodiorite was collected at surface from the location shown in Figure 4.2. Abundant clear, colourless, stubby to elongate prismatic zircon grains of excellent quality were recovered. Most of the grains are > 134 μm in size and contain minor equant or rod-like colourless and/or opaque inclusions. Six fractions of strongly abraded zircons were analyzed. Fraction B (elongate morphology) is almost concordant and fraction C (stubby equant morphology) is concordant (Fig. 12.1). The age of igneous crystallization based on fractions B and C is 99.8 ± 0.4 Ma. Fractions A, D, E, and F returned discordant results reflecting lead loss ± inheritance.

Pale yellow fragments of very clear titanite are abundant in this sample. Four fractions of unabraded titanite were analyzed. Fraction T2 is concordant (Fig. 12.1),

yielding an age of 98.1 ± 0.6 Ma. Fractions T1 and T4 yielded ambiguous age results; fraction T3, however, is nearly concordant at 96.1 ± 0.9 Ma. Inconsistency among the titanite U-Pb ages probably reflects lead loss from the unabraded grains but may also reflect relatively slow cooling of the magma after emplacement.

2: Moosehorn Range Hbl-Bt Granodiorite (00N-14): This sample is from massive coarse-grained unaltered granodiorite collected at surface along the crest of the Moosehorn Range (Fig. 4.1). This sample contains abundant clear, colourless to pale yellow, stubby to elongate prismatic zircon grains. Nearly all the grains are 104-134 μm in size and contain minor colourless to brown rod-like and bubble-shaped inclusions. Four fractions of strongly abraded zircons were analyzed. Fractions A and C are concordant but returned conflicting igneous crystallization ages of 97.9 ± 0.2 Ma and 95.0 ± 0.2 Ma, respectively (Fig. 12.2). Fraction D is discordant. The spread of $^{206}Pb/^{238}U$ ages for the zircon analyses is attributed to post-crystallization lead loss.

Abundant pale yellow fragments of clear inclusion-free titanite were also recovered from the sample. Four fractions of titanite were analyzed; fractions T1 and T2 were not abraded whereas fractions T3 and T4 were strongly abraded. An age of 99.6 ± 0.4 Ma is assigned on the basis of overlapping $^{206}Pb/^{238}U$ ages for concordant analyses of fractions T1, T3, and T4 (Fig. 12.2). This provides a reliable minimum crystallization age for the sample, and is consistent with the age of MRG sample 99N-2. Fraction T2 is nearly concordant but yields a younger $^{206}Pb/^{238}U$ age (95.6 ± 0.4 Ma). This fraction has the highest uranium concentration of all the titanite fractions and was unabraded; the younger $^{206}Pb/^{238}U$ age reflects post-crystallization lead loss.

3: Mylonitic Moosehorn Range Bt-Hbl Granodiorite (99N-66A): This sample of deformed granodiorite was collected at surface immediately west of Kenyon Creek (Fig.

4.1). Abundant clear, colourless to pale yellow, stubby to elongate prismatic zircon grains were recovered. Minor colourless to brown inclusions were present in some grains. Six fractions of strongly abraded zircons were analyzed. Fraction B yielded the only concordant age of 98.3 ± 0.2 Ma (Fig. 12.3). Discordance of fractions A, C, D, E, and F is interpreted to reflect a combination of minor inheritance and post-crystallization lead loss. Titanite was not present in this sample. The $^{206}Pb/^{238}U$ age of the concordant fraction is interpreted as a minimum crystallization age for the sample.

4: Foliated Porphyritic Dyke (99N-77): This sample of porphyritic hornblende-biotite quartz diorite was collected at surface from a dyke at the location shown in Figure 4.2. This unit intrudes the main MRG. Zircon was not as abundant in this rock as in other MRG samples. Four fractions of strongly abraded, clear, colourless to pale yellow, stubby to elongate grains (aspect ratios of up to 6:1) were analyzed. Minor colourless bubble-shaped inclusions were present in nearly all of the grains. All of the analyses are slightly discordant (Fig. 12.4). Fractions C and D, however, plot just off concordia, with $^{206}Pb/^{238}U$ ages of 96.5 ± 0.3 Ma and 96.3 ± 0.3 Ma, respectively (see Fig. 12.4). All of the zircon fractions have high uranium concentrations (up to ~2100 ppm) and, therefore, likely have been affected by post-crystallization lead loss. Inheritance may also have contributed to the discordance of the data.

Four fractions of clear yellow titanite fragments were selected from the sample for analysis. Fraction T1 was not abraded and fractions T3 and T4 were strongly abraded. Fraction T1 is strongly discordant (Fig. 12.4). A best approximation for the minimum igneous crystallization age of this sample is 100.4 ± 0.7 Ma, based on fractions T3 and T4.

5: Mylonitic Biotite-Granodiorite Dyke (99N-31): This sample was collected at surface from a mylonitic granodiorite dyke exposure from the location shown in Figure 4.2.

This unit also cuts the main MRG. Abundant clear, colourless to pale yellow, stubby to elongate prismatic zircons were recovered. Nearly all of the grains contained minor colourless rod- and bubble-shaped inclusions. Five fractions of strongly abraded zircons returned discordant results indicative of significant lead loss and/or inheritance (Fig. 12.5).

Three fractions of clear, colourless to pale yellow, unabraded titanite fragments were analyzed. Fractions T1 and T2 gave $^{206}Pb/^{238}U$ ages of 96.5 ± 0.5 Ma and 93.7 ± 0.4 Ma, respectively (Fig. 12.5). Fraction T3 is discordant. No crystallization age can be assigned for sample 99N-31 based on the zircon and titanite data, but the titanite $^{206}Pb/^{238}U$ ages provide minimum age constraints on the formation of the dyke. A relative age can be constrained by crosscutting relationships in the field; this dyke cuts the 99.8 ± 0.4 Ma MRG (sample 99N-2) and is itself cut by gold bearing quartz veins that were emplaced at around 92.6 ± 0.9 Ma (see Chapter 3 of this study). Therefore, the dyke must have intruded within this time interval.

6: Felsite Dyke (99N-1): This sample was collected at surface (Fig. 4.2); it is a sericite- and pyrite-altered felsite dyke that cuts the MRG. The dyke is itself cut by an auriferous quartz vein emplaced at approximately 92.6 ± 0.9 Ma (see Chapter 3 of this study). Zircon grains in this sample are all of poor quality. The grains are colourless to yellow, fine (<74 μm to at *most* 134 μm), and are commonly cloudy. Nearly all the grains contain minor colourless to brown rod- and bubble-shaped inclusions. Six zircon fractions were analyzed, of which only fraction A was not abraded. Fractions E and F returned ambiguous age results. Fractions B, C, and D have apparently concordant $^{206}Pb/^{238}U$ age ages of 96.1 ± 0.3 Ma, 102.7 ± 0.2 Ma, and 101.3 ± 0.3 Ma, respectively (Fig. 12.6). An igneous crystallization age for the dyke, based on the concordance of fraction B and the overlapping but slightly discordant fraction A, is 96.0 ± 0.4 Ma. Both fractions A and B

Table 1. U-Pb Analytical data for Moosehorn Range area samples analyzed in this study

Fraction[1]	Wt. mg	U[2] ppm	Pb*[3] ppm	$^{206}Pb/^{204}Pb$[4]	Pb[5] pg	^{208}Pb[3] %	Isotopic Ratios (1 sigma, %)[6] $^{206}Pb/^{238}U$	$^{207}Pb/^{235}U$	$^{207}Pb/^{206}Pb$	Apparent Age (2 sigma, Ma)[6] $^{206}Pb/^{238}U$	$^{207}Pb/^{235}U$	$^{207}Pb/^{206}Pb$	Th/U
Moosehorn Range Samples													
Sample 99N-2; Dawson Range Batholith Hornblende-Biotite Granodiorite													
A, c, n2, sp	0.152	725	11.2	16830	6	8.0	0.015715 (0.10)	0.104468 (0.18)	0.048212 (0.10)	100.5 (0.2)	100.9 (0.3)	109.7 (4.6)	0.285
B, c, n2, ep	0.122	630	9.7	8946	8	8.4	0.015588 (0.16)	0.103439 (0.22)	0.048127 (0.13)	99.7 (0.3)	99.9 (0.4)	105.5 (6.2)	0.300
C, c, n2, sp	0.105	516	8.0	3754	14	9.2	0.015640 (0.13)	0.103721 (0.23)	0.048099 (0.16)	100.0 (0.2)	100.2 (0.4)	104.1 (7.5)	0.331
D, c, n2, sp	0.020	853	13.2	284	59	12.5	0.015058 (0.13)	0.098380 (0.64)	0.047385 (0.56)	96.3 (0.2)	95.3 (1.2)	68.7 (26.6)	0.468
E, c, n2, sp	0.036	419	6.6	2119	7	10.3	0.015514 (0.23)	0.106761 (0.49)	0.049910 (0.42)	99.2 (0.5)	103.0 (1.0)	190.8 (19.4)	0.381
F, c, n2, ep	0.027	437	7.5	1425	9	10.9	0.017011 (0.14)	0.115969 (0.46)	0.049443 (0.42)	108.7 (0.3)	111.4 (1.0)	168.9 (19.3)	0.404
T1*, f, m5, a	0.290	197	2.6	103	603	1.4	0.014427 (0.18)	0.091613 (1.45)	0.046057 (1.32)	92.3 (0.3)	89.0 (2.5)	0.6 (62.3)	0.045
T2*, f, m5, a	0.580	567	7.9	247	1350	1.6	0.015293 (0.20)	0.101400 (0.58)	0.048089 (0.45)	97.8 (0.4)	98.1 (1.1)	103.6 (21.1)	0.052
Sample 99N-66A; Mylonitized Dawson Range Batholith Hornblende-Biotite Granodiorite													
A, m, n2, ep	0.097	917	14.0	11030	8	8.7	0.015469 (0.10)	0.102899 (0.17)	0.048245 (0.10)	99.0 (0.2)	99.4 (0.3)	111.3 (4.9)	0.315
B, m, n2, sp	0.063	607	9.3	8135	4	9.8	0.015369 (0.12)	0.101768 (0.22)	0.048023 (0.14)	98.3 (0.2)	98.4 (0.4)	100.4 (6.7)	0.357
C, m, n2, ep	0.045	864	13.0	9012	4	8.7	0.015300 (0.12)	0.101997 (0.21)	0.048348 (0.14)	97.9 (0.2)	98.6 (0.4)	116.3 (6.4)	0.312
D, m, n2, ep	0.074	701	9.9	6864	7	8.7	0.014362 (0.11)	0.095685 (0.21)	0.049321 (0.14)	91.9 (0.2)	92.8 (0.4)	115.0 (6.4)	0.311
E, c, n2, sp	0.039	514	8.3	6479	3	10.0	0.016064 (0.11)	0.106965 (0.20)	0.048293 (0.14)	102.7 (0.2)	103.2 (0.4)	113.6 (6.5)	0.367
F, c, n2, sp	0.044	492	7.9	5813	4	9.8	0.015999 (0.14)	0.107107 (0.24)	0.048554 (0.16)	102.3 (0.3)	103.3 (0.5)	126.3 (7.5)	0.358
Sample 00N-14; Moosehorn Range Hornblende-Biotite Granodiorite													
A, m, n2, ep	0.046	633	9.7	3723	7	10.4	0.015303 (0.12)	0.101489 (0.27)	0.048099 (0.21)	97.9 (0.2)	98.2 (0.5)	104.1 (9.7)	0.380
C, m, n2, sp	0.077	409	6.1	1993	15	10.3	0.014843 (0.12)	0.098126 (0.42)	0.047946 (0.37)	95.0 (0.2)	95.0 (0.8)	96.6 (17.4)	0.376
D, m, n2, ep	0.096	536	8.1	9338	5	9.7	0.015072 (0.12)	0.100114 (0.21)	0.048176 (0.14)	96.4 (0.2)	96.9 (0.4)	107.9 (6.5)	0.351
T1*, m, m10, a	0.190	266	3.9	238	219	3.5	0.015591 (0.11)	0.103461 (0.55)	0.048129 (0.46)	99.7 (0.2)	100.0 (1.0)	105.6 (21.7)	0.120
T2*, m, m10, a	0.270	586	8.3	429	352	5.1	0.014941 (0.19)	0.099249 (0.39)	0.048179 (0.31)	95.6 (0.4)	96.1 (0.7)	108.1 (14.7)	0.175
T3, c, m10, a	0.420	327	4.8	289	483	4.4	0.015535 (0.10)	0.102164 (0.44)	0.047695 (0.35)	99.4 (0.2)	98.8 (0.8)	84.2 (16.9)	0.149
T4, c, m10, a	0.373	369	5.4	382	359	5.1	0.015543 (0.10)	0.102818 (0.37)	0.047977 (0.28)	99.4 (0.2)	99.4 (0.7)	98.1 (13.4)	0.175
Sample 99N-31; Foliated Granodiorite Porphyry Dyke													
A, c, n2, ep	0.045	990	14.6	3256	12	10.9	0.014548 (0.13)	0.096649 (0.24)	0.048184 (0.17)	93.1 (0.2)	93.7 (0.4)	108.3 (8.2)	0.401
B, c, n2, sp	0.088	850	12.9	2267	31	10.3	0.015060 (0.11)	0.101405 (0.47)	0.048834 (0.43)	96.4 (0.2)	98.1 (0.9)	139.9 (20.3)	0.377
D, c, n2, ep	0.056	853	14.0	5934	8	10.3	0.016312 (0.12)	0.110404 (0.21)	0.049088 (0.14)	104.3 (0.2)	106.3 (0.4)	152.0 (6.4)	0.380
E, c, n2, ep	0.014	508	8.1	1433	5	13.0	0.015432 (0.15)	0.104097 (0.64)	0.048923 (0.59)	98.7 (0.3)	100.6 (1.2)	144.2 (28.0)	0.493
F, c, n2, ep	0.032	995	16.8	5717	6	11.8	0.016528 (0.09)	0.110947 (0.23)	0.048686 (0.17)	105.7 (0.2)	106.8 (0.5)	132.7 (8.1)	0.440
T1*, c, m5, a	0.430	128	1.8	52	1530	4.4	0.015085 (0.26)	0.097387 (3.92)	0.046821 (3.71)	96.5 (0.5)	94.4 (7.1)	40.1 (168.7)	0.149
T2*, c, m5, a	0.470	155	2.1	63	1490	4.7	0.014637 (0.20)	0.096413 (2.83)	0.047773 (2.68)	93.7 (0.4)	93.5 (5.1)	88.0 (122.4)	0.161
T3*, m, m5, a	0.130	124	1.7	63	321	3.0	0.014364 (0.23)	0.100961 (2.87)	0.050979 (2.69)	91.9 (0.4)	97.7 (5.3)	239.9 (129.0)	0.102

Table 1 (continued)

Sample 99N-77; Foliated Porphyritic Quartz Diorite Dyke													
A, f, n2, sp	0.022	527	7.7	2138	5	10.3	0.014595 (0.15)	0.097529 (0.45)	0.048466 (0.39)	93.4 (0.3)	94.5 (0.8)	122.1 (18.5)	0.376
B, f, n2, ep	0.065	531	7.8	4041	8	10.4	0.014595 (0.18)	0.099006 (0.29)	0.049199 (0.19)	93.4 (0.3)	95.9 (0.5)	157.3 (8.9)	0.383
C, m, n2, ep	0.025	993	15.3	4426	5	11.4	0.015075 (0.17)	0.101024 (0.32)	0.048604 (0.26)	96.5 (0.3)	97.7 (0.6)	128.8 (12.2)	0.424
D, m, n2, ep	0.007	2131	32.5	2910	5	11.0	0.015058 (0.14)	0.100949 (0.35)	0.048621 (0.29)	96.3 (0.3)	97.7 (0.6)	129.6 (13.7)	0.408
T1*, m, m5, a	0.067	66	1.1	47	144	16.6	0.014838 (0.30)	0.106347 (3.92)	0.051981 (3.67)	94.9 (0.6)	102.6 (7.6)	284.6 (177.1)	0.663
T2*, m, m5, a	0.089	46	0.7	35	229	16.6	0.014665 (0.48)	0.076034 (8.68)	0.037602 (8.27)	93.9 (0.9)	74.4 (12.5)	inconclusive	inconclusive
T3, c, m5, a	0.045	59	1.0	113	27	16.7	0.015656 (0.19)	0.106373 (2.21)	0.049279 (2.10)	100.1 (0.4)	102.6 (4.3)	161.1 (101.1)	0.662
T4, c, m5, a	0.057	103	1.7	86	84	12.7	0.015758 (0.15)	0.107884 (1.58)	0.049653 (1.46)	100.8 (0.3)	104.0 (3.1)	178.8 (69.4)	0.480
Sample 99N-1; Felsite dyke													
A*, m, n1 & m1, sp	0.013	1621	24.7	202	106	11.3	0.014967 (0.12)	0.099091 (0.84)	0.048016 (0.76)	95.8 (0.2)	95.9 (1.5)	100.1 (36.4)	0.416
B, m, n1 & m1, ep	0.009	2578	40.5	323	70	13.7	0.015017 (0.16)	0.099361 (1.28)	0.047989 (1.22)	96.1 (0.3)	96.2 (2.3)	98.7 (58.7)	0.521
C, m, n1 & m1, sp	0.037	902	14.9	224	159	12.5	0.016065 (0.10)	0.108698 (0.54)	0.049073 (0.46)	102.7 (0.2)	104.8 (1.1)	151.3 (21.5)	0.469
D, m, n1 & m1, sp	0.012	602	9.6	2149	3	10.7	0.015831 (0.14)	0.104788 (0.48)	0.048008 (0.43)	101.3 (0.3)	101.2 (0.9)	99.7 (20.2)	0.394
F, f, n1 & m1, sp	0.040	1447	14.3	444	82	12.9	0.009530 (0.27)	0.064645 (0.58)	0.049199 (0.42)	61.1 (0.3)	63.6 (0.7)	157.3 (19.6)	0.488

[1]Upper case letter = zircon fraction identifier (titanite fractions are T1, T2, etc.); all fractions were air abraded except for those marked with *

Grain size: c= >134 μm, m= <134 μm and > 104 μm, f= <104 μm and >74 μm.

Titanites were recovered from magnetic fractions whereas all zircons are non-magnetic on a Frantz magnetic separator at field strength of 1.8-2.0A with a 20˚ front slope; m5=magnetic at side slope of 5˚, m1=magnetic at side slope of 1˚, n2=non-magnetic at side slope of 2˚, n1=non-magnetic at side slope of 1˚

Grain shape: e=elongate, p=prismatic, s=stubby, a=anhedral

[2]U blank correction of 1 pg +/- 20%; U fractionation corrections were measured for each run with a double ^{233}U-^{235}U spike (about 0.005/amu).

[3]Radiogenic Pb

[4]Measured ratio corrected for spike and Pb fractionation of 0.0035/amu +/- 20% (Daly collector) and 0.0012 /amu +/- 20% and laboratory blank Pb of 1-3 pg +/- 20%. Laboratory blank Pb concentrations and isotopic compositions based on total procedural blanks analyzed.

[5]Total common Pb in analysis based on blank isotopic composition

[6]Corrected for blank Pb, U, and common Pb. Common Pb corrections basedon Pb isotpic compositions of feldspars from individual rock samples

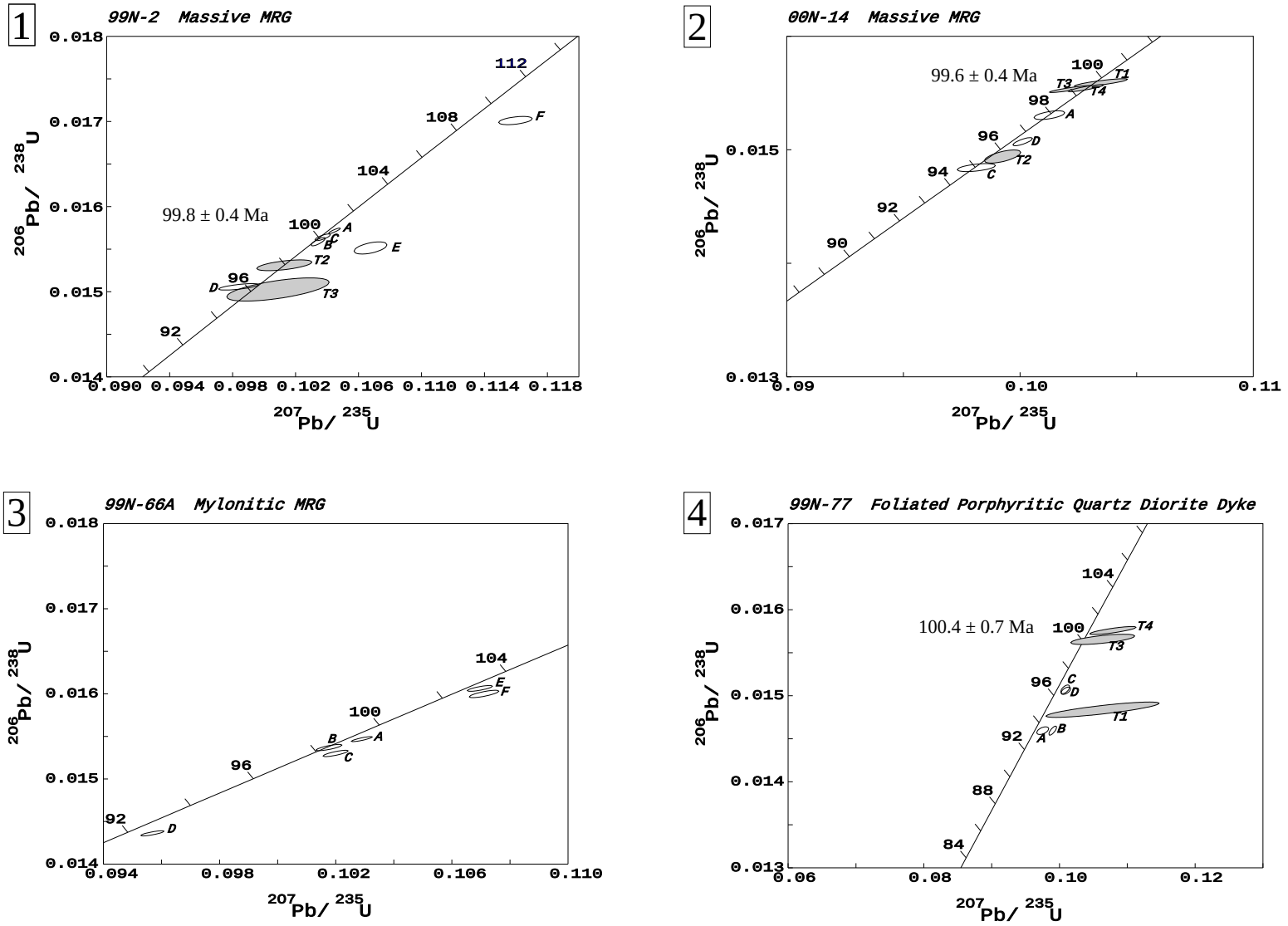

Figure 12 U-Pb concordia plots for various intrusions in the Moosehorn Range area. Sample numbers and rock types are shown. Open and solid ellipses denote zircon and titanite fractions, respectively. Results are discussed in the text.

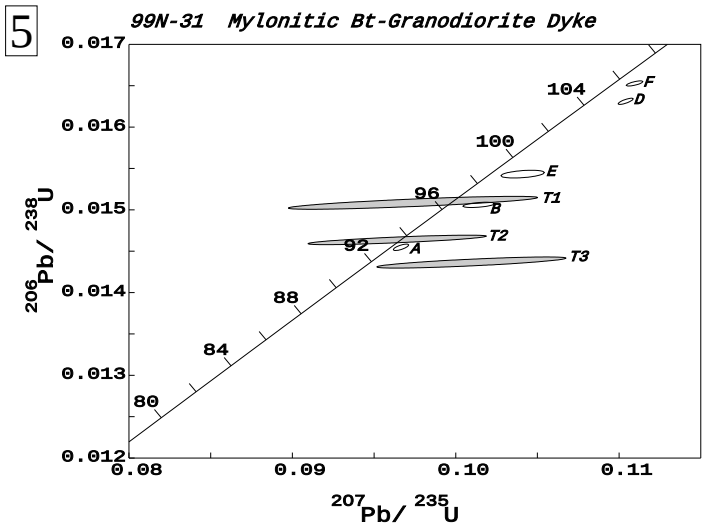

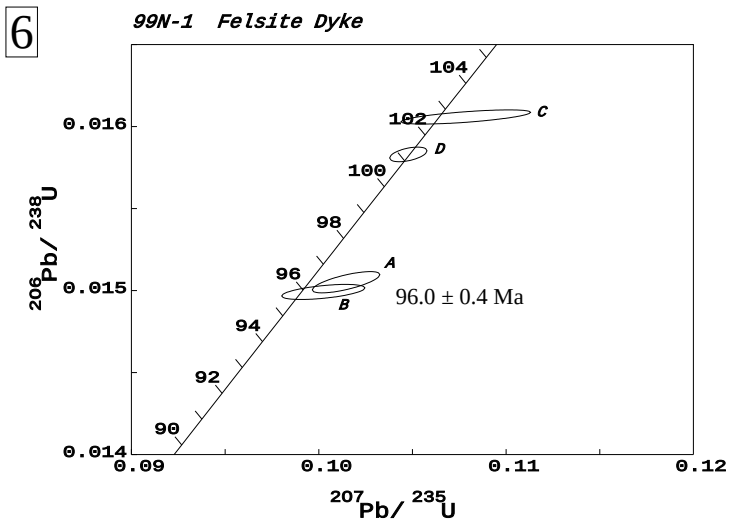

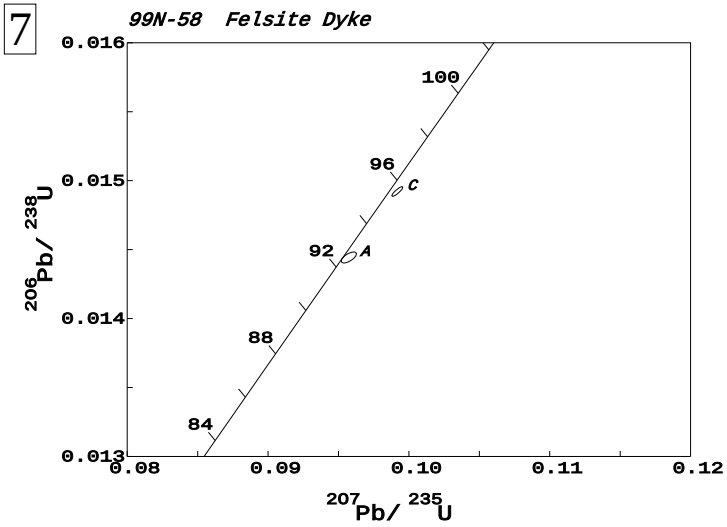

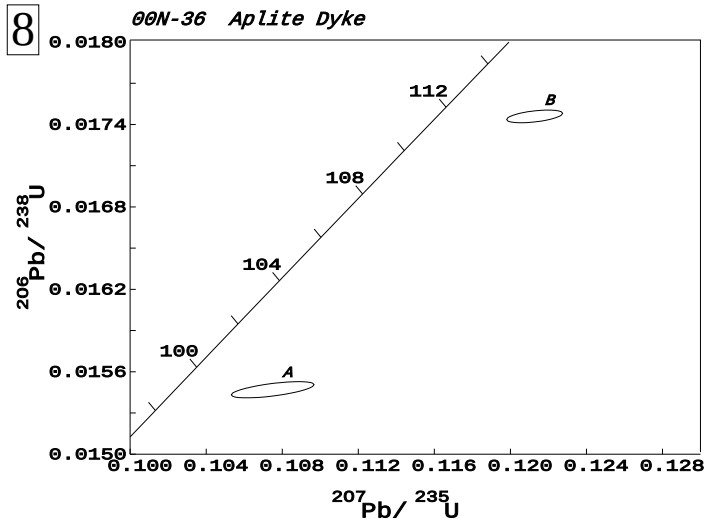

Figure 12 continued.

have high uranium concentrations (> 1600 ppm U) and may have undergone post-crystallization Pb loss, in which case 96.0 ± 0.4 Ma would a minimum estimate for the age of dyke emplacement. The ages obtained for fractions C and D are considered inaccurate because the dyke cannot be older than the wallrock MRG, which formed at 99.8 ± 0.4 Ma. Titanite was not present in this sample.

7 and 8: Zircon analyses from felsite dyke sample 99N-58A and aplite sample 00N-36 (sample locations shown on Fig. 4.1) were strongly discordant and do not yield conclusive age information (Figs. 12.7 and 12.8). Zircon grains from both samples are fine-grained (≤ 74 μm), pervasively fractured, variably cloudy, and consistently uranium-rich (1200-3880 ppm U). The ages of these dykes can only be constrained as younger than the 99.8 ± 0.4 Ma wallrock MRG that they intruded into, and older than the fine-grained mafic dykes that crosscut them.

$^{40}Ar/^{39}Ar$

The $^{40}Ar/^{39}Ar$ age spectrum diagrams are presented in Figures 13.1 to 13.4. An excellent plateau age of 94.4 ± 0.9 Ma was obtained for biotite from the MRG (sample 99N-2). Despite minor excess ^{40}Ar in the early step-heating stages for hornblende from the mylonitized MRG (sample 99N-62B), a satisfactory plateau age of 100.4 ± 1.1 Ma was achieved in the later high-temperature releases. Biotite from the same sample shows considerable loss of ^{40}Ar in the early stages, but in the later stages yielded a good plateau age of 93.4 ± 0.9 Ma. This age is within error of that for biotite from the undeformed granodiorite (sample 99N-2). The first aliquot of sample 00N-72 (biotite) from the late cross cutting minette dyke shows a very good plateau over about 90% of the steps, indicating a significantly younger age of 64.3 ± 0.6 Ma.

Table 2. $^{40}Ar/^{39}Ar$ isotopic data for Moosehorn Range area intrusions.

Power[a]	Volume ^{39}Ar x10^{-11} cc	$^{36}Ar/^{39}Ar$	$^{37}Ar/^{39}Ar$	$^{38}Ar/^{39}Ar$	$^{40}Ar/^{39}Ar$	$\%^{40}Ar$ ATM	$*^{40}Ar/^{39}Ar$	f_{39}[b] (%)	Apparent Age Ma[c]
99N-62B Biotite; from mylonitized MRG; J=.00272080									
Aliquot: A									
3.4	12.5858	0.0054±0.0001	0.012±67.074	0.038±0.001	20.517±0.029	7.7	18.934±0.042	3.2	90.63±0.20
3.9	19.8144	0.0025±0.0000	0.011±37.207	0.036±0.001	19.696±0.076	3.8	18.952±0.075	5.1	90.71±0.35
4.2	13.8841	0.0016±0.0001	0.010±69.856	0.036±0.001	19.430±0.062	2.4	18.963±0.071	3.6	90.76±0.33
5.0	30.2673	0.0012±0.0001	0.014±39.280	0.037±0.001	19.374±0.057	1.8	19.025±0.059	7.8	91.05±0.28
6.0	42.7097	0.0007±0.0001	0.022±42.625	0.036±0.000	19.304±0.051	1	19.112±0.054	11	91.45±0.25
12.0	43.2469	0.0008±0.0001	0.079±16.814	0.036±0.000	19.402±0.044	1.2	19.173±0.048	11.1	91.74±0.22
2.4	1.4246	0.0740±0.0022	0.056±60.268	0.056±0.003	37.463±0.507	58.3	15.603±0.808	0.4	75.01±3.80
3.0	6.2531	0.0141±0.0003	0.021±34.751	0.042±0.001	22.727±0.111	18.3	18.569±0.137	1.6	88.92±0.64
Aliquot: B									
2.4	12.4397	0.0086±0.0003	0.022±0.001	0.042±0.011	21.094±0.085	12.1	18.548±0.107	3.2	88.82±0.50
3.4	14.7473	0.0032±0.0001	0.019±0.001	0.042±0.011	20.025±0.090	4.7	19.075±0.088	3.8	91.28±0.41
3.7	7.8216	0.0025±0.0001	0.016±0.001	0.043±0.011	19.923±0.060	3.6	19.197±0.066	2	91.85±0.31
3.9	7.9751	0.0021±0.0001	0.021±0.001	0.042±0.011	19.844±0.084	3.2	19.209±0.083	2.1	91.90±0.39
4.2	9.8485	0.0021±0.0001	0.025±0.001	0.042±0.011	19.956±0.074	3.2	19.321±0.076	2.5	92.43±0.36
4.6	9.1069	0.0016±0.0001	0.029±0.002	0.043±0.011	19.717±0.080	2.5	19.230±0.080	2.3	92.00±0.37
5.0	9.8401	0.0016±0.0001	0.038±0.002	0.042±0.011	19.857±0.085	2.4	19.379±0.087	2.5	92.70±0.40
5.6	21.5668	0.0013±0.0001	0.040±0.001	0.042±0.011	19.727±0.063	1.9	19.357±0.066	5.6	92.60±0.31
6.0	16.9836	0.0011±0.0001	0.062±0.002	0.043±0.011	19.663±0.074	1.6	19.347±0.074	4.4	92.55±0.35
6.5	10.0513	0.0013±0.0003	0.078±0.002	0.043±0.011	19.800±0.087	1.9	19.423±0.126	2.6	92.91±0.59
12.0	44.7879	0.0011±0.0000	0.072±0.001	0.043±0.011	19.801±0.049	1.6	19.491±0.050	11.5	93.22±0.23
Aliquot: C									
2.4	0.7032	0.0658±0.0032	0.159±0.015	0.045±0.011	34.522±0.743	56.3	15.087±0.929	0.2	72.58±4.38
3.0	4.4969	0.0070±0.0002	0.024±0.002	0.041±0.011	20.999±0.210	9.8	18.944±0.199	1.2	90.67±0.93
3.5	3.3151	0.0030±0.0003	0.023±0.002	0.042±0.011	20.238±0.144	4.4	19.344±0.156	0.9	92.54±0.73
3.9	6.6898	0.0022±0.0002	0.012±0.001	0.042±0.011	20.176±0.125	3.3	19.520±0.130	1.7	93.35±0.61
4.2	4.8779	0.0014±0.0002	0.012±0.001	0.040±0.011	19.949±0.094	2	19.542±0.103	1.3	93.46±0.48
4.6	5.5145	0.0015±0.0002	0.017±0.001	0.040±0.011	20.038±0.148	2.2	19.589±0.157	1.4	93.68±0.73
5.0	3.286	0.0018±0.0004	0.025±0.002	0.042±0.011	19.910±0.143	2.7	19.370±0.175	0.9	92.65±0.82
5.6	8.5414	0.0013±0.0002	0.030±0.001	0.041±0.011	19.884±0.102	1.9	19.514±0.113	2.2	93.33±0.53
6.5	8.6125	0.0006±0.0001	0.051±0.002	0.041±0.011	19.690±0.116	0.9	19.508±0.118	2.2	93.30±0.55
12.0	7.2237	0.0007±0.0001	0.189±0.008	0.043±0.011	19.784±0.072	1	19.577±0.073	1.9	93.62±0.34
99N-62B Hornblende; from mylonitized MRG; J=.00272080									
Aliquot: A									
3	0.3537	0.2238±0.0053	0.771±0.040	0.186±0.013	97.722±1.555	67.7	31.599±1.437	0.7	148.79±6.50
3.9	0.5209	0.0577±0.0018	2.170±0.078	0.167±0.011	37.826±0.604	45.1	20.772±0.587	1	99.18±2.73
4.2	1.9083	0.0103±0.0006	4.618±0.081	0.364±0.014	23.775±0.320	12.9	20.716±0.394	3.7	98.92±1.83
4.6	4.0978	0.0067±0.0003	5.739±0.071	0.563±0.014	23.061±0.209	8.6	21.080±0.349	8	100.61±1.62
5	7.8422	0.0017±0.0001	5.899±0.053	0.591±0.012	21.531±0.072	2.4	21.012±0.302	15.2	100.30±1.40
5.6	1.4967	0.0059±0.0005	5.599±0.057	0.552±0.013	22.775±0.213	7.7	21.029±0.351	2.9	100.37±1.63
12	2.9255	0.0041±0.0003	8.867±0.089	0.603±0.014	22.145±0.152	5.5	20.935±0.467	5.7	99.94±2.17
Aliquot: B									
3	0.3717	0.1929±0.0090	1.014±0.062	0.216±0.012	115.729±1.196	49.2	58.740±2.677	0.7	267.48±11.33
3.9	4.9709	0.0085±0.0002	4.173±0.042	0.395±0.011	23.775±0.096	10.6	21.258±0.231	9.7	101.44±1.07
4.2	5.0379	0.0043±0.0001	5.354±0.060	0.526±0.012	22.356±0.117	5.8	21.067±0.288	9.8	100.55±1.34
4.6	0.5335	0.0140±0.0016	4.536±0.079	0.417±0.016	25.088±0.448	16.6	20.930±0.575	1	99.92±2.67
5	0.9649	0.0107±0.0010	5.080±0.064	0.453±0.014	24.233±0.317	13.1	21.070±0.437	1.9	100.56±2.03
5.6	1.0802	0.0069±0.0007	4.906±0.071	0.444±0.015	23.000±0.305	8.8	20.966±0.387	2.1	100.09±1.80
12	2.2904	0.0057±0.0004	6.828±0.095	0.506±0.014	22.770±0.139	7.4	21.093±0.373	4.5	100.68±1.73
Aliquot: C									
3	0.1135	0.5266±0.0240	1.928±0.179	0.591±0.037	277.831±11.424	56	122.241±6.052	0.2	518.00±22.30
3.9	0.256	0.1292±0.0048	0.565±0.033	0.087±0.011	64.224±1.329	59.5	26.029±1.372	0.5	123.44±6.29
4.2	0.3259	0.0698±0.0030	0.690±0.039	0.073±0.011	40.172±0.811	51.4	19.541±0.904	0.6	93.45±4.22
4.6	1.0249	0.0152±0.0008	3.727±0.083	0.313±0.013	25.759±0.301	17.4	21.268±0.356	2	101.48±1.65
5	6.2304	0.0031±0.0001	5.223±0.102	0.450±0.012	21.899±0.270	4.2	20.973±0.366	12.1	100.12±1.70
5.6	5.3732	0.0017±0.0002	5.459±0.095	0.440±0.012	21.524±0.147	2.4	21.004±0.313	10.4	100.26±1.45
6.5	1.8688	0.0039±0.0004	5.081±0.093	0.383±0.013	22.114±0.195	5.2	20.964±0.322	3.6	100.07±1.50
12	1.8753	0.0014±0.0007	7.559±0.127	0.443±0.011	21.494±0.150	2	21.068±0.441	3.6	100.56±2.05

Power[a]	Volume ^{39}Ar x10^{-11} cc	$^{36}Ar/^{39}Ar$	$^{37}Ar/^{39}Ar$	$^{38}Ar/^{39}Ar$	$^{40}Ar/^{39}Ar$	$\%^{40}Ar$ ATM	$*^{40}Ar/^{39}Ar$	f_{39}[b] (%)	Apparent Age Ma[c]
00N-2 Biotite; from massive MRG; J=.00318840									
Aliquot: A									
2.4	1.1537	0.0477±0.0054	0.040±59.912	0.054±0.003	30.731±0.244	45.9	16.627±1.597	0.4	93.19±8.73
2.8	3.3975	0.0099±0.0005	0.016±25.723	0.047±0.002	19.547±0.077	15	16.613±0.160	1.3	93.11±0.87
3.5	19.588	0.0029±0.0001	0.006±34.751	0.046±0.000	17.648±0.050	4.8	16.797±0.053	7.2	94.12±0.29
3.9	16.6543	0.0008±0.0001	0.005±34.011	0.048±0.001	17.084±0.034	1.3	16.858±0.039	6.1	94.46±0.21
4.2	14.4298	0.0010±0.0001	0.006±49.373	0.048±0.001	17.154±0.044	1.7	16.861±0.044	5.3	94.47±0.24
4.6	13.2936	0.0009±0.0001	0.011±72.787	0.047±0.001	17.119±0.038	1.6	16.850±0.049	4.9	94.41±0.27
5.5	28.0054	0.0005±0.0001	0.023±34.129	0.048±0.001	16.989±0.038	0.8	16.850±0.044	10.3	94.41±0.24
12.0	53.6043	0.0005±0.0000	0.042±19.596	0.046±0.001	17.009±0.044	0.9	16.860±0.046	19.7	94.46±0.25
Aliquot: B									
2.4	1.0338	0.0319±0.0010	0.063±58.699	0.058±0.003	24.352±0.232	38.7	14.926±0.266	0.4	83.87±1.46
2.8	4.0094	0.0068±0.0002	0.014±62.516	0.049±0.001	18.627±0.070	10.8	16.613±0.066	1.5	93.12±0.36
3.5	15.0941	0.0016±0.0001	0.006±34.011	0.047±0.001	17.311±0.046	2.7	16.836±0.047	5.6	94.33±0.26
3.9	14.9612	0.0009±0.0001	0.005±114.138	0.047±0.001	17.079±0.044	1.5	16.820±0.053	5.5	94.25±0.29
4.2	17.1943	0.0008±0.0001	0.008±61.864	0.047±0.001	17.024±0.056	1.3	16.802±0.056	6.3	94.15±0.31
4.6	14.9717	0.0005±0.0001	0.013±64.647	0.046±0.001	16.995±0.022	0.9	16.836±0.032	5.5	94.33±0.18
5.5	22.6689	0.0004±0.0000	0.031±21.076	0.046±0.001	16.968±0.031	0.8	16.837±0.030	8.3	94.34±0.16
12.0	32.0448	0.0005±0.0000	0.035±32.798	0.046±0.001	17.012±0.018	0.8	16.870±0.018	11.8	94.52±0.10
00N-72 Biotite; from a lamprophyre dyke; J=.00316870									
Aliquot: A									
2.4	0.3072	0.1801±0.0032	1.474±21.007	0.055±0.004	64.614±0.954	82.3	11.407±0.991	0.1	64.06±5.47
2.8	0.7255	0.0531±0.0012	2.264±11.324	0.026±0.003	27.051±0.290	58	11.369±0.260	0.2	63.85±1.43
3.5	5.2952	0.0171±0.0006	0.078±36.528	0.010±0.001	16.494±0.065	30.6	11.449±0.169	1.4	64.29±0.93
3.9	5.977	0.0038±0.0004	0.011±57.691	0.010±0.001	12.575±0.091	8.8	11.465±0.146	1.6	64.38±0.81
4.2	15.2387	0.0014±0.0001	0.008±63.788	0.009±0.000	11.850±0.029	3.5	11.439±0.041	4.1	64.23±0.23
4.6	12.1936	0.0008±0.0001	0.006±27.617	0.008±0.000	11.678±0.040	2.1	11.433±0.048	3.3	64.20±0.27
5.0	14.8829	0.0006±0.0001	0.006±90.665	0.009±0.000	11.636±0.022	1.6	11.455±0.020	4	64.32±0.11
6.0	53.8458	0.0005±0.0000	0.004±47.567	0.009±0.000	11.599±0.019	1.2	11.457±0.021	14.5	64.34±0.12
12.0	48.8673	0.0004±0.0000	0.005±24.035	0.009±0.000	11.563±0.025	0.9	11.457±0.026	13.2	64.33±0.14
Aliquot: B									
2.4	0.2377	0.2114±0.0073	0.843±71.021	0.059±0.011	73.925±2.379	84.5	11.455±2.987	0.1	64.32±16.48
2.8	0.3949	0.0801±0.0030	6.889±36.756	0.041±0.003	35.176±0.969	67.3	11.511±1.106	0.1	64.63±6.10
3.5	2.9827	0.0248±0.0003	1.287±20.768	0.012±0.001	18.841±0.094	38.9	11.515±0.083	0.8	64.65±0.46
3.9	5.5835	0.0039±0.0002	0.059±39.281	0.010±0.001	12.663±0.076	9.1	11.506±0.072	1.5	64.61±0.40
4.2	7.4539	0.0021±0.0001	0.027±59.616	0.010±0.001	12.155±0.037	5.2	11.529±0.033	2	64.73±0.18
4.6	9.6613	0.0017±0.0001	0.012±93.892	0.009±0.001	12.039±0.038	4.3	11.525±0.037	2.6	64.71±0.21
5.0	13.6483	0.0010±0.0001	0.008±52.244	0.009±0.001	11.813±0.045	2.5	11.523±0.043	3.7	64.70±0.24
5.5	30.0976	0.0007±0.0000	0.005±0.000	0.009±0.000	11.882±0.022	1.8	11.669±0.025	8.1	65.50±0.14
6.5	58.376	0.0004±0.0000	0.003±35.994	0.008±0.000	11.784±0.024	1	11.663±0.025	15.8	65.47±0.14
12.0	84.5844	0.0002±0.0000	0.004±37.888	0.009±0.000	11.505±0.020	0.5	11.444±0.021	22.8	64.26±0.11

a: As measured by laser in % of full nominal power (10W)

b: Fraction ^{39}Ar as percent of total run

c: Errors are analytical only and do not reflect error in irradiation parameter J

d: Nominal J, referenced to FCT-SAN=28.03 Ma (Renne et al., 1994)

*: Step not included in age determination

All uncertainties quoted at 2σ level

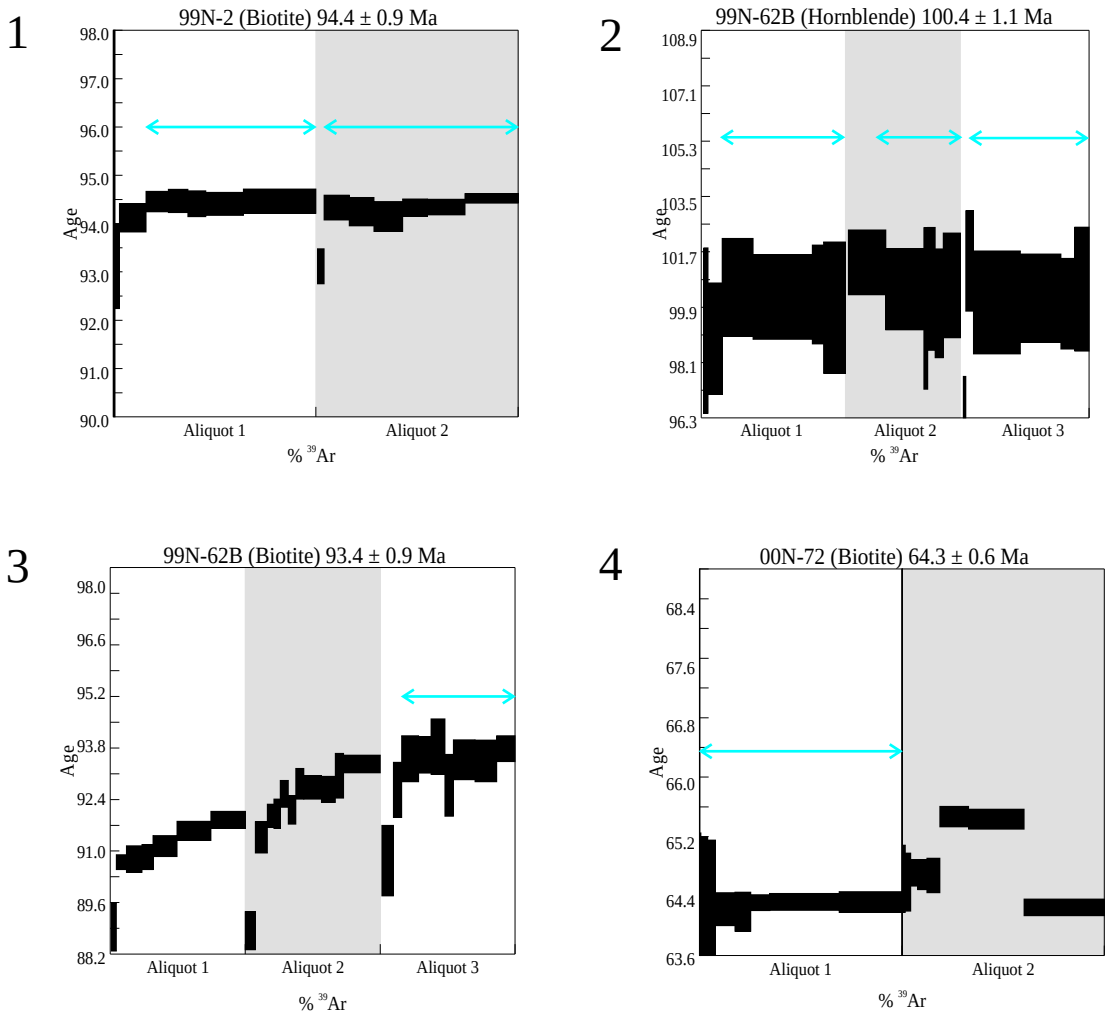

Figure 13 $^{40}Ar/^{39}Ar$ age spectrum diagrams **1.** Massive MRG; biotite yielded an excellent plateau age for both aliquots. **2.** Mylonitized MRG; hornblende spectrum shows minor excess argon in the early stages but yields a fairly consistent age. **3.** Mylonitized MRG; biotite spectrum shows a partial overprint geometry with argon loss in early stages and, in the third aliquot, a good plateau in later higher temperature releases. **4.** Minette dyke; aliquot 1 yielded a very good plateau age.

Table 3. Sample information and K-Ar analytical data for Moosehorn Range fine-grained mafic volcanic dyke rocks.

Sample	Rock Type	Location	Northing	Easting	Depth	$^{40}Ar_{rad}$ (nl/g)	% K	$\%^{40}Ar_{air}$	Age (Ma)
OON-78	mafic volcanic	DDH LL99-8	6 995 830	501 840	211 m	2.742	1.30	67.4	54.5+1.6
OON-78*	mafic volcanic	DDH LL99-8	6 988 650	501 900	211 m	2.888	1.38	64.8	54.1+1.5
OON-79	mafic volcanic	DDH LL00-5	6 988 650	501 900	280 m	2.616	1.27	75.8	53.4+1.7

*Denotes a sample washed in dilute nitric acid to dissolve away carbonate material

K-Ar

The K-Ar whole rock analyses yielded early Eocene ages for the fine-grained mafic dykes (see Table 3). The analysis for the acid-washed sample 00N-78 gave an age of 54.1 ± 1.5 Ma, and the unwashed 00N-78 sample gave an age of 54.5 ± 1.6 Ma. Sample 00N-79 yielded a K-Ar age of 53.4 ± 1.7 Ma, within error of both the analyses for sample 00N-78.

Interpretation of the Geochronology Results

Results of U-Pb dating of the major intrusions on the Longline property indicate that all phases crystallized within a very short period of time (between about 96 Ma and 100 Ma). The various intrusive phases are also compositionally similar and were therefore likely either derived from the same parent magma or are closely related. Consanguinity of the intrusions is further supported by the lead isotopic homogeneity of feldspars from all the different units (Fig. 14 and Table 4).

The foliated varieties of the MRG, most commonly found in the western and northwestern portions of the property, are interpreted to be the earliest intrusions in the Moosehorn Range area (e.g., mylonite sample 99N-66A gave a U-Pb zircon age of 98.3 ± 0.2 Ma). Field relationships indicate that an early S1 mylonitic foliation dipping steeply to the southwest predates later dextral D2 ductile deformation. The S2 mylonitic foliation is moderately to steeply dipping towards the northwest. Hornblende from granodiorite within a D2 shear zone northwest of Kenyon Creek (sample 99N-62A) yielded an $^{40}Ar/^{39}Ar$ age cooling age of 100.4 ± 1.1 Ma, which may indicate that the crystallization age of the granodiorite is, in fact, older than 98.3 ± 0.2 Ma. An $^{40}Ar/^{39}Ar$ age of 93.4 ± 0.9 Ma for biotite from the same granodiorite reflects a minimum metamorphic cooling age related to the D2 deformation.

Table 4 Lead isotope data for samples from the Moosehorn Range study area[1]

Sample #[2]	Mineral[3]	Location	$^{206}Pb/^{204}Pb$	2σ, %	$^{207}Pb/^{204}Pb$	2σ, %	$^{208}Pb/^{204}Pb$	2σ, %	$^{207}Pb/^{206}Pb$	2σ, %	$^{208}Pb/^{206}Pb$	2σ, %
Sulphide and Sulphosalt Analyses												
99M-11 *(a)*	gl	Central Moosehorn Range	18.860	0.01	15.633	0.01	38.667	0.01	0.829	0.01	2.050	0.01
99M-11 *(b)*	gl	Central Moosehorn Range	18.844	0.01	15.635	0.01	38.664	0.01	0.830	0.01	2.052	0.01
99M-12	gl	Central Moosehorn Range	18.812	0.01	15.631	0.01	38.617	0.01	0.831	0.01	2.053	0.01
99M-13 *(a)*	gl	Central Moosehorn Range	18.852	0.02	15.668	0.02	38.749	0.02	0.831	0.01	2.056	0.01
99M-13 *(b)*	gl	Central Moosehorn Range	18.835	0.01	15.626	0.01	38.661	0.02	0.830	0.01	2.053	0.01
99N-3A *(a)*	gl	SC-2	18.911	0.01	15.658	0.01	38.772	0.02	0.828	0.01	2.050	0.01
99N-3A *(b)*	gl	SC-2	18.906	0.01	15.653	0.01	38.759	0.01	0.828	0.01	2.050	0.01
V1	gl	V1	18.818	0.01	15.648	0.01	38.676	0.01	0.832	0.01	2.055	0.01
99N-4G	gl	Central Moosehorn Range	18.822	0.01	15.635	0.01	38.640	0.01	0.831	0.01	2.053	0.01
99N-4H	py	Central Moosehorn Range	18.851	0.01	15.647	0.01	38.704	0.01	0.830	0.01	2.053	0.01
99N-5	gl	Great Bear Creek	18.791	0.01	15.630	0.01	38.597	0.01	0.832	0.01	2.054	0.01
99N-16C	sph	V1	18.882	0.02	15.712	0.01	38.899	0.02	0.832	0.01	2.060	0.01
99N-22B	boul	V3	18.903	0.09	15.737	0.09	38.976	0.09	0.833	0.01	2.062	0.01
99N-23	py	Swede's Pit: vein cutting V2	19.187	0.06	15.705	0.06	39.046	0.08	0.819	0.02	2.035	0.03
99N-29F	gl	V2 (Trench 6)	18.825	0.03	15.628	0.05	38.619	0.06	0.830	0.02	2.052	0.03
99N-38	sph	V2 (Trench 13)	18.953	0.15	15.734	0.11	39.067	0.02	0.830	0.11	2.061	0.06
99N-50	gl	Kenyon Creek	18.788	0.03	15.626	0.05	38.583	0.06	0.832	0.02	2.054	0.03
00N-22	py	DDH LL00-2	18.975	0.03	15.649	0.05	38.781	0.06	0.825	0.02	2.044	0.03
00N-48A	gl	DDH LL99-06 (at 30 m)	18.876	0.03	15.634	0.05	38.686	0.07	0.828	0.02	2.049	0.03
00N-48B	py	DDH LL99-06 (at 30 m)	18.946	0.04	15.665	0.05	38.809	0.07	0.827	0.02	2.048	0.03
00N-49	gl	DDH LL99-06 (at 22 m)	18.856	0.03	15.656	0.05	38.712	0.06	0.830	0.02	2.053	0.03
00N-50 *(a)*	asp	DDH LL99-09 (at 70 m)	18.889	0.04	15.643	0.05	38.711	0.07	0.828	0.02	2.049	0.03
00N-50 *(b)*	asp	DDH LL99-09 (at 70 m)	18.909	0.04	15.654	0.05	38.778	0.07	0.828	0.02	2.051	0.03
00N-51 *(a)*	asp	DDH LL99-09 (at 134 m)	18.891	0.09	15.667	0.09	38.721	0.11	0.829	0.04	2.050	0.05
00N-51 *(b)*	asp	DDH LL99-09 (at 134 m)	18.876	0.07	15.638	0.07	38.709	0.09	0.828	0.03	2.051	0.04
00N-53 *(a)*	asp	DDH LL99-11 (at 179 m)	18.868	0.04	15.628	0.05	38.678	0.07	0.828	0.02	2.050	0.03
00N-53 *(b)*	asp	DDH LL99-11 (at 179 m)	18.838	0.03	15.620	0.05	38.620	0.06	0.829	0.02	2.050	0.03
00N-54	py	DDH LL99-12 (at 154 m)	19.233	0.04	15.691	0.05	39.061	0.07	0.816	0.02	2.031	0.03
00N-71A	po	DDH LL00-5 (at 113 m)	18.979	0.06	15.641	0.06	38.744	0.08	0.824	0.02	2.041	0.03
00N-76A	ccp	DDH LL00-6	19.121	0.05	15.632	0.06	38.751	0.08	0.818	0.02	2.027	0.03
00N-76B	po	DDH LL00-6	19.141	0.48	15.638	0.45	39.135	0.50	0.817	0.18	2.045	0.13

Table 4 (continued)

Sample #[2]	Rock[4]: Mineral[5]	Location	$^{206}Pb/^{204}Pb$	2σ, %	$^{207}Pb/^{204}Pb$	2σ, %	$^{208}Pb/^{204}Pb$	2σ, %	$^{207}Pb/^{206}Pb$	2σ, %	$^{208}Pb/^{206}Pb$	2σ, %
Feldspar Analyses												
99N-2	MRG: Plag	Camp outcrop	19.256	0.05	15.718	0.04	39.216	0.06	0.816	0.02	2.037	0.04
99N-16F	FGD: Ksp	V1 Trench	19.255	0.01	15.692	0.01	39.129	0.01	0.815	0.01	2.032	0.01
99N-56	Pegmatite: Ksp	West of Airport Pup	19.225	0.01	15.672	0.01	39.006	0.01	0.815	0.01	2.029	0.01
99N-62B	Myl. MRG: Ksp	Near Kenyon Creek	19.213	0.01	15.667	0.01	38.972	0.01	0.815	0.01	2.028	0.01
99N-75	MRG: Fsp	Southeast of Swede's Pit	19.242	0.02	15.689	0.02	39.071	0.03	0.815	0.01	2.031	0.02
99N-78	FPQD: Fsp	Camp outcrop	19.285	0.11	15.694	0.11	39.156	0.11	0.814	0.01	2.030	0.01
99N-79	FD: Ksp	Camp outcrop	19.141	0.04	15.582	0.03	38.722	0.04	0.814	0.01	2.023	0.01
00N-12	MRG: Fsp	Southeastern Moosehorn Range	19.419	0.06	15.695	0.07	39.370	0.09	0.808	0.03	2.027	0.04
00N-14 *(a)*	MRG: Fsp	Central Moosehorn Range	19.237	0.12	15.732	0.12	39.042	0.14	0.818	0.05	2.030	0.06
00N-14 *(b)*	MRG: Fsp	Central Moosehorn Range	19.173	0.06	15.634	0.06	38.886	0.09	0.815	0.03	2.028	0.05
00N-15A	PQD: Fsp	Southeastern Moosehorn Range	19.262	0.09	15.685	0.09	39.115	0.10	0.814	0.02	2.031	0.03
00N-20	MRG: Fsp	Southeastern Moosehorn Range	19.208	0.03	15.665	0.05	38.977	0.07	0.816	0.02	2.029	0.03
00N-23	FMRG: Fsp	DDH LL00-2	19.196	0.05	15.654	0.06	38.933	0.08	0.815	0.02	2.028	0.03
00N-25	Granodiorite: Fsp	DDH MH99-6	19.269	0.06	15.718	0.06	39.135	0.08	0.816	0.02	2.031	0.03
00N-36 *(c)*	Aplite: Fsp	Central Moosehorn Range	19.305	0.03	15.699	0.05	39.176	0.07	0.813	0.02	2.029	0.03
00N-36 *(d)*	Aplite: Fsp	Central Moosehorn Range	19.322	0.04	15.707	0.05	39.230	0.07	0.813	0.02	2.030	0.03
00N-38	MRG: Fsp	Central Moosehorn Range	19.473	0.03	15.724	0.04	39.481	0.06	0.807	0.02	2.027	0.03
00N-66	Aplite: Fsp	DDH LL00-4	19.214	0.04	15.664	0.05	38.969	0.07	0.815	0.02	2.028	0.03
00N-67	Granodiorite: Fsp	DDH LL00-4 (at 167 m)	19.412	0.03	15.729	0.05	39.400	0.06	0.810	0.02	2.030	0.03
00N-68	Aplite: Fsp	DDH LL00-4 (at 244 m)	19.413	0.04	15.728	0.05	39.403	0.07	0.810	0.02	2.030	0.03
00N-70	FMRG: Fsp	DDH LL00-5 (at 105 m)	19.188	0.04	15.668	0.05	38.963	0.07	0.817	0.02	2.031	0.04
00N-77 *(a)*	Diorite: Fsp	DDH LL00-6	19.164	0.18	15.650	0.18	38.815	0.19	0.817	0.03	2.025	0.04
00N-77 *(b)*	Diorite: Fsp	DDH LL00-6	19.092	0.07	15.598	0.08	38.672	0.09	0.817	0.02	2.026	0.03
00N-72 *(a)*	Aplite: Fsp	Northwest flank of Kenyon Creek	19.199	0.04	15.659	0.05	38.936	0.07	0.816	0.02	2.028	0.03
00N-72 *(b)*	Aplite: Fsp	Northwest flank of Kenyon Creek	19.215	0.03	15.667	0.05	38.980	0.07	0.815	0.02	2.029	0.03
00N-74	Leucogr.: Fsp	DDH LL00-5 (at 128 m)	19.248	0.03	15.690	0.05	39.048	0.06	0.815	0.02	2.029	0.03
00N-75	FMRG: Fsp	Central Moosehorn Range	19.349	0.05	15.719	0.05	39.361	0.08	0.812	0.03	2.034	0.04
00N-80	FMRG: Fsp	DDH LL00-6	19.219	0.04	15.665	0.05	39.097	0.07	0.815	0.02	2.034	0.03
99M-130	PQD: Fsp	Southeastern Moosehorn Range	19.309	0.05	15.735	0.05	39.254	0.05	0.815	0.01	2.033	0.01
99M-131	7 Mile Pluton: Fsp	East of the Longline property	19.026	0.05	15.609	0.06	39.730	0.07	0.820	0.02	2.037	0.03
Whole Rock Analyses												
99N-9	F.gr. Mafic dyke	Soya Creek	19.227	0.05	15.684	0.03	38.993	0.08	0.816	0.04	2.028	0.06
00N-17	Mafic Xenolith	Southeastern Moosehorn Range	19.444	0.03	15.742	0.05	39.434	0.06	0.810	0.02	2.028	0.03
00N-63	Lamprophyre	DDH LL00-3	19.090	0.04	15.627	0.05	38.819	0.07	0.819	0.02	2.033	0.04

[1]All samples analyzed by the Geochronology Laboratory, University of British Columbia

[2]Letters in brackets denote different fractions of the same mineral

[3]Minerals analyzed: gl = galena, py = pyrite, sph = sphalerite, boul = boulangerite, asp = arsenopyrite, po = pyrrhotite, ccp = chalcopyrite

[4]Rock from which feldspar was obtained: MRG = Moosehorn Range granodiorite, FMRG = foliated MRG, FD = felsite dyke, PQD = massive porphyritic quartz diorite dyke, FPQD = foliated PQD, FGD = foliated granodiorite dyke

[5]Mineral analyzed: Fsp = feldspar (mix of potassium and plagioclase feldspar), Ksp = potassium feldspar, Plag = plagioclase

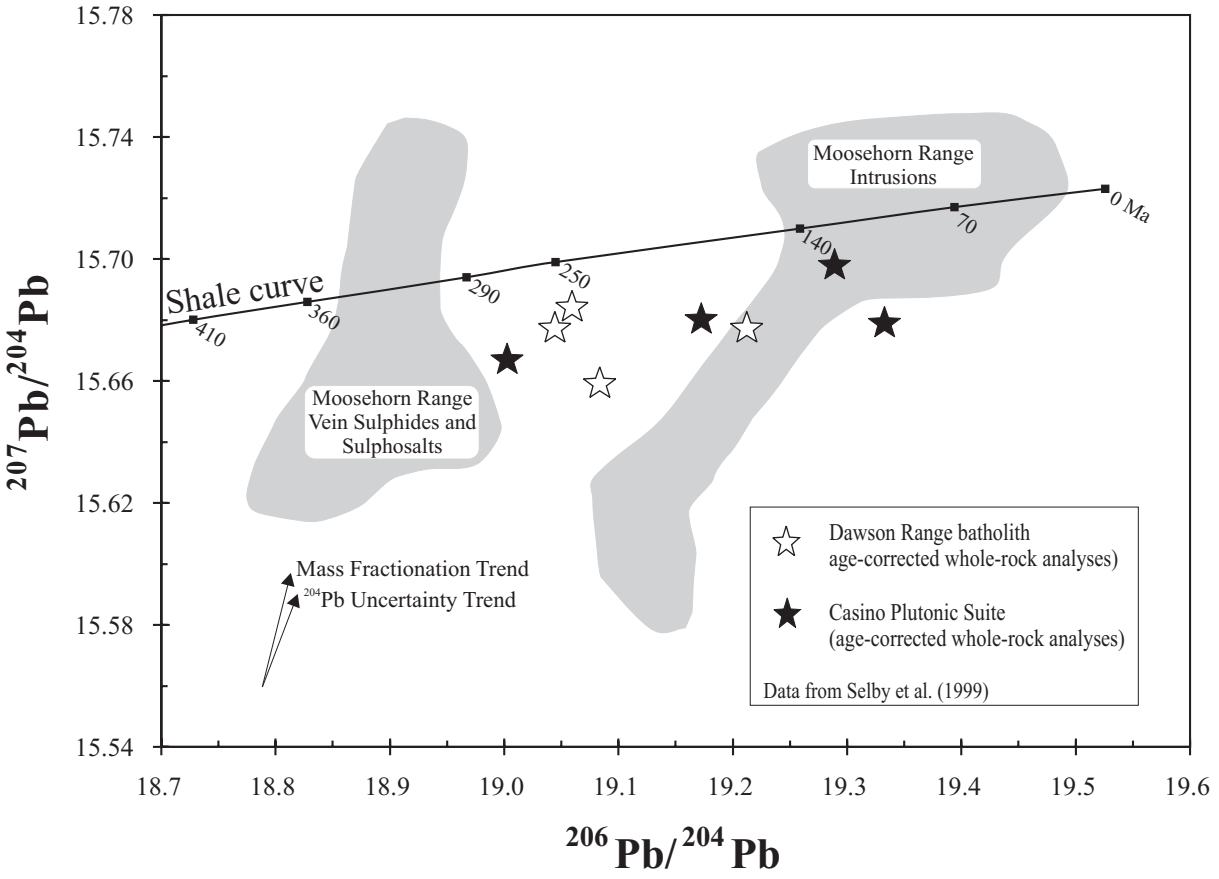

Figure 14 Uranogenic plot showing the lead isotopic compositional fields for Moosehorn Range area intrusions and vein sulphides and sulphides. For comparison, age corrected data for intrusions from the southeastern Dawson Range are included (data from Selby et al., 1999). Clearly the hydrothermal fluids from which the sulphides and sulphosalts were deposited did not originate from the Moosehorn Range area intrusions, nor did they exchange much, if any, lead with them. The Shale curve is from Godwin and Sinclair (1982).

Very weakly foliated MRG sample 99N-2 gave a U-Pb zircon age of 99.8 ± 0.4 Ma and an $^{40}Ar/^{39}Ar$ biotite cooling age of 94.4 ± 0.9 Ma. The batholith therefore cooled through 300˚-350˚C about five million years after emplacement. Independent constraints on the depth and pressure at which the magma crystallized are not available, but can be approximated. Gold-bearing veins that crosscut the MRG at about 92-93 Ma formed at a crustal depth of 5 to 7 km (Chapter 3 of this study); this is a minimum estimate for the depth of MRG crystallization. Evidence for solid-state deformation in the mylonitized MRG samples suggests that the intrusion was below the brittle-ductile transition zone (deeper than 10 km; Twiss and Moores, 1992). However, the presence of fluids in the rocks could have enabled ductile deformation mechanisms at shallower levels.

The southeastern portion of the Moosehorn Range is dominated by undeformed biotite- and hornblende-biotite MRG. Sample 00N-14 (hbl-bt MRG) yielded a U-Pb titanite age of 99.6 ± 0.4 Ma. Because the ages of the foliated and massive phases of MRG are similar, we must draw the conclusion that the textural differences are simply a function of proximity to a strain zone.

Foliated and mylonitic dykes were emplaced within the MRG shortly after the MRG formed. Results of the U-Pb dating of the dykes were fairly inconclusive but field relationships indicate the dykes intruded after 99.8 ± 0.4 Ma (age of the wallrock MRG) and prior to the 92-93 Ma formation of the shallowly east-northeast dipping brittle quartz shear veins in the area (Chapter 3). Similar to the D2 fabrics locally observed in the host MRG, the dyke margins and foliations generally dip moderately to steeply towards the northwest.

The $^{206}Pb/^{238}U$ zircon age of 96.0 ± 0.4 Ma obtained for felsite sample 99N-1 is a minimum age estimate for igneous crystallization. Emplacement of felsite dykes into the MRG is therefore interpreted to have occurred between 96 and 99 Ma. The majority of the

dykes are undeformed; foliated felsite dykes were found within the high strain zone west of Kenyon Creek, and parallel and adjacent to a foliated porphyritic quartz diorite dyke (sample 99N-77).

Cross cutting relationships between the felsite and aplite dykes are unclear. The aplites probably represent latest-stage melts of the batholith, and both massive and foliated varieties were encountered. The dykes are younger than the 99.8 ± 0.4 Ma wallrock MRG that they intruded into, and older than the fine-grained mafic dykes that crosscut them.

Gold-bearing quartz veins were emplaced within the MRG at approximately 92-93 Ma (see Chapter 3). These shallowly east-northeast dipping brittle shear veins were formed during southwest-verging shortening and were locally offset slightly (5 cm to at most 5 m) by moderately west-northwest dipping faults.

Two generations of mafic dykes are present in the Moosehorn Range area. The Ar-Ar biotite age for the shallowly east-dipping minette dykes was 64.3 ± 0.6 Ma. These potassic melts may be related to the voluminous *ca.* 70 Ma Carmacks Group volcanic rocks, which are exposed between Whitehorse and Dawson City, Yukon (Johnston et al., 1996). The more voluminous fine-grained mafic dykes were emplaced in the early Eocene (53.9 ± 2.2 Ma). These dykes dip moderately to steeply to the west-northwest, parallel to the faults that offset the gold-bearing quartz veins.

A cartoon summarizing crosscutting relationships between and ages of the Moosehorn Range area intrusions and gold-bearing veins is presented in Figure 15.

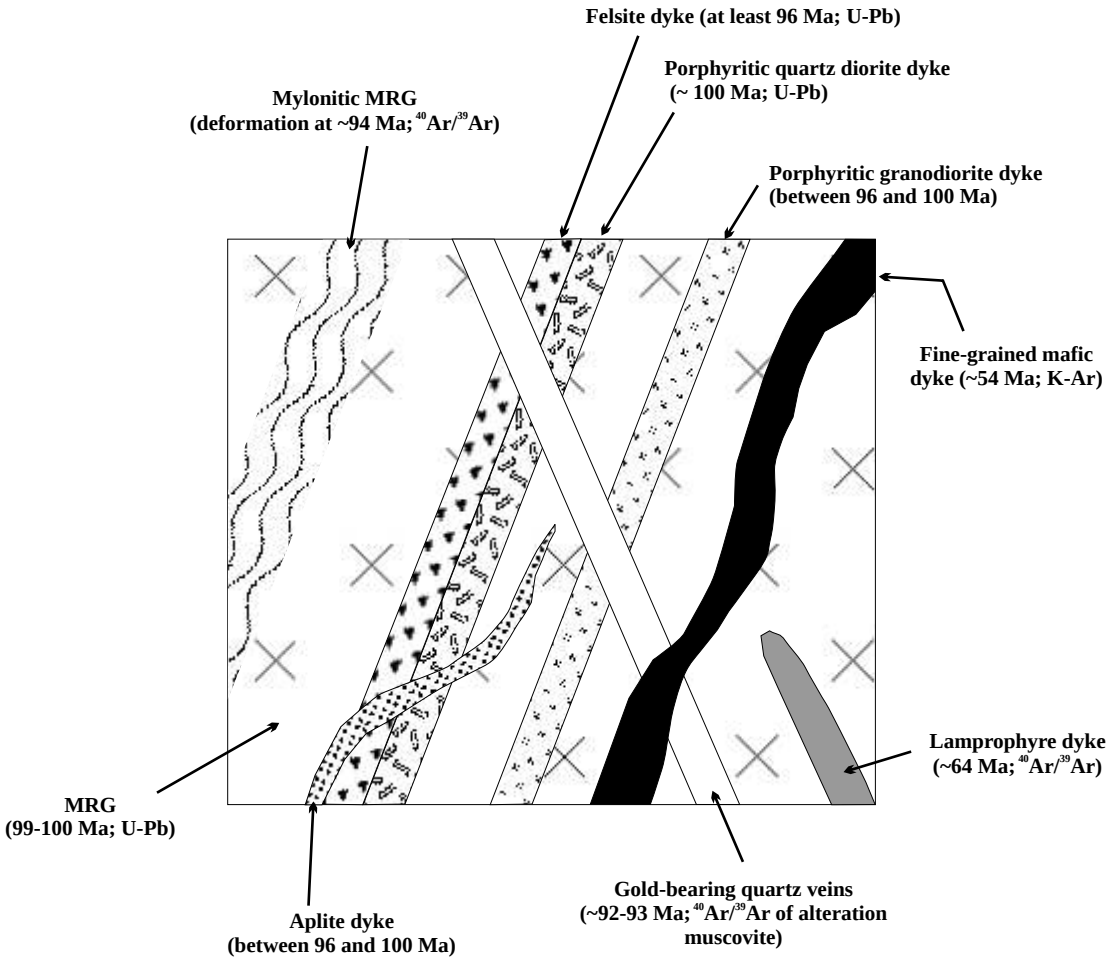

Figure 15 Schematic diagram illustrating the crosscutting relationships and relative ages of the Moosehorn Range area intrusions and gold-bearing veins. The units and ages are labelled; the isotopic system used in age determination are shown.

Lithogeochemistry

A geochemical study of intrusions in the study area was undertaken to provide insight on petrological classification, genetic relationships between the units, and the paleotectonic setting in which the magmatism occurred.

Samples and Methods

Forty-six samples were collected for lithogeochemical analysis. Forty-one of these were either surface or drill core samples of intrusions from the main Moosehorn range study area and five were from regional exposures. Sample locations are shown on Figures 4.1 and 4.2. Sample locations and descriptions are included in Table 5.

Weathered surfaces were first removed using a rock saw. Samples were then crushed and powdered using a standard jaw crusher and a tungsten carbide ring mill. All major, trace, and REE analyses were carried out at ALS Chemex Labs Ltd. in North Vancouver, British Columbia. X-ray fluorescence (XRF) was used for determining major element concentrations and inductively coupled plasma emission mass spectrometry (ICP-MS) methods were used to determine trace and REE concentrations. Major, trace, and REE concentrations are presented in Table 6.

Geochemical Compositions of Moosehorn Range Area Intrusions

Major element analyses from all of the samples are shown on total alkalies versus silica plots, Al/(Na+K) versus Al/(Ca+Na+K) plot, a Winchester and Floyd (1977) plot, and a Nb versus Y plot (Pearce et al., 1984) in Figures 16.1 to 16.4, 17.1 and 17.2. Some of the scatter in the data exhibited in the major element plots (e.g., deformed samples 99N-66A

Table 5. Geochemistry sample numbers, sample locations, and brief descriptions

Sample	Location	Drill Hole Information	Northing	Easting	Description
99N-1	V3 trench	--	6989740	502395	fine-gr ser-py altered felsite
99N-2	Campsite outcrop	--	6988785	501600	weakly foliated Hbl-Bt MRG
99N-9	Soya Creek (near SC-1 Vein)	--	6988680	502100	fine-gr mafic dyke
99N-31	Northwest end of Swede's Pit	--	6989760	501815	med-gr foliated granodiorite dyke
99N-42G	Near SC-2 trench	--	6989335	502480	massive Hbl-Bt porphyritic quartz diorite dyke
99N-50	Northwest of Swede's Pit	--	6990195	501695	fine-gr mafic dyke
99-N57B	Near southern extension of Swamp Creek	--	6986825	500720	fine-gr mafic-intermediate dyke
99N-58A	Near southern extension of Swamp Creek	--	6986880	500700	fine-gr altered felsite dyke
99N-66A	Northwesrn flank of Kenyon Creek	--	6990670	500940	mylonitic Hbl-Bt MRG
99N-68	Northwesrn flank of Kenyon Creek	--	6991200	501535	fine-gr mafic dyke
99N-72	Northern flank of Kenyon Creek	--	6991820	502115	Ksp-Grt pegmatite
99N-75	Southeast of Swede's Pit	--	6989525	502090	massive Hbl-Bt MRG
99N-76	Northwest of the SC-1 trench	--	6988685	501870	med-gr foliated granodiorite dyke
99N-77	North of the campsite outcrop	--	6989085	501630	massive Hbl-Bt porphyritic quartz diorite dyke
99N-78	Campsite outcrop	--	6989790	501615	fol. Hbl-Bt porphyritic quartz diorite dyke
99N-79	Campsite outcrop	--	6989790	501630	fine-gr felsite dyke
99N-80	Campsite outcrop	--	6988785	501600	weakly foliated Hbl-Bt MRG
00N-7	Northwestern Moosehorn Range	--	6994900	501500	massive pink granite
00N-12	Central Moosehorn Range	--	6993231	502640	Bt MRG
00N-14	Southeastern Moosehorn Range	--	6992100	504136	Hbl-Bt MRG
00N-15A	Southeastern Moosehorn Range	--	6990750	504690	massive Hbl-Bt porphyritic quartz diorite dyke
00N-19	Southeastern Moosehorn Range	--	6990230	505150	Bt-phyric felsite dyke
00N-20	Southeastern Moosehorn Range	--	6990890	504620	Bt MRG
00N-23	Northwestern Moosehorn Range	DDH LL00-2	6997810	501513	Bt-Hbl MRG
00N-25	East Central Alaska	DDH MH99-6	6997530	498990	porphyritic diorite (?)
00N-36	Southeastern Moosehorn Range	--	6993486	503582	molybdenite-bearing aplite dyke
00N-38	Southeastern Moosehorn Range	--	6992400	504910	Bt MRG
00N-63	Northwestern Moosehorn Range	DDH LL00-3 (at 163 m)	6997814	500640	lamprophyre
00N-67	Northwestern Moosehorn Range	DDH LL00-4 (at 167 m)	7000517	501123	granodiorite
00N-68	Northwestern Moosehorn Range	DDH LL00-4 (at 244 m)	7000517	501123	aplite dyke
00N-69	Northwestern Moosehorn Range	DDH LL00-4 (at 19 m)	7000517	501123	migmatitic melanosome
00N-70	Central Moosehorn Range	DDH LL00-5 (at 105 m)	6995830	501840	foliated Hbl-Bt MRG
00N-72	Central Moosehorn Range	DDH LL00-5 (at 147 m)	6995830	501840	lamprophyre
00N-73	Central Moosehorn Range	DDH LL00-5 (at 214 m)	6995830	501840	mafic dyke
00N-74	Central Moosehorn Range	DDH LL00-5 (at 128 m)	6995830	501840	leucogranite
00N-75	Central Moosehorn Range	--	6993650	502650	foliated Bt MRG
00N-77	Northwestern Moosehorn Range	DDH LL00-6	6999502	500805	diorite
00N-78	Swamp Creek	DDH LL99-8 (at 211 m)	6988660	501875	mafic dyke
00N-79	Central Moosehorn Range	DDH LL00-5 (at 280 m)	6995830	501840	mafic dyke
00N-80	Northwestern Moosehorn Range	DDH LL00-6	6999502	500805	Hbl-Bt MRG
99M-140	Northwest Moosehorn Range (Tanacross)	--			Bt-Hbl granodiorite
99M-130	Southeastern Moosehorn Range	--			massive Hbl-Bt porphyritic quartz diorite dyke
00M-27	Southeast of the Moosehorn Range area	--			Hbl-Bt qtz monzonite
00M-28	Southeast of the Moosehorn Range area	--			Hbl-Bt qtz monzonite (Coffee Creek granite)
00M-31	Southeast of the Moosehorn Range area	--	6991000	542900	mafic-intermediate volcanic rock
00M-32	East of the Moosehorn Range	--			Kspar-porphyritic monzonite (7-mile pluton)

-- indicates a sample collected at surface

Table 6 Lithogeochemical data for samples from the study area[1]

Sample	Majors[2]															
	Al_2O_3	CaO	Cr_2O_3	Fe Total	FeO	K_2O	MgO	MnO	Na_2O	P_2O_5	SiO_2	TiO_2	LOI	TOTAL	*Fe_2O_3	Fe_2O_3/FeO
99N-1	12.3	0.05	<0.01	0.98	0.1	3.64	0.1	<0.01	0.08	0.02	79.19	0.06	2.04	98.46	0.868865	8.68865
99N-2	16.58	4.46	<0.01	4.61	2.79	2.74	1.55	0.1	3.17	0.16	64.5	0.48	0.78	99.13	1.5093335	0.540979749
99N-9	14.24	7.94	<0.01	11.35	8.36	1.53	5.3	0.18	2.72	0.63	48.25	2.27	4.28	98.69	2.059114	0.246305502
99N-31	14.75	2.19	<0.01	2.89	1.02	3.6	0.58	0.06	3.31	0.1	70.12	0.31	1.11	99.02	1.756423	1.721983333
99N-42G	16.19	4.35	<0.01	3.88	2.35	2.86	1.31	0.09	3.17	0.11	65.62	0.43	0.75	98.76	1.2683275	0.53971383
99N-50	14.26	9.93	<0.01	9.87	6.9	1.45	4.78	0.15	2.3	0.58	49.16	2	4.59	99.07	2.201685	0.319084783
99-N57B	16.33	5.52	<0.01	6.45	3.31	2.66	3.19	0.1	3.16	0.32	56.79	0.91	3.78	99.21	2.7714315	0.837290483
99N-58A	12.52	0.49	<0.01	0.78	0.15	4.17	<0.01	0.02	3.75	<0.01	76.66	0.04	0.64	99.07	0.6132975	4.08865
99N-66A	18.68	4.65	<0.01	6.54	4.18	3.53	2.15	0.14	3.59	0.23	56.96	0.74	1.4	98.61	1.894557	0.453243301
99N-68	14.1	8.01	<0.01	10.37	7.45	1.82	5.03	0.17	2.56	0.55	49.73	1.98	4.22	98.54	2.0904425	0.280596309
99N-72	12.76	1.22	<0.01	0.59	0.13	4.41	<0.01	0.02	3.5	0.02	75.3	0.06	0.26	98.14	0.4455245	3.427111538
99N-75	15.71	4.28	<0.01	4.56	3	2.92	1.52	0.11	3.14	0.17	65.2	0.48	0.61	98.7	1.22595	0.40865
99N-76	14.93	2.64	<0.01	3.01	1.59	3.6	0.74	0.07	3.48	0.11	69.68	0.36	0.9	99.52	1.2429535	0.781731761
99N-77	16.32	4.72	<0.01	5.48	2.84	2.87	2.14	0.11	2.99	0.19	62.63	0.64	1.17	99.26	2.323766	0.818227465
99N-78	16.04	4.48	<0.01	4.93	2.66	2.83	2.02	0.11	3.1	0.15	63.66	0.55	1.23	99.1	1.973809	0.742033459
99N-79	12.75	0.73	<0.01	1.01	0.48	4.69	<0.01	0.05	3.45	0.01	76.2	0.04	0.37	99.3	0.476552	0.992816667
99N-80	15.86	4.44	<0.01	4.96	2.9	2.64	1.71	0.11	3.09	0.19	64.33	0.5	0.59	98.42	1.737085	0.598994828
00N-7	16.04	2.25	<0.01	0.57	0.29	4.37	0.05	0.01	4.02	0.03	70.98	0.05	0.26	98.63	0.2477085	0.854167241
00N-12	13.78	1.76	<0.01	1.75	1.14	3.14	0.44	0.04	3.62	0.07	73.3	0.24	0.42	98.56	0.483061	0.423737719
00N-14	16.02	4.35	<0.01	4.33	2.77	2.96	1.52	0.1	3	0.14	65.16	0.44	0.61	98.63	1.2515605	0.451826895
00N-15A	16.22	4.19	<0.01	4.47	2.88	2.89	1.72	0.1	3.15	0.12	64.48	0.5	0.64	98.48	1.269312	0.440733333
00N-19	12.87	0.66	<0.01	1.16	0.87	4.45	0.01	0.06	3.65	0.01	75.2	0.05	0.29	98.41	0.1931255	0.221983333
00N-20	15.12	3.17	<0.01	3.3	2.06	3.47	1.1	0.09	3.1	0.12	68.51	0.35	0.43	98.76	1.010619	0.490591748
00N-23	15.23	3.42	<0.01	3.69	2.44	3.46	1.13	0.09	2.99	0.14	67.36	0.37	0.45	98.33	0.978306	0.400945082
00N-25	19.36	9.05	<0.01	9.97	6.53	2.27	4.83	0.19	2.81	0.39	47.91	1.04	0.74	98.56	2.7128845	0.415449387
00N-36	13.7	0.97	<0.01	0.77	0.42	6.48	0.08	0.01	2.34	0.03	73.84	0.06	0.34	98.62	0.303233	0.721983333
00N-38	13.85	1.04	<0.01	1.3	0.86	4.7	0.33	0.02	3.51	0.06	73.21	0.15	0.41	98.58	0.344239	0.400277907
00N-63	10.47	9.99	<0.01	8.64	5.33	4.31	11.85	0.17	2.44	0.34	46.12	0.69	3.61	98.63	2.7165045	0.509663133
00N-67	13.5	1.3	<0.01	1.87	1.47	4.69	0.62	0.05	3.09	0.04	72.46	0.25	0.7	98.57	0.2363155	0.160758844
00N-68	12.84	0.32	<0.01	0.62	0.35	8.33	0.11	0.01	1.81	0.05	74.12	0.09	0.52	98.82	0.2310275	0.660078571
00N-69	17.91	7.13	<0.01	8.12	4.66	1.7	3.09	0.17	2.96	0.25	55.55	0.7	0.87	98.45	2.941109	0.63113927
00N-70	15.14	3.36	<0.01	3.36	2.63	3.29	1.03	0.09	3.24	0.12	67.37	0.36	1.36	98.72	0.4371495	0.16621654
00N-72	11.3	9.73	<0.01	8.91	6.38	4.19	9.45	0.17	3.33	0.44	43.98	0.79	6.24	98.53	1.819587	0.285201724
00N-73	13.88	8.53	<0.01	10.28	8.11	1.63	5.1	0.18	2.51	0.56	48.5	1.99	5.65	98.81	1.2669515	0.1562209
00N-74	13.01	1.44	<0.01	0.73	0.51	5.02	0.07	0.02	2.79	0.01	74.62	0.05	0.94	98.7	0.1632115	0.320022549
00N-75	14.11	2.01	<0.01	1.8	1.1	3.54	0.47	0.04	3.72	0.05	72.19	0.24	0.38	98.55	0.577515	0.525013636
00N-77	15.29	8.7	<0.01	9.72	6.76	1.6	5.62	0.15	2.76	0.44	50.03	1.96	2.02	98.29	2.207274	0.326519822
00N-78	14.54	8.25	<0.01	10.52	8.39	1.61	4.91	0.18	2.61	0.57	48.67	2.11	4.33	98.3	1.1957735	0.142523659
00N-79	14.33	8.45	<0.01	10.35	7.12	1.41	7.24	0.17	2.82	0.41	48.77	1.71	2.82	98.48	2.437188	0.342301685
00N-80	16.96	5.64	<0.01	5.8	4.15	2.02	2.53	0.1	3.04	0.1	60.98	0.64	0.78	98.59	1.1878975	0.286240361
99M-140	16.9	5.41	<0.01	6.43	3.82	2.08	2.47	0.13	3.02	0.29	59.64	0.66	1.37	98.4	2.184643	0.571896073
99M-130	16.1	4.37	<0.01	4.25	2.84	2.99	1.69	0.09	3.23	0.13	64.86	0.49	0.66	98.86	1.093766	0.385128873
00M-27	16.07	4.13	<0.01	5.34	3.49	2.45	1.71	0.1	2.97	0.14	64.2	0.5	0.92	98.53	1.4613885	0.41873596
00M-28	16.11	2.33	<0.01	3.92	3.04	5.43	1.05	0.09	3.12	0.24	65.09	0.72	0.67	98.77	0.541496	0.178123684
00M-31	15.83	5.99	<0.01	7.93	5.67	3.66	3.96	0.14	2.68	0.44	55.59	0.91	1.46	98.59	1.6286455	0.287239065
00M-32	15.35	4.17	<0.01	5.5	3.45	4.54	2.41	0.12	3.74	0.33	61.64	0.6	0.46	98.86	1.6658425	0.482852899

[1]Analyses on all samples were carried out by Chemex Labs Ltd. In Vancouver, British Columbia

[2]Major element abundances are expressed as oxide weight %

[3]Trace and REE abundances are reported as parts per million (ppm)

*Calculated based on measured FeO and total Fe

Table 6 (continued)

Sample	Trace/REE[3]											
	Ba	Ce	Cs	Co	Cu	Dy	Er	Eu	Gd	Ga	Hf	Ho
99N-1	2940	51	1.6	11	<5	2.6	1.6	0.6	3.2	13	3	0.6
99N-2	2610	82	1.5	19.5	<5	3	1.9	1.1	4.6	18	4	0.7
99N-9	792	74.5	2.4	37	25	7.7	4.4	2.6	9.7	20	6	1.6
99N-31	1770	54.5	2.7	10	<5	2.6	1.8	0.8	3.3	17	5	0.5
99N-42G	1605	52.5	1.9	17.5	<5	2.2	1.4	0.9	2.8	17	3	0.4
99N-50	678	77.5	1	34.5	25	7.6	4.1	2.4	9.4	19	6	1.5
99-N57B	2970	73	3.5	20	20	3.9	2.3	1.5	5.7	18	4	0.8
99N-58A	255	28.5	1.7	16.5	<5	2.6	1.7	0.2	2.8	14	3	0.5
99N-66A	2690	67	4.6	14.5	<5	3.3	1.8	1.4	4.3	22	5	0.7
99N-68	821	85	2	31.5	20	7.8	4.5	2.4	9.6	19	7	1.6
99N-72	85	3.5	1.5	20	<5	0.7	0.6	0.4	0.7	13	1	0.1
99N-75	2860	67	1.7	21.5	<5	3.4	1.8	1.3	4.5	18	5	0.7
99N-76	1685	64.5	3.2	13	<5	2.8	1.6	0.8	3.4	16	4	0.6
99N-77	1960	60.5	1.9	17.5	10	3.5	2.2	1.3	4.8	18	4	0.8
99N-78	1900	54.5	2	16	<5	3.1	1.7	1	3.9	18	3	0.7
99N-79	1145	40	1.6	13.5	<5	2.4	1.6	0.4	2.8	14	3	0.6
99N-80	2570	74	1.9	15.5	<5	3.7	2.1	1.3	4.7	18	5	0.7
00N-7	1295	21.5	1.1	15.5	<5	0.9	0.7	0.8	0.9	15	1	0.2
00N-12	2560	105.5	0.9	19.5	<5	2.5	1.4	1.4	4.4	15	5	0.5
00N-14	2410	66	2.1	15.5	<5	3.2	2.1	1.4	3.7	19	4	0.6
00N-15A	1800	56.5	2.7	16.5	5	2.8	1.7	1.2	3.4	20	3	0.6
00N-19	1830	45.5	1.9	13	<5	2.9	1.8	0.6	3.2	16	3	0.6
00N-20	2150	54.5	3.1	15.5	<5	3.2	2.2	1.1	3.5	18	4	0.7
00N-23	3530	65	1.8	16.5	<5	2.8	1.9	1.3	3.7	18	4	0.6
00N-25	2440	68	1.1	23.5	30	6.4	3.9	2.1	6.9	26	5	1.3
00N-36	979	32.5	0.7	16.5	<5	2.2	1.4	0.7	2.4	14	3	0.4
00N-38	833	47	1.8	12.5	<5	6.8	4.5	0.7	5.2	17	3	1.5
00N-63	1270	47.5	5.3	35	15	3.8	2.1	1.3	4.2	15	2	0.8
00N-67	1240	89	1.2	13.5	<5	8.3	5.4	1.1	7.6	18	5	1.8
00N-68	1785	52.5	0.6	22	<5	7.1	4.9	0.9	5.1	13	3	1.7
00N-69	1590	42.5	1.1	18	20	4.3	2.7	1.6	4.4	24	3	0.9
00N-70	2540	69	3.5	9.5	<5	3.3	2.4	1.3	4.2	19	5	0.7
00N-72	1535	54	8.9	30	60	4	2.2	1.6	4.9	15	3	0.8
00N-73	818	81.5	1.3	28	40	7.7	4.4	2.4	8.2	20	6	1.5
00N-74	1155	17.5	1.2	19.5	340	0.8	0.6	0.6	1.1	13	1	0.1
00N-75	3160	105.5	0.9	14	<5	3	1.6	1.4	4.7	16	4	0.6
00N-77	987	64	1.4	26.5	25	7.2	3.9	2.3	7.5	22	6	1.5
00N-78	886	79.5	3.4	26.5	430	8	4.6	2.5	8.5	22	6	1.6
00N-79	638	61	2.8	31.5	345	6.1	3.8	2	6.9	20	5	1.4
00N-80	1475	35.5	1.1	19.5	465	3.5	2.2	1.1	3.5	21	4	0.8
99M-140	2490	93.5	1.7	22	<5	3.8	2.3	1.6	5.7	18	3	0.9
99M-130	1645	58.5	2.2	23.5	5	2.4	1.5	0.9	2.8	17	4	0.5
00M-27	1365	45.5	2	14.5	<5	3	1.8	1.1	3.3	19	4	0.6
00M-28	2160	125	6.6	12	20	5.1	2.6	1.7	7.8	22	8	0.9
00M-31	1160	41	24.8	17	5	4.1	2.4	1.3	4.5	20	3	0.9
00M-32	1770	81.5	3.4	20.5	20	4	2.2	1.6	5.2	20	5	0.8

Table 6 (continued)

Sample	La	Pb	Lu	Nd	Ni	Nb	Pr	Rb	Sm	Ag	Sr	Ta	Tb	Tl
99N-1	28.5	135	0.3	17.5	<5	9	5.5	114.5	2.9	2	89	5	0.5	0.5
99N-2	45.5	175	0.3	29.5	<5	9	8.6	85.6	4.6	<1	513	5	0.6	<0.5
99N-9	33	<5	0.6	39.5	60	20	9.7	29.6	8.8	<1	540	2	1.4	<0.5
99N-31	31.5	50	0.3	19	<5	10	5.8	116	3.4	<1	280	3.5	0.5	<0.5
99N-42G	29.5	20	0.2	17.5	<5	8	5.2	90	2.7	<1	393	4.5	0.4	<0.5
99N-50	36	5	0.6	39	80	24	9.6	35	8.6	<1	573	2	1.5	<0.5
99-N57B	39	20	0.3	29.5	25	15	8.3	84.8	6	<1	620	1.5	0.8	<0.5
99N-58A	13.5	35	0.3	11	<5	14	3.1	163	2.5	<1	41.1	7	0.4	0.5
99N-66A	36.5	15	0.3	25	<5	13	7.4	122.5	4.7	<1	550	2	0.6	0.5
99N-68	39.5	5	0.6	41.5	55	23	10.7	47.2	8.8	<1	493	1.5	1.4	<0.5
99N-72	2.5	75	0.1	2	<5	6	0.6	128.5	0.7	<1	79.7	9	<0.1	0.5
99N-75	36.5	65	0.3	26.5	<5	9	7.3	88	4.7	<1	488	6	0.6	<0.5
99N-76	34	25	0.3	20	<5	11	6.2	127.5	3.2	<1	308	4	0.4	0.5
99N-77	32.5	20	0.4	24	<5	9	6.8	74.2	4.5	<1	453	2.5	0.7	<0.5
99N-78	29.5	20	0.3	20.5	<5	8	6.1	86.2	3.8	<1	465	3	0.6	<0.5
99N-79	22	35	0.3	13.5	<5	12	4.4	171.5	2.9	<1	114	6.5	0.4	0.5
99N-80	41	15	0.3	28	<5	9	8.1	86.2	4.7	<1	488	3.5	0.6	<0.5
00N-7	8	20	0.1	6.5	<5	6	2	96.6	1.4	<1	256	8	0.1	<0.5
00N-12	57.5	15	0.3	37	<5	7	10.8	60.2	5.3	<1	181.5	9	0.5	<0.5
00N-14	36	40	0.3	25	<5	10	7.2	92.4	4.4	<1	454	5	0.6	<0.5
00N-15A	31	55	0.3	21.5	<5	9	6.1	97	3.6	<1	413	5.5	0.5	<0.5
00N-19	24	25	0.3	17	<5	12	5	162	3.4	<1	89.1	7.5	0.5	0.5
00N-20	28.5	25	0.4	21	<5	11	6.1	120	3.8	<1	367	6.5	0.6	<0.5
00N-23	35	45	0.3	25.5	<5	10	7.2	96.6	4.2	<1	433	6.5	0.6	0.5
00N-25	32.5	5	0.6	35.5	15	9	8.9	67	7.5	<1	665	2.5	1.1	<0.5
00N-36	16.5	40	0.2	13.5	<5	3	3.6	112	2.7	<1	141	8	0.4	<0.5
00N-38	23	20	0.7	18	<5	8	5.2	118	4.5	<1	84.3	6.5	1	<0.5
00N-63	23.5	5	0.3	24	230	13	6	185.5	4.9	<1	637	1.5	0.7	0.5
00N-67	44	20	0.8	36	<5	13	10	135	7.9	<1	108	6.5	1.3	0.5
00N-68	27	30	0.8	21	<5	7	5.9	193	4.6	<1	97	11	1.1	0.5
00N-69	20	25	0.4	23	<5	7	5.4	63.2	5	<1	538	3	0.8	<0.5
00N-70	36	20	0.4	28.5	<5	9	7.8	104.5	4.9	<1	408	4	0.6	0.5
00N-72	26	30	0.3	26.5	130	13	6.6	185	5.3	<1	983	0.5	0.7	0.5
00N-73	38.5	<5	0.6	40.5	70	23	10.2	39.6	8.6	<1	539	2.5	1.4	<0.5
00N-74	8.5	30	0.1	7	<5	5	2.1	118.5	1.5	2	212	9.5	0.1	<0.5
00N-75	60	20	0.2	38	<5	8	11.3	74.2	5.7	<1	236	7	0.6	<0.5
00N-77	29.5	<5	0.6	35.5	50	19	8.4	43.6	7.5	<1	456	2.5	1.2	<0.5
00N-78	35.5	<5	0.6	42.5	45	23	10.2	38.6	8.6	<1	535	2.5	1.4	<0.5
00N-79	28.5	<5	0.6	33	105	18	8	44.6	7.2	<1	431	2	1.1	<0.5
00N-80	17.5	5	0.4	16.5	<5	8	4.2	68.2	3.6	<1	299	5	0.6	<0.5
99M-140	51	15	0.4	36	<5	7	10.3	60	5.9	<1	704	4	0.8	<0.5
99M-130	32.5	15	0.2	18	5	11	6.2	92.6	3.3	<1	387	7	0.4	<0.5
00M-27	23.5	15	0.3	20	<5	8	5.3	74.4	3.8	<1	350	4	0.6	<0.5
00M-28	59.5	30	0.3	52	10	29	14	187	9.4	<1	450	5	1.1	0.5
00M-31	20	15	0.4	20.5	5	8	5	112	4.6	<1	599	2	0.7	<0.5
00M-32	42.5	25	0.3	33.5	30	17	9.3	136.5	6.3	<1	910	6	0.8	<0.5

Table 6 (continued)

Sample	Th	Tm	Sn	W	U	V	Yb	Y	Zn	Zr
99N-1	15	0.3	1	112	4	<5	1.6	16	35	86
99N-2	16	0.3	<1	116	4	60	2.2	17.5	60	144.5
99N-9	3	0.6	<1	25	0.5	155	4.2	40.5	105	229
99N-31	14	0.3	<1	62	3.5	50	1.9	16	115	156
99N-42G	14	0.2	<1	91	2.5	65	1.4	13	45	103
99N-50	4	0.6	<1	16	1.5	150	3.8	40	105	231
99-N57B	11	0.3	1	13	2.5	135	2.1	20.5	60	141
99N-58A	18	0.2	<1	149	3	<5	2.1	15.5	30	67.5
99N-66A	17	0.3	1	33	2.5	80	1.9	17.5	85	167
99N-68	5	0.7	2	14	2	145	4.3	40	105	245
99N-72	8	0.1	<1	192	3.5	<5	1.1	4.5	10	37.5
99N-75	14	0.3	1	137	3	60	1.8	17.5	55	149.5
99N-76	19	0.2	1	85	3	35	1.9	14.5	45	129
99N-77	14	0.3	<1	50	3.5	105	2.5	20.5	50	118
99N-78	13	0.3	<1	54	3	90	2.1	17	55	102
99N-79	19	0.2	<1	131	3	<5	1.9	14.5	15	71.5
99N-80	16	0.3	<1	69	3.5	65	2.3	19.5	60	153
00N-7	23	0.1	<1	166	4	5	1	5.5	25	42
00N-12	28	0.2	<1	206	2	15	1.4	12.5	35	138.5
00N-14	16	0.3	1	102	5	75	1.9	18	55	123.5
00N-15A	17	0.3	1	103	4	85	1.8	15.5	60	104.5
00N-19	19	0.3	3	141	3	5	2.1	17	40	59.5
00N-20	17	0.4	1	134	4	50	2.4	19	55	109.5
00N-23	16	0.3	1	141	6	55	1.9	16	65	124.5
00N-25	7	0.6	1	46	1.5	215	3.7	32	120	165
00N-36	18	0.1	<1	188	3.5	10	1.3	12	10	55
00N-38	17	0.7	1	145	2	15	4.8	41.5	35	69
00N-63	4	0.3	<1	18	1.5	180	2	19	115	76
00N-67	29	0.8	2	140	3	20	5.2	47.5	35	135
00N-68	14	0.8	<1	250	3	10	5.5	43	5	64.5
00N-69	4	0.4	1	65	2	135	2.5	22.5	100	105
00N-70	19	0.3	1	72	8.5	50	2.9	19.5	55	141
00N-72	5	0.3	1	13	1.5	185	2	18.5	95	83.5
00N-73	5	0.6	1	28	1.5	155	4.4	37.5	130	214
00N-74	19	<0.1	<1	235	12	10	0.8	4.5	80	28.5
00N-75	30	0.2	1	152	2	20	1.5	14.5	35	113
00N-77	6	0.6	1	32	2	135	3.7	34.5	120	226
00N-78	5	0.7	11	23	1.5	165	4.3	40.5	125	236
00N-79	5	0.5	1	22	2	160	3.5	31.5	115	191.5
00N-80	4	0.3	1	109	1.5	130	2.1	18.5	75	134.5
99M-140	17	0.4	<1	95	1.5	115	2	21	70	120
99M-130	18	0.2	9	148	4	80	1.7	14.5	35	112.5
00M-27	9	0.3	1	86	2	70	2	16	70	118
00M-28	13	0.3	5	84	3	35	2	23	95	314
00M-31	5	0.4	1	32	2	185	2.5	22.5	75	109.5
00M-32	13	0.3	2	115	3.5	100	2.2	21	95	159

1.

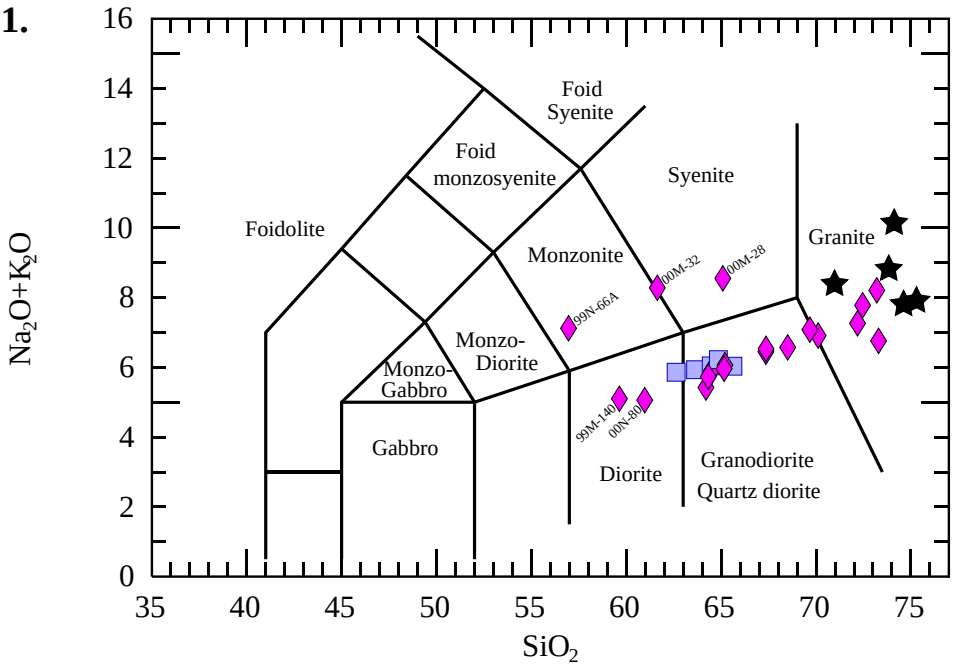

2.

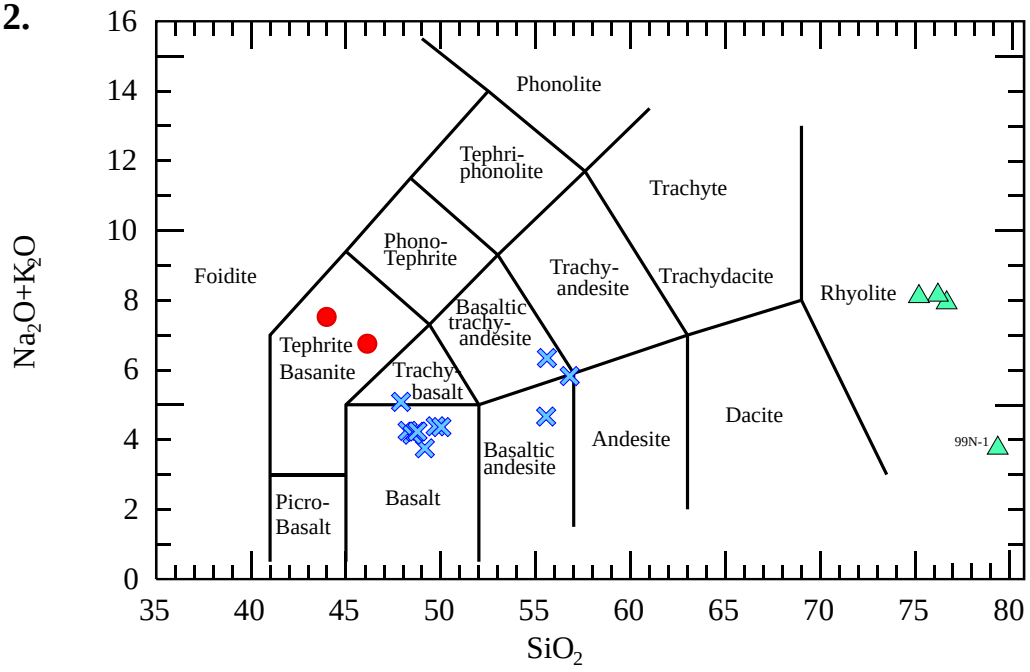

Figures 16 1. and 2. Total alkali versus silica diagrams (Le Bas et al., 1986) showing range of rock type in the Moosehorn Range area. Symbols are as follows:

♦ - MRG and granodioritic dykes, □ - quartz diorite porphyritic intrusions, ★- aplite, pegmatite, or leucogranitic dykes, △ - fine-grained felsite dykes, ● - lamprophyric dykes, ✕ - fine- to medium-grained mafic dykes. Samples that plot outside of their expected compositional field are labelled and discussed in the text.

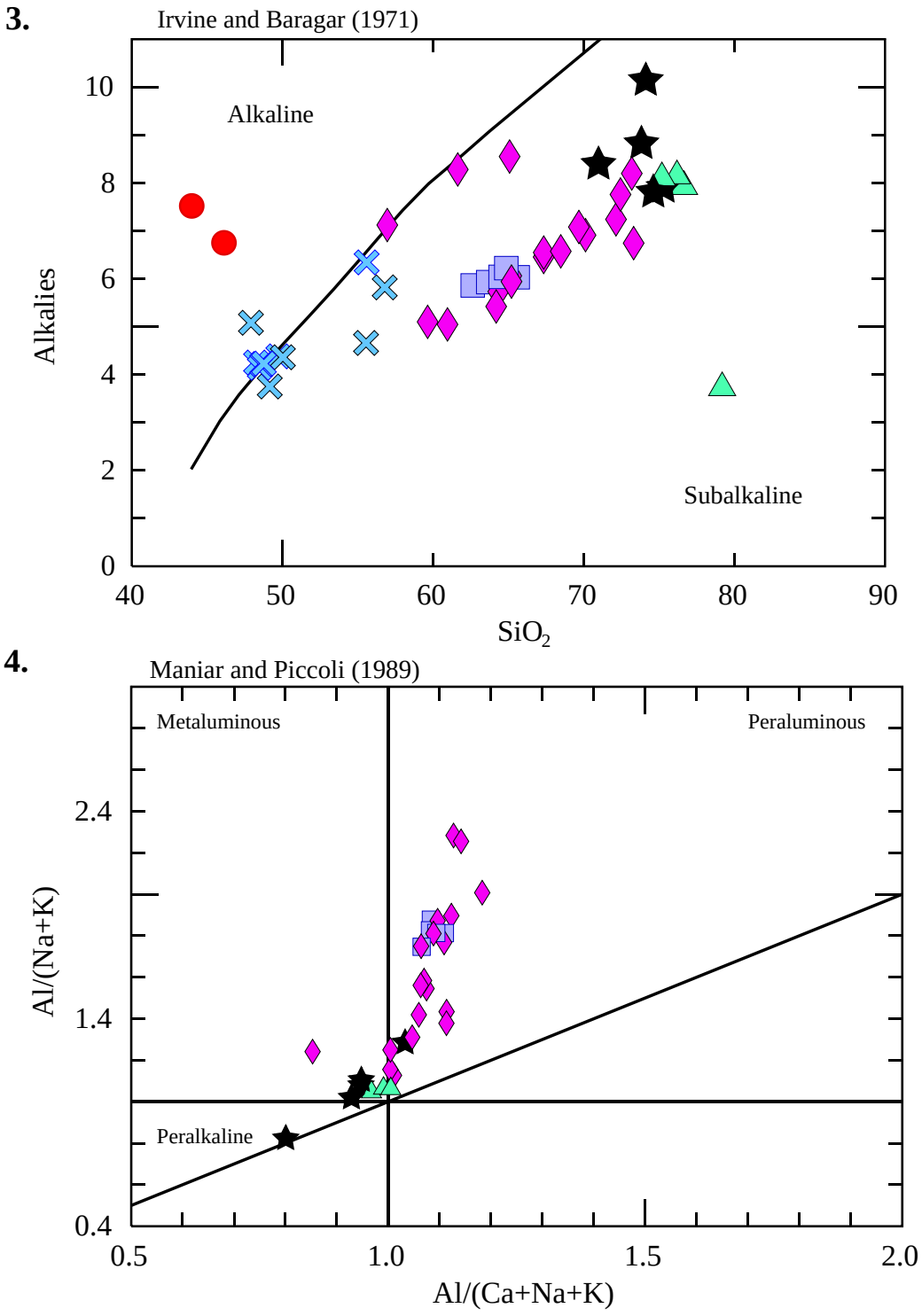

Figure 16.3 Total alkali versus silica for Moosehorn Range area intrusions after Irvine and Baragar (1971). Most intrusions are subalkaline; the mafic intrusions are distinctly more alkaline. **4.** Al/(Na+K) versus Al/(Ca+Na+K) diagram after Maniar and Piccoli (1989). The MRG intrusions and quartz diorite dykes are peraluminous and the felsite and aplite dykes are weakly metaluminous.

1.

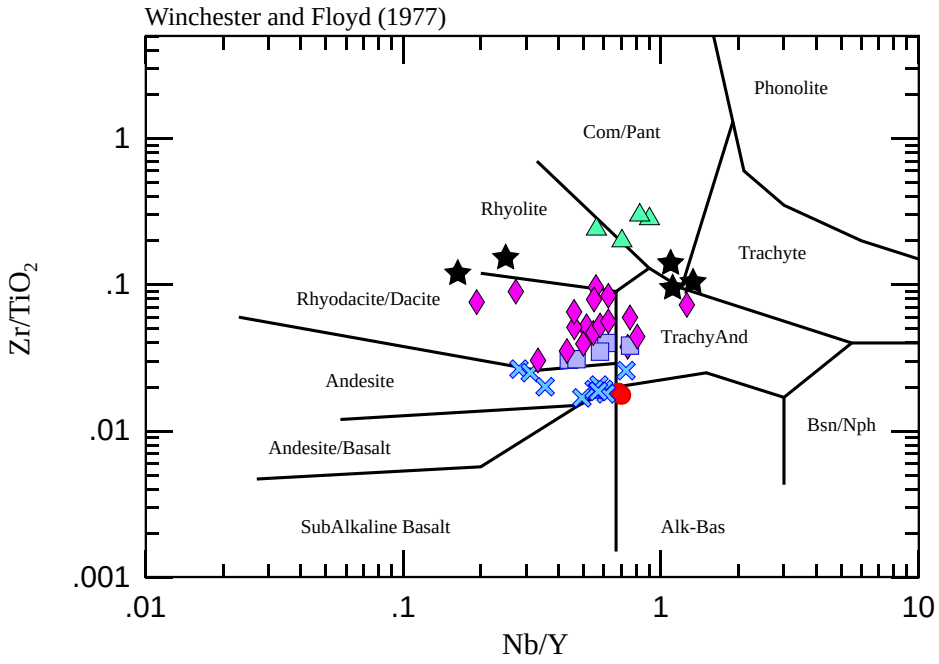

2.

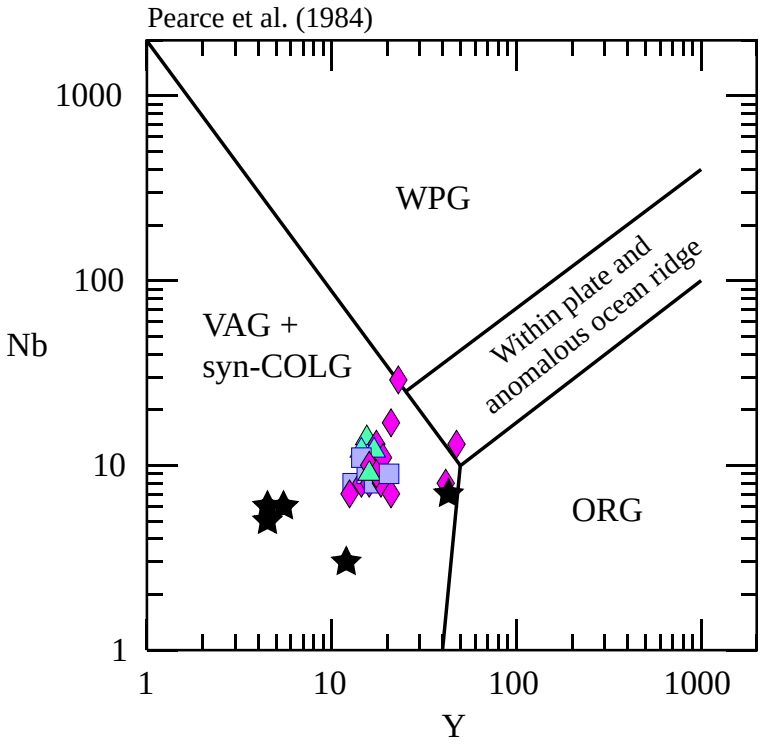

Figure 17 Immobile element plots. **1.** Range of rock compositions based on immobile elements. There is less scatter of samples on this plot as compared to the total alkali versus silica plots. **2.** Nb versus Y plot for the felsic to intermediate Moosehorn Range area intrusions; the majority of the samples fall within the volcanic arc granitoid field.

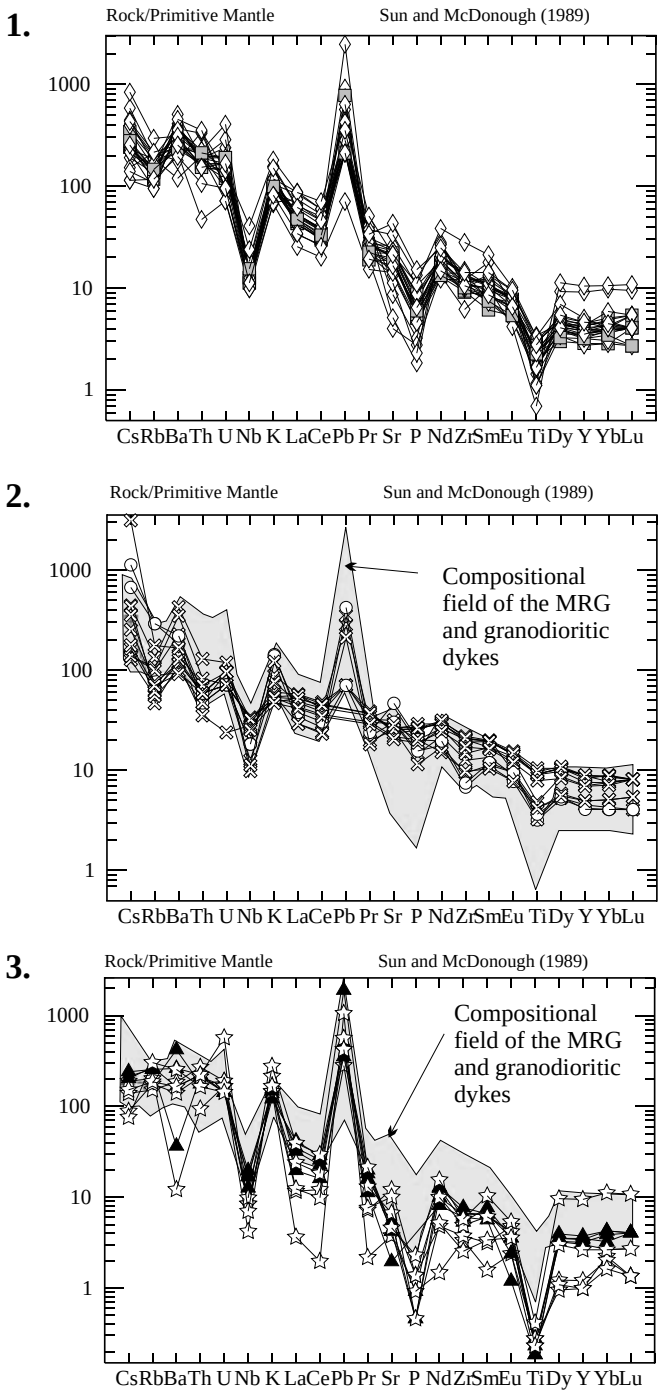

Figure 18 Primitive mantle-normalized rare-earth element diagrams for all the intrusions in the Moosehorn Range area. **1.** MRG and granodioritic dykes. **2.** Aplite, pegmatite, leucogranite, and felsite dykes with the compositional field of the granodiorites in the background. **3.** Lamprophyre and fine-grained mafic dykes with granodiorite field in the background. ♦ - MRG and granodioritic dykes, □ - porphyritic quartz diorite intrusions, ★- aplite, pegmatite, or leucogranitic dykes, △ - fine-grained felsite dykes, ● - lamprophyric dykes, ⨯ - fine- to medium-grained mafic dykes.

and 00N-80) likely reflects major element mobility (note that the plutonic compositions cluster more tightly on the Winchester and Floyd (1977) immobile element plot).

For this section, the rocks in the study area have been separated into groups on the basis of temporal relationship, lithology, and geochemical signatures. These groups include the plutonic rocks and porphyry dykes, the aplite-pegmatite-felsite dykes, and the mafic dykes. Age data supports a close temporal and possibly comagmatic relationship between all of the rocks except for the mafic dykes, which are much younger.

Plutonic Rocks and Porphyritic Dykes

Major element data indicates that most plutonic rocks in the study area range from diorite to granite (mainly granodiorite and quartz diorite), are subalkaline, and are predominantly peraluminous to weakly metaluminous in composition. These phases are all approximately the same age and are probably comagmatic. Samples 99M-140, 00M-28, and 00M-32 were collected from plutons immediately southeast of the study area and may not be directly related to those in the immediate Moosehorn Range area.

On the Nb versus Y discrimination diagram of Pearce et al. (1984), the felsic intrusions plot consistently in the volcanic arc field (Fig. 17.2). Figures 18.1 to 18.3 show the trace and REE patterns for these intrusions, employing the primitive mantle normalization scheme of Sun and McDonough (1989). These rocks are enriched in low field strength elements (LFSE) and show low normalized abundances of Nb and Ti; these characteristics are typical of I-type volcanic arc or subduction-related granitoids (Whalen et al., 1994; Jenner, 1996; Christiansen and Keith, 1996; Morris et al., 2000). Depletion of P, commonly seen in I-type granites, is likely due to fractionation of apatite (Chappell and White, 1992). Because Pb is a relatively mobile element (Jenner, 1996), the pronounced

positive Pb anomaly may be a result of melt interaction with Pb-rich crust (e.g., Devono-Mississippian syn-sedimentary sulphide deposits of the Yukon-Tanana terrane).

Aplite-Pegmatite-Felsite Dykes

All of these felsic dyke phases fall within the volcanic arc field of Pearce et al. (1984) (Fig. 17.2), and within the granite or rhyolite fields on total alkalies versus silica diagrams (Figs. 16.1 and 16.2). Sample 99N-1 is pervasively sericitized and pyritized, and as such does not plot with the other felsite units in Figure 16.2. Immobile element ratios on the Winchester and Floyd (1977) plot (Fig. 17.1) suggest the rocks range in composition from rhyolite to comendite-pantellerite to trachyte. On the total alkalies versus silica plot and Al/(Na+K) versus Al/(Ca+Na+K) plot in Figures 16.3 and 16.4, most of the felsic dykes are metaluminous to very weakly peraluminous, and subalkaline.

Figure 18.2 shows the aplite, pegmatite, and felsite trace and REE signatures plotted relative to the compositional field of the main intrusions. The rocks are variably depleted in the light rare earth elements (LREE) such as La, Ce, Pr, and Nd. In addition, they exhibit slightly more pronounced negative Nb and Ti anomalies, relative to those of the main intrusions. These phenomena are consistent with greater degrees of fractionation of a volatile-rich melt (Christiansen and Keith, 1996; Pearce et al., 1984; Miller and Mittlefehldt, 1982; Halleran and Russell, 1993).

Mafic Dykes

The fine-grained mafic dykes from the study area range in composition from basalts to basaltic andesites (Fig. 16.2). Samples 00N-63 and 00N-72, which are relatively unaltered biotite-phyric minettes collected from drill core, plot within the tephrite-basanite

field of LeBas et al. (1986) but are distinguished from typical alkalic mafic volcanics by their relative enrichment in potassium (Métais and Chayes, 1963; Hall, 1996). Most of the mafic dykes generally fall within the arc-basalts field on the Wood (1980) plot in Figure 19, and straddle the alkaline-subalkaline boundary. The minettes, however, are considerably more alkaline than any of the other intrusions.

The trace and REE signatures of the late minette and fine-grained mafic dykes can be compared to those of the main intrusions in Figure 18.3. The negative P, Nb, and Ti anomalies are far less pronounced than those of the granitoids. The variable Pb contents of the mafic volcanics could be indicative of either Pb mobility or interaction of the melts with heterogeneous mantle and/or chemically evolved continental crustal material (e.g., Taylor and McLennan, 1985).

Interpretation of Paleotectonic Setting of mid-Cretaceous Magmatism

Plutonic Rocks and Porphyry Dykes

Mortensen et al. (2000) and Driver et al. (2000) concluded that all of the mid-Cretaceous intrusive suites in the Yukon have been extensively contaminated by continental crust. Numerous lines of evidence from DRB and MRG intrusions, including lead isotopic, $^{87}Sr/^{86}Sr$, $\delta^{18}O$, εNd_T, and trace and REE geochemical data, support this conclusion.

The immediate wallrocks to the MRG (and the DRB) are predominantly biotite-quartz-feldspar schists and gneisses with both sedimentary and igneous protoliths, at least one of which has been inferred to be mid-Paleozoic in age. Very little is known about the thickness and composition of the crust underlying the Yukon-Tanana terrane, and thus the degree of crustal involvement with mid-Cretaceous magmatism is difficult to assess. Recent

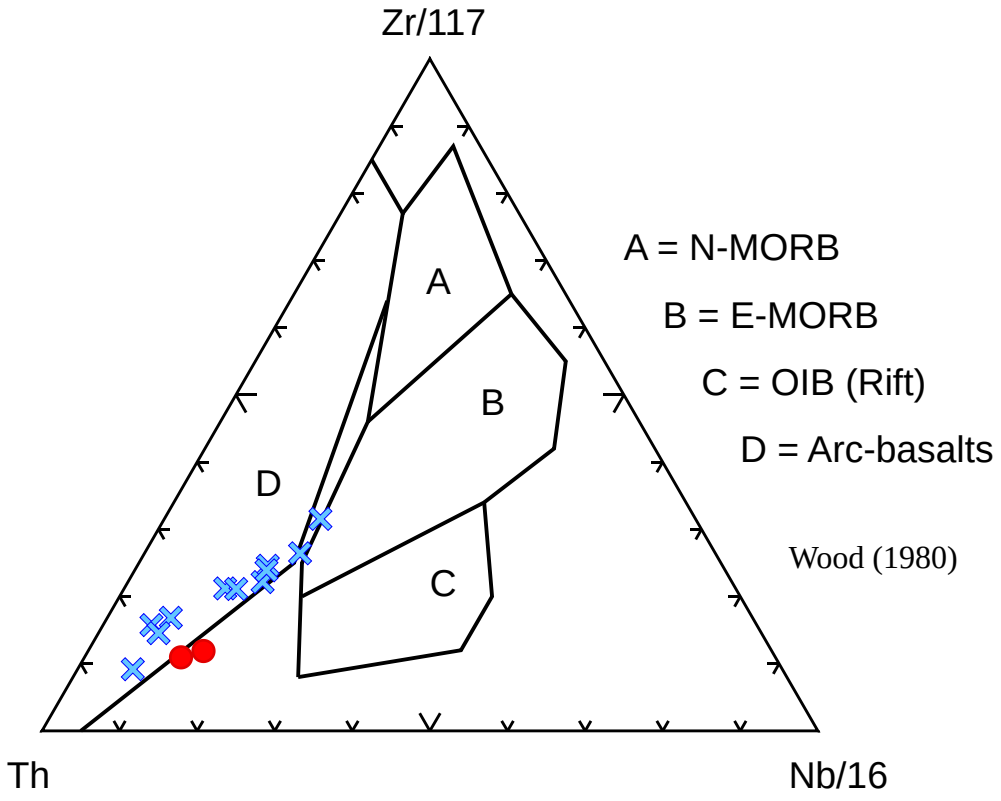

Figure 19 Ternary diagram on which the Moosehorn Range area mafic rocks plot predominantly in the arc-basalt field. ✕ - fine-grained mafic dykes, ● - lamprophyre dykes.

studies indicate that the YTT may only be about 10 km thick (Cook and Erdmer, 2002). MRG magmas would, therefore, probably have interacted predominantly with the thicker underlying North American continental crust.

All of the intrusions from the study area have similar lead isotopic compositions and thus were probably derived from the same parent magma. Elevated $^{207}Pb/^{204}Pb$ compositions of feldspars for the intrusions (Fig. 14 and Table 4) are consistent with those for rocks of old upper crustal origin (Tosdal et al., 1999). The $^{206}Pb/^{204}Pb$ ratios range from 19.026 to 19.473, the $^{207}Pb/^{204}Pb$ range from 15.582 to 15.732, and the $^{208}Pb/^{204}Pb$ range from 38.672 to 39.730. Comparable compositions were obtained from DRB samples southeast of the study area by Selby et al. (1999). In addition, $^{87}Sr/^{86}Sr$ values reported by Selby et al. (1999) are between 0.7066 and 0.7075 (for crustal evolution of about 104 Ma), εNd_{104} values for the same samples are –4.5 to –7.4, and T_{DM} model ages range from 1.13 to 1.53 Ga. No Sr or Nd isotopic data are available from MRG intrusions; however, it is probable that they would show similar isotopic characteristics. This information points towards a significant crustal contribution to the DRB and probably MRG magmas, if not an entirely crustal origin (Rollinson, 1993; Aleinikoff et al., 1987). This hypothesis is further substantiated by the peraluminous nature of the MRG intrusions and the ubiquitous presence of a minor component of inherited zircon in the samples. Zircon fractions showing inheritance typically fall on or just off concordia; therefore the rocks from which the inherited zircons were derived are not significantly older than the MRG. If significant amounts of zircon from the mid-Paleozoic metamorphic rocks of the YTT were incorporated into the magma, the fractions would have plotted further off concordia.

An additional argument supporting a crustal or crustally contaminated source for the MRG magmas is the low values for Nb/Ta. Pearce et al. (1984) and Brown (1991)

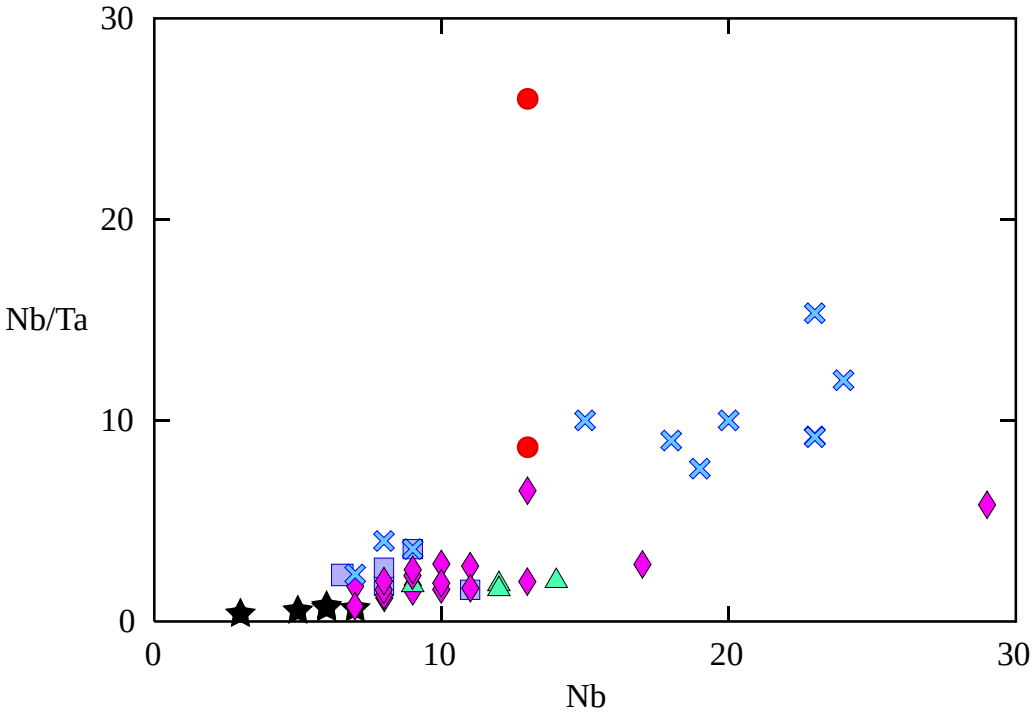

Figure 20 Nb/Ta versus Nb plot of all the Moosehorn Range area intrusions. The rocks have Nb/Ta < 10, and some are < 5; Green (1995) states that melts generated in the crust generally have Nb/Ta of less than 11. The felsic to intermediate rocks have therefore either been entirely crustally derived or have been extensively contaminated by continental crust.

The symbols are as follows:

♦ - MRG and granodioritic dykes, □ - quartz diorite porphyritic intrusions, ★- aplite, pegmatite, or leucogranitic dykes, △ - fine-grained felsite dykes, ● - lamprophyric dykes, ✕ - fine- to medium-grained mafic dykes.

recognized the low Nb/Ta relationship in collision-zone granites and volcanic arc granites, probably due to Ti-rich mineral fractionation and/or fluid/melt partitioning (Green, 1995). A plot of Nb/Ta versus Nb in Figure 20 shows that the Moosehorn Range intrusive rocks have Nb/Ta < 10, and some are < 5. Green (1995) states that melts generated in the crust generally have Nb/Ta ≤ 11.

Several possible paleotectonic scenarios can be envisaged to explain the origin and chemical signatures of the MRG intrusions. The melts may have been subduction-related mantle-derived magmas that interacted extensively with evolved and/or thick continental crust (Selby et al., 1999; Driver et al., 2000; Aleinikoff et al., 2000). The Cretaceous WCCS, including intrusions associated with the Dawson Range batholith, is currently thought to have formed between 111 and 99 Ma in a southwest-facing continental magmatic arc setting (Plafker and Berg, 1994; Mortensen et al., 2000). The lack of deep crustal exposures and the absence of confirmed coeval mafic magmatism (Johnston, pers. comm., 2001), make it difficult to conclusively constrain the ultimate paleotectonic setting in which this voluminous intermediate to felsic magmatism occurred.

The abundance of hornblende, biotite, titanite, epidote, and allanite in Moosehorn Range area granites and granodiorites suggests that the rocks are I-type granitoids (Christiansen and Keith, 1996). Furthermore, they are enriched in the large ion lithophile elements (LILE) relative to high field strength elements (HFSE) and have deep negative Nb anomalies; these characteristics are common in I-type magmas (Christiansen and Keith, 1996). Subduction-related granites normally exhibit negative Nb, Ti, *and* Eu anomalies due to fractionation of mantle-derived basalts (Hildreth and Moorbath, 1988; Selby et al., 1999). Because the Moosehorn Range intrusions are not markedly depleted in Eu, and there is a lack of contemporaneous mafic magmatism, it is conceivable that the felsic magmas formed

entirely by partial melting of evolved crust and inherited its subduction signature (e.g., Selby et al., 1999).

If crustally derived, there are at least four possible scenarios in which the mid-Cretaceous magmas in the Moosehorn Range area may have formed. Crustal melts may have been formed due to heat input from underplated mafic magma possibly related to slab break-off (van de Zedde and Wortel, 2001) or mantle or crustal delamination (Thompson, 1999; Whalen et al., 1994). Crustal extension, which has been documented in parts of the YTT (eg., Hansen and Dusel-Bacon, 1998; Pavlis et al., 1993) may have generated melts with a strong crustal signature. Alternatively, overthickening of the crust during contractional deformation may have driven crustal melting and subsequent magmatism (Plafker and Berg, 1994, and references therein). Entirely crustally-derived melts are more typically formed in areas of overthickened crust, possibly attributed to collisional thrust faulting and shortening (Rubin et al., 1995; Ducea, 2001) or to mantle underplating (Thompson, 1999; Pitcher, 1993).

Stanley et al. (1990) proposed that mid-Cretaceous magmas in the western YTT in Alaska were derived predominantly from melting of Mesozoic flysch that was thrust beneath the crystalline YTT rocks during terrane accretion. Intrusions derived from sediments (i.e., S-type granites) are typically very peraluminous (Pitcher, 1993; Christiansen and Keith, 1996; Patiño Douce, 1999; Aleinikoff et al, 2000); most of the mid-Cretaceous intrusions of the YTT are peraluminous to only slightly metaluminous. However, Aleinikoff et al. (2000) found that with decreasing age of Cretaceous YTT intrusions, the $^{207}Pb/^{204}Pb$, $^{87}Sr/^{86}Sr$, and $\delta^{18}O$ values decrease and the εNd_T values increase. If flysch had been a dominant component of the melts, much higher values of $\delta^{18}O$ would be expected for the resulting intrusions (Aleinikoff et al., 2000).

In summary, from the available geochemical data, the felsic to intermediate Moosehorn Range area intrusions are interpreted to have formed in the later stages of a southwest-facing continental magmatic arc setting active between approximately 111 and 99 Ma. The magmas were probably mantle-derived, but were extensively contaminated by continental crust underlying the YTT.

Interpretation of Early Tertiary Paleotectonic Setting

Mafic Dykes

Early tertiary mafic volcanic suites have been recognized throughout the northern Canadian Cordillera (Foster et al., 1994; Francis et al., 1999; Abraham et al., 2001). The alkalic minette and fine-grained mafic volcanic dykes in the Moosehorn Range, dated at 64.3 ± 0.6 Ma (biotite $^{40}Ar/^{39}Ar$ age) and 53-54 Ma (whole rock K-Ar), respectively, differ from Tertiary volcanics documented by Abraham et al. (2001) and Francis et al. (1999) in that the samples from this study exhibit trace and rare earth element signatures typical of volcanic arc lavas. They are enriched in LFSE and LREE, and depleted in HFSE, particularly Nb, Zr, and to a lesser extent Ti and P. These signatures are comparable to those of post-orogenic minettes in the Sierra Nevada region of California (Feldstein and Lange, 1999).

Minettes commonly occur as late-stage dykes in orogenic systems (McBirney, 1993), and the melts are consequently vulnerable to contamination by tectonically thickened crust. There is significant evidence for crustal contamination of the Moosehorn Range minettes and fine-grained mafic volcanics. Upon normalization to the North American Shale Composite (Gromet et al., 1984), the resulting REE profiles of the mafic dyke rocks are

essentially flat, which is consistent with a significant chemical contribution from continentally-derived sediment. Moreover, the Pb enrichment and relatively radiogenic Pb isotopic compositions of the mafic dyke rocks (Table 4) probably reflects interaction of the melts with evolved continental crust (Tosdal et al., 1999). Nb/Ta values less than 17 (Fig. 20) also indicate the melts were not purely mantle-derived.

Early Tertiary mafic volcanism in west-central Yukon may have been related to Kluane Arc magmatism and a change in the relative motion of the North American plate with respect to the Kula plate (Gabrielse and Yorath, 1991; Plafker and Berg, 1994). Large-scale dextral displacements along the Tintina and Denali faults were also active at this time, which resulted in the formation of localized extensional basins in the northern Cordillera (Plafker and Berg, 1994; Jackson and Mortensen, 2000). The mafic volcanism may have been a product of decompression melting of the mantle in response to resultant crustal thinning.

Summary and Conclusions

U-Pb ages, Pb isotopic compositions, and geochemical characteristics for all the felsic to intermediate intrusions in the Moosehorn Range area suggest that all the units are petrogenetically related and were emplaced between approximately 96 Ma and 100 Ma. The intrusions are considered to be part of the Dawson Range batholith, which is believed to have formed during mid-Cretaceous northeastward subduction of the Farallon plate (Selby et al., 1999; Mortensen et al., 2000). Geochemical data for intrusions of the Moosehorn Range area suggest that the voluminous magmas were probably mantle-derived and extensively contaminated by continental North American crust during ascent. This is further substantiated by the presence of inherited zircons in the rocks and by the lack of

contemporaneous mafic magmatism. Batholiths of similar geochemical nature can also be formed from decompression melting of mantle material and subsequent crustal contamination related to crustal extension (ex. backarc or gravity spreading) (e.g., Hansen and Dusel-Bacon, 1998), mantle or crustal delamination (Thompson, 1999; Whalen et al., 1994), or subducting slab break-off (van de Zedde and Wortel, 2001). Because contemporaneous mafic rocks are not present in the region for geochemical analysis, the ultimate source for the 96-100 Ma intrusions in the Moosehorn Range area remains uncertain.

The MRG is locally foliated; the moderately to steeply southwest-dipping S1 foliation probably formed during to shortly after intrusion, perhaps related to dextral strike-slip displacement along the Big Creek fault that forms the northern contact of the DRB with the YTT. A second deformation event, D2, dextrally offset the S1 foliation at approximately 94 Ma, along a moderately to steeply northwest-dipping D2 mylonitic strike-slip shear zone. Many of the foliated granodiorite, quartz diorite, and felsite dykes throughout the study area are oriented and foliated parallel to S2.

The gold-bearing shallowly east-northeast-dipping quartz veins were emplaced within the MRG at approximately 92-93 Ma during a southwestward contractional brittle deformation event. Therefore, between about 94 and 93 Ma, the rocks cooled through 300˚C. The regional structural context for the formation of these brittle reverse fault-hosted veins remains unclear and is discussed in further detail in Chapter 3.

Two mafic intrusive events post-date the vein formation. At 64 Ma, lamprophyres locally intruded the MRG and may be related to the voluminous mafic alkalic Carmacks Group volcanics. At about 54 Ma, fine-grained mafic dykes were emplaced throughout the Moosehorn Range area. Felsic and mafic dykes of similar age have been found in east-

central Alaska and in other locales throughout west-central Yukon Territory (Newberry et al., 1995; Newberry, 2000; Ebert et al., 2002; Mortensen, 2002, pers. comm.). Although these melts are volumetrically minor, they are fairly regionally widespread and may have formed from partial melting of the mantle in response to crustal thinning associated with Eocene movements along the Tintina, Denali, and related faults.

REFERENCES

Abraham, A., Francis, D., and Polvé, M. 2001. Recent alkaline basalts as probes of the lithospheric mantle roots of the Northern Canadian Cordillera. Chemical Geology, **175**: 361-386.

Aleinikoff, J.N., Farmer, G.L., Rye, R.O., and Nokleberg, W.J. 2000. Isotopic evidence for the sources of Cretaceous and Tertiary granitic rocks, east-central Alaska; implications for the tectonic evolution of the Yukon-Tanana terrane. Canadian Journal of Earth Sciences, **37**: 945-956.

Aleinikoff, J.N., Dusel-Bacon, C., Foster, H.L., and Nokleberg, W.J. 1987. Lead isotopic fingerprinting of tectonostratigraphic terranes, east-central Alaska. Canadian Journal of Earth Sciences, **24**: 2089-2098.

Bostock, H.G. 1936. Carmacks district, Yukon (115I). Geological Survey of Canada Memoir 189.

Brodie, K.H., and Rutter, E.H. 1985. On the relationship between deformation and metamorphism, with special reference to the behaviour of basic rocks. *In* Metamorphic reactions; Kinetics, textures, and deformation, *Edited by* A.B. Thompson and D.C. Rubie, pp. 138-179.

Brown, M. 1991. Comparative geochemical interpretation of Permian-Triassic plutonic complexes of the Coastal Range and Altiplano, 25º30' to 26º30'S, Northern Chile. *In* Andean magmatism and its tectonic setting, Geological Society of America, Special Paper 265. *Edited by* R.S. Harmon and C.W. Rapela, pp.157-178.

Cairnes, D.D. 1917. Investigations and mapping in Yukon Territory. Geological Survey of Canada, Memoir 284.

Carlson, G.G. 1987. Geology of Mount Nansen (115-I/3) and Stoddart Creek (115-I/6) map areas, Dawson Range, central Yukon. Exploration and Geological Services Division, Yukon, Indian and Northern Affairs Canada, Open File 1987-2.

Chappell, B.W., and White, A.J.R. 1992. I- and S-type granites in the Lachlan fold belt. Transactions of the Royal Society of Edinburgh, **83**: 1-26.

Christiansen, E.H., and Keith, J.D. 1996. Trace element systematics in silicic magmas: a metallogenic perspective. *In* Trace element geochemistry of volcanic rocks: Applications for massive sulphide exploration: Geological Association of Canada, Short Course Notes. *Edited by* D.A. Wyman, **12**: 115-151.

Cockfield, W.E. 1921. Silver-lead deposits of the Keno Hill area, Mayo District, Yukon. Geological Survey of Canada, Summary Report, pp. 1-6.

Colpron, M., and Yukon-Tanana Working Group. 2001. Ancient Pacific Margin – An update on stratigraphic comparison of potential volcanogenic massive sulphide-hosting successions of Yukon-Tanana Terrane, northern British Columbia and Yukon. *In* Yukon exploration and geology 2000, Exploration and Geological Services Division, Yukon, Indian and Northern Affairs Canada. *Edited by* D.S. Emond and L.H. Weston, pp. 97-100.

Cook, F.A., and Erdmer, P. 2002. Cross-section of the lithosphere from the Slave province to Kula plate constructed from seismic reflection data: The supracrustal crust. *In* Slave-Northern Cordillera Lithospheric Evolution (SNORCLE) Transect and Cordilleran tectonics workshop meeting (Feb.21-23), Pacific Geoscience Centre, Sidney, B.C., Lithoprobe report No. 72. *Compiled by* F. Cook and P. Erdmer, pp.

Ducea, M. 2001. The California Arc: Thick granitic batholiths, eclogitic residues, lithospheric-scale thrusting, and magmatic flare-ups. GSA Today, **11**: 4-10.

Driver, L.A., Creaser, R.A., Chacko, T., and Erdmer, P. 2000. Petrogenesis of the Cretaceous Cassiar batholith, Yukon-British Columbia, Canada: Implications for magmatism in the North American Cordilleran Interior. Geological Society of America Bulletin, **112**: 1119-1133.

Ebert, S., Mortensen, J.K., and Tosdal, R. 2002. Comments on the U-Pb geochronology from the Pogo district, Alaska. *In* Regional geologic framework and deposit-specific exploration models for intrusion-related gold mineralization, Yukon and Alaska – Notes from the Mineral Deposit Research Unit third annual Technical Meeting (Jan. 19), University of British Columbia. *Compiled by* S. Ebert, pp.70-72.

Etheridge, M.A., Wall, V.J., Cox, S.F., and Vernon, R.H. 1984. High fluid pressures during regional metamorphism and deformation: implications for mass transport and deformation mechanisms. Journal of Geophysical Research, **89**: 4344-4358.

Feldstein, S.N., and Lange, R.A. 1999. Pliocene potassic magma from the Kings River region, Sierra Nevada, California; evidence for melting of a subduction-modified mantle. Journal of Petrology, **40**: 1301-1320

Foster, H.L., Keith, T.E., and Menzie, W.D. 1994. Geology of the Yukon-Tanana area of east-central Alaska. *In* The geology of Alaska: Boulder, Colorado, Geological Society of America, The geology of North America, v. G-1. *Edited by* G. Plafker and H.C. Berg, pp. 205-240.

Francis, D., Abraham, A., and Polvé, M. 1999. Volcanic probes of the craton's edge beneath the northern Canadian Cordillera. *In* Slave-Northern Cordillera Lithospheric Evolution (SNORCLE) Transect and Cordilleran tectonics workshop meeting (March 5-7), University of Calgary, Lithoprobe report No. 69. *Compiled by* F. Cook and P. Erdmer, pp. 142-145.

Gabrielse, H., and Yorath, C.J. 1991. Tectonic synthesis. *In* Geology of the Cordilleran orogen in Canada, Geological Survey of Canada, Geology of Canada, No. 4. *Edited by* H. Gabrielse and C.J. Yorath, pp. 677-705.

Godwin, C.I. 1975. Alternative interpretations for the Casino complex and Klotassin batholith in the Yukon Crystalline terrane. Canadian Journal of Earth Sciences, **12**: 1910-1916.

Godwin, C.I., and Sinclair, A.J. 1982. Average lead isotope growth curves for shale-hosted zinc-lead deposits, Canadian Cordillera. Economic Geology, **77**: 208-211.

Green, T.H. 1995. Significance of Nb/Ta as an indicator of geochemical processes in the crust-mantle system. Chemical Geology, **120**: 347-359.

Gromet, L.P., Dymek, R.F., Haskin, L.A., Korotev, R.L. 1984. The "North American shale composite"; its compilation, major and trace element characteristics. Geochimica et Cosmochimica Acta, **48**: 2469-2482.

Grond, H.C., Churchill, S.J., Armstrong, R.L., Harakal, J.E., and Nixon, G.T. 1984. Late Cretaceous age of the Hutshi, Mount Nansen, and Carmacks groups, southwestern Yukon Territory and northwestern British Columbia. Canadian Journal of Earth Sciences, **21**: 554-558.

Hall, A. 1996. Igneous petrology. Longman Group Limited, Essex, England, 551 pp.

Halleran, A.A.D., and Russell, J.K. 1993. Rare-earth element bearing pegmatites in the Wolverine metamorphic complex: A new exploration target (93N/9E, 93O/12W, 5W). *In* Geological Fieldwork 1992, British Columbia Mineral Resources Division Paper 1993-1. *Edited by* B. Grant and J.M. Newell, pp. 301-306.

Hansen, V.L., and Dusel-Bacon, C. 1998. Structural and kinematic evolution of the Yukon-Tanana upland tectonites, east-central Alaska: A record of late Paleozoic to Mesozoic crustal assembly. Geological Society of America Bulletin, **110**: 211-230.

Hart, C.J.R., and Langdon, M. 1998. Geology and mineral deposits of the Mount Nansen camp, Yukon. *In* Yukon Exploration and Geology 1997, Exploration and Geological Services Division, Yukon, Indian and Northern Affairs Canada. *Edited by* C.F. Roots and D.S. Emond, pp. 129-138.

Hildreth, W., and Moorbath, S. 1988. Crustal contributions to arc magmatism in the Andes of central Chile. Contributions to Mineralogy and Petrology, **98**: 455-489.

Hobbs, B.E., Means, W.D., and Williams, P.F. 1976. An outline of structural geology. Wiley, New York, NY, 571 pp.

Hunt, P.A., and Roddick, J.C. 1991. A compilation of K-Ar ages: Report 20. *In* Radiogenic age and isotopic studies: Report 4. Geological Survey of Canada, Paper 90-2. pp. 113-143.

Irvine, T.N., and Baragar, W.R.A. 1971. A guide to the chemical classification of the common volcanic rocks. Canadian Journal of Earth Sciences, **8**: 523-548.

Jackson, L.E. and Mortensen, J.K. 2000. New constraints indicate mainly Early Paleogene displacement on the Tintina Fault Zone in the northern Cordillera. Geological Society of America, Cordilleran Section Meeting, Program with Abstracts, **32**: 21.

Jenner, G.A. 1996. Trace element geochemistry of igneous rocks: geochemical nomenclature and analytical geochemistry. *In* Trace element geochemistry of volcanic rocks: Applications for massive sulphide exploration: Geological Association of Canada, Short Course Notes. *Edited by* D.A. Wyman, **12**: 51-77.

Johnston, S.T. 1995. Geological compilation with interpretation from geophysical surveys of the northern Dawson Range, central Yukon (115-J/9 and 10, 115-I/12, 1:100 000 scale map). Exploration and Geological Services Division, Yukon, Indian and Northern Affairs Canada, Open File 1995-2(G).

Johnston, S.T. 1999. Large-scale coast-parallel displacements in the Cordillera: a granitic resolution to a paleomagnetic dilemma. Journal of Structural Geology, **21**: 1103-1108.

Johnston, S.T., Timmerman, J.T., and Shives, R.B.K. 1995. Results of an airborne multiparameter geophysical survey of the Dawson Range, Yukon: Revised geology and implications for mineral exploration. *In* Programs with Abstracts, Geological Association of Canada/Mineralogical Association of Canada Joint Annual Meeting, **20**: 50.

Johnston, S.T., Wynne, P.J., Francis, D., Hart, C.J.R., Enkin, R.J., Engebretson, D.C. 1996. Yellowstone in Yukon; the Late Cretaceous Carmacks Group. Geology, **24**: 997-1000.

Krogh, T.E. 1982. Improved accuracy of U-Pb zircon ages by the creation of more concordant systems using an air abrasion technique. Geochimica et Cosmochimica Acta, **46**: 637-649.

Le Bas, M.J., Le Maître, R.W., Streckeisen, A., and Zanettin, B. 1986. A chemical classification of volcanic rocks based on the total alkali-silica diagram. Journal of Petrology, **27**: 745-750.

Le Couteur, P.C., and Tempelman-Kluit, D.J. 1976. Rb/Sr ages and a profile of initial $^{87}Sr/^{86}Sr$ ratios for plutonic rocks across the Yukon Crystalline terrane. Canadian Journal of Earth Sciences, **13**: 319-330.

McBirney, A. 1993. Igneous petrology. Jones and Bartlett Publishers, Inc., Boston, 508 pp.

McCoy, D., Newberry, R.J., Layer, P., DiMarchi, J.J., Bakke, A., Masterman, J.S., and Minehane, D.L. 1997. Plutonic-related gold deposits of interior Alaska. *In* Mineral deposits of Alaska, Economic Geology Monograph 9, *Edited by* R.J. Goldfarb and L.D. Miller, pp. 191-241.

McDougall, I., and Harrison, T.M. 1999. Geochronology and thermochronology by the $^{40}Ar/^{39}Ar$ method. Oxford University Press, New York, 269 pp.

Maniar, P.D., and Piccoli, P.M. 1989. Tectonic discrimination of granitoids. Geological Society of America Bulletin, **101**: 635-643.

Métais, D., and Chayes, F. 1963. Varieties of lamprophyre. Carnegie Institute of Washington Yearbook, **62**: 156-157.

Mihalynuk, M.G., Nelson, J., Murphy, D.C., Brew, D.A., and Erdmer, P. 1999. Structural and kinematic evolution of the Yukon-Tanana upland tectonites, east-central Alaska: A record of late Paleozoic to Mesozoic crustal assembly: Discussion and Reply. Geological Society of America Bulletin, **111**: 1416-1422.

Miller, C.F., and Mittlefehldt, D.W. 1982. Depletion of light rare-earth elements in felsic magmas. Geology, **10**: 129-133.

Monger, J.W.H., Wheeler, J.O., Tipper, H.W., Gabrielse, H., Harms, T., Struik, L.C., Campbell, R.B., Dodds, C.J., Gehrels, G.E., and O'Brien, J. 1992. Upper Devonian to Middle Jurassic Assemblages: Part B. Cordilleran Terranes. *In* Geology of Canada, no. 4, Geology of the Cordilleran Orogen in Canada, *Edited by* H. Gabrielse and C.J. Yorath, pp. 281-327.

Morin, J.A. 1977. Geology, lode and placer gold mineralization of the Moosehorn Range, 115 N 2. Department of Indian Affairs and Northern Development Mineral Industry Report 1976, EGS 1977-1, pp. 33-54.

Morris, G.A., Larson, P.B., and Hooper, P.R. 2000. 'Subduction style' magmatism in a non-subduction setting: the Colville igneous complex, NE Washington State, USA. Journal of Petrology, **41**: 43-67.

Mortensen, J.K. 1992. Pre-mid-Mesozoic tectonic evolution of the Yukon-Tanana terrane, Yukon and Alaska. Tectonics, **11**: 836-853.

Mortensen, J.K., Emon, K., Johnston, S.T., and Hart, C.J.R. 1999. Age, geochemistry, paleotectonic setting and metallogeny of Late Triassic-Early Jurassic intrusions in Yukon and eastern Alaska: A preliminary report. *In* Yukon Exploration and Geology 1999, Exploration and Geological Services Division, Yukon, Indian and Northern Affairs Canada. *Edited by* D.S. Emond and L.W. Weston, pp. 139-144.

Mortensen, J.K., Hart, C.J.R., Murphy, D.C., and Heffernan, S. 2000. Temporal evolution of Early and Mid-Cretaceous magmatism in the Tintina Gold Belt. *In* The Tintina Gold Belt: Concepts, exploration, and discoveries, British Columbia and Yukon Chamber of Mines Cordilleran Roundup Special Volume 2, Vancouver, British Columbia, pp. 49-57.

Newberry, R.J. 2000. Mineral deposits and associated Mesozoic and Tertiary igneous rocks within the interior Alaska and adjacent Yukon portions of the "Tintina Gold Belt": A progress report. *In* The Tintina Gold Belt: Concepts, exploration, and discoveries, British Columbia and Yukon Chamber of Mines Cordilleran Roundup Special Volume 2, Vancouver, British Columbia, pp. 59-88.

Newberry, R.J., Bundtzen, T.K., Mortensen, J.K., and Weber, F.R. 1998a. Petrology, geochemistry, age, and significance of two foliated intrusions in the Fairbanks district, Alaska. *In* Geologic studies in Alaska by the U.S. Geological Survey, 1996: U.S. Geological Survey Bulletin. *Edited by* J.E. Gray, and J.R. Riehle, pp. 117-129.

Newberry, R.J., Layer, P.W., Burleigh, R.E., and Solie, D.N. 1998b. New $^{40}Ar/^{39}Ar$ dates for intrusions and mineral prospects in the eastern Yukon-Tanana terrane, Alaska – regional patterns and significance. *In* Geologic studies in Alaska by the U.S. Geological Survey, 1996: U.S. Geological Survey Bulletin. *Edited by* J.E. Gray, and J.R. Riehle, pp. 131-159.

Newberry, R.J., McCoy, D.T., and Brew, D.A. 1995. Plutonic-hosted gold ores in Alaska: Igneous vs. metamorphic origins. Resource Geology Special Issue, No. 18, pp. 57-100.

Page, R.A., Plafker, G., and Pulpan, H. 1995. Block rotation in east-central Alaska: A framework for evaluating earthquake potential? Geology, **23**: 629-632.

Parrish, R., Roddick, J.C., Loveridge, W.D., and Sullivan, R.W. 1987. Uranium-lead analytical techniques at the geochronology laboratory, Geological Survey of Canada. *In* Radiogenic age and isotopic studies, Report 1, Geological Survey of Canada Paper 87-2, pp. 3-7.

Passchier, C.W., and Trouw, R.A.J. 1996. Microtectonics, Springer-Verlag, New York, 289 pp.

Patiño Douce, A.E. 1999. What do experiments tell us about the relative contributions of crust and mantle to the origin of granitic magmas? *In* Understanding granites: Integrating new and classical techniques, Geological Society, London, Special Publication No. 168. *Edited by* A. Castro, C. Fernandez, and J.L. Vigneresse, pp. 55-75.

Pavlis, T.L., Sisson, V.B., Foster, H.L., and Plafker, G. 1993. Mid-Cretaceous extensional tectonics of the Yukon-Tanana terrane, Trans-Alaska Crustal Transect (TACT), east-central Alaska. Tectonics. **12**:103-122.

Pearce, J.A., Harris, N.B.W., and Tindle, A.G. 1984. Trace element discrimination diagrams for the tectonic interpretation of granitic rocks. Journal of Petrology, **25**: 956-983.

Pitcher, W.S. 1993. The nature and origin of granite. Blackie Academic and Professional, London, England, 321 pp.

Plafker, G., and Berg, H.C. 1994. Overview of the geology and tectonic evolution of Alaska. *In* The geology of Alaska: Boulder, Colorado, Geological Society of America, The geology of North America, v. G-1. *Edited by* G. Plafker and H.C. Berg, pp. 989-1021.

Poirier, J.P., and Guillope, M. 1979. Deformation induced recrystallisation of minerals. Bulletin de Mineralogie, **102**: 67-74.

Poulsen, K.H. 1989. Investigations by the Geological Survey of Canada in Manitoba and Saskatchewan during the 1984-1989 Mineral Development Agreements. Geological Survey of Canada Open File 2133, pp. 50-55.

Poulsen, K.H., Ames, D.E., and Galley, A.G. 1986a. Gold mineralization in the Star Lake Pluton, La Ronge belt, Saskatchewan: a preliminary report. Geological Survey of Canada Current Research, Part A, Paper 86-1A, pp. 205-212.

Renne, P.R., Deino, A.L., Walter, R.C., Turrin, B.D., Swisher, C.C., Becker, T.A., Curtis, G.H., Sharp, W.D., and Jaouni, A-R. 1994. Intercalibration of astronomical and radioisotopic time. Geology, **22**: 783-786.

Roddick, J.C. 1987. Generalized numerical analysis with application to geochronology and thermodynamics. Geochimica et Cosmochimica Acta, **51**: 281-304.

Roddick, J.C. 1998. The assessment of errors in $^{40}Ar/^{39}Ar$ dating. *In* Radiogenic age and isotopic studies: Report 2. Geological Survey of Canada, Paper 88-2, pp. 7-16.

Rollinson, H.R. 1993. Using geochemical data: evaluation, presentation, interpretation. Longman Group Limited, Essex, England, 352 pp.

Sears, S. 1999. Summary of geological field work – 1998; A geological, geochemical, and geophysical report for the Longline Project, Moosehorn Range, Yukon Territory. 1999 Assessment Report, Whitehorse Mining District.

Selby, D., Creaser, R.A., and Nesbitt, B.E. 1999. Major and trace element compositions and Sr-Nd-Pb systematics of crystalline rocks from the Dawson Range, Yukon, Canada. Canadian Journal of Earth Sciences, **36**: 1463-1481.

Shives, R.B.K., Carson, J.M., Ford, K.L., Holman, P.B., Grant, J.A., Gordey, S., and Abbott, G. 2001. Airborne multisensor geophysical survey, Stewart River area, Yukon; Phase 1. Geological Survey of Canada Open File D4009 (digital format).

Smith, M., Thompson, J.F.H., Bressler, J., Layer, P., Mortensen, J.K., and Takaoka, I.A.H. 1999. Geology of the Liese Zone, Pogo property, east-central Alaska. Society of Economic Geology Newsletter, No. 38, pp. 11-21.

Stanley, W.D., Labson, V.F., Nokleberg, W.J., Csejtey, Jr., B., and Fisher, M.A. 1990. The Denali fault system and Alaska Range of Alaska: Evidence for underplated Mesozoic flysch from magnetotelluric surveys. Geological Society of America Bulletin, **102**: 160-173.

Sun, S.-s., and McDonough, W.F. 1989. Chemical and isotopic systematics of oceanic basalts: implications for mantle composition and processes. *In* Magmatism in the ocean basins, Geological Society Special Publication 42. *Edited by* A.D. Saunders and M.J. Norry, pp. 313-345.

Taylor, S.R., and McLennan, S.M. 1985. The continental crust: its composition and evolution. Blackwell Scientific Publications, Oxford, U.K., 311 pp.

Tempelman-Kluit, D.J. 1974. Reconnaissance geology of Aishihik Lake, Snag, and part of Stewart River map-areas, west-central Yukon. Geological Survey of Canada, Paper 73-41.

Tempelman-Kluit, D.J. 1984. Geology of the Lebarge and Carmacks map sheets. Geological Survey of Canada, Open File 1101.

Tempelman-Kluit, D.J., Gabrielse, H., Evenchick, C.A., Mansy, J.L., Brown, R.L., Journeay, J.M., Lane, L.S., Struik, L.C., Murphy, D.C., Rees, C.J., Simony, P.S., Fyles, J.T., Hoy, T., Gordey, S.P., Thompson, R.I., McMechan, M.E., and Harms, T.A. 1991. Structural Styles; Omineca Belt. *In* Geology of the Cordilleran orogen in Canada, Geological Survey of Canada, Geology of Canada, No. 4. *Edited by* H. Gabrielse and C.J. Yorath, pp. 571-675.

Tempelman–Kluit, D.J., and Wanless, R.K. 1980. Zircon ages for the Pelly Gneiss and Klotassin granodiorite in western Yukon. Canadian Journal of Earth Sciences, **17**: 297-306.

Thirlwall, M.F. 2000. Inter-laboratory and other errors in Pb isotope analyses investigated using a ^{207}Pb-^{204}Pb double spike. Chemical Geology, **163**: 299-322.

Thompson, A.B. 1999. Some time-space relationships for crustal melting and granitic intrusion at various depths. *In* Understanding granites: Integrating new and classical techniques, Geological Society, London, Special Publication No. 168. *Edited by* A. Castro, C. Fernandez, and J.L. Vigneresse, pp. 7-25.

Tosdal, R.M., Wooden, J.L., and Bouse, R.M. 1999. Pb isotopes, ore deposits and metallogenic terranes: Economic Geology Reviews, **12**: 1-28.

Tullis, J. 1983. Deformation of feldspars. *In* Feldspar mineralogy: Reviews in Mineralogy, Mineralogical Society of America, v. 2. *Edited by* P.H. Ribbe, pp. 297-323.

Tullis, J., and Yund, R.A. 1985. Dynamic recrystallization of feldspar: A mechanism for ductile shear zone formation. Geology, **13**: 238-241.

Twiss, R.J., and Moores, E.M. 1992. Structural geology. W.H. Freeman and Company, New York, 532 pp.

Urai, J.L., Means, W.D., and Lister, G.S. 1986. Dynamic recrystallization of minerals. *In* Mineral and rock deformation: Laboratory studies, American Geophysical Union Monograph 36. *Edited by* B.E. Hobbs and H.C. Heard, pp. 161-200.

van de Zedde, D.M.A., and Wortel, M.J.R. 2001. Shallow slab detachment as a transient source of heat at midlithospheric depths. Tectonics, **20**: 868-882.

Villeneuve, M.E., and MacIntyre, D.M. 1997. Laser $^{40}Ar/^{39}Ar$ ages of the Babine Porphyries and Newman Volcanics, Fulton Lake map area (93 L/16), west-central British Columbia. *In* Radiogenic age and isotopic studies: Report 10. Geological Survey of Canada, Paper 1997-F, pp. 131-140.

Werdon, M.B., Newberry, R.J., Szumigala, D.J., and Pinney, D.S. 2001. Geologic map of the Eagle A-2 quadrangle, Fortymile mining district, Alaska. Alaska Division of Geological and Geophysical Surveys Map and Preliminary Report 2001-3a.

Whalen, J.B., Jenner, G.A., Currie, K.L., Barr, S.M., Longstaffe, F.J., and Hegner, E. 1994. Geochemical and isotopic characteristics of granitoids of the Avalon Zone, southern New Brunswick: Possible evidence for repeated delamination events. Journal of Geology, **102**: 269-282.

Wilson, F.H., Smith, J.G., and Shew, N. 1985. Review of radiometric data from the Yukon Crystalline Terrane, Alaska and Yukon Territory. Canadian Journal of Earth Sciences, **22**: 525-537.

Winchester, J.A., and Floyd, P.A. 1977. Geochemical discrimination of different magma series and their differentiation products using immobile elements. Chemical Geology, **20**: 325-343.

Wood, D.A. 1980. The application of the Th-Hf-Ta diagram to problems of tectonomagmatic classification and to establishing the nature of crustal contamination of basaltic lavas of the British Tertiary volcanic province. Earth and Planetary Science Letters, **50**: 11-30.

Yardley, B.W.D. 1989. An introduction to metamorphic petrology. Longman Group Limited, Essex, England, 248 pp.

CHAPTER 3

Nature and Structural Evolution of Intrusion-Hosted Gold-Bearing Veins at the Longline Occurrence, Moosehorn Range Area of the Dawson Range Batholith, West-Central Yukon Territory

Introduction

The Longline gold occurrence is the only known intrusion-hosted shallowly dipping sheeted vein system in the northern Cordillera, other than the Pogo deposit in east-central Alaska. The Longline occurrence is located in the Moosehorn Range, immediately east of the Yukon-Alaska border in the southwestern portion of the Stewart River map area (115N/02), approximately 140 km south-southwest of Dawson City, Yukon (Fig. 21). Quartz vein-hosted mineralization in the Moosehorn Range area occurs entirely within a northwestern extension of the mid-Cretaceous Dawson Range batholith (Fig. 22). Mineralization occurs within an area approximately 3.5 km east-west and 5 km north-south. Its location within the Tintina Gold Belt and its history of productive placer mining makes the Moosehorn Range area an attractive target for gold exploration (Greig, 1975; Morin, 1977; Smith, 2000). Poor understanding of the geology in this region warranted a detailed deposit-specific investigation of the Longline occurrence to help elucidate the nature of and controls on the gold mineralization.

Exploration History

High-grade gold-bearing quartz veins were discovered in 1970 along the crest of the Moosehorn Range by Quintana Minerals Corporation. Great Bear Mining Limited acquired the claims in 1974 and carried out mapping, soil sampling, trenching, VLF-EM surveying, and diamond drilling (19 holes totalling 625 m). J.M. Kenyon prospected part of the Moosehorn Range during the summer of 1974, and in early 1975 sold the claims to

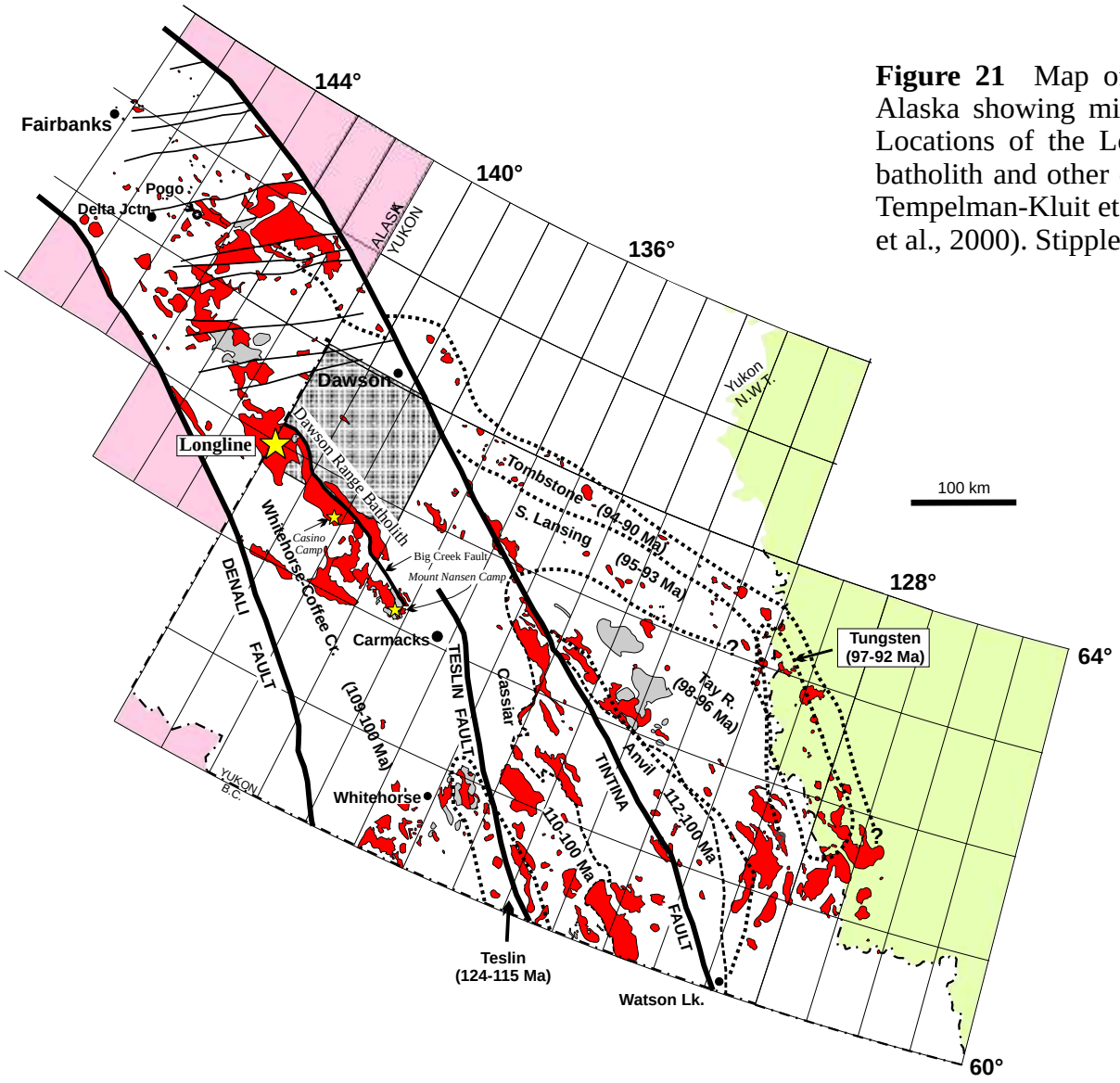

Figure 21 Map of southern Yukon Territory and east-central Alaska showing mid-Cretaceous intrusions and volcanic rocks. Locations of the Longline property within the Dawson Range batholith and other deposits of interest are shown (adapted from Tempelman-Kluit et al., 1991; Newberry et al., 1998b; Mortensen et al., 2000). Stippled area is the map area shown in Figure 22.

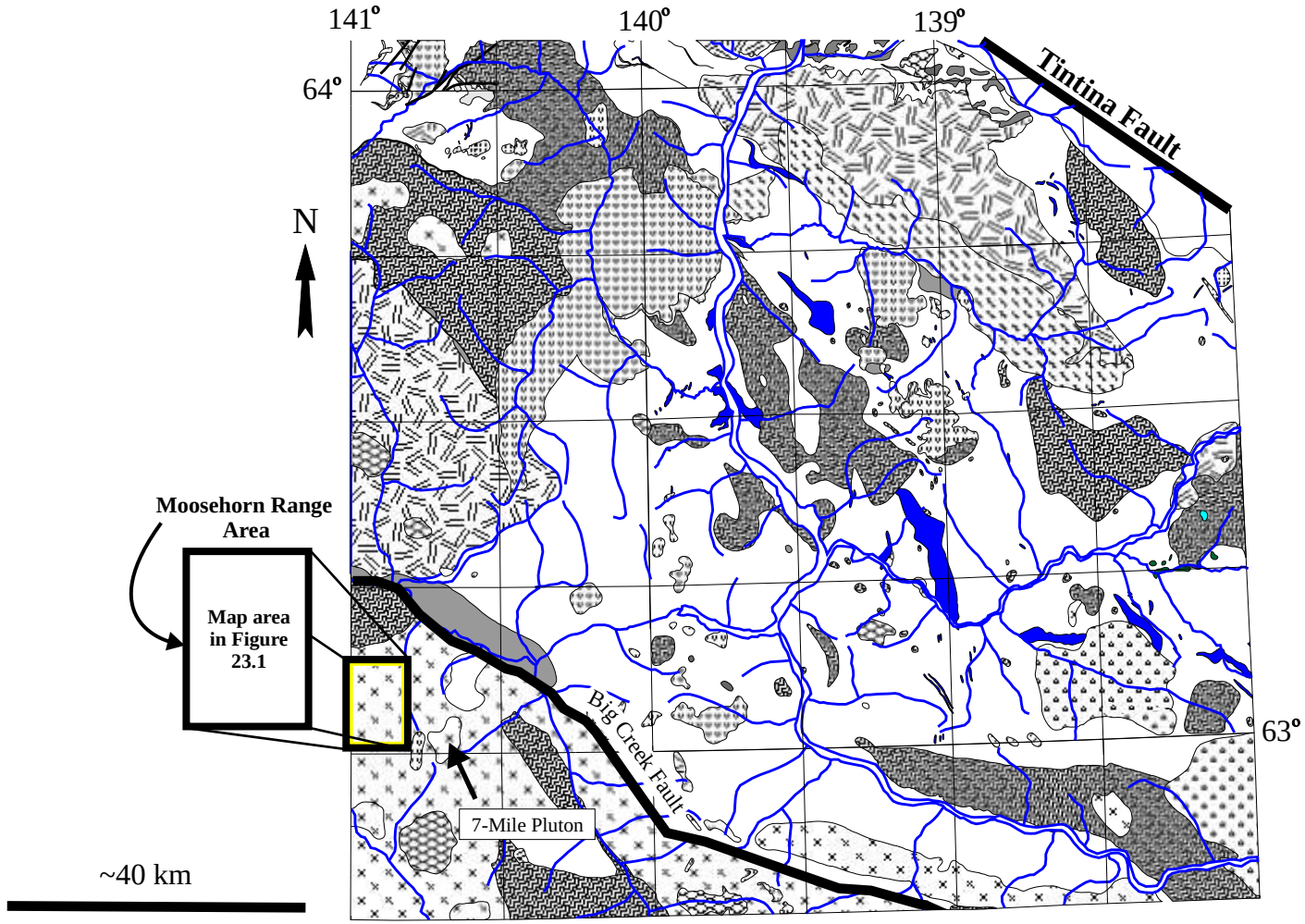

Figure 22 Regional geology of west-central Yukon Territory. The area is underlain predominantly by mid-Paleozoic metamorphic rocks of the pericratonic Yukon-Tanana terrane. Geology modified after Tempelman-Kluit (1974). Legend for map is on the following page.

Legend


Eocene felsic volcanic rocks and high level intrusions


Paleocene sedimentary rocks within the Tintina fault zone


Late Cretaceous volcanic rocks (Carmacks Gp.) and associated sedimentary rocks (Tantalus Fm)


Permian Klondike Schist - metavolcanic and metasedimentary rocks


Paleozoic marble


mainly mid-Paleozoic undifferentiated metasedimentary and metavolcanic rocks of the Yukon-Tanana Terrane

Intrusive Rocks


Late Cretaceous intermediate to felsic intrusions


Early to mid-Cretaceous intermediate to felsic intrusions


Late Triassic-Early Jurassic mafic to felsic intrusions


Permian granite and quartz monzonitic gneiss


Devonian-Mississippian intermediate to felsic composition metaplutonic rocks


Paleozoic(?) greenstone and serpentinized ultramafic rocks


Fault


Rivers/Creeks

Claymore Resources Limited. Results of additional soil sampling, trenching, and diamond drilling (18 holes totalling 696 m) by Claymore in 1975 were disappointing and the focus was shifted from bedrock to placer gold exploration. Profitable placer mining of Kenyon Creek (referred to as Discovery Creek in older reports) was subsequently undertaken (Waugh, 1975, Greig, 1975). Geological mapping of this poorly exposed area was done by D.J. Tempelman-Kluit of the Geological Survey of Canada (1974) and J.A. Morin of the Department of Indian Affairs and Northern Development (1977). Morin's study constitutes the only detailed geologic work carried out in the area prior to this study. It includes a geologic map of the southeastern Moosehorn Range, geochemical analyses of various intrusive phases, and petrographic descriptions of the intrusions, veins, and alteration assemblages. The report also provides a comprehensive summary of previous exploration and placer mining efforts.

During the 1980's and early 1990's, G.S. Hartley's placer gold exploration in the area involved mapping, percussion drilling, prospecting, and soil sampling (Hartley and Almberg, 1994). Meanwhile, I. Warrick and K. Robertson of Moosehorn Exploration Program Limited staked many of the bedrock occurrences along the crest of the Moosehorn Range and identified several gold-rich quartz veins during their placer mining efforts at Kenyon and Swamp creeks (Warrick and Robertson, 1989). In the late 1980's, placer mining of Swamp and Soya creeks was done by Canada Tungsten Mining Corporation. Sikanni Oilfield Construction Limited placer mined sections of Swamp, Kenyon, and Soya creeks between 1990 and 1996, and also carried out bedrock mining of the V1 and V2 veins (near Swamp creek; Fig. 23). Over 3200 ounces of gold were extracted from these veins using a gravity mill (Ritcey *et al.*, 2000). An estimated 54 000 ounces of placer gold have been extracted from the streams west of the Moosehorn Range, and Moosehorn Exploration

Program Limited continues to successfully placer mine Great Bear creek and Roo Pup on the eastern flank of the range (Fig. 23.1). Mining of placer deposits on the Hartley Creek tributary of Swamp Creek also continues to be productive (Ritcey *et al.*, 2000, Sears *et al.*, 2000).

From 1996 to 2000, Barramundi Gold Limited carried out programs of prospecting, mapping, trenching, soil sampling, rock sampling, airborne and ground geophysical surveys, and diamond drilling (44 holes totalling 4616.4 m). The 2000 exploration program was conducted under a joint venture agreement between Barramundi Gold Limited and Newmont Exploration of Canada Limited.

Airborne magnetic and gamma ray surveys were conducted by the Geological Survey of Canada in 2000 over the southwestern area of the Stewart River map sheet (Shives et al., 2001).

Geologic Setting

The pericratonic Yukon-Tanana terrane in the western Yukon comprises predominantly Devonian to Permian orthogneisses, paragneisses, metapelites, and quartzofeldspathic schists (Tempelman-Kluit, 1974; Mortensen, 1992; Hart and Langdon, 1998). This metamorphic basement has subsequently been intruded and overlain by felsic and mafic plutonic and volcanic rocks between Triassic and Neogene time (Mortensen, 1992; Francis et al., 1999; Mortensen et al. 2000; Abraham et al., 2001). The Dawson Range batholith (DRB), which is part of the Whitehorse-Coffee Creek Suite (WCCS), was emplaced into the Yukon-Tanana terrane in mid-Cretaceous time (99-111 Ma) (Hart and Langdon, 1998; Selby et al., 1999; Mortensen et al., 2000). This batholith extends continuously from just west of Carmacks into east-central Alaska. The WCCS consists

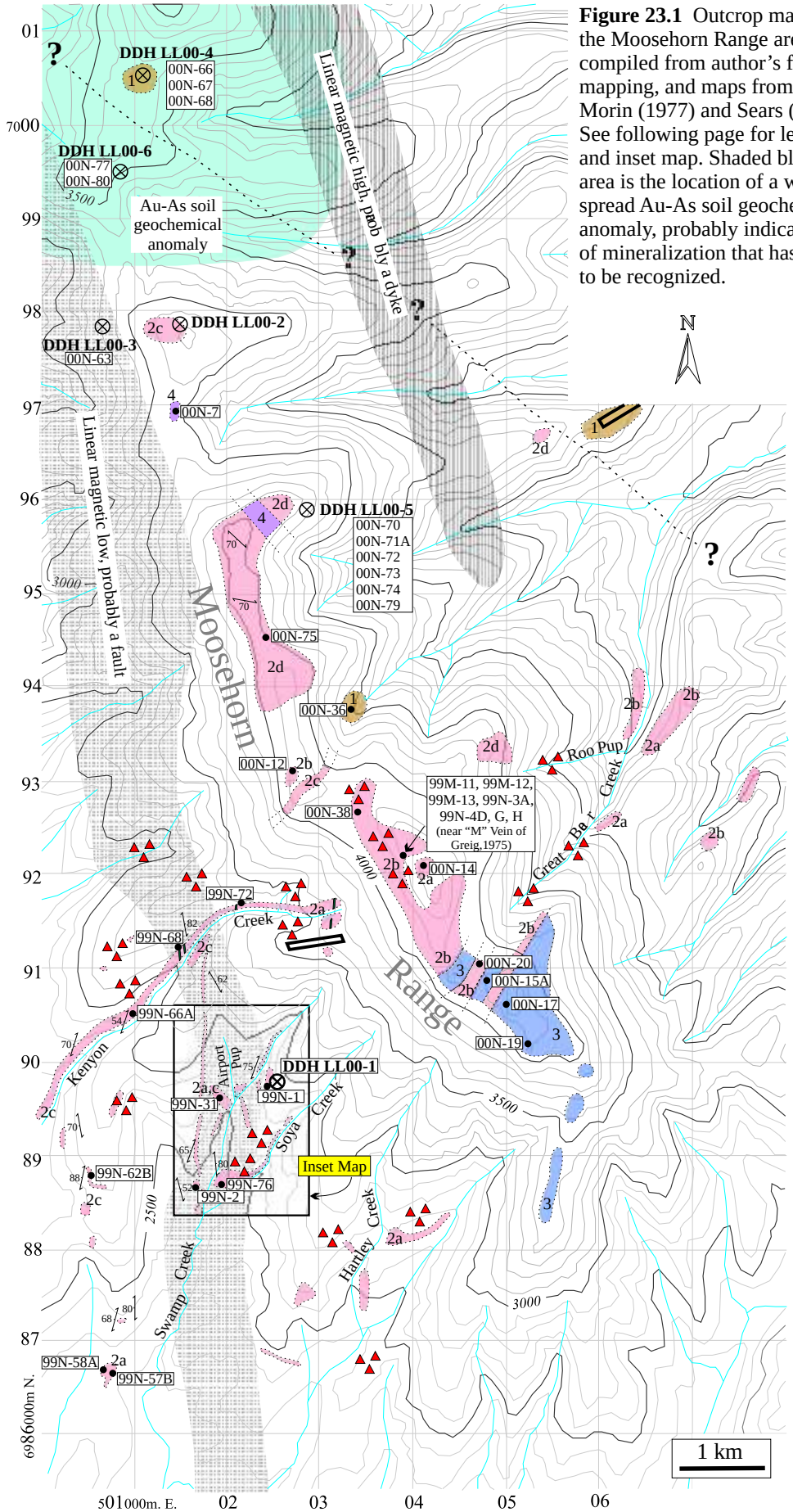

Figure 23.1 Outcrop map for the Moosehorn Range area, compiled from author's field mapping, and maps from Morin (1977) and Sears (1999). See following page for legend and inset map. Shaded blue area is the location of a wide-spread Au-As soil geochemical anomaly, probably indicative of mineralization that has yet to be recognized.

Legend for Moosehorn Range Area Outcrop Map

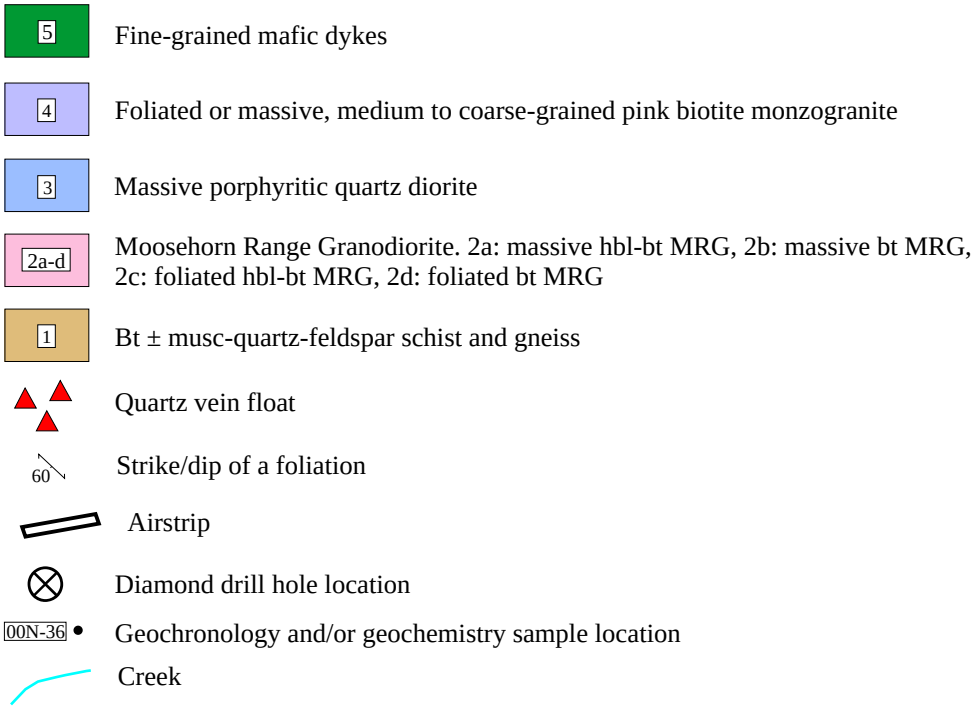

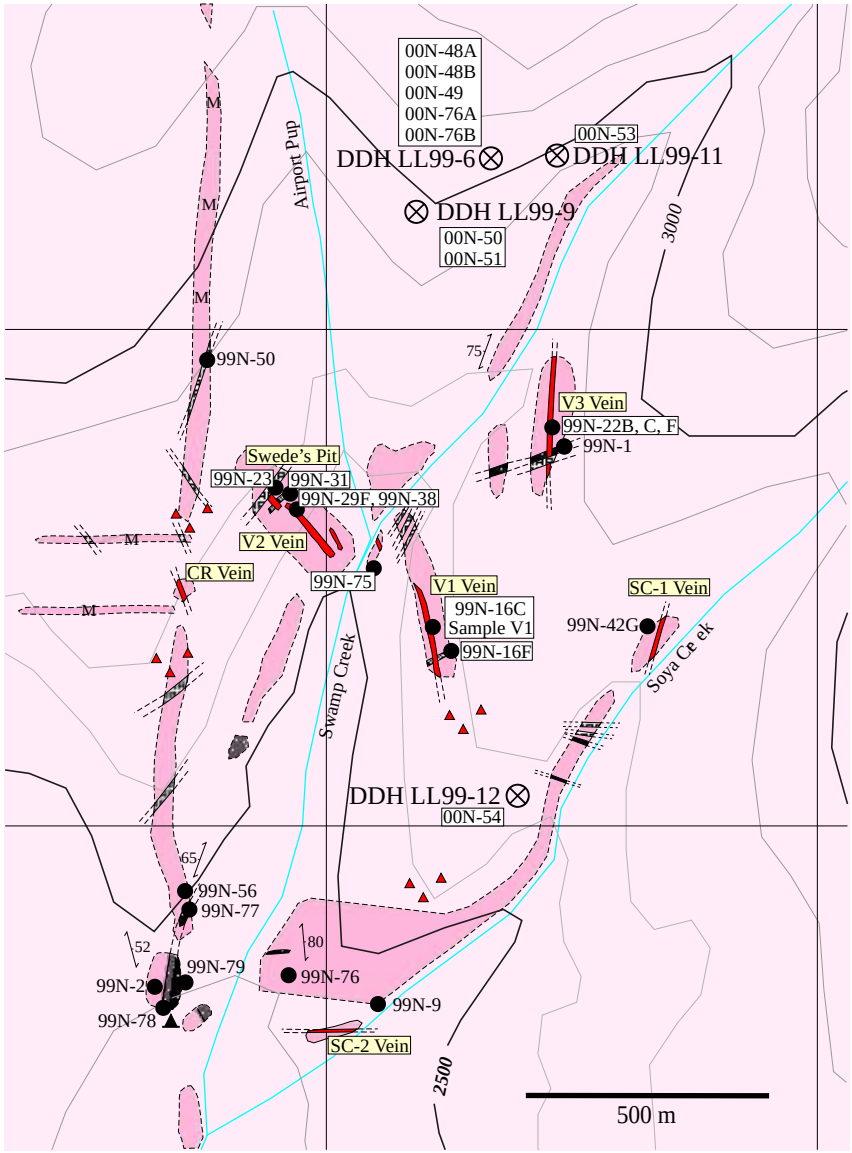

Legend for Inset Map

- Fine-grained mafic dykes
- Massive tan to grey felsite dykes
- Massive porphyritic quartz diorite
- Foliated to mylonitic porphyritic hornblende-biotite granodiorite dykes
- Massive to weakly foliated Moosehorn Range Granodiorite
- M — Outcrop of fine-grained mafic dykes 10cm to 1m thick
- Quartz vein
- Quartz vein float
- 60 — Strike/dip of a foliation
- 00N-36 • — Lead isotope or fluid inclusion sample location
- Diamond drill hole location
- Camp
- Creek

Figure 23.2 Inset map of main study area showing location of the main gold-bearing veins on the Longline property. Lead isotope sample locations are also shown. A more detailed map of Swede's Pit area is presented in Figure 30.

mostly of biotite ± hornblende granodiorite, quartz monzonite, and minor alaskite, aplite, felsic volcanic, pegmatite, and granitic dykes and plugs, all of which are thought to be subduction related (Mortensen et al., 2000; Chapter 2 of this study). The intrusions are calc-alkaline, peraluminous to slightly metaluminous, predominantly I-type, and probably crystallized from mantle-derived melts that underwent extreme crustal contamination (Selby et al., 1999; Mortensen et al., 2000; Chapter 2 of this study). The only contemporaneous mafic volcanic rocks are the volumetrically minor 105-108 Ma Mount Nansen andesitic volcanic units located near the southeastern end of the batholith (Appel, 1998; Hart and Langdon, 1998; Mortensen et al., 2000). Late Cretaceous (70 Ma) shoshonitic Carmacks Group volcanic rocks have been documented throughout west-central Yukon Territory (Johnston et al., 1996; Hart and Langdon, 1998; Francis et al., 1999; Abraham et al., 2001). They have not been recognized in the immediate Moosehorn Range area, but basaltic and lamprophyric minette dykes of Tertiary and Eocene age are abundant.

Previous Investigations of the Longline Occurrence

The geometry of the veins in the Moosehorn Range area was poorly constrained before trenching was undertaken in the late 1980's and early 1990's, largely because of the generally poor bedrock exposure in the area. Assessment reports that predate the trenching consist mainly of descriptions of vein minerals and textures, trends of quartz vein float trails, and summaries of early drilling projects from the crest of the Moosehorn Range.

The quartz veins have been described as 5-50 cm thick with milky white, ribboned, and/or banded textures (Greig, 1975; Morin, 1977). Diamond drilling along the crest of the range intersected a series of parallel vein sets and fractures, consistently oriented north-northwest, dipping 20-40º east (Greig, 1975; Morin, 1977).

Vein mineralogy described by Greig (1975), Morin (1977), and Hartley and Almberg (1994) from different occurrences in the Moosehorn Range area varies somewhat but generally includes galena, sphalerite, arsenopyrite, pyrite, jamesonite, boulangerite, tetrahedrite, calcite, and visible gold. Minor stibnite, scheelite, anglesite, cerussite, chalcopyrite, pyrrhotite, and molybdenite have also been reported (Yukon Minfile, 2001, # 115N 024). These minerals occur as coarse crystals, lenses, and streaky fine-grained bands parallel to vein margins (Greig, 1975; Morin, 1977). The gold is spatially associated with galena, arsenopyrite, sphalerite, and boulangerite, and commonly occurs within limonite-, malachite-, and/or azurite-encrusted vugs (Morin, 1977; Yukon Minfile # 115N 024). Reported gold grades for veins on the Moosehorn Range range from 5.1 g/t over 1.5 m to 686.0 g/t over 8 cm (Yukon Minfile, 2001, # 115N 024).

Results of this Study

During two field seasons in the summers of 1999 and 2000, detailed maps of the trenches exposing the gold-bearing veins were generated, and are presented as Figures 43-58 in Appendix A. Structural data, and vein, sulphide, and altered wallrock samples were collected from the trenches. The following section summarizes field observations and results of petrographic, geochronological, fluid inclusion, lead isotopic, and structural investigations carried out by the author.

Nature and Geometry of Longline Veins

Four different vein types have been recognized on the Longline property. Crosscutting relationships indicate the earliest phase of veining generated the main gold-bearing quartz veins, which are stacked, parallel, and shallowly east-northeast-dipping (20-

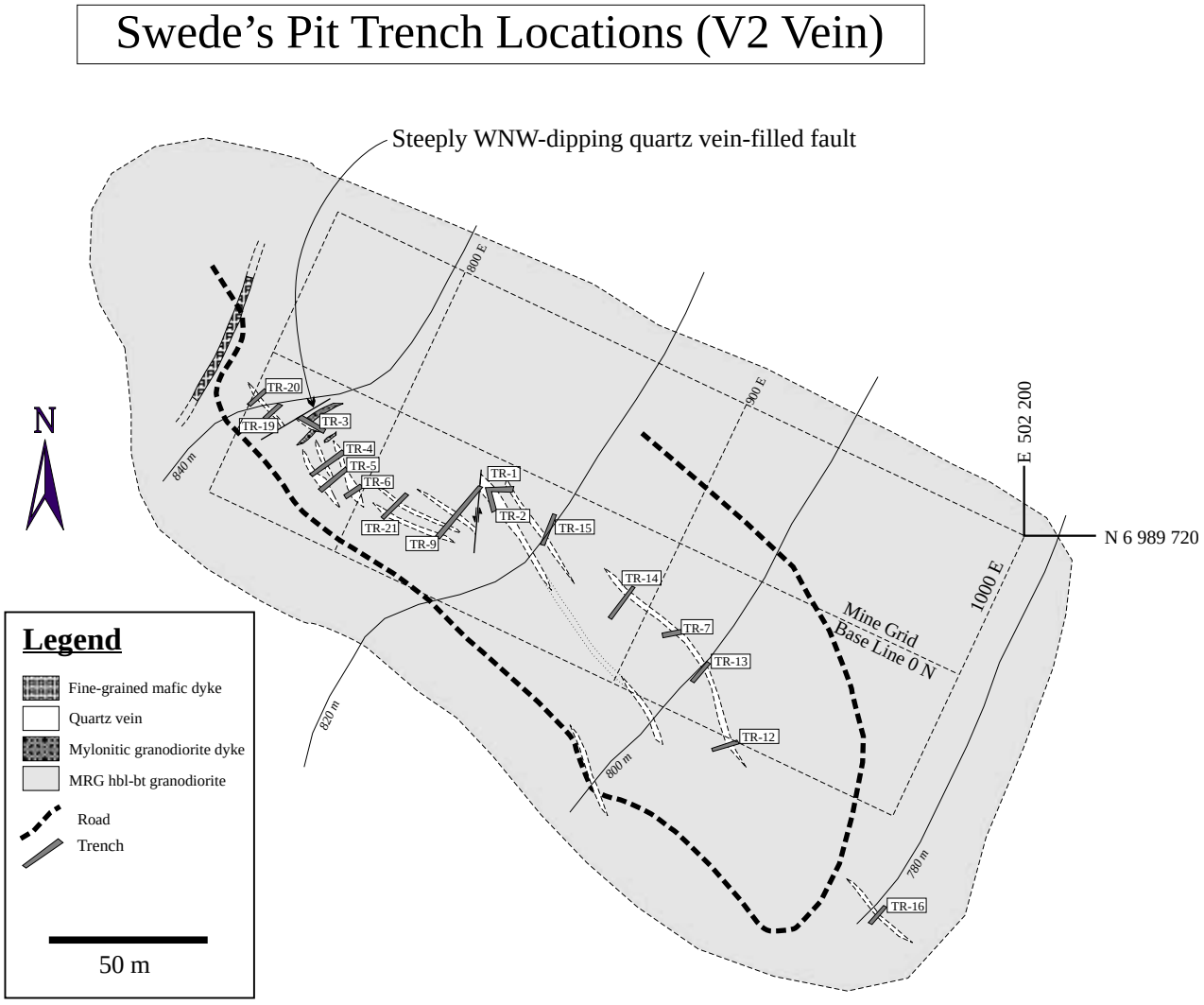

Figure 24 Map of Swede's Pit showing the locations of trenches that were mapped in detail. The V2 vein is not, in fact, a single vein, but a series of sheeted discontinuous lenticular veins. Surface traces of these shallowly east-northeast-dipping veins are shown in yellow. (Modified after Sears et al., 2000)

30º). Average vein thickness is about 15 cm, but ranges from 1 cm to 1 m, and average gold grades are approximately 30 g/t Au (Ritcey et al., 2000). Temporal relationships among the younger veins are unclear. In Swede's Pit (Fig. 24) the V2 vein is clearly cut by steeply west-northwest-dipping quartz veins 1-15 cm thick. These veins carry low gold grades, are generally rich in pyrite, and contain significantly higher levels of bismuth than the gold-bearing veins (Sears et al., 2000). Numerous joints and faults with similar orientations to these veins are common, across which the V2 vein is normally offset by at most several meters. A third vein type was only recognized in drill core, and consists of thin (0.5-5 cm) subvertical quartz-carbonate veinlets. A fourth variety, generally found in the southern portion of the property, includes veinlets (0.5-3 cm thick) containing carbonate, amethyst, barite, clay, and drusy to comb-textured quartz. These features are commonly found in association with epithermal mineralization (Hedenquist et al., 1996). The latter three vein types are unrelated to the gold mineralization and henceforth will not be discussed in any detail.

Gold-Bearing Quartz Veins

About a dozen gold-bearing quartz veins of significant thickness have been found within the part of the study area mapped in detail (Fig. 23.2). Four of these, including the V1, V2, V3, and Soya Creek (SC-1) veins, were examined in detail in this study. The SC-1 vein is somewhat unusual in that it dips about 45º to the west. The geometry of the veins is best seen in Swede's Pit where many trenches were excavated perpendicular to the strike of the V2 vein (Fig. 24). Trenches exposing the V1, V3, and SC-1 veins are oriented parallel to the strike of the veins.

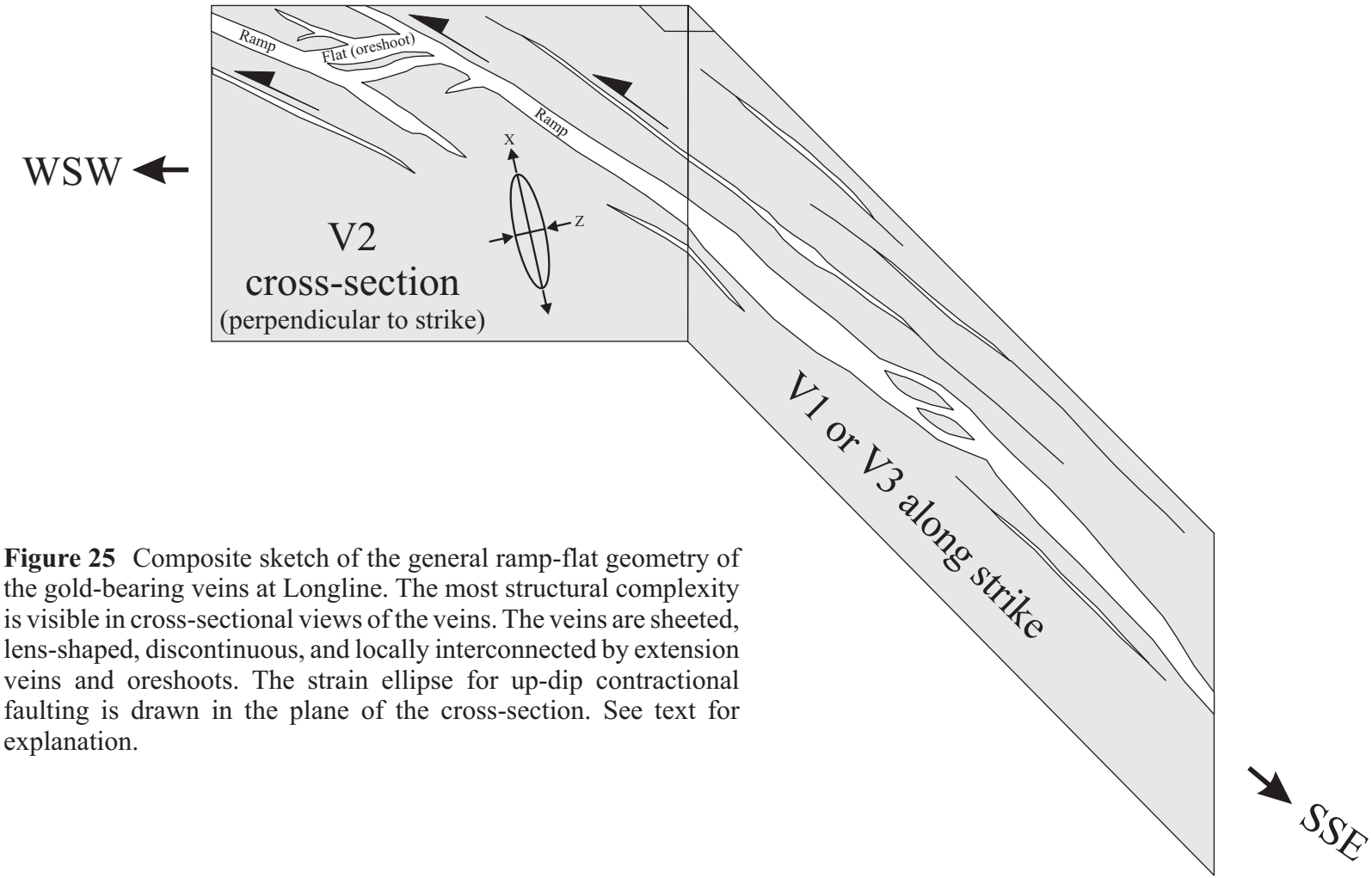

Figure 25 Composite sketch of the general ramp-flat geometry of the gold-bearing veins at Longline. The most structural complexity is visible in cross-sectional views of the veins. The veins are sheeted, lens-shaped, discontinuous, and locally interconnected by extension veins and oreshoots. The strain ellipse for up-dip contractional faulting is drawn in the plane of the cross-section. See text for explanation.

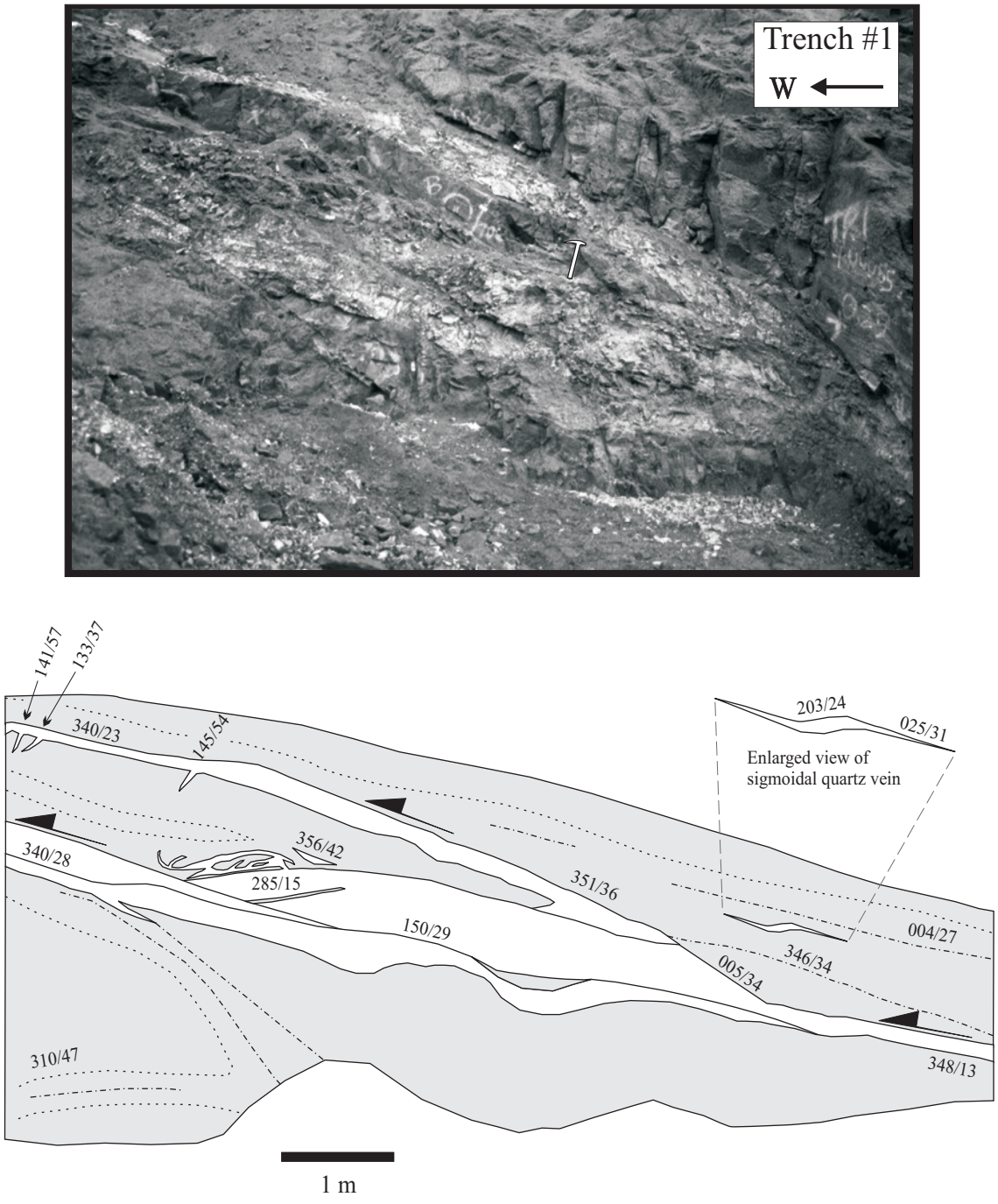

Figure 26 Trench #1 in Swede's Pit. **Top**: Photograph of the trench looking approximately due north. Hammer for scale. **Bottom:** Trench map; Wallrock granodiorite is grey, quartz veins are white. This trench exhibits a classic ramp-flat geometry, with the central subhorizontal lens-shaped oreshoot connecting two thinner veins. In upper left area of the topmost vein are little tapered extension veinlets that contain vuggy quartz. The enlarged sigmoidal vein is a small scale equivalent of the overall vein geometry. Dash-dot lines are quartz veinlets, fine dashed lines delineate the alteration envelope around the vein. Vein orientations are as shown.

The four main veins are not individual discrete veins but rather each comprises a series of parallel, shallowly east-dipping, discontinuous, milky white, lens-like veins locally interconnected by subhorizontal east-southeast-striking bridging dilatant oreshoots (Figure 25). The trench map in Figure 26 illustrates the sheeted nature of the veins in a portion of Swede's Pit. Above and below the main veins there are fractures and discontinuous quartz veinlets that also dip shallowly to the north-northeast (Fig. 25). Small extensional offshoot veinlets from the main veins also strike north-northwest and variably dip 20-70º towards the east-northeast. These 0.5-5 cm thick and 5-100 cm long offshoots locally connect the main veins but more commonly taper and terminate within the wallrock.

Most marginal areas of the veins are sheared, and locally contain sheared lenses and slivers composed entirely of fine-grained tourmaline. Bull, comb, and vuggy quartz textures are present in the cores of veins and extensional offshoots, commonly encapsulating thicker and sigmoidal margin-parallel lenses of altered wallrock. Individual quartz crystal faces with lengths of up to 10 to 25 cm were observed in the cores of blowouts in Trenches 5 and 6 (Figs. 47 and 48, Appendix A). Offsetting, jointing, and brecciation of portions of the veins are attributed to brittle post-vein deformation that locally imparted a fissile, crumbly, and granulated quality to the quartz. Vein outcrops are colourfully encrusted with black manganese oxide, yellow-green scorodite, rusty orange and brown limonite, and minor azurite and malachite.

Vein Petrography

Quartz Textures

In thin section, quartz in the gold-bearing veins is weakly to moderately deformed, and exhibits variable development of subgrains, undulatory extinction, deformation bands,

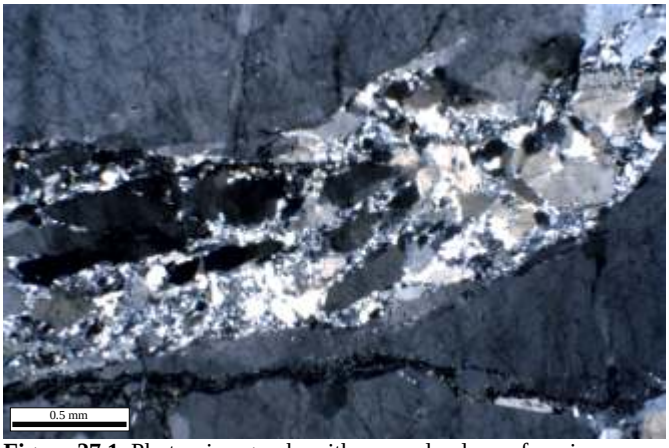

Figure 27.1 Photomicrograph, with crossed polars, of a micro-shear zone in a gold-bearing quartz vein. Fine quartz subgrains which surround larger grains formed during dynamic recrystallization

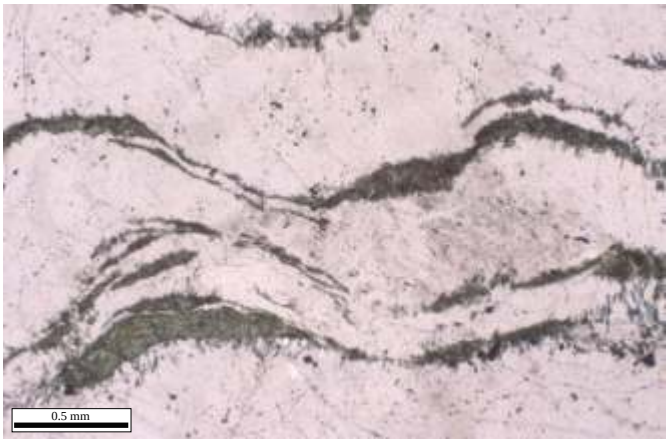

Figure 27.2 Photomicrograph of a quartz vein, in plane light; parallel curviplanar slivers of tourmalinized wallrock inside the gold-bearing veins were incorporated as episodic dilation and fluid infill took place along the fault surface.

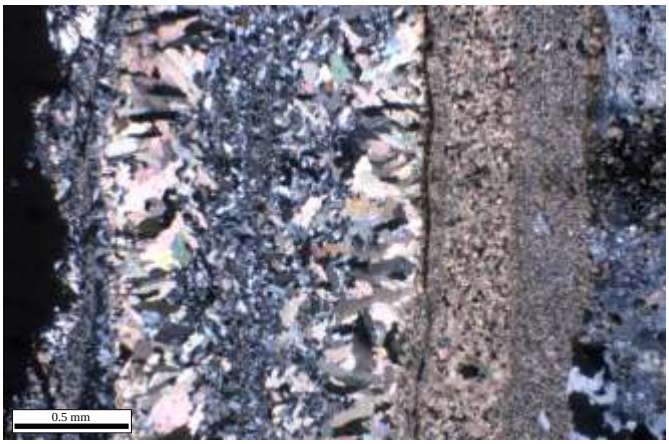

Figure 27.3 Photomicrograph, with crossed polars, of an extension veinlet. The vein is texturally zoned; calcite on the right side of the vein is microcrystalline and at the centre of the photo is comb-textured with fine-grained quartz at its core. These textures are indicative of open-space filling.

and irregular to serrated or sutured grain boundaries. Locally micro-shear zones in the quartz were observed (Fig. 27.1). Where quartz has been recrystallized or annealed, the crystals are optically clear. Vuggy cavities are commonly partially or entirely infilled with sulphides, quartz, and/or carbonate. Euhedral quartz terminations within the vugs locally contain pseudosecondary fluid inclusion trails, and are consistently less clouded with secondary inclusion trails than the surrounding groundmass quartz grains.

There is abundant evidence indicating that crack-seal activity occurred in these veins (Ramsay, 1980). Most veins thicker than about 2 cm contain numerous margin-parallel, tourmaline-rich, crack-seal inclusion bands or sheets up to about 1-2 mm thick. These bands are wavy but remarkably parallel (Fig. 27.2) and are almost identical to those seen in the extension vein shown in Figure 9b of Cox et al. (2001). Euhedral needles of tourmaline are randomly oriented along these bands, between which the quartz is recrystallized, thus likely having destroyed the original cockscomb texture. Fractures parallel to these bands locally contain sulphides, sulphosalts, gold and/or muscovite. Comb-textured and banded quartz and calcite textures are common (Fig. 27.3), particularly within extension veinlets.

Gold, Sulphide, and Sulphosalt Compositions

The veins are composed of quartz with minor calcite, tourmaline, and muscovite, and typically contain less than 5% metallic minerals including galena, sphalerite, arsenopyrite, boulangerite, tetrahedrite, pyrite, scheelite, and native gold. The sulphides and sulphosalts occur as fine- to coarse-grained crystal aggregates, or are concentrated in discrete zones or streaky bands parallel to the vein margins. Sulphides and sulphosalts were co-precipitated with quartz and were also deposited inside vugs and along fractures within the quartz veins.

Visible gold is common as isolated grains (<0.5 mm – 2 mm), as 0.1 – 0.8 mm inclusions and fracture fillings in sulphides and sulphosalts, and less commonly as clusters of grains (up to about 5-6 mm). Gold is spatially associated with arsenopyrite, galena (Fig. 28), and particularly sphalerite. Gold is also commonly found within rusty masses of limonite (after pyrite) in vugs.

Petrography and scanning electron microscopy reveal textures of the vein minerals indicating that the gold, sulphides, and sulphosalts were deposited simultaneously throughout the vein formation. Sequences of mineral overgrowths observed are rarely consistent from section to section.

Assay results show that there is up to about 420 g/t silver within the main gold-bearing veins (Sears et al., 2000). Greig (1975) determined that the gold to silver ratio for the veins on top of the Moosehorn Range averages about 1.3, and that the gold has a fineness of about 850. Dumala and Mortensen (2002) analyzed placer gold from Swamp Creek, Great Bear Creek, and Roo Pup and determined its average fineness to be approximately 835. Bulk bullion fineness for placer gold from Great Bear Creek on the eastern flank of the Moosehorn Range is 825 (I. Warrick, pers. comm., 1999). Results of electron microprobe analyses of sulphide and sulphosalt phases are summarized in Appendix B. The bulk of the silver content in the veins is likely carried by tetrahedrite, which contains about 19 weight percent silver (Appendix B).

Alteration

Because the area was not glaciated during the Pleistocene, there is typically a thick weathering profile, and fresh samples of the veins and alteration envelopes are available only from drill core. The granodiorite that hosts the gold-bearing quartz veins has

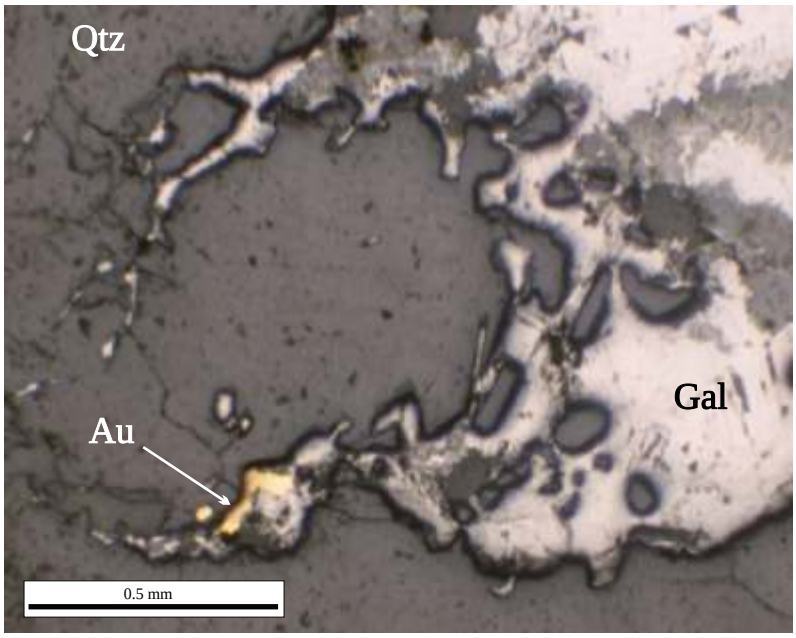

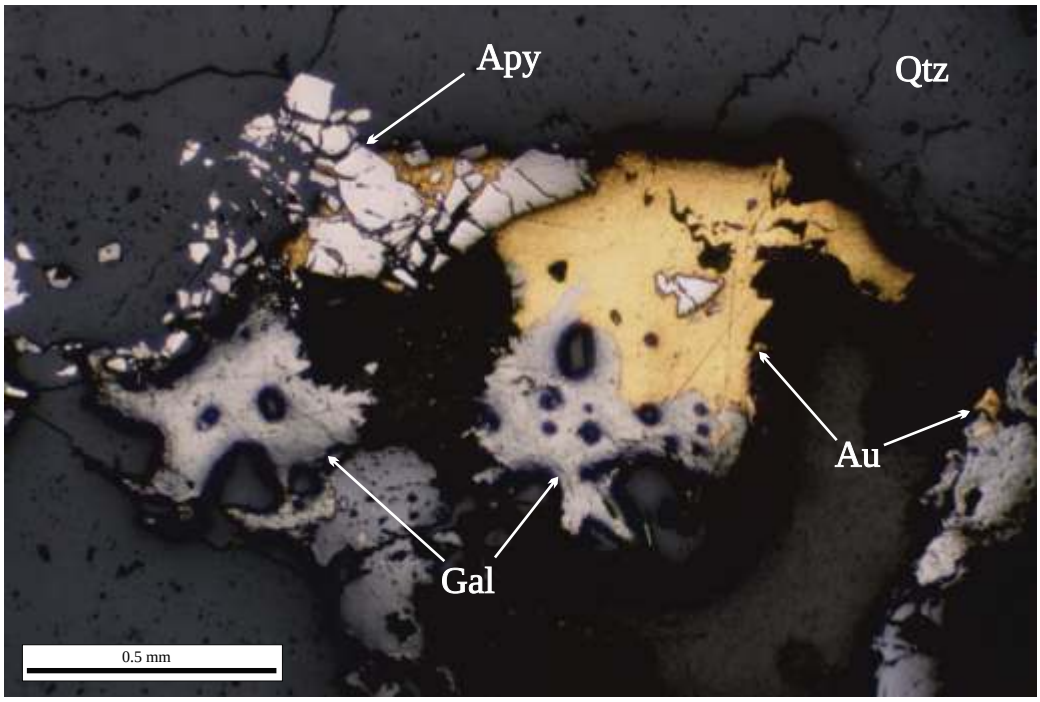

Figure 28 Photomicrographs of vein material showing spatial relationships between gold and sulphides. Here, gold envelops grains of arsenopyrite and galena, and occurs as fracture infills in arsenopyrite. In other sections (not shown), gold occurs as free grains, and as inclusions in arsenopyrite, sphalerite, pyrite, galena, and locally boulangerite.

undergone pervasive magnetite-destructive, muscovite-sericite, clay, pyrite and/or arsenopyrite, iron carbonate, and localized chloritic and potassium feldspar alteration in the vicinity of the veins. Cream to pale green coloured alteration envelopes around the veins are 1-100 cm thick (Fig. 29.1), and the thicknesses of these envelopes do not correlate with the thicknesses of the veins themselves (Morin, 1977). The alteration assemblage comprises quartz, sericite and/or muscovite, pyrite, arsenopyrite, clay, ferroan dolomite, and locally chlorite. Disseminated patches of red hematite are also commonly encountered. Average gold grade of altered granodiorite adjacent to the V2 vein is 3.13 g/t (Sears et al., 2000).

Zonation of alteration phases is subtle, inconsistent, and in hand specimen, commonly indiscernible. Alteration described here pertains to that of hornblende-biotite granodiorite, because the majority of veins and veinlets were emplaced into this rock type. The following example is a summary of footwall alteration adjacent to the V3 vein that was intersected in DDH LL00-1 (Fig. 23.1).

0-2 cm from the vein: Vein margins are seldom linear and are defined by the jagged outlines of wallrock minerals that have been pseudomorphed by alteration minerals. Tourmalinization extends at most 5 mm into the wallrock, and widespread muscovite-sericite-clay-carbonate-arsenopyrite alteration obscures the original granodioritic textures within 2 cm of the vein margin. Relatively coarse muscovite, similar to that associated with greisen-type alteration, with laths up to 1-2 mm long, has replaced feldspars and occurs in mats, sprays, and bowtie-shaped clots (Fig. 29.2). Sericite alteration of plagioclase is pervasive, but is particularly concentrated along twins. Biotite and hornblende grains are entirely pseudomorphed by muscovite, clay minerals, carbonate minerals, and sericite. Carbonate minerals are interstitial among the phyllosilicates and clusters of arsenopyrite are disseminated throughout the groundmass.

Figure 29 Alteration adjacent to the gold-bearing quartz veins. **1.** Hand sample showing the banded texture in the vein (black bands are the tourmalinized wallrock slivers). The alteration envelope is 4-5 cm wide and consists of muscovite/ sericite, pyrite, arsenopyrite, Fe-carbonate, and quartz. **2.** Photomicrograph, under crossed polars, of the alteration envelope within 2 cm of the vein. Minerals present include quartz, pyrite (Py), arsenopyrite (Apy), bowtie-shaped muscovite after feldspars, muscovite/sericite pseudomorphs after hornblende and biotite, and in the fine-grained groundmass there is sericite and carbonate.

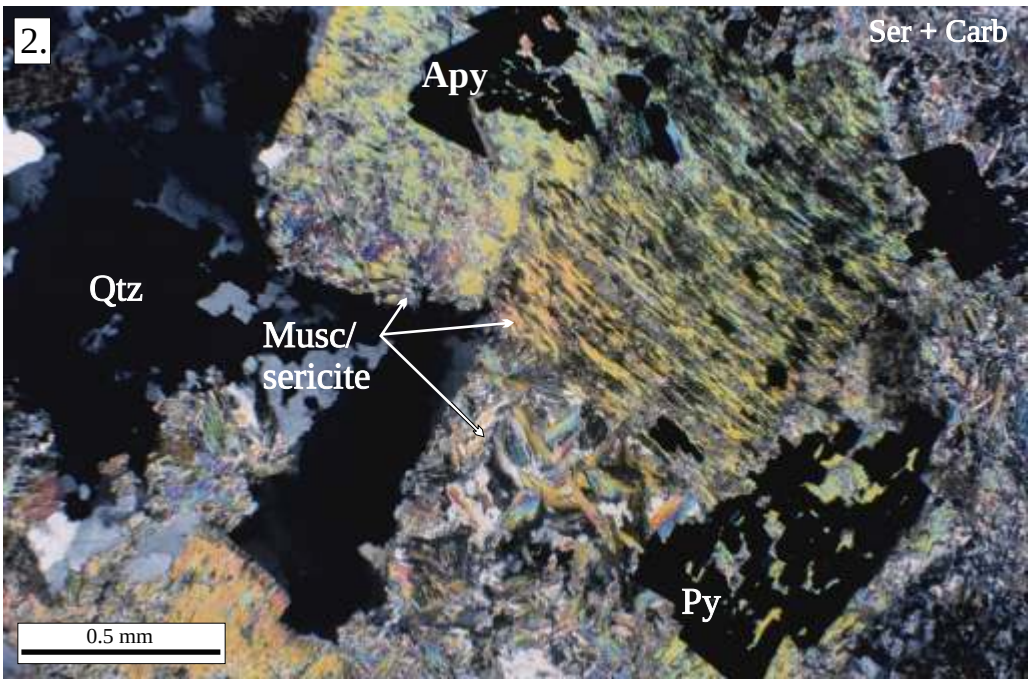

2-5 cm from the vein: Mats and sprays of muscovite, sericite, and clay minerals are much finer grained in this zone, with the largest laths reaching 200μm. Carbonate alteration is not as strong as in the zone closest to the vein, and occurs interstitially in the groundmass, and as microcrystalline aggregates pseudomorphing feldspars. Arsenopyrite is more abundant, but occurs as much finer grained clusters that volumetrically comprise 5-10 % of the rock. Biotite and hornblende are replaced by relatively coarse muscovite.

5-7.5 cm from the vein: Locally, remnant portions of feldspar grains are recognizable amidst the sericitized and clay-altered patches within the crystals. Biotite and hornblende are entirely replaced by muscovite, sericite, and clay. This small zone contains 1-2% fine-grained disseminated pyrite and goëthite, and carbonate alteration is insignificant.

7.5-10 cm from the vein: Carbonate is absent and pyrite comprises <1% of the rock volume. There is partial to total replacement of feldspar, particularly of plagioclase, by sericite and clay. Biotite is also locally preserved, or is partially epitaxially replaced by chlorite. Hornblende is almost entirely replaced by biotite, clay, and chlorite.

10-17 cm from the vein: Within this zone, the alteration intensifies again, and a prograde sequence of alteration assemblages this far from the vein is due to the presence of another parallel quartz veinlet (0.5 cm thick). The zoning within this hangingwall alteration exactly mirrors that of the V3 vein footwall alteration.

Alteration envelopes adjacent to all the shallowly east-dipping veins and veinlets intersected in drill core exhibited similar zoning to that of the V3 alteration. Alteration mineralogy does not appear to depend on vein sulphide mineralogy or abundance. The only observed variation in the alteration was the zoning of pyrite and arsenopyrite, the control on which remains unknown. Generally, the most sulphide-rich portion (up to 5-7% volume) of the alteration envelopes occurs 2-4 cm away from the vein. In envelopes where arsenopyrite

or pyrite is present directly adjacent to the vein, the sulphide assemblage in the sulphide-rich zone is either entirely comprised of arsenopyrite or pyrite, respectively, or is a combination of the two. More than 4 cm away from the vein, pyrite is the only sulphide found in the wallrock.

Reconnaissance diamond drilling in the northern portion of the property (DDH LL00-4 and DDH LL00-6, Fig. 23.1) was undertaken to investigate a relatively large zone (5-6 km^2) of anomalous Au-As concentration in the soils. Drill core revealed intersections with wide zones (tens of metres) of pervasive alteration comprising alteration assemblages similar to those in the main mineralized area to the south. These zones are essentially barren of quartz veins and veinlets and the cause of the extensive alteration remains unclear.

Age Constraints on Mineralization

Constraints on the age of the gold mineralization were interpreted from crosscutting field relationships of units dated using U-Pb, and K-Ar methods (Chapter 2 of this study) and from $^{40}Ar/^{39}Ar$ ages of muscovite from within the gold-bearing quartz veins and within their alteration envelopes. Molybdenite within an aplite sample from near the crest of the Moosehorn Range was dated using Re-Os to test a possible temporal relationship with the hydrothermal vein formation.

U-Pb

The gold-bearing V3 vein crosscuts a felsite dyke but is itself cut by a mafic dyke. The felsite dyke gives a U-Pb zircon age of 96.0 ± 0.4 Ma (Chapter 2 of this study), which constrains a maximum age for the vein formation. A minimum age is 53.4 ± 1.7 Ma, which is the whole rock K-Ar age of the fine-grained mafic dykes on the property (Chapter 2).

$^{40}Ar/^{39}Ar$

Three samples of muscovite (grains ~200-300 μm in size) from within quartz veins or from the alteration envelopes were dated by the Geological Survey of Canada in Ottawa using step-heating $^{40}Ar/^{39}Ar$ methods. The ages obtained from these analyses are considered to represent the actual time of the vein formation as opposed to a minimum age. A sample of biotite from the Moosehorn Range Granodiorite (sample 99N-2) yielded a $^{40}Ar/^{39}Ar$ age of 94.4 ± 0.9 Ma (Chapter 2). The wallrock had, therefore, already cooled through the 300ºC $^{40}Ar/^{39}Ar$ closure temperature of biotite (McDougall and Harrison, 1999) by this time. Muscovite, which has a higher closure temperature of about 350ºC (McDougall and Harrison, 1999), formed in the alteration envelopes adjacent to the veins at a temperature cooler than its $^{40}Ar/^{39}Ar$ closure temperature, and thus records the age of alteration and veining.

The analytical data and age spectra are shown in Table 7 and Figures 30.1, 30.2, and 30.3. Sample 99N-4a in Figure 30.1 is muscovite from within a gold-bearing quartz vein that outcrops along the crest of the Moosehorn Range. It was dated at 93.0 ± 0.9 Ma. Muscovite in sample 99N-16J was collected at surface from the alteration envelope adjacent to the V1 vein and yielded a plateau age of 92.6 ± 0.9 Ma (Fig. 30.2). Muscovite for sample 00N-62 was taken from an alteration envelope of a shallowly east-dipping veinlet intersected in drill core (DDH LL00-3). A considerably younger age of 88.7 ± 0.9 Ma was obtained for this sample; evidence in the age spectrum for significant ^{40}Ar loss is an indication that this is a minimum age estimate for the formation of the muscovite (Fig. 30.3). Vein formation and gold mineralization is interpreted to have taken place episodically between about 92 Ma and 93 Ma.

Table 7. $^{40}Ar/^{39}Ar$ isotopic data for alteration muscovite associated with the gold-bearing veins.

Power[a]	Volume ^{39}Ar x10^{-11} cc	$^{36}Ar/^{39}Ar$	$^{37}Ar/^{39}Ar$	$^{38}Ar/^{39}Ar$	$^{40}Ar/^{39}Ar$	%^{40}Ar ATM	$^{*40}Ar/^{39}Ar$	f_{39}[b] (%)	Apparent Age Ma[c]
99N-4a Muscovite; J=.00276590									
Aliquot: A									
2.0	0.1297	0.1612±0.0104	0.101±0.033	0.039±0.016	62.290±3.005	76.5	14.645±2.509	0	71.63±12.04
2.8	0.2178	0.0678±0.0049	0.081±0.006	0.018±0.016	32.901±1.568	60.9	12.848±1.355	0.1	63.00±6.53
3.0	0.5819	0.0373±0.0018	0.033±0.004	0.009±0.011	27.225±0.693	40.5	16.198±0.595	0.2	79.07±2.84
3.4	3.5134	0.0123±0.0005	0.006±0.001	0.003±0.011	22.351±0.135	16.3	18.703±0.179	1	90.99±0.85
3.8	21.3306	0.0010±0.0000	0.001±0.000	0.002±0.011	19.245±0.074	1.5	18.957±0.073	6.1	92.20±0.35
4.2	10.528	0.0019±0.0001	0.002±0.000	0.002±0.011	19.502±0.081	2.8	18.953±0.081	3	92.18±0.38
5.0	42.38	0.0005±0.0000	0.001±0.000	0.002±0.011	19.217±0.053	0.8	19.070±0.054	12.1	92.73±0.26
12.0	152.1416	0.0005±0.0000	0.001±0.000	0.002±0.011	19.291±0.055	0.7	19.147±0.055	43.4	93.10±0.26
2.4	0.1306	0.1464±0.0087	0.102±0.021	0.044±0.014	61.930±2.258	69.9	18.649±2.457	0	90.74±11.66
Aliquot: B									
2.4	0.082	0.6914±0.0476	0.746±0.084	0.030±0.015	210.835±11.185	96.9	6.536±9.291	0	32.32±45.54
3.0	0.7707	0.2715±0.0052	0.075±0.006	0.006±0.011	96.016±1.572	83.6	15.790±0.880	0.2	77.12±4.21
3.5	1.7082	0.0089±0.0007	0.032±0.005	0.005±0.011	20.995±0.325	12.6	18.358±0.330	0.5	89.36±1.57
3.9	20.9087	0.0030±0.0001	0.003±0.000	0.002±0.011	19.985±0.115	4.5	19.093±0.111	6	92.84±0.53
4.2	15.3128	0.0036±0.0001	0.005±0.001	0.003±0.011	20.116±0.088	5.3	19.041±0.089	4.4	92.59±0.42
4.6	16.7166	0.0011±0.0001	0.004±0.000	0.002±0.011	19.415±0.077	1.6	19.102±0.079	4.8	92.88±0.37
5.0	7.9098	0.0007±0.0002	0.008±0.001	0.003±0.011	19.239±0.101	1.1	19.023±0.114	2.3	92.51±0.54
5.6	11.4972	0.0006±0.0001	0.005±0.001	0.002±0.011	19.322±0.091	1	19.133±0.094	3.3	93.03±0.44
6.5	24.3766	0.0004±0.0001	0.003±0.000	0.003±0.011	19.292±0.053	0.7	19.164±0.058	7	93.18±0.28
12.0	20.4406	0.0005±0.0001	0.003±0.000	0.003±0.011	19.285±0.065	0.7	19.146±0.067	5.8	93.09±0.32
99N-16K Muscovite; J=.00276700									
Aliquot: A									
2.0	0.7545	0.0329±0.0023	0.079±94.015	0.017±0.003	19.433±0.391	50	9.712±0.687	0.6	47.84±3.34
2.4	1.94	0.0031±0.0007	0.017±243.167	0.005±0.001	18.784±0.220	4.9	17.854±0.260	1.4	87.00±1.24
2.8	3.3747	0.0018±0.0004	0.016±99.250	0.002±0.000	19.267±0.148	2.8	18.730±0.160	2.5	91.16±0.76
3.0	10.2302	0.0008±0.0001	0.009±92.708	0.002±0.001	19.011±0.117	1.2	18.781±0.119	7.6	91.40±0.56
3.4	11.4596	0.0006±0.0002	0.008±176.595	0.002±0.000	18.827±0.083	0.9	18.662±0.096	8.5	90.83±0.46
4.2	6.7115	0.0011±0.0002	0.014±38.717	0.002±0.000	18.537±0.092	1.7	18.219±0.096	5	88.73±0.46
12.0	4.138	0.0015±0.0002	0.370±43.345	0.005±0.000	18.364±0.133	2.4	17.930±0.130	3.1	87.36±0.62
Aliquot: B									
2.0	0.5024	0.0508±0.0029	0.085±148.630	0.021±0.006	21.957±0.519	68.4	6.947±0.842	0.4	34.35±4.12
2.4	0.591	0.0086±0.0027	0.042±222.569	0.002±0.004	19.971±0.519	12.8	17.424±0.831	0.4	84.95±3.96
2.8	2.5795	0.0019±0.0004	0.019±169.107	0.003±0.000	19.116±0.195	3	18.551±0.204	1.9	90.31±0.97
3.0	6.9533	0.0019±0.0001	0.010±137.878	0.001±0.000	19.068±0.070	2.9	18.512±0.072	5.1	90.12±0.34
3.4	9.1964	0.0007±0.0002	0.007±75.776	0.001±0.000	18.697±0.098	1.1	18.489±0.103	6.8	90.01±0.49
3.8	6.9887	0.0011±0.0001	0.007±122.633	0.001±0.000	18.658±0.115	1.7	18.338±0.116	5.2	89.30±0.55
4.2	13.4224	0.0007±0.0001	0.006±118.489	0.002±0.000	18.447±0.067	1.1	18.253±0.068	9.9	88.89±0.33
5.0	3.2498	0.0034±0.0003	0.183±39.077	0.004±0.001	18.677±0.183	5.4	17.670±0.179	2.4	86.12±0.85
12.0	3.2471	0.0025±0.0003	0.183±29.604	0.004±0.000	18.701±0.159	3.9	17.965±0.159	2.4	87.52±0.75
Aliquot: C									
2.0	0.5313	0.0224±0.0017	0.125±111.749	0.028±0.002	16.319±0.477	40.5	9.713±0.434	0.4	47.85±2.11
2.4	1.1518	0.0052±0.0007	0.058±218.190	0.007±0.001	18.196±0.298	8.4	16.663±0.262	0.9	81.32±1.25
3.0	11.4607	0.0008±0.0001	0.012±135.510	0.003±0.000	18.839±0.085	1.2	18.607±0.085	8.5	90.57±0.41
3.5	16.0309	0.0005±0.0001	0.008±134.918	0.002±0.000	18.707±0.066	0.8	18.554±0.068	11.8	90.32±0.32
3.9	14.0006	0.0006±0.0001	0.009±110.793	0.002±0.000	18.501±0.102	0.9	18.333±0.102	10.3	89.27±0.48
4.2	3.1379	0.0010±0.0003	0.035±66.098	0.003±0.000	18.384±0.181	1.6	18.099±0.180	2.3	88.16±0.86
12.0	3.6963	0.0007±0.0004	0.225±46.894	0.005±0.000	18.125±0.120	1.2	17.907±0.151	2.7	87.24±0.72

99N-16J Muscovite; J=.00269630

Aliquot: A

2.0	0.1248	0.2914±0.0140	0.122±531.897	0.096±0.011	103.308±4.771	83.3	17.212±5.891	0.1	81.84±27.39
2.8	2.1957	0.0192±0.0010	0.017±110.202	0.007±0.000	24.703±0.178	23	19.015±0.333	1	90.20±1.54
3.0	11.5319	0.0044±0.0002	0.002±227.387	0.004±0.000	20.880±0.038	6.2	19.576±0.055	5.3	92.80±0.25
3.4	17.5797	0.0017±0.0001	0.002±164.931	0.004±0.000	20.069±0.066	2.6	19.553±0.067	8.1	92.69±0.31
3.8	13.746	0.0012±0.0001	0.002±113.398	0.004±0.000	19.920±0.067	1.7	19.579±0.066	6.3	92.81±0.31
4.2	12.6818	0.0011±0.0001	0.002±70.863	0.005±0.000	19.846±0.040	1.7	19.519±0.041	5.8	92.53±0.19
5.0	6.7481	0.0006±0.0002	0.004±139.298	0.005±0.000	19.683±0.080	0.9	19.506±0.086	3.1	92.48±0.40
12.0	20.8538	0.0004±0.0000	0.001±143.205	0.005±0.000	19.668±0.045	0.6	19.541±0.044	9.6	92.64±0.20

Aliquot: B

2.0	0.1215	0.0867±0.0114	0.232±424.797	0.116±0.013	44.088±3.058	58.1	18.463±3.922	0.1	87.65±18.17
2.4	0.3889	0.0607±0.0049	0.038±509.222	0.023±0.004	37.178±0.614	48.2	19.243±1.404	0.2	91.26±6.49
2.8	2.0527	0.0133±0.0011	0.013±273.418	0.008±0.001	23.172±0.266	16.9	19.249±0.400	0.9	91.28±1.85
3.0	10.5411	0.0033±0.0001	0.004±124.409	0.006±0.000	20.389±0.080	4.8	19.415±0.081	4.8	92.05±0.38
3.4	8.2865	0.0010±0.0001	0.002±102.653	0.004±0.000	19.712±0.105	1.4	19.428±0.104	3.8	92.11±0.48
3.8	11.6279	0.0005±0.0001	0.001±456.255	0.004±0.000	19.594±0.069	0.7	19.448±0.069	5.3	92.21±0.32
4.2	16.5594	0.0013±0.0001	0.002±184.734	0.004±0.000	19.854±0.100	1.9	19.467±0.101	7.6	92.30±0.47
5.0	15.9821	0.0004±0.0001	0.002±129.352	0.004±0.000	19.667±0.041	0.6	19.557±0.045	7.3	92.71±0.21
12.0	12.8115	0.0005±0.0001	0.002±137.315	0.004±0.000	19.637±0.068	0.7	19.496±0.067	5.9	92.43±0.31

Aliquot: C

2.4	0.8017	0.0287±0.0021	0.073±122.787	0.007±0.001	24.181±0.417	35.1	15.705±0.657	0.4	74.82±3.07
3.0	11.2038	0.0019±0.0001	0.007±130.981	0.004±0.000	19.694±0.027	2.9	19.122±0.036	5.2	90.70±0.17
3.5	13.3595	0.0004±0.0001	0.005±146.728	0.004±0.000	19.474±0.078	0.7	19.341±0.079	6.1	91.71±0.36
3.9	10.0489	0.0003±0.0001	0.006±103.156	0.004±0.000	19.478±0.101	0.5	19.380±0.102	4.6	91.89±0.47
4.2	5.9783	0.0005±0.0001	0.010±141.903	0.005±0.000	19.434±0.128	0.8	19.282±0.126	2.8	91.44±0.58
4.6	2.2088	0.0001±0.0004	0.025±159.961	0.006±0.000	19.192±0.124	0.2	19.162±0.109	1	90.88±0.50
12.0	10.2469	0.0002±0.0001	0.006±123.403	0.004±0.000	19.605±0.039	0.3	19.544±0.039	4.7	92.65±0.18

00N-62 Muscovite; J=.00317880

Aliquot: A

2.4	0.7646	0.0272±0.0052	0.533±21.971	0.045±0.003	24.046±0.292	33.5	15.996±1.525	0.2	89.48±8.32
2.8	2.5282	0.0065±0.0003	0.526±9.742	0.008±0.000	16.701±0.129	11.5	14.783±0.113	0.8	82.85±0.62
3.5	22.8528	0.0012±0.0000	0.265±6.306	0.004±0.000	15.633±0.030	2.3	15.267±0.029	7.1	85.50±0.16
3.9	25.9835	0.0007±0.0000	0.074±8.348	0.004±0.000	15.924±0.056	1.3	15.711±0.056	8.1	87.92±0.31
4.2	22.8896	0.0006±0.0000	0.016±43.483	0.003±0.000	16.033±0.050	1.1	15.860±0.050	7.1	88.74±0.27
4.6	10.3173	0.0012±0.0001	0.012±53.902	0.004±0.001	16.227±0.049	2.2	15.872±0.049	3.2	88.80±0.27
12.0	54.0171	0.0007±0.0001	0.013±15.540	0.004±0.000	16.068±0.023	1.2	15.872±0.037	16.8	88.80±0.20

Aliquot: B

2.4	0.553	0.0472±0.0014	0.392±36.240	0.066±0.003	26.461±0.408	52.7	12.513±0.268	0.2	70.37±1.48
2.8	2.5958	0.0052±0.0003	2.035±11.827	0.010±0.000	15.606±0.118	9.9	14.066±0.097	0.8	78.91±0.53
3.5	39.9287	0.0009±0.0000	0.508±6.781	0.003±0.000	15.660±0.017	1.7	15.386±0.018	12.4	86.15±0.10
3.9	37.5929	0.0004±0.0000	0.023±27.262	0.003±0.000	15.742±0.018	0.7	15.624±0.021	11.7	87.45±0.12
4.2	33.0601	0.0003±0.0000	0.013±23.443	0.004±0.000	15.889±0.032	0.6	15.800±0.031	10.3	88.41±0.17
4.6	14.5655	0.0001±0.0001	0.009±78.500	0.003±0.000	15.862±0.023	0.3	15.818±0.042	4.5	88.51±0.23
5.5	20.7176	0.0003±0.0000	0.022±57.099	0.003±0.000	15.883±0.023	0.5	15.801±0.024	6.4	88.42±0.13
12.0	33.4912	0.0003±0.0000	0.051±28.003	0.003±0.000	15.988±0.032	0.6	15.900±0.032	10.4	88.95±0.18

a: As measured by laser in % of full nominal power (10W)

b: Fraction ^{39}Ar as percent of total run

c: Errors are analytical only and do not reflect error in irradiation parameter J

d: Nominal J, referenced to FCT-SAN=28.03 Ma (Renne et al., 1994)

*: Step not included in age determination

All uncertainties quoted at 2σ level

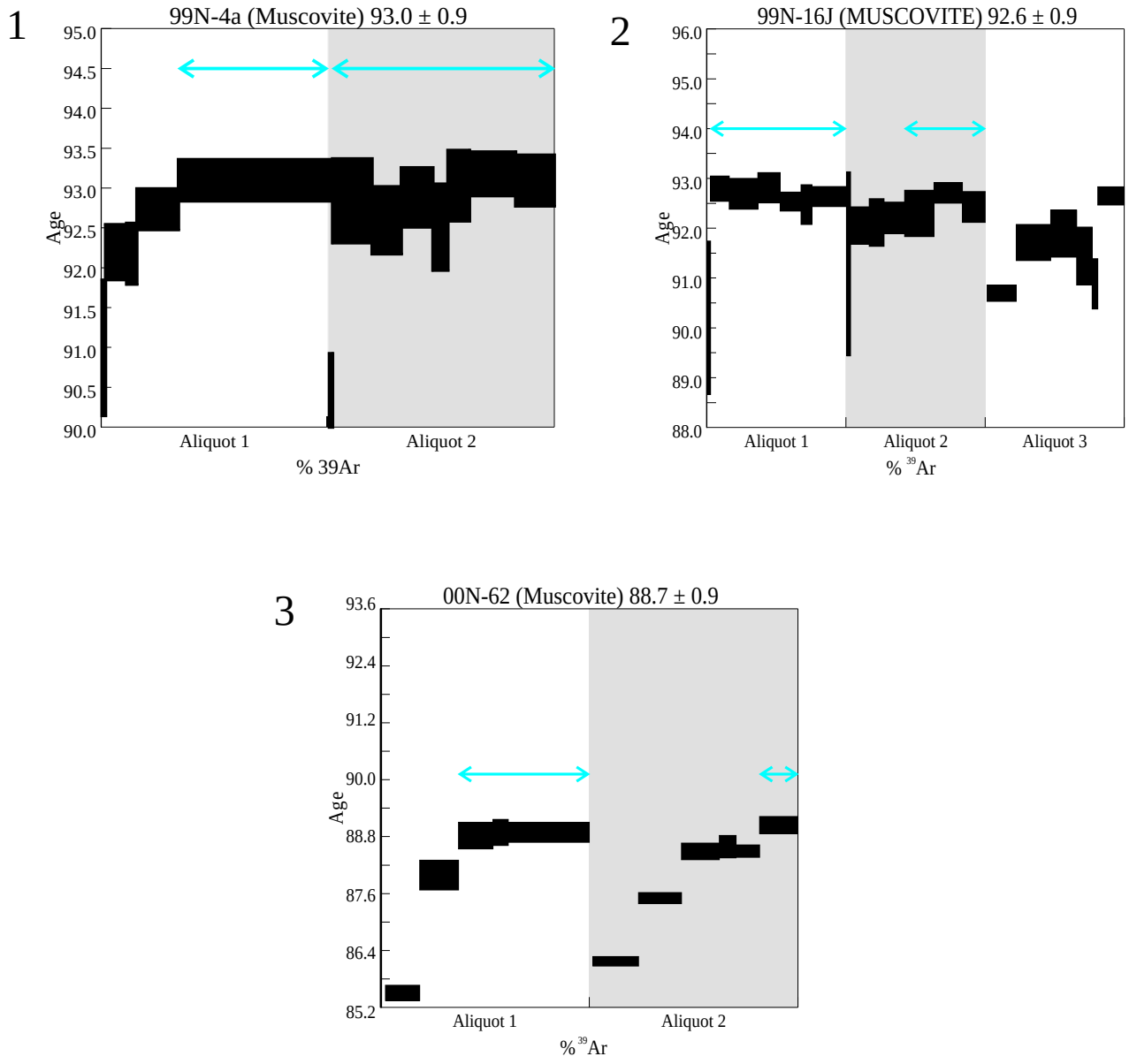

Figure 30 $^{40}Ar/^{39}Ar$ age spectrum diagrams for muscovite from inside the gold-bearing veins and from within alteration envelopes adjacent to the veins. **1.** Muscovite from within a quartz vein on the crest of the Moosehorn Range; spectrum shows minor loss of ^{40}Ar in early stages but a good plateau age of 93.0 ± 1.0 Ma was obtained for higher temperature releases. **2.** Muscovite from the alteration envelope adjacent to the V1 vein (collected at surface); first aliquot yields a very good plateau age of 92.6 ± 0.9 Ma. **3.** Muscovite from fresh alteration envelope adjacent to a veinlet intersected in DDH LL00-3; ^{40}Ar loss is evident in early step-heating stages, and a plateau age of 88.7 ± 0.9 Ma was obtained in later stages. Plateau ages yielded from the first two samples are considered more reliable as they are based on more than 50% of the argon release and more than 50% of the heating steps.

Re-Os

Molybdenite was found in aplite within a creek bed immediately northwest of Kenyon Creek (Ritcey, 2000, pers. comm.), and near the crest of the Moosehorn Range (Fig. 23.1). A Re-Os age of 103.9 ± 0.5 Ma, obtained at the University of Alberta Radiogenic Isotope Facility in Edmonton, Alberta, confirms that the molybdenite was deposited long before the gold-bearing veins formed. U-Pb zircon analyses give very imprecise ages for the aplite but it can be no older than the 99.8 ± 0.4 Ma granodiorite that it cuts. The 104 Ma Re-Os age is, therefore, anomalously old. The Re-Os dating method has been shown to give anomalously old ages in other studies (e.g., Suzuki et al., 1996). This problem may be symptomatic of analytical problems (Selby, 2001, pers. comm.), the relatively poorly constrained Re decay constant, uncertainty about the closure temperature of the Re-Os system in molybdenite, and/or how weathering and alteration affect the Re-Os systematics in molybdenite (McCandless et al., 1993; Suzuki et al., 1996; Suzuki et al., 2000).

Reconnaissance Fluid Inclusion Study of the Longline Gold-Bearing Veins

A reconnaissance fluid inclusion study of the gold-bearing veins was undertaken to estimate the chemical composition of ore-forming fluids, and to constrain temperature and pressure at which these fluids were trapped. Approximately 240 fluid inclusions in quartz were analyzed from doubly polished wafers of three different samples of vein material.

Methodology

Microthermometric measurements of fluid inclusions were carried out using a FLUID INC.-adapted USGS gas-flow heating-freezing stage at the University of British Columbia. Accuracy of the measurements was ensured by initially using synthetic fluid inclusions provided by FLUID INC. to calibrate against the triple point of pure CO_2 (-56.6°C), the freezing point of water (0.0°C), and the critical point of water (374.1°C). Accuracy of the temperatures recorded in this study was ±0.1°C for freezing runs, and ±2.0°C for heating runs between 30°C and 350°C. Doubly-polished wafers of vein material were cooled to approximately –120°C and then warmed slowly such that precise measurements of first and final ice melting for water (eutectic temperature T_{eu} and melting temperature $T_{m_{Ice}}$, respectively), the final melting temperature of CO_2 ($T_{m_{CO_2}}$), and the final melting temperature of clathrate ($T_{m_{Clath}}$) could be obtained. Where possible, subsequent heating runs were carried out on inclusions from which melting temperatures were obtained, but difficulties in relocating the small inclusions following freezing runs precluded the determination of *both* the melting and homogenization temperatures for many inclusions. Total homogenization temperatures (T_h) were obtained for aqueous inclusions, and CO_2- and total homogenization temperatures ($T_{h_{CO_2}}$ and T_h, respectively) were determined for CO_2-bearing inclusions. Reduction of the microthermometric data was done employing the methods outlined by Shepherd et al. (1985), Swanenberg (1979), and Brown and Lamb (1989).

Fluid Inclusion Petrography

Most quartz in the gold-bearing veins is milky white in hand sample and extremely turbid in thin section. Fluid inclusions in quartz from samples of vein material were classified as primary, pseudosecondary, and secondary, following the criteria given by Roedder (1984). Growth zones in quartz along which classical primary-pseudosecondary inclusions are generally found are rare in the studied samples. Secondary inclusion trails cloud most of the quartz groundmass, thus further complicating the positive identification of genuinely primary inclusions. Moreover, determining which inclusions were related to gold deposition was difficult. Inclusions selected for analysis were at least 8-10 μm in diameter, and were located in clear quartz, either near sulphide crystals or within euhedral quartz terminations in vugs, away from fracture planes and secondary inclusion trails. As gold is spatially related to sulphides and vugs, these fluid inclusions are interpreted to represent the fluid from which the gold and sulphides were deposited. Inclusions considered to be primary are isolated, round, or oval-shaped with curviplanar walls and those measured were commonly clustered in groups with consistent liquid-vapour ratios.

The three samples for the reconnaissance study were from main gold-bearing quartz veins, which average about 30 g/t Au. Samples 99N-22C and 99N-22F are from the V3 trench and were collected from the core of the thickest vein and from a parallel thinner vein, respectively. Sample 99N-4D was collected from what Greig (1975) defined as the "M" Vein on the crest of the Moosehorn Range (Fig. 23.1). Similar inclusion populations were found in all the samples.

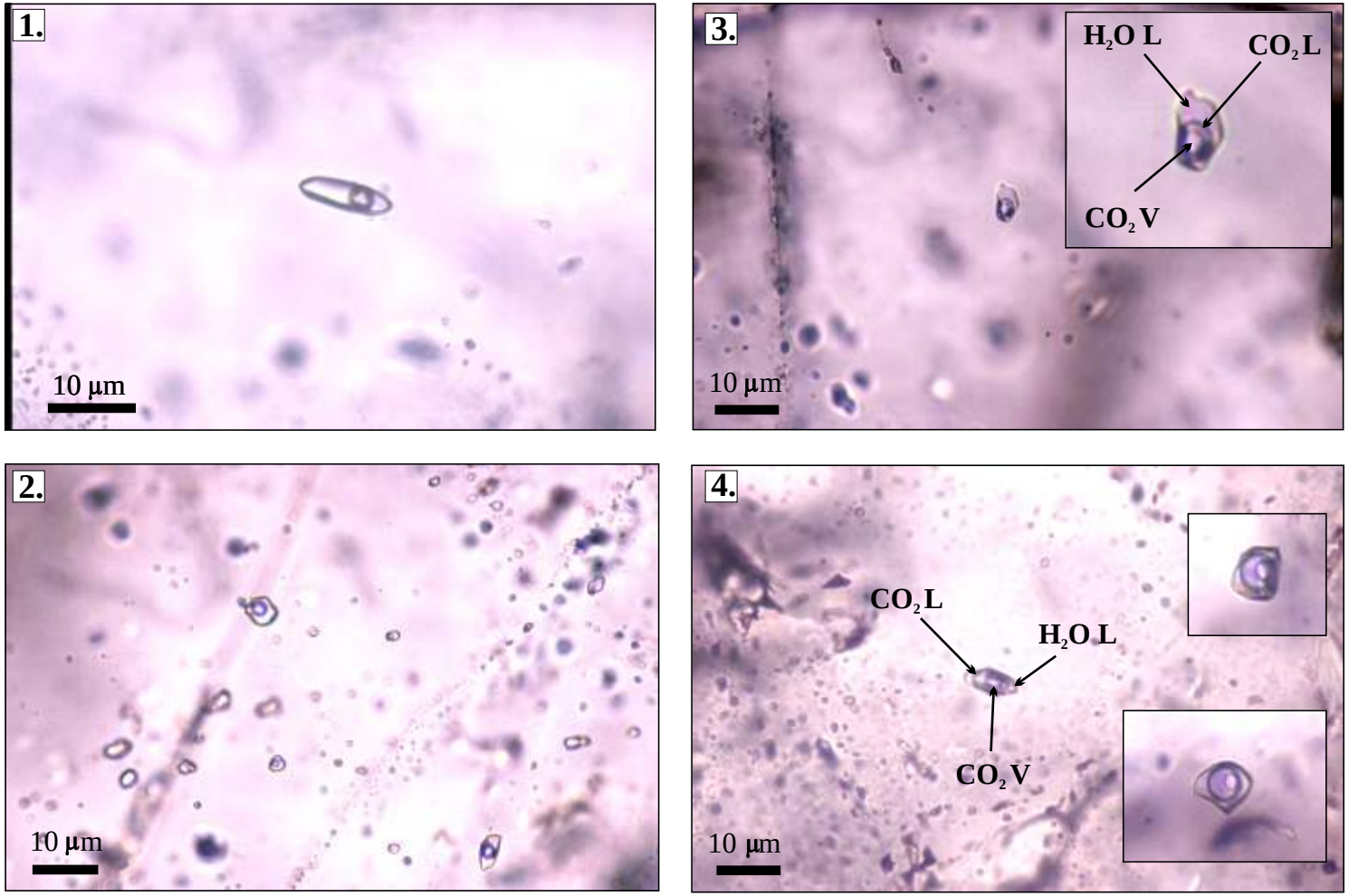

Figure 31 Photomicrographs of fluid inclusions from the gold-bearing quartz veins. **1.** An aqueous inclusion with 15% H_20 vapour. **2.** A population of aqueous fluid inclusions. **3.** An aqueous-carbonic fluid inclusion with lessCO_2 than the inclusions in Figure 38.4. The inset photograph is the same inclusion magnified.**4.** Three CO2-rich inclusions showing the range of liquid-vapour ratios.

Two main types of primary fluid inclusions, both of which coexist in quartz, were identified at room temperature on the basis of phase proportions and compositions. These include:

Type I: Two-phase, aqueous $(H_2O)_L$ + $(H_2O)_V$ fluid inclusions with L:V ratios of 60:40 to 95:5, averaging about 90:10. Type I inclusions range in diameter from 5 to 18 μm and are typically round or oval-shaped (Figs. 31.1 and 31.2). No daughter crystals were observed.

Type II: Three-phase, $(CO_2)_L$ + $(CO_2 \pm CH_4)_V$ + $(H_2O)_L$ fluid inclusions with H_2O:CO_2 ratios of 20:80 to 70:30, averaging 50:50. Type II inclusions range in diameter from 6-35 μm and are typically round, oval, or teardrop-shaped. Types IIa and IIb were distinguished on the basis of the phase into which the inclusions homogenized. Type IIa inclusions are aqueous-carbonic (Fig. 31.3) and homogenized into $(H_2O)_L$ whereas type IIb inclusions (Fig. 31.4) are carbonic-aqueous and homogenized into $(CO_2)_L$. No daughter crystals were observed. Types IIa and IIb coexist, have similar microthermometric properties, and were therefore classified as a single fluid inclusion population.

Microthermometric Data

A summary of classification, properties, and microthermometric data for fluid inclusions from the gold-bearing quartz veins is presented in Table 8 and Appendix C. Relocating inclusions after freezing runs was difficult. As a result, microthermometric data for the majority of the inclusions consists of either all melting temperatures or all temperatures of homogenization.

Type I: Eutectic temperatures (T_{eu}) were measured for 46 fluid inclusions in order to estimate the composition of the fluid. The T_e values ranged from –26.6° to –17.2°C, with a

	Type I	Type IIa	Type IIb
Size (microns)	5-18 **(10)**	8-35 **(10)**	6-17 **(10)**
Degree of fill	0.60-0.95 **(0.85)**	0.20-0.50 **(0.50)**	0.45-0.65 **(0.50)**
T_{eu} (°C)	-26.6 to -17.2 **(-22.6)**	--	--
T_{mIce} (°C)	-12.1 to -2.2 **(-5.4)**	--	--
T_{mCO2} (°C)	--	-58.5 to -55.2 **(-56.6)**	-59.9 to -54.7 **(-56.7)**
T_{mClath} (°C)	--	-2.2 to + 8.9 **(+ 3.5)**	-3.5 to + 8.0 **(+ 3.3)**
T_{hCO2} (°C)	--	24.6 to 30.7 **(28.4) (L)**	25.6 to 29.5 **(28.5) (L)**
T_h (°C)	170-340 **(236) (V)**	231-308 **(271) (H_2O)**	261-320 **(291) (CO_2)**
Mole % CH_4	--	0 to 12.5 **(~2)**	0 to 10 **(~2)**
Equivalent CO_2 Density (g/cm^3)	--	0.40 - 0.70 **(0.57)**	0.30 - 0.69 **(0.54)**
Bulk Density (g/cm^3)	0.82 - 0.97 **(0.89)**	0.70 - 0.91 **(0.81)**	0.67 - 0.85 **(0.76)**
Wt. % CO_2	--	17.58 - 41.18 **(31.96)**	26.47 - 52.70 **(37.39)**
Salinity (Wt. % NaCl Equiv.)	3.3 - 16.0 **(7.9)**	0 - 10	0 - 10

Table 8 Summary of classification, properties, and microthermometric data for Longline fluid inclusions. Data ranges are shown, with average values in brackets. Abbreviations: (L) = homogenized into the liquid CO_2 phase, (H_2O) = homogenized into H_2O, (CO_2) = homogenized into CO_2

mean of –22.6°C (Fig. 32.1). The slight depression of T_e below –21.2°C indicates the fluid is almost purely H_2O + NaCl with a possible minor component of K^+ (Borisenko, 1977; Crawford, 1981a). Final ice melting temperatures ($T_{m_{Ice}}$) for type I fluid inclusions ranged from –12.1° to –2.1°C (n = 60), with a mean of –5.4°C (Fig. 32.2). Salinities of the type I inclusions, calculated using graphical methods of Shepherd et al. (1985), are between 3.3 and 16.0 wt % NaCl equivalent, with a mean of 7.9 wt % NaCl equivalent (n = 60). Some of the apparent salinity values could be attributed to undetected CO_2 in these inclusions. Homogenization temperatures for type I inclusions ranged from 170° to 340°C (n = 84), with an average of 236°C (Fig. 32.3). All type I inclusions homogenized to the liquid phase.

Type II: The final melting temperatures of solid CO_2 ($T_{m_{CO_2}}$) for type II inclusions ranged from –59.9° to –54.7°C (n = 55), with a mean of –56.7°C (Fig. 33.1). Final melting of CO_2 commonly occurred over a temperature interval of greater than 0.1°C, which, in addition to the slight depression of the triple point of CO_2 for some samples, indicates that CH_4 (and/or possibly N_2) is likely present in about half of the inclusions (Shepherd et al., 1985). The fact that many type II inclusions have values greater than –56.6°C could indicate that *another* phase is present, which may offset the effect of methane. Difficulty in getting the apparatus to heat slowly enough may also have contributed to the high $T_{m_{CO_2}}$ temperatures. The presence of a gaseous phase other than CO_2 is commonly recognized by final clathrate melting temperatures ($T_{m_{Clath}}$) values exceeding +10°C (Shepherd et al., 1985), but $T_{m_{Clath}}$ values for 49 type II inclusions in this study were between –3.5° and +8.9°C. Most $T_{m_{Clath}}$ fell between 2° and 4°C, with an average of 3.4°C (Fig. 33.2). Thomas and Spooner (1988) suggest that the presence of NaCl in these kinds of inclusions is

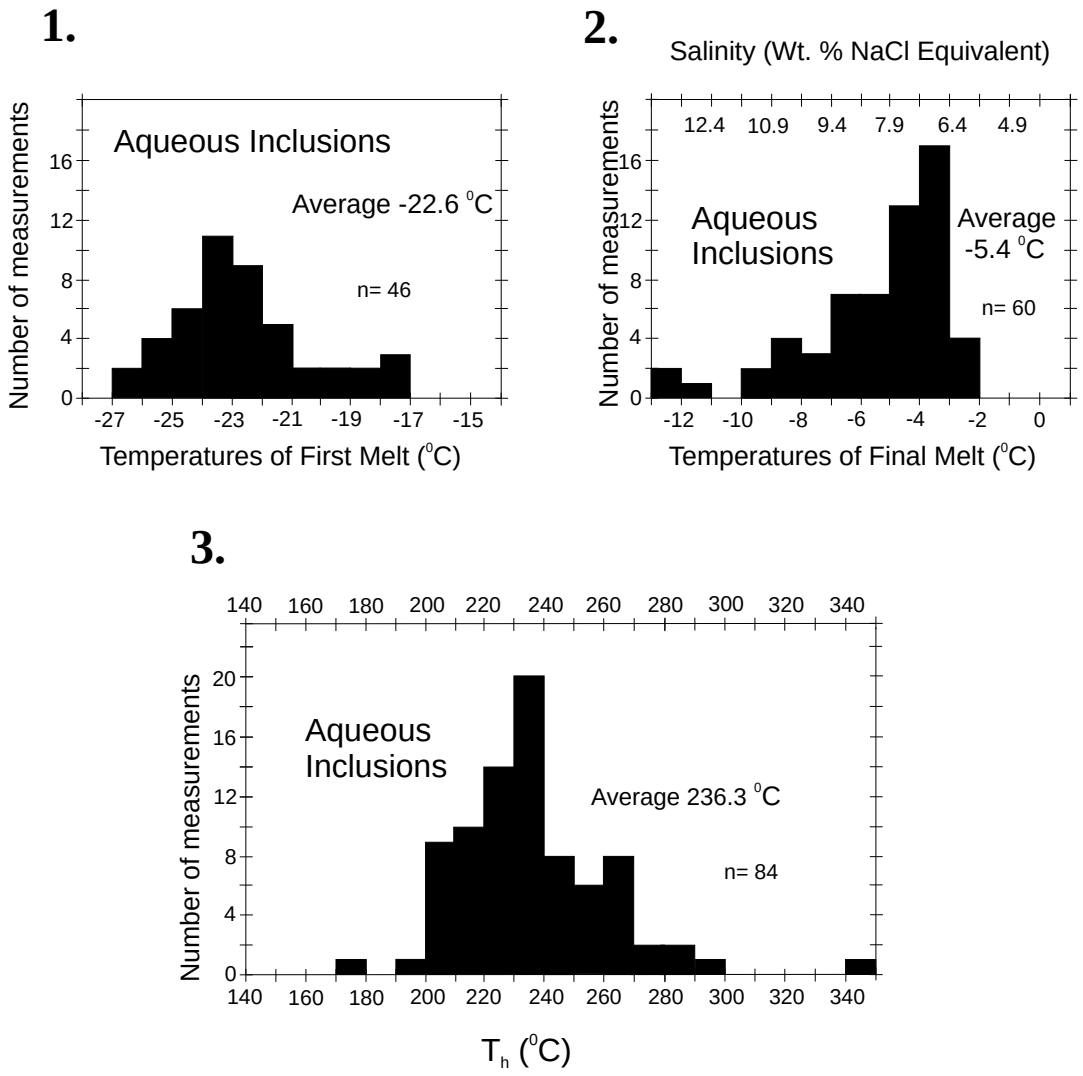

Figure 32 Histograms for aqueous type I inclusions. **1.** First melt temperatures (T_{eu}) **2.** Final melt temperatures (T_{mIce}). **3.** Homogenization temperatures (T_h).

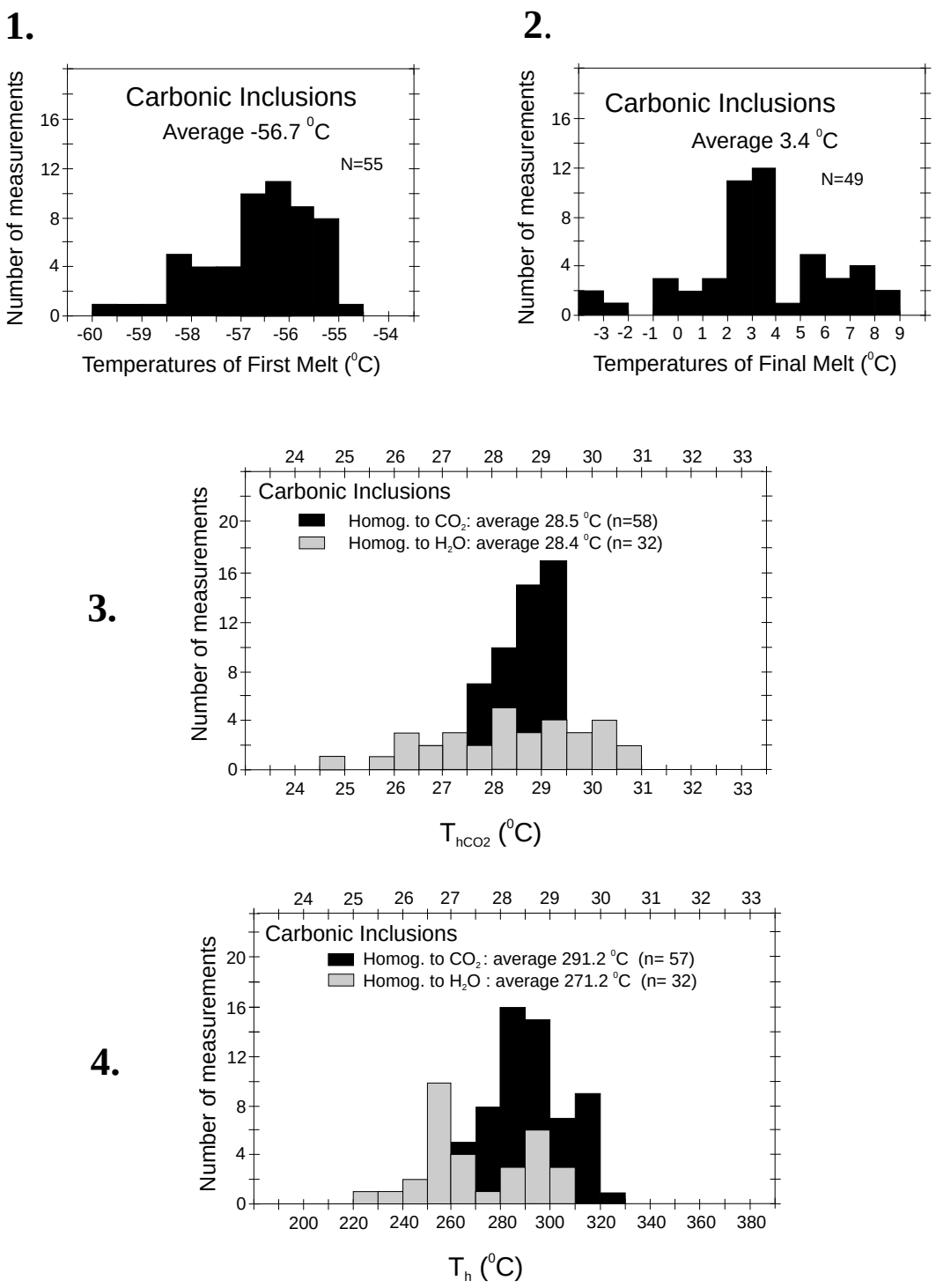

Figure 33 Histograms for carbonic inclusion types IIa and IIb. **1.** CO_2 melting temperatures (T_{mCO2}). **2.** Temperatures of final melt (T_{mClath}). **3.** CO_2 homogenization temperatures (T_{hCO2}). **4.** Total homogenization temperatures (T_h).

responsible for the depression of $T_{m_{Clath}}$ below 10°C. Maximum salinities can be determined based on the final melt temperatures of ice ($T_{m_{Ice}}$) but clathration in all type II inclusions obscured the ice crystals and $T_{m_{Ice}}$ could not be accurately measured. However, maximum salinity estimates for type II inclusions, based on clathrate melting temperatures, range from about 2 to 19 wt % NaCl equivalent, with an average of about 10 wt % NaCl equivalent (using the method of Shepherd et al., 1985). These salinities are similar to those of the type I inclusions, and consistent with other CO_2-bearing fluid inclusions associated with economic gold deposits of interior Alaska, which have salinities of 0-12% (McCoy et al., 1997). Laser Raman spectroscopic investigations would be necessary to determine more precise quantitative fluid inclusion compositions.

Temperatures of homogenization for both type IIa and IIb inclusions are very similar (Fig. 33.3 and 33.4). Homogenization temperatures of the carbonic phase ($T_{h_{CO_2}}$ = L + V $\Rightarrow$ L) for types IIa and IIb vary from 24.6° to 30.7°C, and from 25.6° to 29.5°C, respectively. Average $T_{h_{CO_2}}$ values for each are 28.4°C (type IIa, n = 32) and 28.5°C (type IIb, n = 58) (Fig. 33.3). Total homogenization temperatures (T_h) range from about 229° to 308°C for type IIa inclusions, and from about 261° to 320°C for type IIb inclusions (Fig. 33.4). Most T_h values for all type II inclusions fall between 250° and 320°C, with average T_h values of 281°C (n = 90).

Bulk density of the fluid inclusions was calculated using methods outlined by Shepherd et al. (1985). The aqueous type I inclusions have densities of 0.82 to 0.97 g/cm^3 (average 0.89 g/cm^3, n = 23).

Determination of mole % CH_4 and equivalent CO_2 densities requires both $T_{m_{CO_2}}$ and $T_{h_{CO_2}}$ for each type II inclusion. Because *both* of these values could not be acquired for the majority of inclusions, it was necessary to apply average $T_{m_{CO_2}}$ or $T_{h_{CO_2}}$ values for groups of similar inclusions. Moreover, phase equilibria for the H_2O-CO_2-CH_4-NaCl ± N_2 system are not well quantified (McCoy et al., 1997; Bakker, 1999). Therefore, mole % CH_4 and equivalent CO_2 densities presented here are at best rough estimates.

Mole % CH_4 and equivalent CO_2 densities of the type II inclusions were determined using the graphical methods of both Shepherd et al. (1985) and Swanenberg (1979), respectively. For type IIa inclusions, mole % CH_4 varies between 0 and about 12.5 %, with an average of about 2 %. Type IIb inclusions contain approximately 0 to 10 mole % CH_4, also with an average of about 2 %. Estimated equivalent CO_2 densities for type IIa inclusions are between 0.40 and 0.70 g/cm^3, averaging 0.57 g/cm^3. Those for type IIb inclusions are 0.30 to 0.69 g/cm^3, with an average of 0.54 g/cm^3.

Bulk inclusion densities and weight % CO_2 for all type II inclusions were calculated using the method of Shepherd et al. (1985). Thirty-two type IIa fluid inclusions have bulk densities ranging between 0.70 and 0.91 g/cm^3, with an average of 0.81 g/cm^3. Bulk densities for fifty-eight type IIb inclusions vary between 0.67 and 0.85 g/cm^3, with an average of 0.76 g/cm^3. Weight % CO_2 for type IIa inclusions varies from 17.85 to 41.18 (average 31.96 wt % CO_2, n = 32), and for type IIb inclusions, varies from 26.47 to 52.70 (average 37.39 wt % CO_2, n = 58). Most type II inclusions contain 30-45 wt % CO_2.

A range of estimated trapping pressures was determined employing graphical methods of Brown and Lamb (1989), using end-member volume percent CO_2 estimations for type IIa and type IIb inclusions, and an average salinity of 10 wt % NaCl equivalent. A

value of 20 volume % CO_2 was used for type IIa inclusions and 70 volume % CO_2 was used for type IIb inclusions. Pressures of about 3.4 kbar ± 0.25 kbar and 1.6 kbar ± 0.25 kbar were obtained for type IIa and type IIb inclusions, accordingly. Respective depths associated with these trapping pressures, calculated using the method of Shepherd et al. (1985) and assuming near-lithostatic conditions, are 12.8 ± 0.9 km and 6.0 ± 0.9 km. Pressure and depth estimates for the CO_2-rich type IIb inclusions are considered to be the most reasonable (e.g. Brown and Lamb, 1989) and consistent with the brittle nature and temperatures of the Longline veins.

Uncertainties in the pressure estimates may have been introduced by inaccurate phase volume estimations, imprecise graphical extrapolations, and the complexity of the inclusion chemistry. Because phase equilibria for the H_2O-CO_2-CH_4-NaCl ± N_2 system are still poorly understood and isochore locations vary in the literature, the pressure estimates for this study were determined assuming a relatively simple chemical system. However, useful information may still be gleaned from the data.

Discussion

Types IIa and IIb inclusions occur together, homogenize to H_2O and to CO_2 respectively, have variable densities and H_2O:CO_2 ratios, and have similar T_h. These observations provide convincing evidence for the entrapment of two immiscible fluids and the homogenization temperatures of approximately 250°-320°C are, therefore, equivalent to the trapping temperatures (Ramboz et al., 1982).

Type I inclusions represent an aqueous-dominated, lower temperature, low to moderate salinity fluid. The temperature of this fluid partially overlaps with that of the carbonic fluid and the salinity is approximately the same. Type I inclusions appear primary

and are spatially related to type II inclusions, and may represent a late-stage evolution from CO_2-rich to H_2O-rich fluids.

In summary, gold-bearing quartz ± carbonate veins in the Moosehorn Range area formed from aqueous and aqueous-carbonic fluids of the system H_2O-CO_2-CH_4-NaCl ± N_2, with moderate salinities (approximately 10 wt % NaCl equivalent). Homogenization temperatures range from 170˚ to 340˚C, but most values fall between 220˚ and 300˚C. The fluid pressures are between 1.3 and 1.9 kbar, corresponding to depths of 5-7 km, assuming near-lithostatic fluid pressures. This depth range is consistent with many mesothermal lode gold deposits (Goldfarb et al., 1997; McCuaig and Kerrich, 1998; Jia et al., 2000). The coexistence of both CO_2-rich and H_2O-rich aqueous-carbonic inclusions is indicative of H_2O-CO_2 fluid immiscibility, which was a likely mechanism for gold deposition.

Lead Isotopic Study

A lead isotopic study was undertaken to attempt to constrain the source(s) of the lead (Pb) and other metals in veins at the Longline occurrence. Determining and comparing the Pb isotopic compositions of epigenetic sulphide minerals *and* their host rocks can provide insight on the source reservoir(s) from which metals in the mineralizing fluids were derived (e.g., Tosdal et al. 1999, and references therein). This approach is founded on the assumption that these metals and the Pb were derived from the same source(s) and were transported and deposited from the same hydrothermal fluid (Tosdal et al., 1999).

Samples and Methods

Lead isotopic compositions were determined for a suite of sulphides, sulphosalts, and feldspars collected from the entire Longline property, including both surface and drill core samples. Whole rock Pb isotopic compositions were also obtained from three samples of least altered mafic dykes that postdate the gold-bearing veins. Most of the sulphides and sulphosalts analyzed, including galena, sphalerite, pyrite, arsenopyrite, and boulangerite, occur as phases within the main gold-bearing vein sets. Veinlets and disseminated sulphide blebs containing pyrrhotite and chalcopyrite were intersected in drill holes LL00-4 and LL00-6 (Fig. 23.1) in the northern Moosehorn Range area, and these appear to represent a completely different style of mineralization. Lead isotopic compositions of these sulphide occurrences were also measured to compare with compositions of the gold-related sulphides. In addition, pyrite from a molybdenite-bearing aplite was analyzed.

All sample preparation, geochemical separations, and isotopic measurements were carried out at the Geochronology Laboratory at the University of British Columbia. Small clean cubes of galena were handpicked, washed, and dissolved in HCl. Clean grains of sulphides and feldspars were handpicked, and the sulphides were leached in HCl to remove surface contamination before dissolution in nitric acid. Feldspar samples were ground and sieved, and the 100-200 mesh fraction was first leached in dilute HCl, then in a mixture of dilute HF and HBr, and was subsequently dissolved in concentrated HF. For each of the whole rock samples, about 50 mg of crushed rock material was leached in the same manner as the feldspars, and was dissolved in HF and nitric acid.

Separation and purification of Pb for trace Pb analyses employed ion exchange column techniques. The samples were converted to bromide, and the solution was passed

through ion exchange columns in HBr, and the lead eluted in 6N HCl. The total procedural blank on the trace lead chemistry was 100-110 pg.

Approximately 10-25 ng of the lead in chloride form was loaded onto a rhenium filament using a phosphoric acid-silica gel emitter, and isotopic compositions were determined on a Faraday collector in peak-switching mode using a modified VG54R thermal ionization mass spectrometer. The measured ratios were corrected for instrumental mass fractionation of 0.12% per mass unit based on repeated measurements of the N.B.S. SRM 981 Standard Isotopic Reference Material and the values recommended by Todt et al. (1996). Uncertainties reported in Table 9 were obtained by numerically propagating all mass fractionation and analytical errors throughout the calculations, and are presented at the 2σ level.

Results and Discussion

Whole rock, feldspar, sulphide, and sulphosalt lead isotopic compositions for samples in the Moosehorn Range area are plotted in uranogenic, thorogenic, and $^{208}Pb/^{206}Pb$ vs. $^{207}Pb/^{206}Pb$ space in Figures 34, 35, and 36, respectively. The data points generally fall near or below the "shale curve" (Godwin and Sinclair, 1982) in all three plots. The "shale curve" models the evolution of Pb in the miogeocline of the Canadian Cordillera, and also provides an approximate model for the evolution of upper crustal Pb in the YTT (Lange et al., 1993; Mortensen, 1994). The relatively high $^{207}Pb/^{204}Pb$ values for all the samples suggest they were derived from evolved crust (Doe and Zartman, 1979; Tosdal et al., 1999).

Also shown in Figures 43, 44, and 45 are Pb isotopic compositional fields based on available data for east-central Alaskan "K-T granites" (Aleinikoff et al., 2000), Early Cretaceous Mount Nansen volcanic rocks (Smuk, 1999) and galenas from associated

Table 9 Lead isotope data for samples from the Moosehorn Range study area[1]

Sample # [2]	Mineral[3]	Location	$^{206}Pb/^{204}Pb$	2σ, %	$^{207}Pb/^{204}Pb$	2σ, %	$^{208}Pb/^{204}Pb$	2σ, %	$^{207}Pb/^{206}Pb$	2σ, %	$^{208}Pb/^{206}Pb$	2σ, %
Sulphide and Sulphosalt Analyses												
99M-11 *(a)*	gl	Central Moosehorn Range	18.860	0.01	15.633	0.01	38.667	0.01	0.829	0.01	2.050	0.01
99M-11 *(b)*	gl	Central Moosehorn Range	18.844	0.01	15.635	0.01	38.664	0.01	0.830	0.01	2.052	0.01
99M-12	gl	Central Moosehorn Range	18.812	0.01	15.631	0.01	38.617	0.01	0.831	0.01	2.053	0.01
99M-13 *(a)*	gl	Central Moosehorn Range	18.852	0.02	15.668	0.02	38.749	0.02	0.831	0.01	2.056	0.01
99M-13 *(b)*	gl	Central Moosehorn Range	18.835	0.01	15.626	0.01	38.661	0.02	0.830	0.01	2.053	0.01
99N-3A *(a)*	gl	SC-2	18.911	0.01	15.658	0.01	38.772	0.02	0.828	0.01	2.050	0.01
99N-3A *(b)*	gl	SC-2	18.906	0.01	15.653	0.01	38.759	0.01	0.828	0.01	2.050	0.01
V1	gl	V1	18.818	0.01	15.648	0.01	38.676	0.01	0.832	0.01	2.055	0.01
99N-4G	gl	Central Moosehorn Range	18.822	0.01	15.635	0.01	38.640	0.01	0.831	0.01	2.053	0.01
99N-4H	py	Central Moosehorn Range	18.851	0.01	15.647	0.01	38.704	0.01	0.830	0.01	2.053	0.01
99N-5	gl	Great Bear Creek	18.791	0.01	15.630	0.01	38.597	0.01	0.832	0.01	2.054	0.01
99N-16C	sph	V1	18.882	0.02	15.712	0.01	38.899	0.02	0.832	0.01	2.060	0.01
99N-22B	boul	V3	18.903	0.09	15.737	0.09	38.976	0.09	0.833	0.01	2.062	0.01
99N-23	py	Swede's Pit: vein cutting V2	19.187	0.06	15.705	0.06	39.046	0.08	0.819	0.02	2.035	0.03
99N-29F	gl	V2 (Trench 6)	18.825	0.03	15.628	0.05	38.619	0.06	0.830	0.02	2.052	0.03
99N-38	sph	V2 (Trench 13)	18.953	0.15	15.734	0.11	39.067	0.02	0.830	0.11	2.061	0.06
99N-50	gl	Kenyon Creek	18.788	0.03	15.626	0.05	38.583	0.06	0.832	0.02	2.054	0.03
00N-22	py	DDH LL00-2	18.975	0.03	15.649	0.05	38.781	0.06	0.825	0.02	2.044	0.03
00N-48A	gl	DDH LL99-06 (at 30 m)	18.876	0.03	15.634	0.05	38.686	0.07	0.828	0.02	2.049	0.03
00N-48B	py	DDH LL99-06 (at 30 m)	18.946	0.04	15.665	0.05	38.809	0.07	0.827	0.02	2.048	0.03
00N-49	gl	DDH LL99-06 (at 22 m)	18.856	0.03	15.656	0.05	38.712	0.06	0.830	0.02	2.053	0.03
00N-50 *(a)*	asp	DDH LL99-09 (at 70 m)	18.889	0.04	15.643	0.05	38.711	0.07	0.828	0.02	2.049	0.03
00N-50 *(b)*	asp	DDH LL99-09 (at 70 m)	18.909	0.04	15.654	0.05	38.778	0.07	0.828	0.02	2.051	0.03
00N-51 *(a)*	asp	DDH LL99-09 (at 134 m)	18.891	0.09	15.667	0.09	38.721	0.11	0.829	0.04	2.050	0.05
00N-51 *(b)*	asp	DDH LL99-09 (at 134 m)	18.876	0.07	15.638	0.07	38.709	0.09	0.828	0.03	2.051	0.04
00N-53 *(a)*	asp	DDH LL99-11 (at 179 m)	18.868	0.04	15.628	0.05	38.678	0.07	0.828	0.02	2.050	0.03
00N-53 *(b)*	asp	DDH LL99-11 (at 179 m)	18.838	0.03	15.620	0.05	38.620	0.06	0.829	0.02	2.050	0.03
00N-54	py	DDH LL99-12 (at 154 m)	19.233	0.04	15.691	0.05	39.061	0.07	0.816	0.02	2.031	0.03
00N-71A	po	DDH LL00-5 (at 113 m)	18.979	0.06	15.641	0.06	38.744	0.08	0.824	0.02	2.041	0.03
00N-76A	ccp	DDH LL00-6	19.121	0.05	15.632	0.06	38.751	0.08	0.818	0.02	2.027	0.03
00N-76B	po	DDH LL00-6	19.141	0.48	15.638	0.45	39.135	0.50	0.817	0.18	2.045	0.13

Table 9 (continued)

Sample #[2]	Rock[4]: Mineral[5]	Location	$^{206}Pb/^{204}Pb$	2σ, %	$^{207}Pb/^{204}Pb$	2σ, %	$^{208}Pb/^{204}Pb$	2σ, %	$^{207}Pb/^{206}Pb$	2σ, %	$^{208}Pb/^{206}Pb$	2σ, %
Feldspar Analyses												
99N-2	MRG: Plag	Camp outcrop	19.256	0.05	15.718	0.04	39.216	0.06	0.816	0.02	2.037	0.04
99N-16F	FGD: Ksp	V1 Trench	19.255	0.01	15.692	0.01	39.129	0.01	0.815	0.01	2.032	0.01
99N-56	Pegmatite: Ksp	West of Airport Pup	19.225	0.01	15.672	0.01	39.006	0.01	0.815	0.01	2.029	0.01
99N-62B	Myl. MRG: Ksp	Near Kenyon Creek	19.213	0.01	15.667	0.01	38.972	0.01	0.815	0.01	2.028	0.01
99N-75	MRG: Fsp	Southeast of Swede's Pit	19.242	0.02	15.689	0.02	39.071	0.03	0.815	0.01	2.031	0.02
99N-78	FPQD: Fsp	Camp outcrop	19.285	0.11	15.694	0.11	39.156	0.11	0.814	0.01	2.030	0.01
99N-79	FD: Ksp	Camp outcrop	19.141	0.04	15.582	0.03	38.722	0.04	0.814	0.01	2.023	0.01
00N-12	MRG: Fsp	Southeastern Moosehorn Range	19.419	0.06	15.695	0.07	39.370	0.09	0.808	0.03	2.027	0.04
00N-14 *(a)*	MRG: Fsp	Central Moosehorn Range	19.237	0.12	15.732	0.12	39.042	0.14	0.818	0.05	2.030	0.06
00N-14 *(b)*	MRG: Fsp	Central Moosehorn Range	19.173	0.06	15.634	0.06	38.886	0.09	0.815	0.03	2.028	0.05
00N-15A	PQD: Fsp	Southeastern Moosehorn Range	19.262	0.09	15.685	0.09	39.115	0.10	0.814	0.02	2.031	0.03
00N-20	MRG: Fsp	Southeastern Moosehorn Range	19.208	0.03	15.665	0.05	38.977	0.07	0.816	0.02	2.029	0.03
00N-23	FMRG: Fsp	DDH LL00-2	19.196	0.05	15.654	0.06	38.933	0.08	0.815	0.02	2.028	0.03
00N-25	Granodiorite: Fsp	DDH MH99-6	19.269	0.06	15.718	0.06	39.135	0.08	0.816	0.02	2.031	0.03
00N-36 *(c)*	Aplite: Fsp	Central Moosehorn Range	19.305	0.03	15.699	0.05	39.176	0.07	0.813	0.02	2.029	0.03
00N-36 *(d)*	Aplite: Fsp	Central Moosehorn Range	19.322	0.04	15.707	0.05	39.230	0.07	0.813	0.02	2.030	0.03
00N-38	MRG: Fsp	Central Moosehorn Range	19.473	0.03	15.724	0.04	39.481	0.06	0.807	0.02	2.027	0.03
00N-66	Aplite: Fsp	DDH LL00-4	19.214	0.04	15.664	0.05	38.969	0.07	0.815	0.02	2.028	0.03
00N-67	Granodiorite: Fsp	DDH LL00-4 (at 167 m)	19.412	0.03	15.729	0.05	39.400	0.06	0.810	0.02	2.030	0.03
00N-68	Aplite: Fsp	DDH LL00-4 (at 244 m)	19.413	0.04	15.728	0.05	39.403	0.07	0.810	0.02	2.030	0.03
00N-70	FMRG: Fsp	DDH LL00-5 (at 105 m)	19.188	0.04	15.668	0.05	38.963	0.07	0.817	0.02	2.031	0.04
00N-77 *(a)*	Diorite: Fsp	DDH LL00-6	19.164	0.18	15.650	0.18	38.815	0.19	0.817	0.03	2.025	0.04
00N-77 *(b)*	Diorite: Fsp	DDH LL00-6	19.092	0.07	15.598	0.08	38.672	0.09	0.817	0.02	2.026	0.03
00N-72 *(a)*	Feldspar	DDH LL00-5	19.199	0.04	15.659	0.05	38.936	0.07	0.816	0.02	2.028	0.03
00N-72 *(b)*	Feldspar	DDH LL00-5	19.215	0.03	15.667	0.05	38.980	0.07	0.815	0.02	2.029	0.03
00N-74	Leucogr.: Fsp	DDH LL00-5 (at 128 m)	19.248	0.03	15.690	0.05	39.048	0.06	0.815	0.02	2.029	0.03
00N-75	FMRG: Fsp	Central Moosehorn Range	19.349	0.05	15.719	0.05	39.361	0.08	0.812	0.03	2.034	0.04
00N-80	FMRG: Fsp	DDH LL00-6	19.219	0.04	15.665	0.05	39.097	0.07	0.815	0.02	2.034	0.03
99M-130	PQD: Fsp	Southeastern Moosehorn Range	19.309	0.05	15.735	0.05	39.254	0.05	0.815	0.01	2.033	0.01
99M-131	7 Mile Pluton: Fsp	East of the Longline property	19.026	0.05	15.609	0.06	39.730	0.07	0.820	0.02	2.037	0.03
Whole Rock Analyses												
99N-9	F.gr. Mafic dyke	Soya Creek	19.227	0.05	15.684	0.03	38.993	0.08	0.816	0.04	2.028	0.06
00N-17	Mafic Xenolith	Southeastern Moosehorn Range	19.444	0.03	15.742	0.05	39.434	0.06	0.810	0.02	2.028	0.03
00N-63	Lamprophyre	DDH LL00-3	19.090	0.04	15.627	0.05	38.819	0.07	0.819	0.02	2.033	0.04

[1]All samples analyzed by the Geochronology Laboratory, University of British Columbia

[2]Letters in brackets denote different fractions of the same mineral

[3]Minerals analyzed: gl = galena, py = pyrite, sph = sphalerite, boul = boulangerite, asp = arsenopyrite, po = pyrrhotite, ccp = chalcopyrite

[4]Rock from which feldspar was obtained: MRG = Moosehorn Range granodiorite, FMRG = foliated MRG, FD = felsite dyke, PQD = massive porphyritic quartz diorite dyke, FPQD = foliated PQD, FGD = foliated granodiorite dyke

[5]Mineral analyzed: Fsp = feldspar (mix of potassium and plagioclase feldspar), Ksp = potassium feldspar, Plag = plagioclase

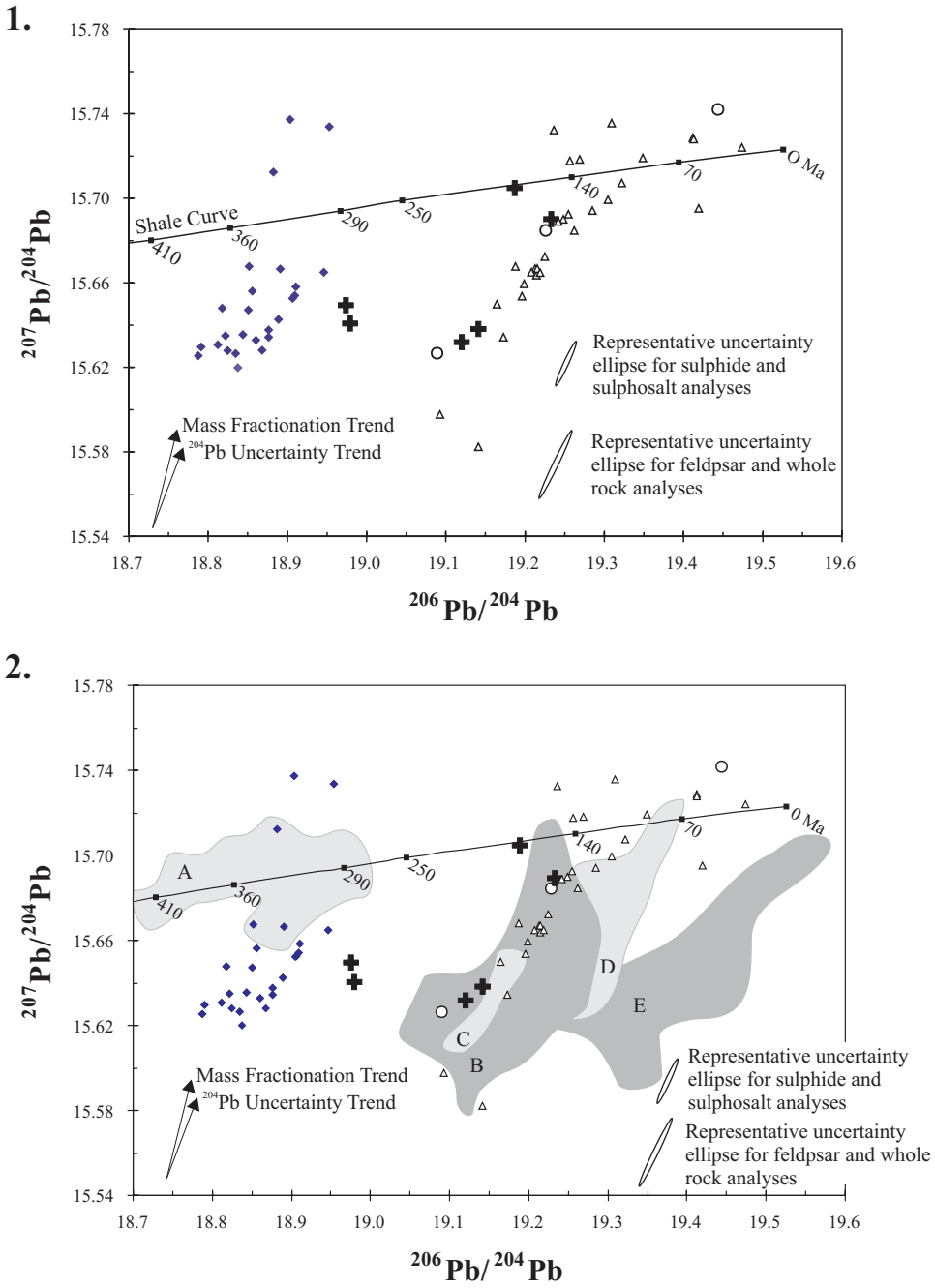

Figure 34 Uranogenic diagrams. **1.** Lead isotopic compositions of Moosehorn Range area vein minerals and host intrusions. The symbols are as follows: ◆ - sulphides and sulphosalts spatially associated with gold, ✚ - sulphides not spatially associated with gold hosted within structures unrelated to the shallow gold-bearing veins, Δ - feldspars from felsic to intermediate intrusions in the Moosehorn Range area, ○ - mafic dykes in the Moosehorn Range area (whole rock analyses). **2.** Same plot as above with lead isotopic compositional fields of other sulphides and intrusions in western Yukon and eastern Alaska. Field A encompasses galena analyses from various Yukon-Tanana terrane sedimentary exhalative deposits (Mortensen, 2002, unpublished data). Field B includes galena analyses for the Mount Nansen area (Appel, 1998). Field C includes galena analyses from the southeastern Dawson Range area (Smuk, 1999). Feldpsar data for various intrusions in east-central Alaska fall within field D (Aleinikoff et al., 2000). Field E includes whole rock compositions for Carmacks Group volcanic rocks in the southeastern Dawson Range (Smuk, 1999). Results are discussed in the text.

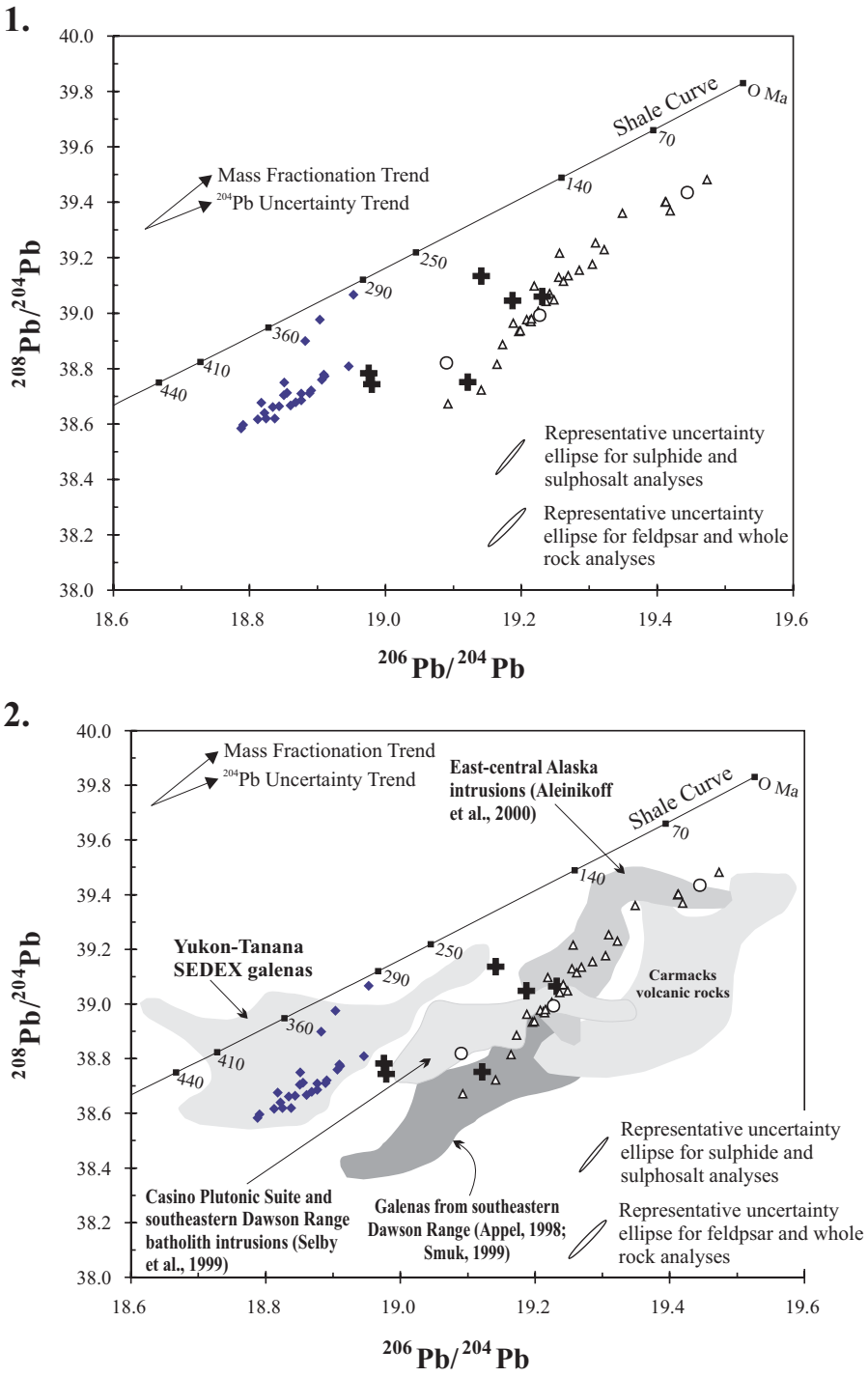

Figure 35 Thorogenic diagrams. **1.** Lead isotopic compositions of Moosehorn Range vein sulphides and sulphosalts, and host intrusions. Symbols are the same as in Fig. 34. **2.** Same diagram as above with lead isotopic compositional fields for other sulphides and intrusions in western Yukon and east-central Alaska. Whole rock compositions of Casino Plutonic Suite and southeastern Dawson Range batholith intrusions (Selby et al., 1999) are also shown. Interpretations of the diagrams are discussed in the text.

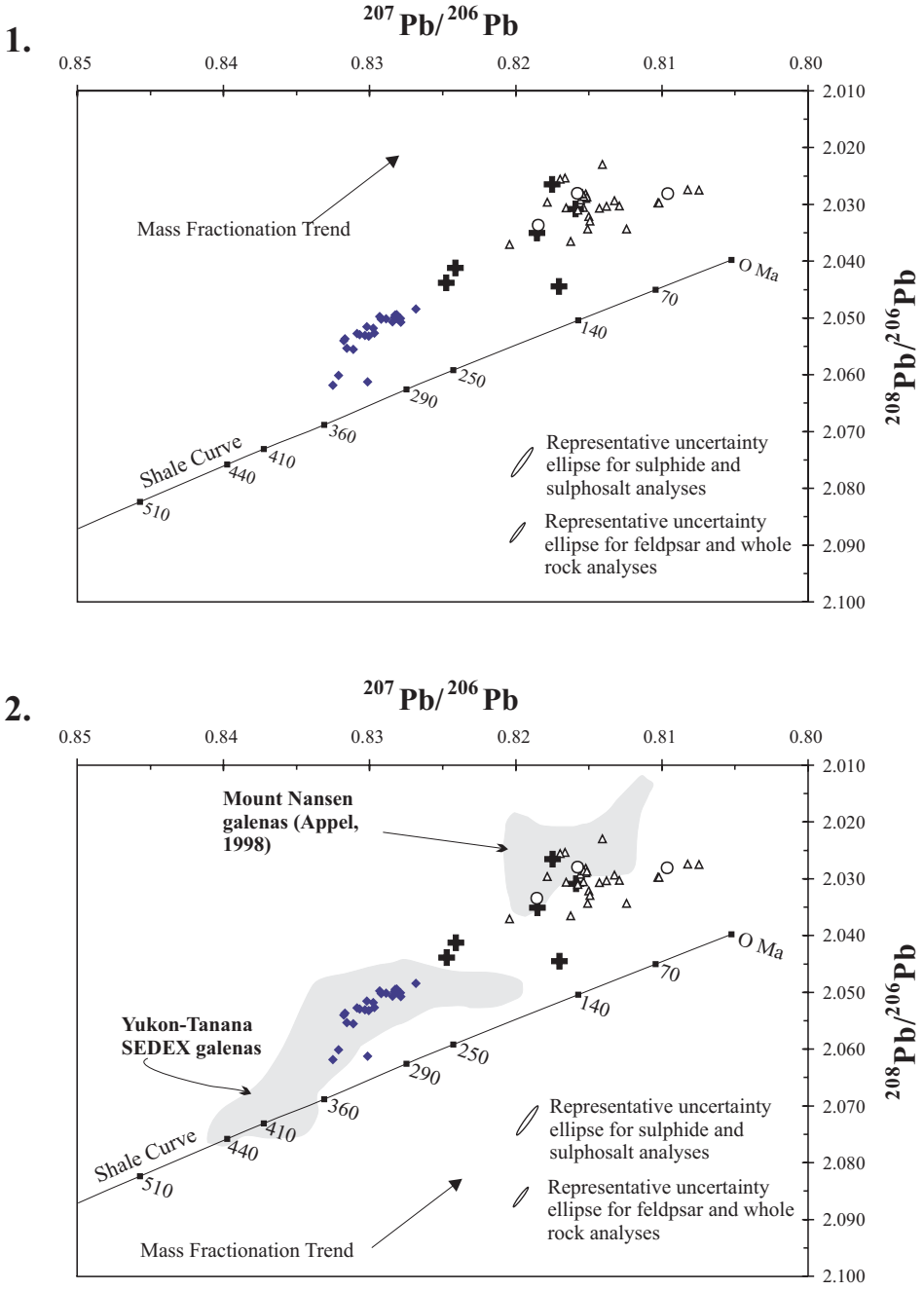

Figure 36 $^{208}Pb/^{206}Pb$ versus $^{207}Pb/^{206}Pb$ plots. **1.** Lead isotopic compositions of Moosehorn Range sulphides and sulphosalts, and host intrusions. Symbols are the same as in Figs. 34 and 35. The ^{204}Pb uncertainty is eliminated in this plot and the data are more tightly clustered. **2.** Same plot as above with the lead isotopic compositional fields of Yukon-Tanana sedimentary exhalative galenas and Mount Nansen area galenas plotted for comparison. Data was not available for the other suites seen in Figs. 34 and 35. Results are discussed in the text.

mineralization (Appel, 1998; Smuk, 1999), Late Cretaceous shoshonitic Carmacks Group volcanic rocks (Smuk, 1999), galenas from mid-Paleozoic Yukon-Tanana terrane sedimentary exhalative deposits (Mortensen, 2002, unpublished data), and other Early Cretaceous granitoids in the Dawson Range batholith and the Casino Plutonic Suite (Selby et al., 1999) in the Yukon Territory. These isotopic compositions are similar to those of the Moosehorn Range area intrusions, and are also reflected in granites from the Fairbanks region of Alaska (not shown) (McCoy et al., 1997). All the intrusions in the region plot in a fairly tight cluster, which suggests they were derived either from a single Pb isotopic reservoir, or from two or more reservoirs that were well homogenized over time. Scatter of the data due to analytical ^{204}Pb uncertainty is reduced in $^{208}Pb/^{206}Pb$ vs. $^{207}Pb/^{206}Pb$ space (Fig. 36) where the data fall into a more distinct homogeneous cluster. However, the slightly linear trend of Moosehorn Range whole rock and feldspar Pb isotopic data on the uranogenic and thorogenic plots may indicate mixing took place between a reservoir with low $^{207}Pb/^{204}Pb$ (< 15.6) and one with high $^{207}Pb/^{204}Pb$ (> 15.7).

The Pb isotopic compositions of sulphides and sulphosalts from shallowly east-dipping veins in the Moosehorn Range area are significantly less radiogenic than those of all recognized intrusive wallrocks in the region, and of many intrusions in the southeastern Dawson Range and east-central Alaska. The sulphides and sulphosalts are for the most part isotopically homogeneous. Note that sulphide/sulphosalt analyses that plot outside of the main cluster of vein mineral data points (denoted by black cross symbols) are from mineralization that is likely not related to the main gold-bearing vein event. Galenas from Yukon-Tanana terrane sedimentary exhalative deposits have comparable Pb isotopic compositions to the sulphides and sulphosalts in the Moosehorn Range area.

Interpretation of the Pb isotope data is not straightforward. Pb isotopic compositions for all recognized intrusions in the region do not match those of the metallic vein minerals in the Moosehorn Range (Figs. 34, 35, and 36). This suggests that little if any of the Pb in the mineralizing fluids was derived directly from the host rocks. Pb transfer between the hydrothermal fluids and wallrock was minimal, which could be explained in two ways. First, if the source reservoir for the hydrothermal fluids was nearby, the residency time of the fluids within the Moosehorn Range intrusions would have been relatively short, thus minimizing the effect of Pb exchange with the wallrock. Alternatively, regardless of fluid residency time within the wallrock, if the fluid had a Pb isotopic composition and/or concentration similar to that of the wallrock it flowed through, its composition is unlikely to have changed as a result of fluid-rock interaction (Tosdal et al., 1999).

The position of the sulphide/sulphosalt data points along the Shale curve suggests the source of the metals is older and less radiogenic than the host granodiorite. The relative homogeneity of the Pb isotopic compositions suggests that metals were derived either from a single source, or from two or more reservoirs that were well homogenized. If the latter is the case, then the hydrothermal system would have been relatively large such that the initial Pb isotopic heterogeneity in the source reservoirs was homogenized during fluid-rock interactions *distal* from the area of sulphide and sulphosalt deposition (Tosdal et al., 1999, and references therein).

The data indicate that the granodiorite in the Moosehorn Range is simply a passive host to the mineralized veins and the ultimate source of the Pb, and thus gold and other metals in the Moosehorn Range, remains to be identified. Although the Pb isotopic compositional field for galenas from Yukon-Tanana terrane sedimentary exhalative deposits overlaps with the Moosehorn Range area sulphide and sulphosalt compositions, these

stratiform deposits are probably not the source of the metals in the Longline veins. It is unlikely that hydrothermal fluids would preferentially exchange Pb with these localized deposits and then be transported and preferentially precipitated within discrete fault structures in the Moosehorn Range area. The source(s) of the gold mineralization are probably less radiogenic intrusive rocks that have not yet been recognized on surface or in drill core. An alternative possible source is the Paleozoic metamorphic rocks adjacent to the Dawson Range batholith. The overall homogeneity of the sulphide and sulphosalt lead isotopic compositions may suggest that the core of a large hydrothermal system existed outside of the main study area, and would thus warrant exploration for other larger gold occurrences in the region.

Structural Controls on Vein Formation

Regional Structural Setting

Scarcity of outcrop precludes a detailed structural interpretation of the region encompassing the Longline property. However, airborne magnetic maps and a LandSat 7 image of the area both show very prominent linear features that are presently interpreted to reflect significant fault structures. Pronounced features on the vertical gradient magnetic map are NNW-SSE magnetic lows and less prominent NE-SW magnetic lows (Shives et al., 2001). The most notable NNW-SSE-trending magnetic low shows a prominent jog immediately northwest of the main mineralized zone (Fig. 23.1). This magnetic low is possibly related to an unexposed strike-slip fault, and structures that localized gold-bearing veins on the property may have been generated from compressional or tensional stresses developed in the vicinity of the jog.

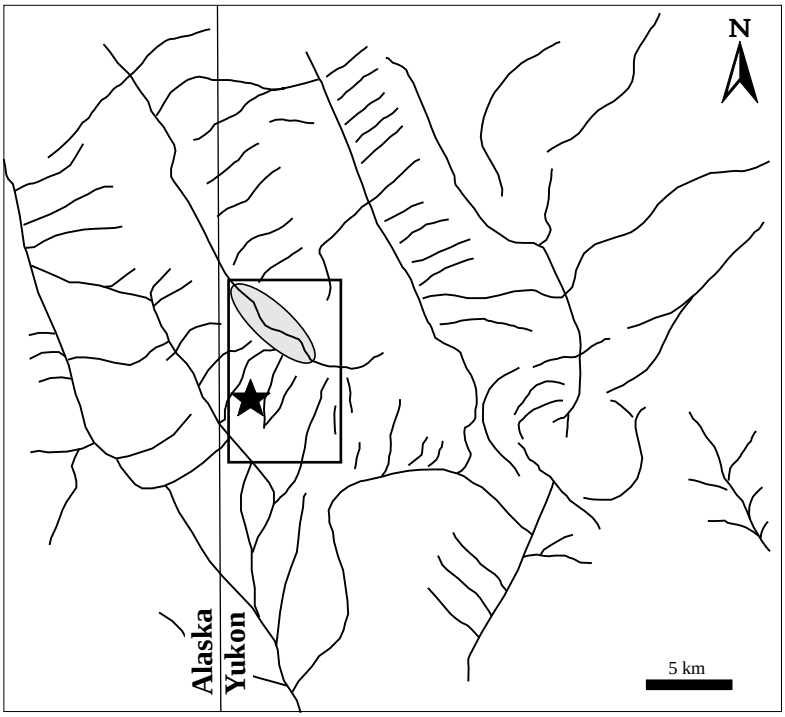

Figure 37 Lineaments in the Moosehorn Range area, traced from a satellite image of the region. The rectangle outlines the main study area and the shaded oval outlines the Moosehorn Range. The star represents the location of gold-bearing veins. Below are two possible scenarios for possible fault geometry based on the lineament orientations. Note that there are no temporal constraints on these structures, and the relationship between them is unknown. However, if the NNW-oriented lineaments are dextral strike-slip faults, the interconnecting NE-striking structures could be (A) conjugate Riedel (R') sinistral shear fractures *or* (B) sets of normal faults (after Twiss and Moores, 1992). In (A), the dextral Riedel shears (R) are essentially parallel to the mylonites near Kenyon Creek, which also exhibit dextral kinematics. Alternatively, if the NNW-oriented structures are sinistral faults, the NE-striking structures may be sinistral conjugate Riedel shears (R') or thrust faults. The NE-striking structures may be related to NE-striking sinistral and/or oblique normal faults generated as the dextral Tintina and Denali faults became active in the early Tertiary (Page et al., 1995), in which case, they would be unrelated to the formation of the Longline gold-bearing veins.

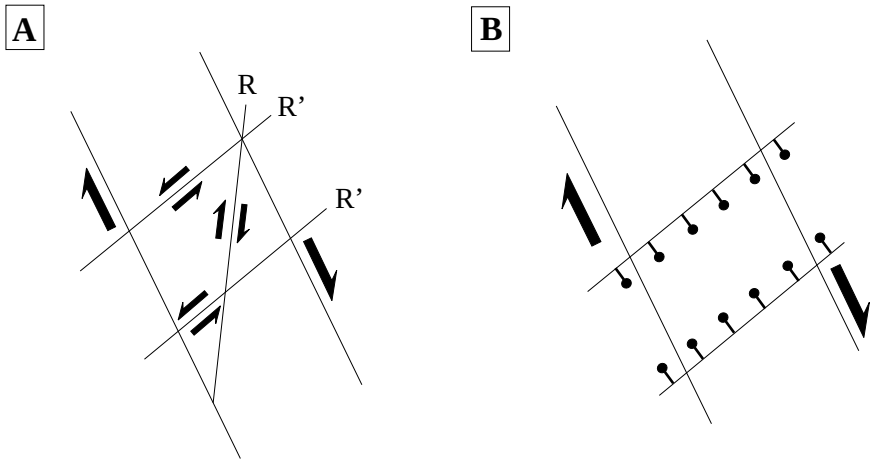

On the satellite image there are many continuous NNW-SSE-trending lineaments (>25 km long) interconnected by numerous NE-SW-trending lineaments (2-8 km long), thus creating a ladder-like geometry (Fig. 37). The temporal relationship between the regional- and local-scale structures remains unknown, but the geometry of the regional lineaments could represent a system of NNW-SSE dextral strike-slip faults accompanied by either normal faults or conjugate Riedel (R') shear fractures oriented NE-SW. In this scenario, the dextral displacement associated with NNE-SSW-oriented mylonites exposed near Kenyon Creek would represent Riedel (R) shears. Alternatively, the NNW-SSE trending faults could be sinistral, interconnected by NE-SW thrust faults. The geometry of the Moosehorn Range itself could be structurally controlled. The ridge appears sinistrally offset in an en-echelon manner (see Fig. 23.1).

The faults interpreted from the satellite image may entirely post-date the gold-bearing vein formation in the Moosehorn Range area. Regional-scale northeast sinistral and/or oblique normal faults are common in east central Alaska and probably formed during dextral displacement along the Tintina and Denali faults in the Early Tertiary (Page et al., 1995; McCoy et al., 1997; Smith et al., 1999).

Local Structural Setting

The majority of the intrusions in the Longline property are undeformed, with the exception of minor brittle jointing and offsetting, and localized development of foliation. Two generations of fabrics are present in the MRG. An early, variably developed S1 foliation is moderately to steeply southwest dipping, and may have formed during or shortly after intrusion of the MRG. Along the northwest flank of Kenyon Creek, S1 is mylonitic, and a north-northeast-striking, moderately to steeply northwest-dipping D2 mylonitic shear

zone dextrally offsets S1. Sub-horizontal stretching lineations on S2 planes indicate the movement along the fault zone was strike-slip. Quartz and feldspar exhibit microstructures indicative of ductile deformation, and, therefore, the temperature of the shear zone deformation may have reached 500˚-550˚C (Tullis, 1983; Passchier and Trouw, 1996). The greenschist-facies mineral assemblage in the rocks, however, indicates the temperature of deformation was somewhat cooler (probably around 350˚-400˚C). Kinematic indicators seen in the outcrops include deflected foliations and asymmetric σ-type and δ-type porphyroclasts. Those in thin section include C'-type shear bands, mica fish, and asymmetric σ-type and δ-type porphyroclasts (see Chapter 2). The geometry of these structures is consistent with a *dextral* sense of shear (Passchier and Trouw, 1996).

Biotite granodiorite along the crest of the northwestern portion of the Moosehorn Range is moderately foliated and boulders of strongly mylonitized biotite granodiorite occur locally. Only very limited outcrop is present within the felsenmeer in this area; hence structural measurements were very difficult to obtain. However, the foliations in this area generally strike east and southeast, and dip 45˚-70˚ south and southwest, parallel to S1.

All the dyke phases are locally foliated. The orientations of the foliations are inconsistent from one dyke to another but are generally steeply west to northwest dipping, parallel to S2. A mylonitic biotite granodiorite dyke in Swede's pit is cross cut by the V2 vein, so the dyke deformation clearly predated formation of the vein.

Ductile deformation (D1 and D2) probably predated the formation of the gold-bearing veins, which were emplaced within the brittle regime. There was some brittle reactivation along S1 and S2, as reflected in Figure 38, which shows orientations of brittle joint sets in the area. Clearly there are joints parallel to both of these fabrics, and to the gold bearing veins.

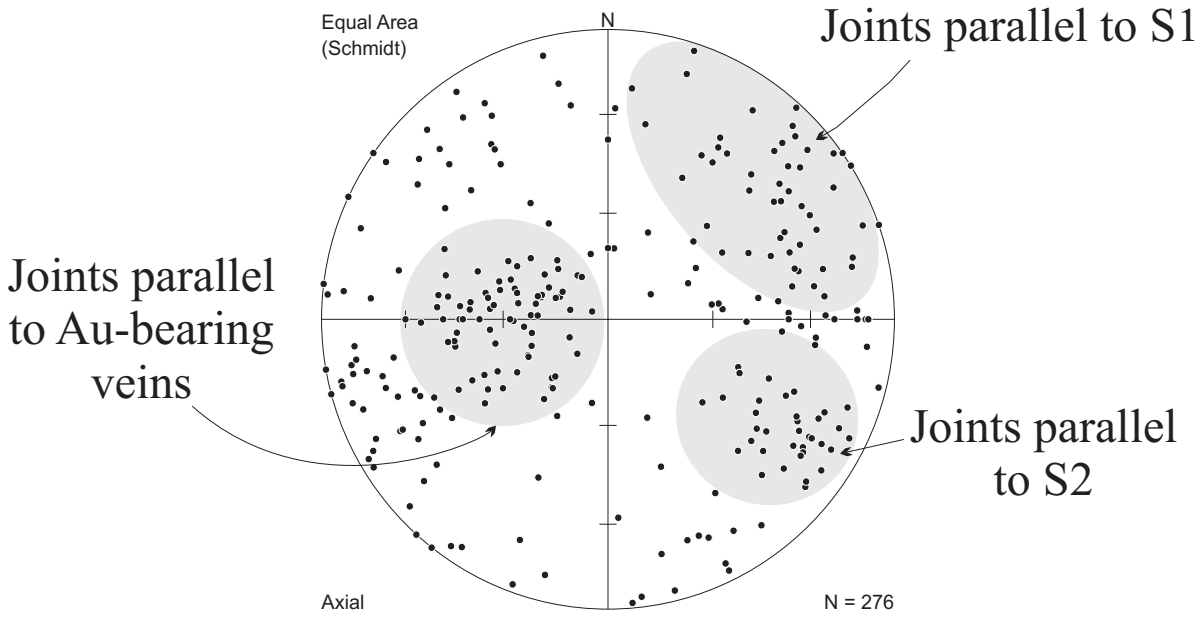

Figure 38 Stereonet showing poles to planes of all measured joints in the Moosehorn Range area. Joints parallel to S1 and S2 are probably a result of brittle reactivation along originally ductile fault planes. Joints parallel to the gold-bearing quartz veins are common throughout the area.

Shear Model for Vein Formation

Features observed in the gold-bearing veins in the Moosehorn Range area are consistent with vein formation during brittle shallow reverse fault movement accompanied by repeated episodes of dilation and infill, or cracking and sealing (e.g., Ramsay, 1980; Hodgson, 1989; Cox, 1995; Cox et al., 2001; Robert and Poulsen, 2001). Fault movement was confined to the veins and did not exploit older S1 and S2 planes of weakness. A ramp-flat geometry defined by the veins (ramps) and interconnecting oreshoots (flats) can be seen in Figure 39 below, and in trench maps in Figures 46, 47, and 52 of Appendix A. The shallowly east-dipping veins lie within the fault plane and the large lens-like oreshoots are in the orientation of dilation for a thrust system (Fig. 39, after Cox et al., 2001). Also oriented within the dilatant field are small offshoot veinlets from the main veins. These taper into the wallrock and contain vuggy and comb-textured quartz in their cores.

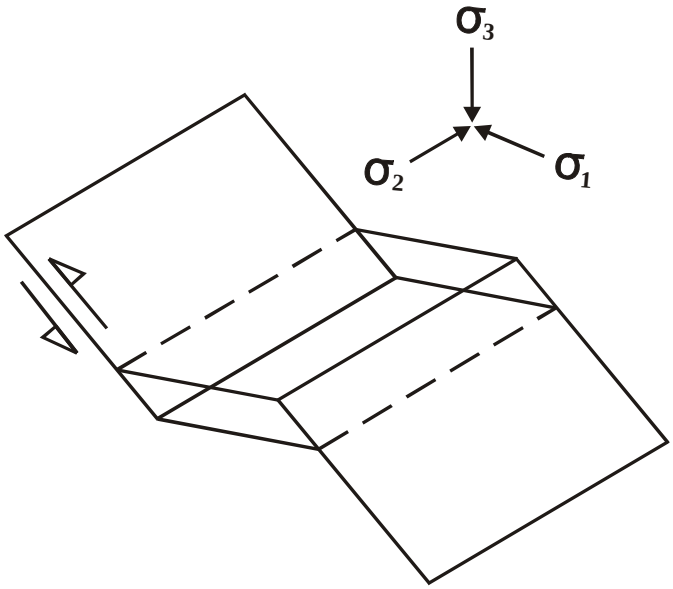

Figure 39 Geometry of a dilatant jog in a shallow thrust fault system. The long axis of the dilatant zone or oreshoot is the strike orientation of the oreshoot. After Cox et al. (2001).

Figure 25 shows the general geometry of the veins, both in cross section and parallel to strike. The ramp-flat geometry is visible in the cross-sectional view, and the representative two-dimensional finite strain ellipse for the contractional slip is shown. The dilatant oreshoots occupy the plane containing the maximum finite shortening direction, Z, and the intermediate axis Y. The maximum finite stretching direction, X, is perpendicular to this plane.

In along-strike exposures of the veins, the discontinuous pancake-like geometry of the veins is revealed. Fractures and yellow to grey quartz veinlets enveloped by narrow quartz-sericite-pyrite alteration haloes are common above, below, and parallel to the main veins (Fig. 25). Figure 40 illustrates how these fractures or fault surfaces formed fluid pathways that led to vein and oreshoot formation. These structures represent either leading edges or trailing edges of variably developed lenticular quartz veins that swell either down-dip or up-dip, respectively. As a ramp-oriented fault propagated upward through the wallrock, it locally bifurcated such that secondary flat-oriented wing fractures or fault jogs branched off and intersected with neighbouring ramp structures. The fault jogs oriented perpendicular to the maximum finite stretching direction dilated, providing a locus for influx of large volumes of hydrothermal fluids. These dilational structures hence developed into oreshoots. Dilational jogs *along* the strike of the veins are also locally developed; quartz veins along these laterally stepping structures (Fig. 25) are only up to 3-4 cm thick and are not classified as oreshoots. Quartz veins are locally present along contractional jogs, but are volumetrically negligible.

Banded textures within the veins likely formed during dilation and the crack-seal process. Vein margin-parallel zoning of sulphides and sulphosalts suggests that metal concentrations in the fluids fluctuated throughout the veining event. Wallrock lenses and

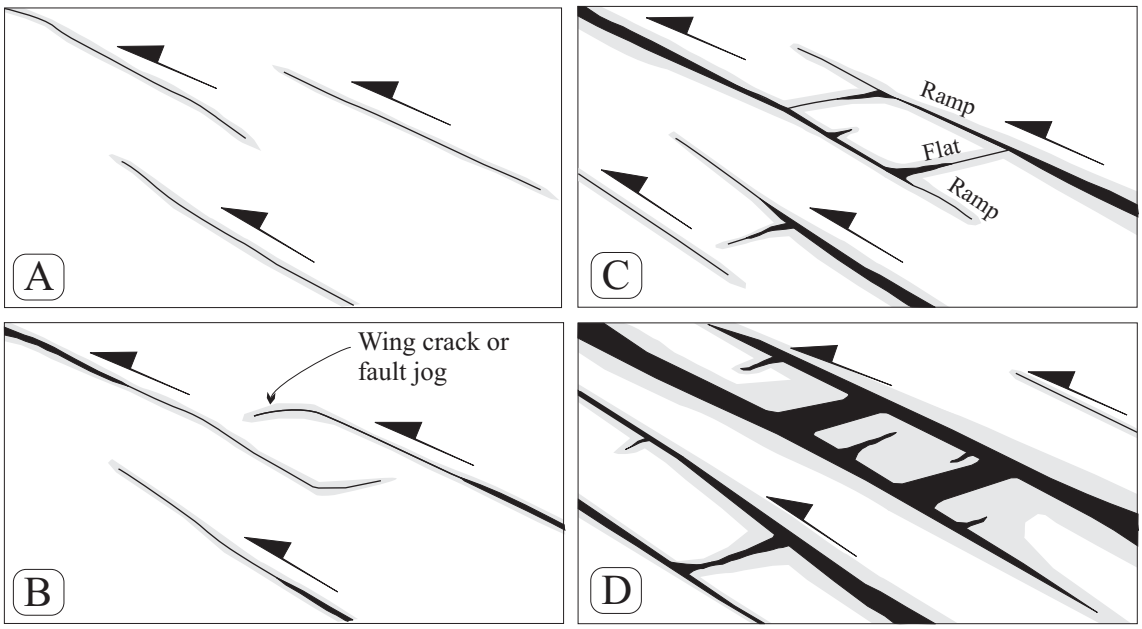

Figure 40 Series of schematic sketches illustrating how the Longline veins formed. **A.** Regional contraction generates thin sheeted brittle reverse faults along which small amounts of fluid are transported. No veins are formed at this stage but thin alteration envelopes about 2-3 cm wide form around the faults. **B.** Fluid flow increases as dilation occurs along fault planes and thin discontinuous veinlets start to develop. The fault planes propagate further into the wallrock and wing cracks or jogs begin form, splaying towards neighbouring fault planes. Together, the veins and the fault jogs form a ramp-flat geometry. **C.** Dilation and fault propagation continues and veins become thicker. New fault planes develop in the wallrock and begin to dilate. Dilation along fault jogs forms extension veinlets that taper into the wallrock or connect with neighbouring fault planes. Crack-seal and vuggy textures develop in the veins and extension veinlets during episodic dilation and fluid infill. Alteration envelopes widen. **D.** Veins become still thicker and more extension veinlets form. Oreshoots form along the sub-horizontal dilational fault jogs. More fault surfaces form and with continued regional contraction additional extension veinlets and oreshoots form.

slivers oriented parallel to the planes of dilatant oreshoots are also consistent with episodic crack-seal activity having occurred (Ramsay, 1980; Cox et al., 2001).

Measured vein orientations are presented in the stereoplot in Figure 41. The angle between the ramp-oriented veins and flat-oriented oreshoots and veinlets is approximately 50˚. The intersection line of these two planes defines the long axis of the lens-like oreshoots, and is sub-horizontally oriented NNW-SSE. Slip direction is perpendicular to that line of intersection, in the plane of the main ramp-oriented veins. Results of the equal-area stereonet analysis indicate the thrust direction was towards 240°-260°, or up-dip towards WSW. This is consistent with the approximately E-W oriented slickensides observed on vein walls and on sheared wallrock slivers inside the veins.

The SC-1 vein in the eastern portion of the property is the only exposed vein that dips about 45° to the west. Otherwise, it is identical to the other veins. There are four different possible explanations for its deviant orientation. The first is that it is completely unrelated to the other veins but this is unlikely based on textural and compositional similarities. SC-1 could be interpreted as an extension vein in a flat orientation, but this is also unlikely because extensive vuggy or comb-textured quartz is not present in the vein. The most likely scenarios are either that the vein is a conjugate partner of the shallowly east-dipping veins, or that SC-1 is within a rotated block that shifted during post-veining deformation. Lack of exposure along strike of SC-1 precludes a definite explanation for the vein orientation.

Regional Structural Context for Shallow Brittle Reverse Faulting

Although the gold-bearing veins locally crosscut granodiorite and quartz diorite dykes containing foliations parallel to S2, the mylonite formation northwest of Kenyon

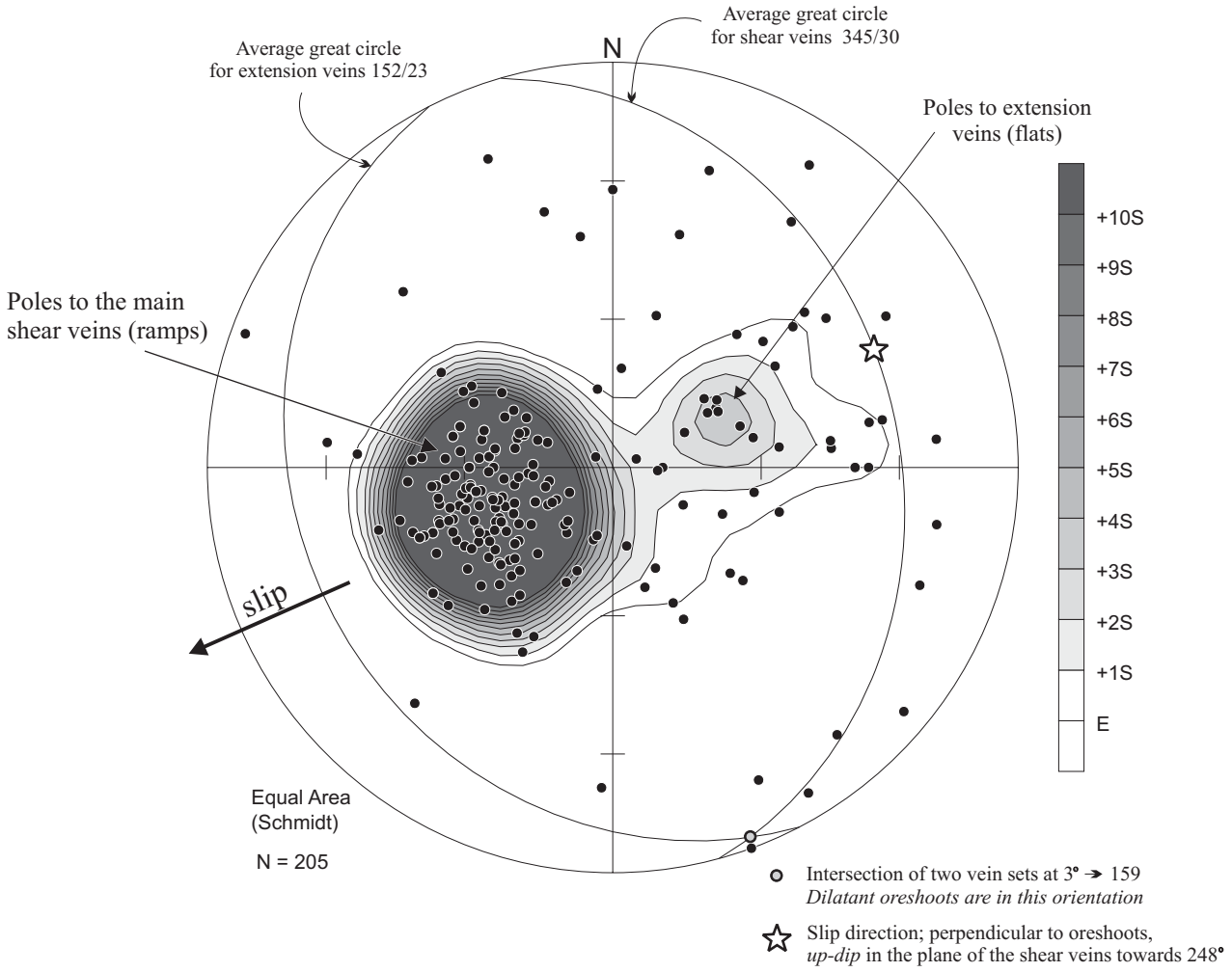

Figure 41 Stereonet summarizing the orientations of veins measured in trench exposures. The angle between the ramp-oriented shear veins and the flat-oriented oreshoots is approximately 50°. The long axis of the oreshoots is defined by the line of intersection between the ramps and flats, which is sub-horizontal and trends NNW-SSE. Slip direction is perpendicular to the long axis of the oreshoots, up-dip along the shear veins towards the WSW.

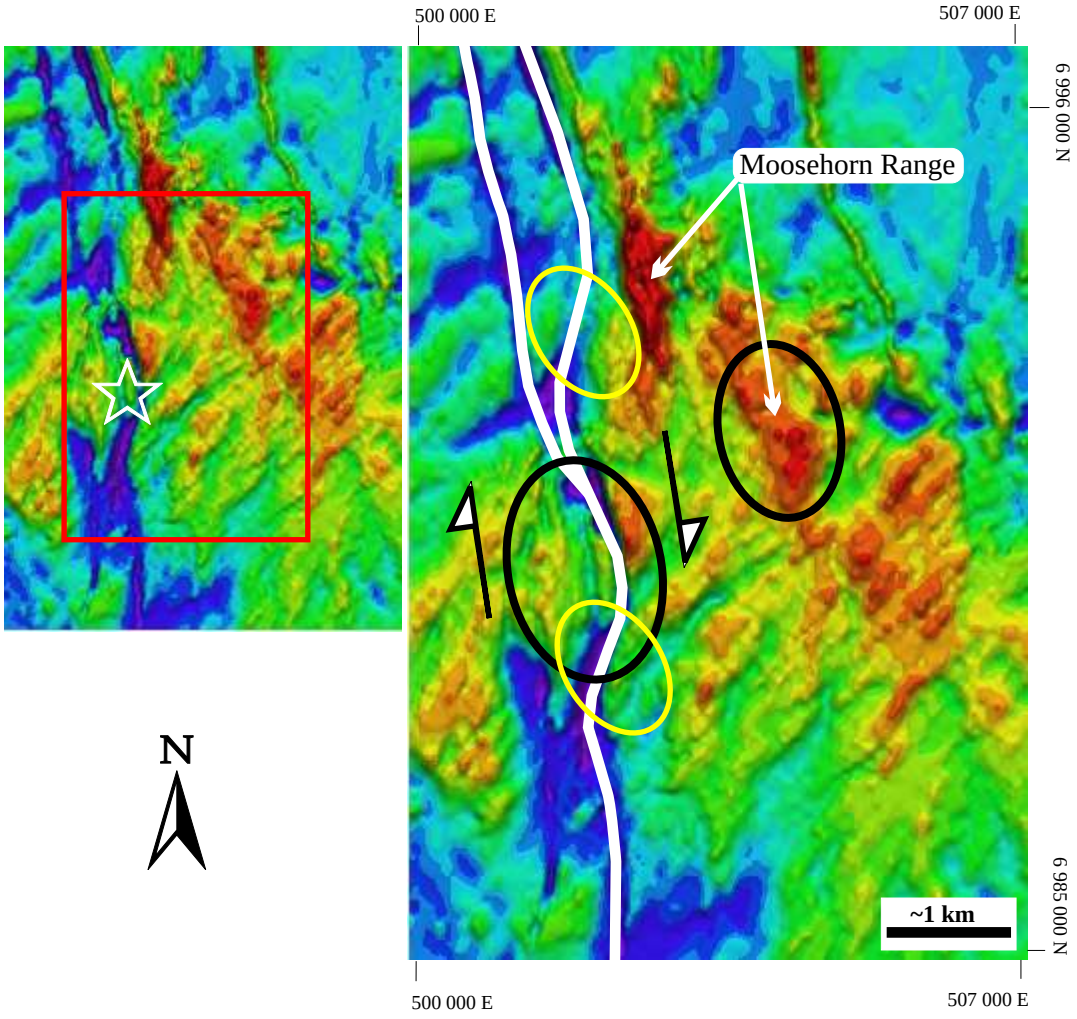

Figure 42 Aeromagnetic map of the Moosehorn Range area. Above, the red rectangle outlines the main area of mineralization at Longline. The star is the approximate location of Swede's Pit (V2 vein). The prominent NNW-trending magnetic high (red) reflects the topographic relief of the Moosehorn Range. Blue and green colours denote areas with low and moderate magnetic susceptibilities, respectively. At right: the white lines outline prominent linear magnetic lows that may represent a NNW-striking dextral strike-slip fault system. The shallowly ENE-dipping gold-bearing veins are located within areas denoted by the black ovals. The V1, V2, and V3 veins are located within the leftmost black oval, which is in the vicinity of the jog in the NNW-striking fault. Contraction would have been localized here whereas extension would have been localized in the areas marked with yellow ovals. Where the ovals overlap, both contraction and extension may have taken place simultaneously. Veins associated with contemporaneous normal faults may be present in the extensional environments but they were not recognized in the field. (Map is adapted from Sherlock, 1998)

Creek may have been contemporaneous with brittle formation of the gold-bearing veins. Biotite from the D2 shear zone in this area gave an $^{40}Ar/^{39}Ar$ age of 93.4 ± 0.9 Ma and alteration muscovite adjacent to the veins yielded almost exactly the same $^{40}Ar/^{39}Ar$ age. If the linear NNW-SSE-trending magnetic low represents a dextral strike-slip fault, the stresses generated in the vicinity of the "z-shaped" fault jog during dextral strike-slip displacement could conceivably have generated the shallowly east-northeast-dipping brittle contractional faults along which the gold-bearing veins formed (Fig. 42). The NNE-striking mylonites near Kenyon Creek (S2) may have formed at this time along dextral Riedel shears (R).

Dextral north-northwest-oriented strike-slip faults have not been widely recognized in west-central Yukon Territory but Morin (1977) documented a 10m-wide approximately north-south trending mylonite zone within the Seven Mile pluton about 6 km southeast of the Moosehorn Range (Fig. 22). This fault trend may also be reflected by the linear NNW-SSE orientation of Claymore Creek. Regional NNW-SSE dextral strike-slip faults and associated along-strike fault jogs may therefore be important guides to other mineralized NNW-striking, shallowly ENE-dipping brittle reverse fault structures.

Global Analogies

Most intrusion-related gold deposits, such as those associated with the Tombstone Plutonic Suite in the Yukon, and gold deposits associated with Archean granite-greenstone belts (e.g. Abitibi Greenstone Belt in Ontario/Quebec), consist of steeply dipping quartz vein sheets. The Longline gold occurrence is distinguished by its shallowly dipping sheets of quartz veins, which are also characteristic of deposits elsewhere in the world. These include the Pogo deposit in east-central Alaska, the Charters Towers goldfields in

Queensland, Australia, quartz veins in the Parcoy mining district of the Pataz region of Peru, the La Choya deposit in northwest Sonora, Mexico, and the mineralization associated with the Hyde Macraes shear zone in east Otago, New Zealand.

Pogo Deposit – East-Central Alaska

The intrusion-related Pogo deposit, located about 145 km southeast of Fairbanks, boasts a reserve of 9.98 million tons of ore at an average grade of 0.52 oz/t for a total of 5.2 million contained ounces (Smith et al., 1999). Gold mineralization is concentrated within the Liese zone, which consists of at least three shallowly-dipping tabular quartz veins emplaced into amphibolite-facies gneiss (Smith et al., 1999; Smith, 2000). The structural context in which the veins formed is uncertain.

Similar to the Longline veins, the Liese zone veins are lens-shaped, with milky white massive quartz, crack-seal textures, visible gold, and typically contain less than 5% ore minerals (Smith et al., 1999). Gold mineralization at both Pogo and Longline is generally associated with elevated As-Sb-Bi values. Both systems also exhibit extension veinlets that connect the main vein units (Smith et al., 1999).

Otherwise, Pogo and Longline differ in vein mineralogy, temperature of vein formation, vein evolution, alteration, and quartz textures. Pogo veins contain pyrrhotite, löellingite, chalcopyrite, pyrite, arsenopyrite, bismuthinite, native bismuth, and locally biotite (Smith et al., 1999). Vuggy quartz textures and carbonate are not found in the various vein varieties, but brecciated quartz and sugary quartz textures are common. Temperatures of vein formation, determined from fluid inclusion studies, range between 310 ºC and over 570 ºC (Smith et al., 1999), which are significantly higher than those for the Longline veins. These temperatures are consistent with veins formed under ductile conditions.

Charters Towers Goldfield – Northeastern Australia

The Charters Towers Goldfield is an intrusive-hosted system located in northeastern Queensland, Australia. As Australia's richest gold field with a historical average grade of 34 g/t Au, 6.6 million ounces of Au have been recovered over 45 years of production. Charters Towers Gold Mines Ltd. (2001) has reported a current resource of 1 million ounces at a grade of 9.4 g/t.

Mineralization in this area is remarkably similar to that at Longline. The gold-bearing quartz veins are found most commonly within shallowly dipping reverse faults parallel to wallrock mylonite fabrics. Ellipsoidal oreshoots are formed in dilatant "flats" that locally connect the main vein structures (Peters, 1990; Peters, 1993). Rafts and slivers of wallrock material are caught up in the veins, which exhibit buck, comb, ribbon, and brecciated quartz textures (Peters and Golding, 1989; Peters 1993). Vuggy textures are not characteristic of the Charters Towers veins but internal metre-scale cuspate geometries in the quartz and planar zoning of sulphides in the veins are indicative of repeated dilation and infill (Peters, 1990; Peters, 1993). Aggregates and irregular bands of pyrite, galena, sphalerite, tetrahedrite, arsenopyrite, and chalcopyrite comprise up to 10% of the vein volume. Gold occurs as blebs, stringers, veinlets, or open space fill associated with calcite (Peters and Golding, 1989). Gangue minerals include quartz, calcite, ankerite, and locally muscovite (Peters, 1990).

Fluid inclusions in the quartz are generally single-phase, water-rich, and have low to moderate salinities. Alteration envelopes adjacent to the veins, the widths of which are not proportional to the vein thicknesses, consist of an inner muscovite-rich zone and an outer montmorillonite-illite-chlorite-epidote zone (Peters and Golding, 1989).

The most significant difference between Longline and Charters Towers mineralization is that the structural controls at Charters Towers are pre-existing wallrock fabrics and geologic contacts whereas at Longline the veins crosscut geologic contacts and dominantly homogeneous plutons.

Parcoy Mining District, Pataz, Peru

The Parcoy mining district is located in the Pataz province of the Department of La Libertad in the Eastern Cordillera of Peru. Basement rocks in the region consist predominantly of Proterozoic metapelites and metavolcanic rocks of the Marañón complex (MacFarlane et al., 1999). The Carboniferous granodioritic Pataz batholith, which intrudes the Marañón complex, is host to brittle reverse shear zones along which gold-bearing veins formed.

Vein geometry and formation in the Pataz region is closely analogous to that of the Longline vein system. Compressional tectonics generated the shallowly (10º to 55º) northeast-dipping brittle reverse fault structures occupied by the gold-bearing veins (Schreiber et al., 1990). The gold-bearing veins are sheeted, lenticular, shallow en echelon veins connected by dilational jogs along strike and along the dip of the veins, formed during sinistral oblique thrust slip (MacFarlane et al., 1999). Highest gold grades are associated with the dilational structures.

Visible gold is rare in the veins; gold grades vary between 1 and 100 ppm, with an average of about 10 ppm Au (Schreiber et al., 1990; MacFarlane et al., 1999). Other minerals present in the veins include pyrite, sphalerite, arsenopyrite, and lesser galena and chalcopyrite. Alteration envelopes adjacent to the veins contain predominantly sericite, pyrite, quartz, and up to 0.5 to 1.5 ppm Au (MacFarlane et al., 1999).

Lead isotopic studies have shown that the predominant source of metallic minerals in the auriferous veins was the Pataz batholith (MacFarlane et al., 1999), despite the fact that the veins formed about 43 million years after intrusion of the host granodiorite. Lead in the hydrothermal fluids may have been derived from later intrusive phases of the Pataz batholith but became isotopically equilibrated with the Carboniferous granodioritic wallrocks (MacFarlane et al., 1999).

Hyde-Macraes Shear Zone Mineralization, Otago Schist, New Zealand

Gold mineralization in east Otago, New Zealand is hosted within the low angle Hyde-Macraes shear zone. Brittle-ductile thrust faulting in this case occurred within graphitic pelitic schist, but the veins were formed in the same manner as the intrusion-hosted shear vein system at Longline. The Hyde-Macraes mineralization comprises a gold reserve of 8.2 million tons at a grade of 2.2 g/t (Teagle et al., 1990).

Teagle et al. (1990) summarized that the gold-bearing veins formed mainly in dilational jogs or localized extensional zones on flatter parts of intrashear thrust systems. These mineralized ramps are elongate perpendicular to the thrust direction. Unlike the massive granodiorite host rocks at Longline, the host rock Otago schist at Hyde-Macraes is not isotropic; compositional layering and different layer competencies are a strong control on the thrust plane geometries. Vein geometries at Hyde-Macraes, therefore, are more irregular than the more consistently planar or lens-shaped veins in the Moosehorn Range.

La Choya Au Deposit, Northwest Sonora, Mexico

La Choya, located 190 km southwest of Tucson, Arizona, is a gold deposit with an average grade of 0.04 oz/t and a reserve of 300 000 ounces Au (Durgin and Teran, 1996).

Low angle faults and related folding associated with deformation within the Mojave-Sonora Megashear are strong controls on the La Choya vein geometries.

Exploration at La Choya is complicated by lack of exposure, and complex vein and alteration paragenesis. Durgin and Teran (1996) describe the veins and gold mineralization as confined within a complex imbricate thrust ramp duplex. The gold, which is associated with anomalous amounts of Pb, Bi, and Mo, occurs predominantly in the flat faults within a porphyritic granitic host rock. There are at least five different types of quartz veins distinguished on the basis of quartz textures, vein mineralogy, and attitude. Although this style of veining differs from Moosehorn Range mineralization, alteration is similar to that at Longline and includes an inner sericite-rich zone grading to chlorite-(Fe)-carbonate away from the veins. Hematite alteration is also pervasive throughout the ore body.

These global examples earmark the fact that prospective and economic gold-bearing sheeted vein systems are not necessarily restricted within steeply dipping structures. They furthermore emphasize the economic potential for the analogous veins of the Moosehorn Range area. Recognition of ramp-flat geometries is undeniably the key for locating oreshoots in these contractional fault systems.

Summary and Implications for Exploration

Since the late 1990's, several districts within the Tintina Gold Belt have become attractive targets of exploration for mid-Cretaceous intrusion-related gold deposits. Gold mineralization at the Longline property, located within the Tintina Gold Belt, is the only known intrusion-hosted shallowly dipping vein system in the northern Cordillera, other than the Pogo deposit in east-central Alaska.

The hornblende-biotite Moosehorn Range Granodiorite wallrock is generally massive but is locally foliated. S1 is moderately to steeply southwest dipping, variably developed throughout the study area, and probably formed during to shortly after intrusion of the granodiorite, prior to the formation of the gold-bearing veins. S2 is moderately to steeply northwest dipping and dextrally offsets S1. A $^{40}Ar/^{39}Ar$ age for biotite within a D2 shear zone records a minimum age of 93.4 ± 0.9 Ma for the deformation. This deformation may have been partly contemporaneous with the formation of the gold-bearing veins. Many dykes in the MRG are oriented and locally foliated parallel to this fabric.

Between approximately 92 and 93 Ma, an east-northeast-west-southwest-directed contractional event of uncertain regional extent generated the shallowly east-northeast dipping fault structures along which the gold-bearing veins formed. Brittle shear slip along the planes of the veins was up-dip towards about 250º. Somewhat discontinuous elongate lens-shaped oreshoots formed at dilational jogs along the fault planes, creating ramp-flat geometries whereby the oreshoots occupy the flat orientations. The long axis of the oreshoots is perpendicular to the slip direction, plunging about 3º towards 159º. Lateral ramp structures locally connect the discontinuous lens-shaped veins but dilation along these structures was relatively minimal.

Zoning of sulphide material and the incorporation of sheared and tourmalinized vein margin-parallel wallrock slivers within the veins indicates that the veins formed as a result of repeated episodes of fracture dilation and fluid infill. Bull, vuggy, and comb-textures in quartz and locally calcite are common in the veins, particularly within the dilational oreshoots.

Fluids that formed the gold-bearing quartz ± carbonate veins in the Moosehorn Range area were aqueous and aqueous-carbonic of the system H_2O-CO_2-CH_4-NaCl ± N_2,

with moderate salinities (approximately 10 wt % NaCl equivalent). The coexistence of both CO_2-rich and H_2O-rich aqueous-carbonic inclusions is indicative of H_2O-CO_2 fluid immiscibility, and thus no pressure correction for fluid trapping temperatures was required. Homogenization temperatures range from 170˚ to 340˚C, but most values fall between 220˚ and 300˚C. Trapping pressures are between 1.3 and 1.9 kbar, corresponding to depths of 5-7 km, assuming near-lithostatic fluid pressures. Fluid immiscibility and rapid pressure drops in episodically dilatant zones were likely mechanisms for deposition of the sulphides and the gold.

Implications for Exploration

Exploration programs carried out in western Yukon and the Alaska interior are hindered by a lack of outcrop. Finding a gold occurrence in the vicinity of the Moosehorn Range is also complicated by the fact that the source of the metals at Longline remains uncertain and hence no particular mineralizing rock unit(s) can be identified. The occurrence of similar vein systems will not necessarily be spatially related to mid-Cretaceous Dawson Range batholith intrusions.

Additional Pb isotopic studies may reveal that the Paleozoic schists and gneisses adjacent to the Dawson Range batholith were sources of the metals in the Moosehorn Range veins. Existing Pb isotope data for the vein minerals suggest there was either a single metal source or there were more than one source, the isotopic compositions of which mixed and were eventually homogenized. In the latter case, the hydrothermal system required to homogenize the Pb isotopic signatures would have to have been fairly large (Bierlein and McNaughton, 1998). A more significant and possibly larger gold occurrence could, therefore, exist outside of the immediate Moosehorn Range area.

Elevated Au, As, Sb, and Bi values in soil samples and provenance studies of placer gold may provide additional information on possible vein locations. Mineralization at Longline is located near a distinct jog in a linear N-S magnetic low on vertical gradient magnetic maps. If this feature represents a dextral strike-slip fault, then compressional or tensional forces in the vicinity of the jog during either ductile or brittle fault movement may have localized the mineralizing fluids along associated flat-lying thrust structures. Because flat-lying structures are not visible on magnetic maps, regional exploration should focus on other locales where similar offsets may be related to analogous shallow thrust systems.

Mid-Cretaceous deformation in west-central Yukon likely generated shallowly east-dipping thrust structures and related vein systems in areas other than the Moosehorn Range. Expected orientations of associated oreshoots in the region would be subhorizontal with long axes trending NNW-SSE. In general, effective predictions of dilational oreshoot locations and orientations can be made from interpretations of the relationship between ramp-flat vein geometries and slip directions.

References

Abraham, A., Francis, D., and Polvé, M., 2001, Recent alkaline basalts as probes of the lithospheric mantle roots of the Northern Canadian Cordillera: Chemical Geology, v. 175, p. 361-386.

Aleinikoff, J.N., Farmer, G.L., Rye, R.O., and Nokleberg, W.J., 2000, Isotopic evidence for the sources of Cretaceous and Tertiary granitic rocks, east-central Alaska; implications for the tectonic evolution of the Yukon-Tanana terrane: Canadian Journal of Earth Sciences, v. 37, p. 945-956.

Appel, V., 1998, Geological, geochronological, and Pb isotopic constraints on the age and origin of the Mount Nansen epithermal Au-Ag vein deposit, eastern Dawson Range, Yukon: unpublished Bachelor's thesis, University of British Columbia, 38 p.

Bakker, R.J., 1999, Adaptation of the Bowers and Helgeson (1983) equation of state to the H_2O-CO_2-CH_4-N_2-NaCl system: Chemical Geology, v. 154, p. 225-236.

Bierlein, F.P., and McNaughton, N.J., 1998, Pb isotope fingerprinting of mesothermal gold deposits from central Victoria, Australia: Implications for ore genesis: Mineralium Deposita, v. 33, p. 633-638.

Borisenko, A.S., 1977, Study of salt composition and solutions of gas-liquid inclusions in minerals by the cryometric method: Soviet Geology and Geophysics, v. 18, p. 11-18.

Brown, P.E., and Lamb, W.M., 1989, P-V-T properties of fluids in the system $H_2O \pm CO_2 \pm$ NaCl: New graphical presentations and implications for fluid inclusion studies: Geochimica et Cosmochimica Acta, v. 53, p. 1209-1221.

Charter Towers Gold Mines Ltd. Web Site, 2001, www.mycommunity.com.au/CTGold.nsf

Cox, S.F., 1995, Faulting processes at high fluid pressures: An examples of fault valve behavior from the Wattle Gully Fault, Victoria, Australia: Journal of Geophysical Research, v. 100, p. 12 841-12 859.

Cox, S.F., Knackstedt, M.A., and Braun, J., 2001, Principles of structural control on permeability and fluid flow in hydrothermal systems: Reviews in Economic Geology, v. 14, p. 1-24.

Crawford, M.L., 1981a, Phase equilibria in aqueous fluid inclusions, *in* Hollister, L.S., and Crawford, M.L., eds., Short course in fluid inclusions: Applications to petrology: Mineralogical Association of Canada, v. 6, p. 75-100.

Doe, B.R., and Zartman, R.E., 1979, Plumbotectonics I, The Phanerozoic, *in* Branes, H.L., ed., Geochemistry of hydrothermal ore deposits. 2nd ed.: New York, Wiley Interscience, p. 22-70.

Dumala, M.R., and Mortensen, J.K., 2002, Composition of placer and lode gold as an exploration tool in the Stewart River map area, western Yukon, *in* Emond, D.S., Weston, L.S., and Lewis, L.L., eds., Yukon Exploration and Geology 2001, Exploration and Geological Services Division, Yukon Region, Indian and Northern Affairs Canada, p. 87-102.

Durgin, D.C., and Teran, P.I., 1996, La Choya Au deposit, NW Sonora, Mexico, *in* Coyner, A.R., and Fahey, P.L., eds., Geology and ore deposits of the American Cordillera: Geological Society of Nevada Symposium Proceedings, Reno/Sparks, Nevada, April 1995, p. 1369-1373.

Francis, D., Abraham, A., and Polvé, M., 1999, Volcanic probes of the craton's edge beneath the northern Canadian Cordillera, *in* Cook, F., and Erdmer, P., compilers, Slave-Northern Cordillera Lithospheric Evolution (SNORCLE) Transect and Cordilleran tectonics workshop meeting (March 5-7), University of Calgary, Lithoprobe report No. 69, p. 142-145.

Godwin, C.I., and Sinclair, A.J., 1982, Average lead isotope growth curves for shale-hosted zinc-lead deposits, Canadian Cordillera: Economic Geology, v. 77, p. 208-211.

Goldfarb, R.J., Miller, L.D., Leach, D.L., and Snee, L.W., 1997, Gold deposits in metamorphic rocks of Alaska: Economic Geology Monograph 9, p. 151-190.

Greig, J.A., 1975, Geological, geochemical and drilling report on the LORI claim group Yukon: 1975 Yukon Assessment Report, Whitehorse Mining District.

Hart, C.J.R., and Langdon, M., 1998, Geology and mineral deposits of the Mount Nansen camp, Yukon, *in* Roots, C.F., and Emond, D.S., eds., Yukon Exploration and Geology 1997, Exploration and Geological Services Division, Yukon, Indian and Northern Affairs Canada, p. 129-138.

Hartley, G.S., and Almberg, G.A., 1994, Geo-chemical investigation of the SEE 1-6 and SAY 1-3 claims, and percussion drilling of the WOMP 1-20 claims: 1994 Yukon Assessment Report, Whitehorse Mining District.

Hedenquist, J.W., Izawa, E., Arribas, A., and White, N.C., 1996, Epithermal gold deposits: Styles, characteristics, and exploration: Resource Geology Special Publication Number 1, The Society of Resource Geology poster.

Hodgson, C.J., 1989, The structure of shear-related, vein-type gold deposits: A review: Ore Geology Reviews, v. 4, p. 231-273.

Jia, Y., Li, X., and Kerrich, R., 2000, A fluid inclusion study of Au-bearing quartz vein systems in the Central and North Deborah deposits of the Bendigo Gold Field, central Victoria, Australia: Economic Geology, v. 95, p. 467-494.

Johnston, S.T., Wynne, P.J., Francis, D., Hart, C.J.R., Enkin, R.J., Engebretson, D.C., 1996, Yellowstone in Yukon; the Late Cretaceous Carmacks Group: Geology, v. 24, p. 997-1000.

Lange, I.M., Nokleberg, W.J., Newkirk, S.R., Aleinikoff, J.N., Church, S.E., and Krouse, H.R., 1993, Devonian volcanogenic massive sulfide deposits and occurrences, southern Yukon-Tanana terrane, eastern Alaska Range, Alaska: Economic Geology, v. 88, p. 344-376.

MacFarlane, A.W., Tosdal, R.M., Vidal, C.E., and Paredes, J., 1999, Geologic and isotopic constraints on the age and origin of auriferous quartz veins in the Parcoy mining district, Pataz, Peru, *in* Skinner, B.J., ed., Geology and ore deposits of the central Andes, Society of Economic Geologists Special Publication No. 7, p. 267-279.

McCandless, T.E., Ruiz, J., and Campbell, A.R., 1993, Rhenium behavior in molybdenite in hypogene and near-surface environments: Implications for Re-Os geochronometry: Geochimica et Cosmochimica Acta, v. 57, p. 889-905.

McCoy, D., Newberry, R.J., Layer, P., DiMarchi, J.J., Bakke, A., Masterman, J.S., and Minehane, D.L., 1997, Plutonic-related gold deposits of interior Alaska, *in* Goldfarb, R.J. and Miller, L.D., eds., Mineral deposits of Alaska, Economic Geology Monograph 9, p. 191-241.

McCuaig, C.T., and Kerrich, R., 1998, P-T-t-deformation–fluid characteristics of lode gold deposits: Evidence from alteration systematics: Ore Geology Reviews, v. 12, p. 381-435.

McDougall, I., and Harrison, T.M., 1999, Geochronology and thermochronology by the $^{40}Ar/^{39}Ar$ method, Oxford University Press, New York, 269 p.

Morin, J.A., 1977, Geology, lode and placer gold mineralization of the Moosehorn Range, 115 N 2: Department of Indian Affairs and Northern Development Mineral Industry Report 1976, EGS 1977-1, p. 33-54.

Mortensen, J.K., 1992, Pre-mid-Mesozoic tectonic evolution of the Yukon-Tanana terrane, Yukon and Alaska: Tectonics, v. 11, p. 836-853.

Mortensen, J.K., 1994, Nd, Sr and Pb isotopic constraints on mechanism of crustal growth in the Yukon-Tanana terrane in Yukon Territory, Canada, and eastern Alaska, U.S.A.: Abstracts of the Eighth International Conference on Geochronology, Cosmochronology and Isotope Geology, Berkeley, California, U.S.A., June 5-11, 1994, U.S. Geological Survey Circular 1107, p. 227

Mortensen, J.K., Hart, C.J.R., Murphy, D.C., and Heffernan, S., 2000, Temporal evolution of Early and Mid-Cretaceous magmatism in the Tintina Gold Belt, *in* The Tintina Gold Belt: Concepts, exploration, and discoveries, British Columbia and Yukon Chamber of Mines Cordilleran Roundup Special Volume 2, Vancouver, British Columbia, p. 49-57.

Newberry, R.J., Layer, P.W., Burleigh, R.E., and Solie, D.N, 1998b, New $^{40}Ar/^{39}Ar$ dates for intrusions and mineral prospects in the eastern Yukon-Tanana terrane, Alaska – regional patterns and significance, *in* Gray, J.E. and Riehle, J.R., eds., Geologic studies in Alaska by the U.S. Geological Survey, 1996: U.S. Geological Survey Bulletin, p. 131-159.

Page, R.A., Plafker, G., and Pulpan, H., 1995, Block rotation in east-central Alaska: A framework for evaluating earthquake potential?: Geology, v. 23, p. 629-632.

Passchier, C.W., and Trouw, R.A.J., 1996, Microtectonics, Springer-Verlag, New York, 289 p.

Peters, S.G., 1990, Lode controls of the Charters Towers goldfield, northeastern Queensland: Proceedings of the Australasian Institute of Mining and Metallurgy, v. 2, p. 51-60.

Peters, S.G., 1993, Nomenclature, concepts and classification of oreshoots in vein deposits: Ore Geology Reviews, v. 8, p. 3-22.

Peters, S.G., and Golding, S.D., 1989, Geologic, fluid inclusion, and stable isotope studies of granitoid-hosted gold-bearing quartz veins, Charters Towers, northeastern Australia: Economic Geology Monograph 6, p. 252-265.

Ramboz, C., Pichavant, M., and Weisbrod, A., Fluid immiscibility in natural processes: Use and abuse of fluid inclusion data: II. Interpretation of fluid inclusion data in terms of immiscibility, *in* Kreulen, R., and Touret, J., eds., Current research of fluid inclusions: Chemical Geology, v. 37, p. 29-48.

Ramsay, J.G., 1980, The crack-seal mechanism of rock deformation: Nature, v. 284, p. 135-139.

Ritcey, D., Sears, S., and Conroy, P., and Gorton, R., 2000, Exploration at the Longline Gold Project, Moosehorn Range, Yukon Territory, *in* The Tintina Gold Belt: Concepts, exploration, and discoveries, Cordilleran Roundup Special Volume 2: British Columbia and Yukon Chamber of Mines, p. 173-180.

Robert, F., and Poulsen, K.H., 2001, Vein formation and deformation in greenstone gold deposits: Reviews in Economic Geology, v. 14, p. 111-155.

Roedder, E., 1984, Fluid inclusions: Reviews in Mineralogy, v. 12, 644 p.

Sears, S., Ritcey, D., and Conroy, P., 2000, Summary of geological field work – 1999; Prospecting, geochemical, geophysical, trenching, and drilling report; Technical report for the Longline Project, Moosehorn Range, Yukon Territory: 2000 Assessment Report, Whitehorse Mining District.

Sears, S., 1999, Summary of geological field work – 1998; A geological, geochemical, and geophysical report for the Longline Project, Moosehorn Range, Yukon Territory, 1999 Assessment Report, Whitehorse Mining District.

Schreiber, D.W., Fontbonté, L., and Lochmann, D., 1990, Geologic setting, paragenesis, and physicochemistry of gold quartz veins hosted by plutonic rocks in the Pataz region: Economic Geology, v. 85, p. 1328-1347.

Selby, D., Creaser, R.A., and Nesbitt, B.E., 1999, Major and trace element compositions and Sr-Nd-Pb systematics of crystalline rocks from the Dawson Range, Yukon, Canada: Canadian Journal of Earth Sciences, v. 36, p. 1463-1481.

Shepherd, T.J., Rankin, A.H., and Alderton, D.H.M., 1985, A practical guide to fluid inclusion studies: Blackie, Chapman and Hall, New York, 240 p.

Sherlock, R. 1998. Geology and prospectivity analysis of the Longline gold project, Yukon, Canada. Internal report prepared by Steffen Robertson & Kirsten Consulting Engineers and Scientists for Barramundi Gold Ltd., 17 p.

Shives, R.B.K., Carson, J.M., Ford, K.L., Holman, P.B., Grant, J.A., Gordey, S., and Abbott, G., 2001, Airborne multisensor geophysical survey, Stewart River area, Yukon; Phase 1, Geological Survey of Canada Open File D4009 (digital format).

Smith, M., 2000, The Tintina Gold Belt: An emerging gold district in Alaska and Yukon, *in* The Tintina Gold Belt: Concepts, exploration, and discoveries, Cordilleran Roundup Special Volume 2: British Columbia and Yukon Chamber of Mines, p. 1-3.

Smith, M., Thompson, J.F.H., Bressler, J., Layer, P., Mortensen, J.K., and Takaoka, I.A.H., 1999, Geology of the Liese Zone, Pogo property, east-central Alaska: Society of Economic Geology Newsletter, No. 38, p. 11-21.

Smuk, K.A., 1999, Metallogeny of epithermal gold and base metal veins of the southern Dawson Range, Yukon: unpublished Masters thesis, McGill University, 155 p.

Suzuki, K., Shimizu, H., and Masuda, A., 1996, Re-Os dating of molybdenites from ore deposits in Japan: Implications for the closure temperature of the Re-Os system for molybdenite and the cooling history of molybdenite in ore deposits: Geochimica et Cosmochimica Acta, v. 60, p. 3151-3159.

Suzuki, K., Kagi, H., Nara, M., Takano, B., and Nozaki, Y., 2000, Experimental alteration of molybdenite of the Re-Os system, infrared spectroscopic profile and polytype: Geochimica et Cosmochimica Acta, v. 64, p. 223-232.

Swanenberg, H.E.C., 1979, Phase equilibria in carbonic systems, and their application to freezing studies of fluid inclusions: Contributions to Mineralogy and Petrology, v. 68, p. 303-306.

Teagle, D.A.H., Norris, R.J., and Craw, D., 1990, Structural controls on gold-bearing quartz mineralization in a duplex-thrust system, Hyde-Macraes Shear Zone, Otago schist, New Zealand: Economic Geology, v. 85, p. 1711-1719.

Tempelman-Kluit, D.K., 1974, Reconnaissance geology of Aishihik Lake, Snag and part of Stewart River map-areas, west-central Yukon (115H, 115K-J and 115N-O): Geological Survey of Canada Paper 73-41, 97 p.

Thomas, A.V., and Spooner, E.T.C., 1988, Fluid inclusions in the system H_2O-CH_4-NaCl-CO_2 from metasomatic tourmaline within the border unit of the Tanco zoned granitic pegmatite, S.E. Manitoba: Geochimica et Cosmochimica Acta, v. 52, p. 1065-1075.

Todt, W., Cliff, R.A., Hanser, A., and Hofman, A.W., 1996, Evaluation of a ^{202}Pb-^{205}Pb double spike for high-precision lead isotope analysis: Geophysical Monograph, v. 95, p. 429-437.

Tosdal, R.M., Wooden, J.L., and Bouse, R.M., 1999, Pb isotopes, ore deposits and metallogenic terranes: Economic Geology Reviews, v. 12, p. 1-28.

Tullis, J., 1983, Deformation of feldspars, *in* Ribbe, P.H., ed., Feldspar mineralogy: Reviews in Mineralogy, Mineralogical Society of America, v. 2, p. 297-323.

Twiss, R.J., and Moores, E.M., 1992, Structural Geology, W.H. Freeman and Company, New York, 532 p.

Warrick, I., and Robertson, K., 1989, Exploration Incentive Program Report # 093106 (EIP89-057); Trenching and bulk sampling report: 1989 Yukon Assessment Report, Whitehorse Mining District.

Waugh, D.H., 1975, A comprehensive report and recommendations on the DEA mineral claims and DEA placer prospecting leases and the 7 Mile Creek prospecting leases – 1975 summer programs in the Moosehorn Range, 7 Mile Creek areas, Yukon Territory: Great Bear Mining Limited: 1975 Yukon Assessment Report, Whitehorse Mining District.

Yukon Minfile #115N 024

CHAPTER 4

General Conclusions and Recommendations for Future Research

The geology of the Moosehorn Range area was very poorly understood prior to this study. Structural controls on the formation of high-grade gold-bearing quartz veins in the area were particularly unclear, and constraining these controls has been critical to evaluate the potential for larger-scale gold mineralization in the region. This study represents the most complete and detailed investigation of geology and metallogeny of the southwestern Stewart River map area, and has greatly enhanced the understanding of local structural and fluid evolution of the shallowly dipping, intrusion-hosted auriferous veins in the Moosehorn Range area.

Field mapping, lithogeochemistry studies, U-Pb, K-Ar, and $^{40}Ar/^{39}Ar$ geochronology studies have shed light on the nature and age of the various vein-hosting intrusions in the study area. The main MRG was emplaced at 99.8 ± 0.4 Ma. Variably foliated porphyritic granodiorite and quartz diorite dykes intruded very shortly thereafter, followed by the emplacement of felsite dykes at 96.0 ± 0.4 Ma. Results of lithogeochemical analyses for these felsic to intermediate intrusions indicate that the melts were probably of mantle origin and were extensively contaminated by crustal material in a continental magmatic arc setting. Highly radiogenic and homogeneous Pb isotopic compositions for the intrusions demonstrate that the magmas were likely consanguineous and that the magmas incorporated a significant amount of evolved crustal material. This is further substantiated by the presence of inherited zircons in the samples.

From limited outcrop, two generations of foliations that predate the gold-bearing veins were recognized in the MRG. D1 probably took place during to shortly after intrusion

and is manifested as moderately to steeply southwest-dipping weak flow foliations and localized mylonitic strike-slip shear zones (S1). S1 fabrics were dextrally offset by a D2 shear zone that strikes south-southwest and dips moderately to steeply to the northwest. Moderately developed to ultramylonitic S2 foliations are locally developed in the MRG and a $^{40}Ar/^{39}Ar$ age of 93.4 ± 0.9 Ma records the minimum age for the deformation. Dykes throughout the property are oriented and foliated parallel to S2.

Between approximately 92 and 93 Ma, ENE-WSW-directed shortening, possibly related to contraction in the vicinity of a jog in a NNW-striking dextral strike-slip fault, generated the shallowly ENE-dipping structures along which the sheeted gold-bearing veins formed. The veins have a ramp-flat geometry whereby sub-horizontal oreshoots occupy the flats. Brittle shear slip was up-dip along the ramp segments towards about 250º. Long axes of the oreshoots, which are lens-shaped, somewhat discontinuous, and up to 3-4 m thick, are oriented NNW-SSE.

The veins consist of less than 5% sulphide and sulphosalt material, and contain quartz, galena, sphalerite, arsenopyrite, boulangerite, tetrahedrite, pyrite, scheelite, native gold, tourmaline, and minor muscovite and calcite. Distinct differences between the Pb isotopic compositions of vein minerals and intrusions indicate that the mineralizing fluids were neither derived from the host intrusions nor did they obtain much Pb (or presumably other metals) from them. The ultimate source of the metals is significantly less radiogenic than the adjacent wallrocks but remains unidentified. Fluids associated with gold and sulphide mineralization contain H_2O-CO_2-CH_4-NaCl ± N_2, and typically have low to moderate amounts of NaCl and CH_4. Coexistence of CO_2-rich and H_2O-rich aqueous-carbonic inclusions in the studied samples is indicative of fluid immiscibility, which probably promoted gold and sulphide deposition. Trapping temperatures and pressures were

about 220º-300ºC and 1.3-1.9 kbar, respectively. Assuming near-lithostatic fluid pressures, the corresponding depth for vein formation is about 5-7 km, which is typical for mesothermal lode gold systems.

The veins have been brecciated and slightly offset by at most a few metres along moderately northwest dipping brittle normal faults. Shallowly ENE-dipping lamprophyres intruded the MRG at around 64 Ma, and may be related to the latest Cretaceous Carmacks Group volcanics. Still younger (54 Ma) fine-grained mafic dykes are oriented nearly parallel the small-scale faults that offset the gold-bearing veins. Mafic magmatism at 54 Ma has been documented at several other locales in the northern Cordillera and was probably triggered by crustal thinning in response to Eocene dextral strike-slip movement along the Tintina, Denali, and associated fault systems.

The results of this study constrain the ages of the host intrusions and of the mineralization, the nature of the mineralizing fluids, and the local structural controls on the vein formation. Clearly, understanding the ramp-flat geometries of the veins at Longline was key for developing the model for the vein and oreshoot formation. This model should be taken into account when developing exploration strategies in west-central Yukon and east-central Alaska, and as demonstrated by the global analogies discussed in Chapter 3, can be applied to other deposits elsewhere in the world.

Recommendations for Future Research

As with most scientific studies, many questions were raised throughout the course of this research. Although the intrusions in the Moosehorn Range area are not genetically linked to the gold mineralization at Longline, understanding their magmatic evolution in the context of the regional structural setting is important for elucidating the 90-100 Ma regional

tectonic evolution of west-central Yukon Territory. In the absence of contemporaneous mafic magmatism, lithogeochemical and isotopic signatures of the felsic to intermediate intrusions of the Dawson Range batholith provide the only evidence for the source of the magmas. This study examined the major, trace, rare earth element, and Pb isotopic compositions of the intrusions; additional information about magma sources and degrees of crustal contamination may be gleaned from $\delta^{18}O$, Sr, Nd, and Hf isotopic studies.

Results of the Pb isotopic study confirmed that the gold mineralizing fluids were *not* derived from the host intrusions, and that the ultimate source remains uncertain. The source may, in fact, not be of igneous origin at all. A more thorough understanding of the fluid source would be achieved through more in-depth fluid inclusion studies (including Laser-Raman spectroscopy), stable isotope studies (H, S, and O), and additional Pb isotopic investigations of lithologies outside of the immediate Moosehorn Range area.

Further investigation of a widespread (5-6 km^2) Au-As soil geochemistry anomaly in the northwestern Moosehorn Range area may uncover additional mineralization. Reconnaissance diamond drilling in this vicinity revealed wide zones (tens of metres) of intense phyllic, argillic, and carbonate alteration similar to that associated with the veins in the main study area. Influx of a large volume of hydrothermal fluid was presumably responsible for this widespread alteration, but significant veining has not been recognized thus far. A network of fluid pathways with similar structural controls as the main veins to the south probably exists at depth, and additional drilling may uncover them.

The fact remains that scarcity of outcrop in west-central Yukon has inhibited our understanding of the regional tectonic history. Clarifying the regional structural context for the formation of the Longline veins and oreshoots would require significantly more extensive regional-scale structural mapping. Tighter constraints on the temperature and

timing of D1 and D2 mylonitization relative to formation of the gold-bearing veins would require additional $^{40}Ar/^{39}Ar$ geochronology and a more thorough study of the metamorphic mineral assemblage(s) in the rocks. Constraining the relationship between and the nature and age of major lineaments recognized on the satellite image and airborne magnetic maps is particularly critical, especially for the purpose of locating other structurally controlled gold deposits of economic interest.

APPENDIX A

Longline Trench Maps; V2 Exposures in Swede's Pit

*The trench maps are presented beginning with those from the northwestern end of Swede's Pit (at the highest elevation) through to those from the southwestern end of the pit (at the lowest elevation). See Figure 24 in Chapter 3 for the trench locations.

Legend for Trench Maps

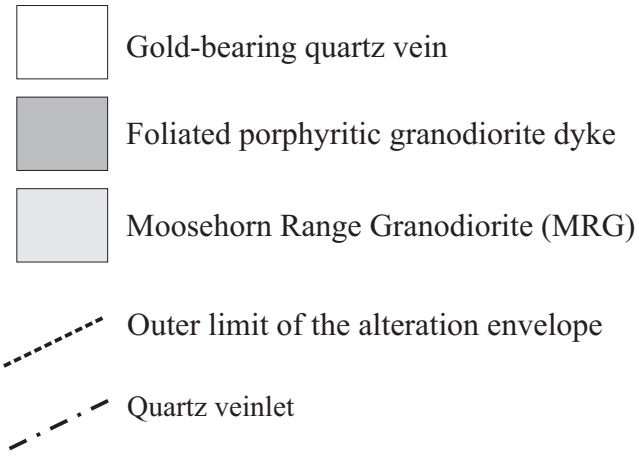

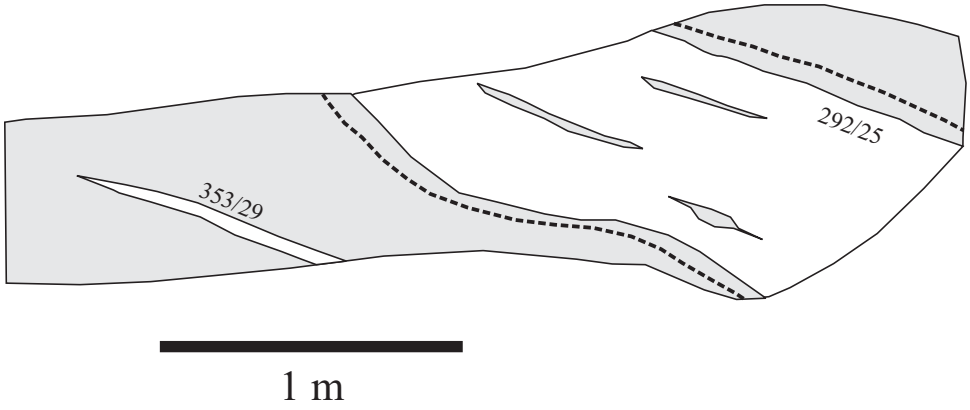

Figure 43 Trench #20: Drawn looking northwest. Vein orientations are shown.

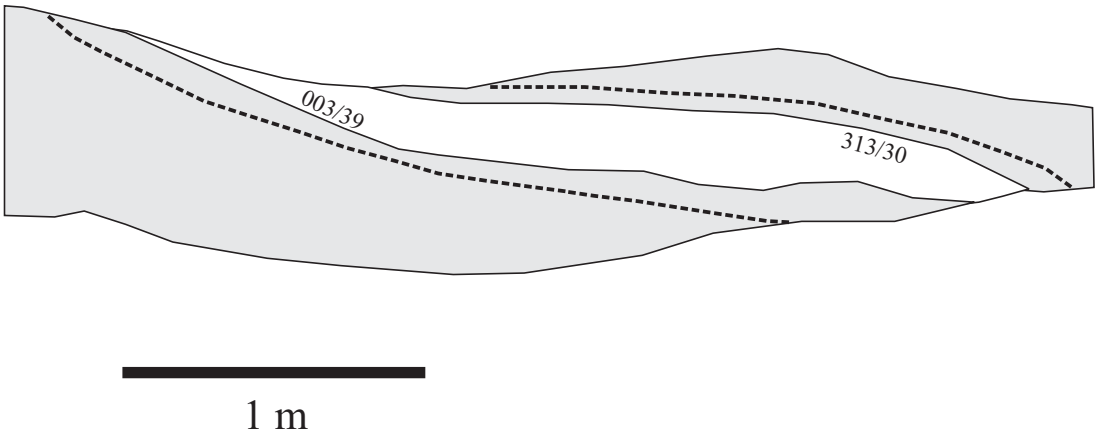

Figure 44 Trench #19: Drawn looking due north. Vein orientations shown.

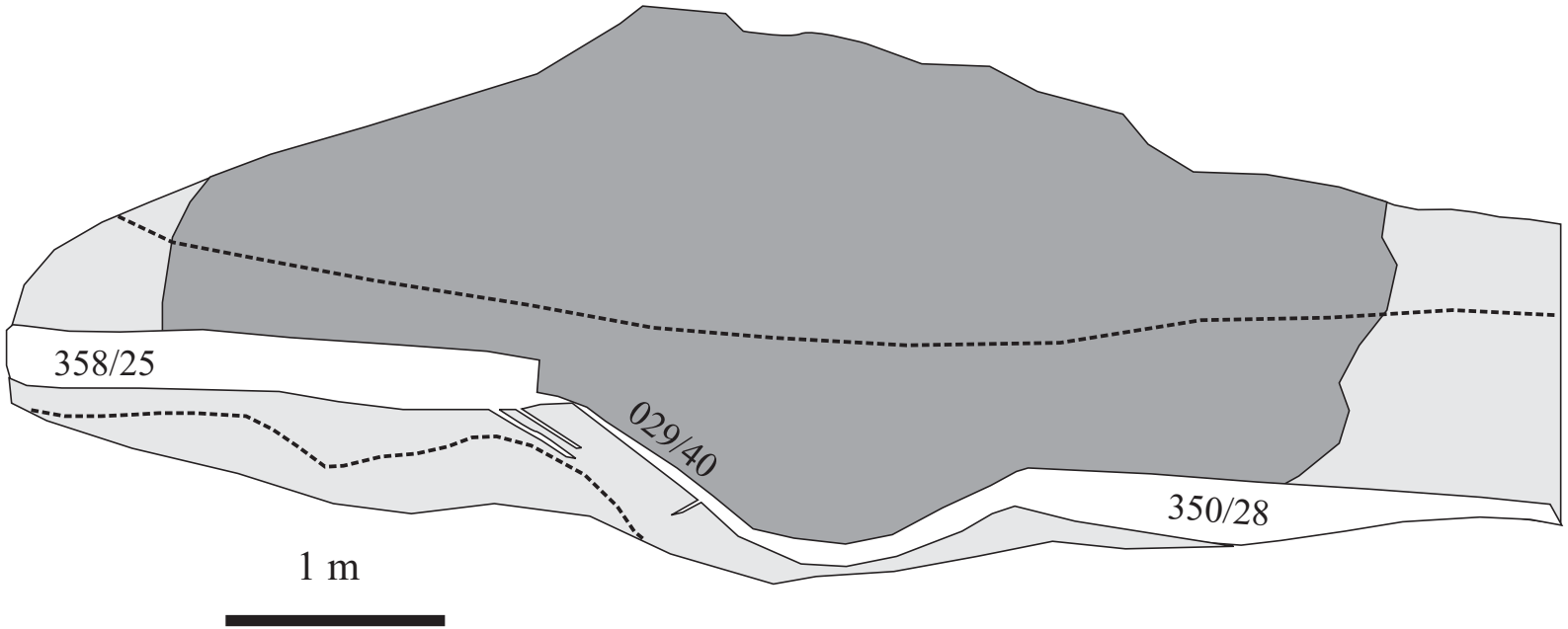

Figure 45 Trench#3: Drawn looking northeast. Vein orientations are shown.

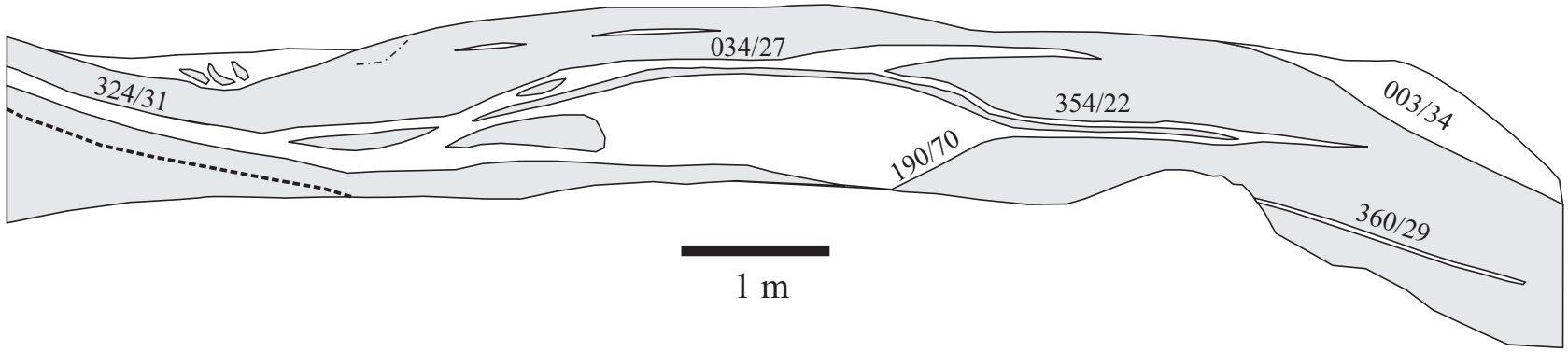

Figure 46 Trench #4: Drawn looking northwest. Vein orientations are shown.

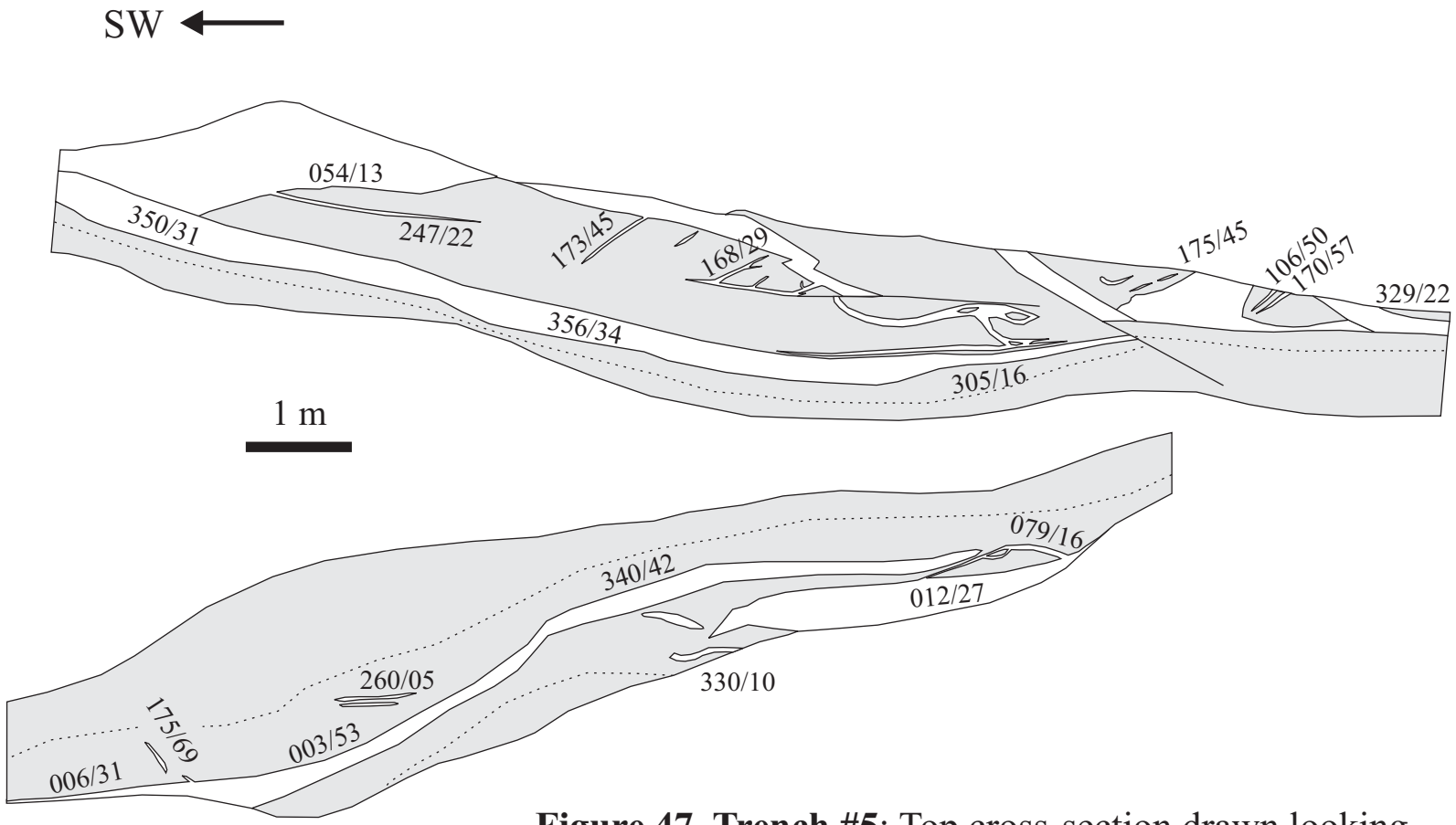

Figure 47 Trench #5: Top cross-section drawn looking northwest. Bottom cross-section is from the opposite wall of the trench, flipped upside-down so that the space in between the sections would be the "floor" of the trench. Vein orientations are as shown.

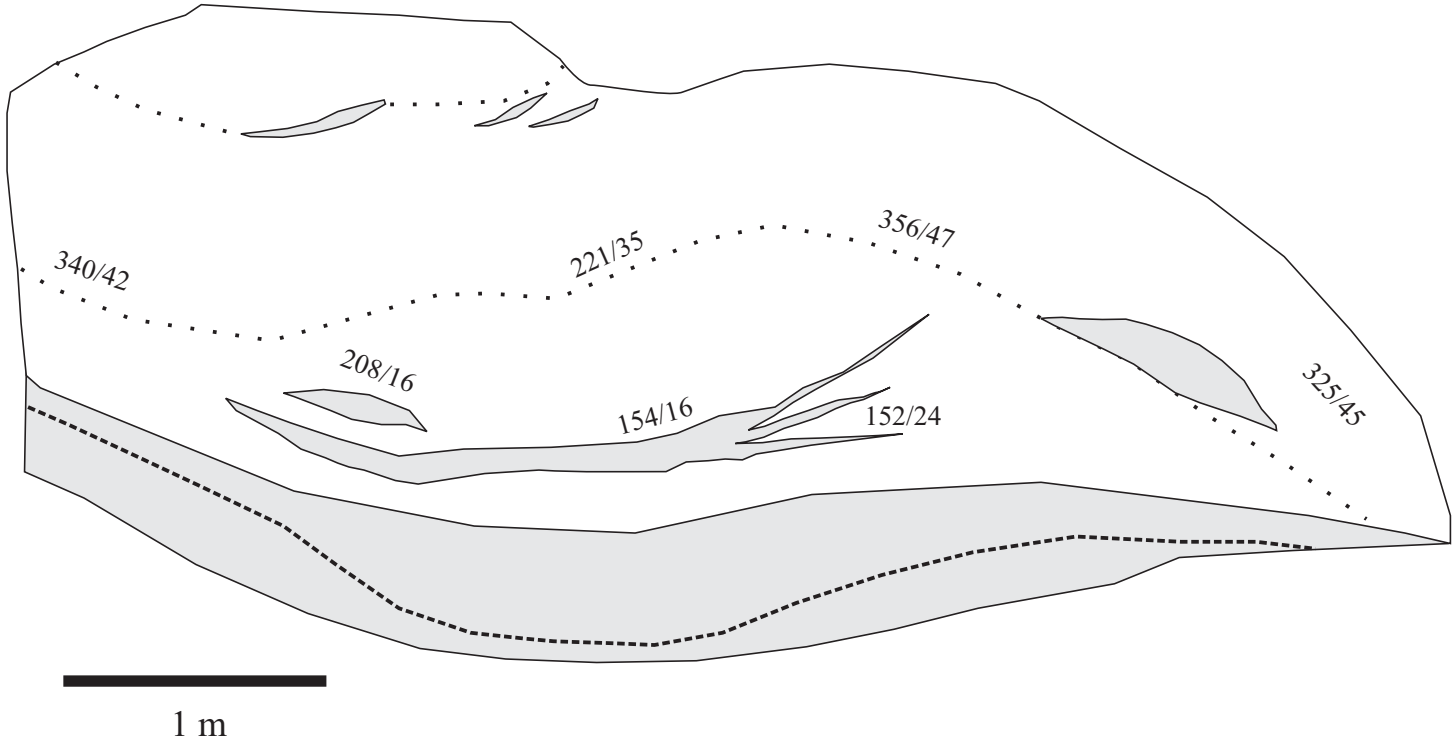

Figure 48 Trench #6: Drawn looking northwest. This is a cross-section through an orsehoot lens and represents the thickest exposure of quartz vein material. Dotted lines inside the oreshoot illustrate the internal fabric within the quartz (fractures, locally containing slivers of wallrock).

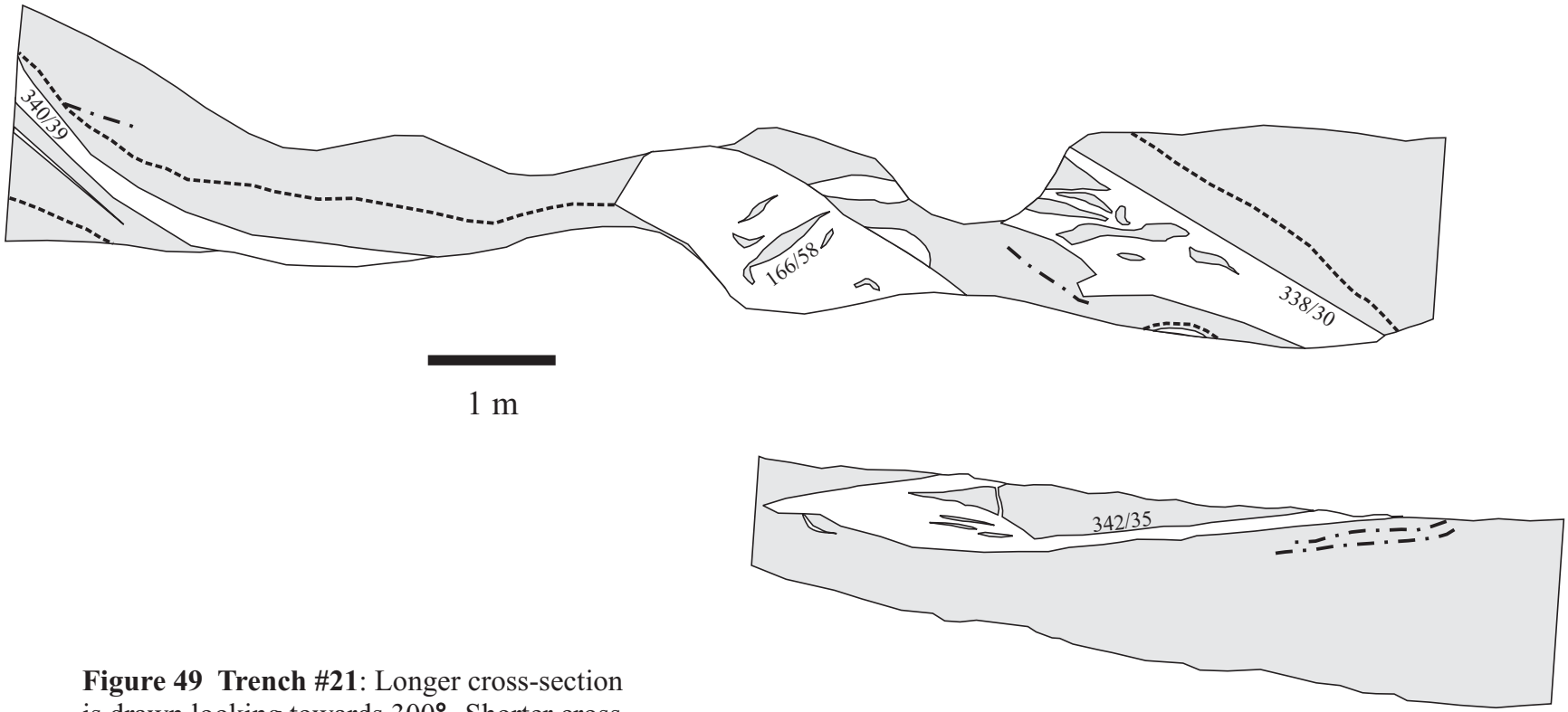

Figure 49 Trench #21: Longer cross-section is drawn looking towards 300°. Shorter cross-section is the opposite wall of the trench drawn such that the space between the two map segments is the floor of the trench.

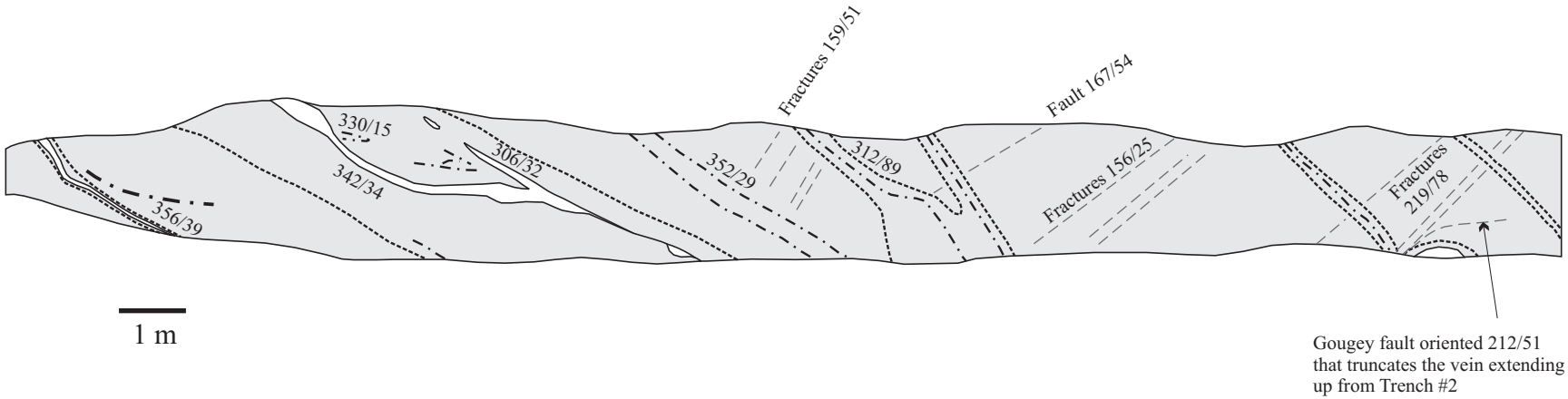

Figure 50 Trench #9: Drawn looking northwest. Vein orientations are as shown. The portion of quartz vein material on the far right is the extension of the vein seen in Trench #2. Here, the vein is truncated by the shown fault, which is sinistral and downdropped the northwest block (hanging wall) by about 5 m.

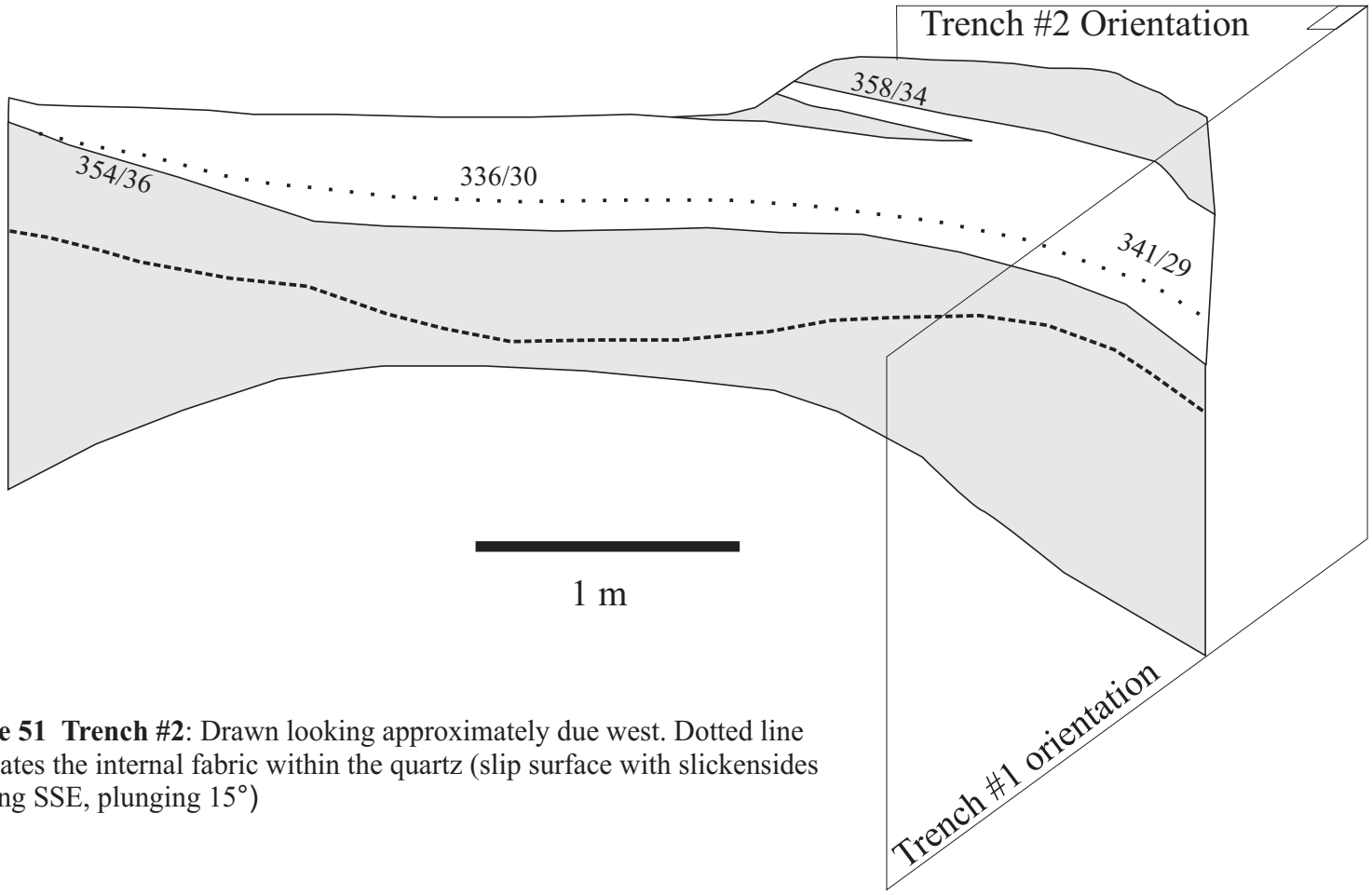

Figure 51 Trench #2: Drawn looking approximately due west. Dotted line delineates the internal fabric within the quartz (slip surface with slickensides trending SSE, plunging 15°)

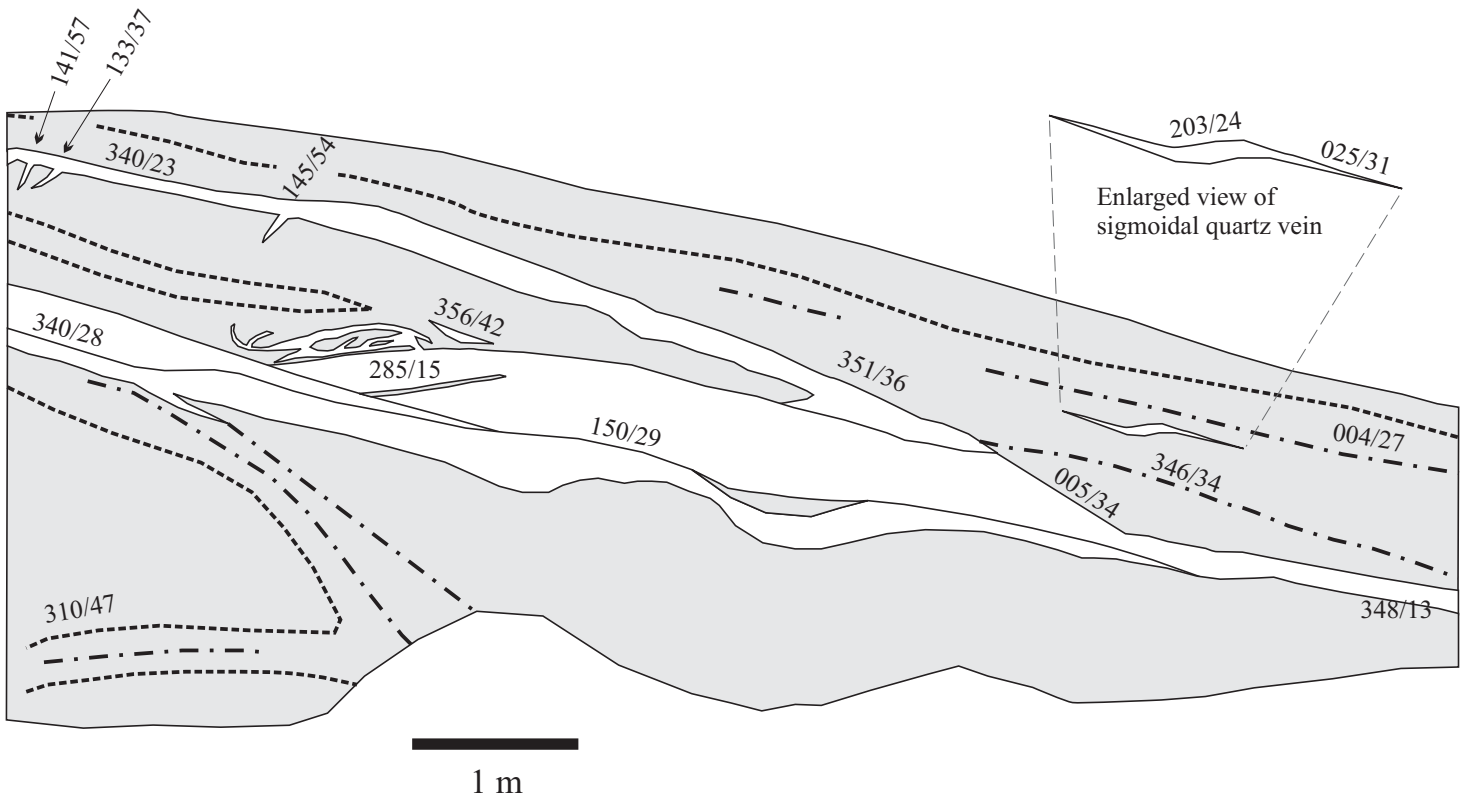

Figure 52 Trench #1: Drawn looking approximately due north. This trench exhibits a classic shear vein geometry, with the central sub-horizontal lens-shaped oreshoot connecting two thinner veins. In upper left area are little tapered extension veinlets that contain vuggy quartz. The enlarged sigmoidal vein is a small scale equivalent of the overall vein geometry. Vein orientations are as shown.

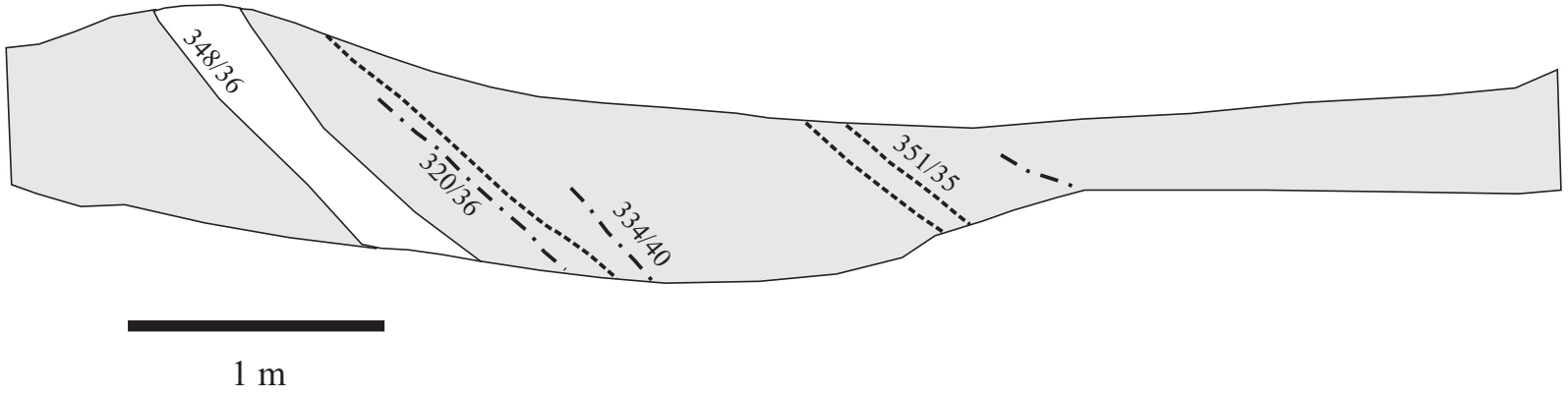

Figure 53 Trench #15: Drawn looking west-northwest. Vein orientations are as shown.

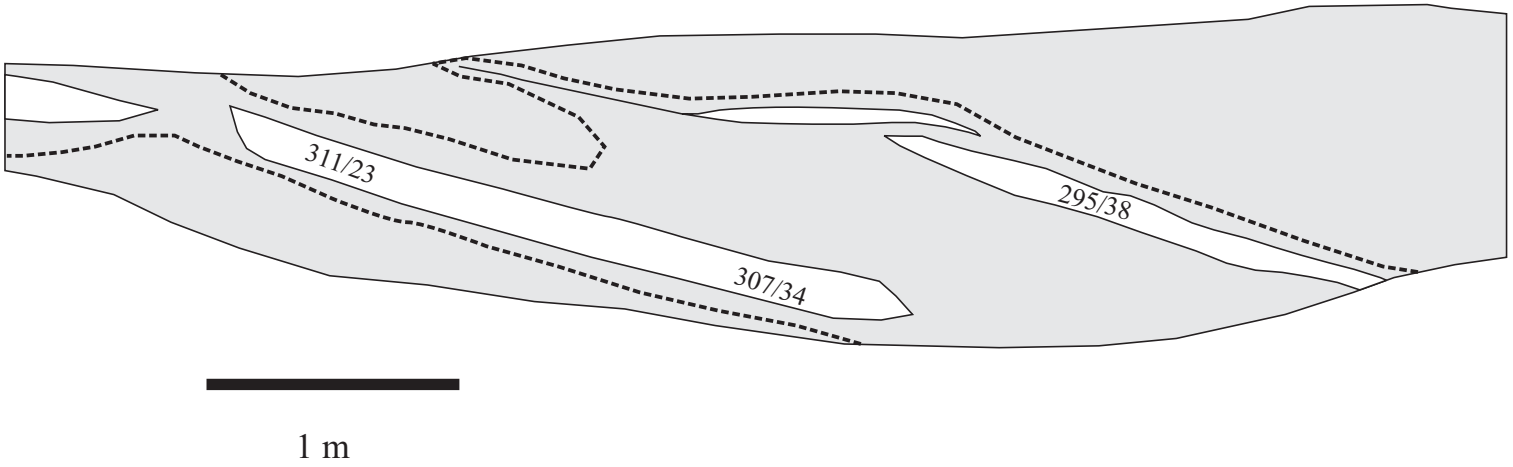

Figure 54 Trench #14: Drawn looking west-northwest. Vein orientations are as shown.

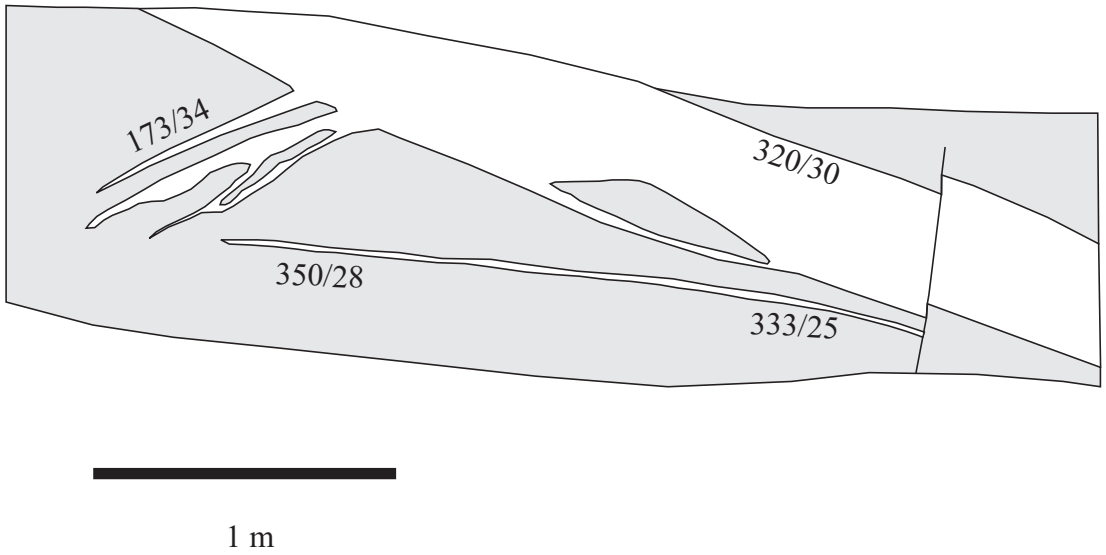

Figure 55 Trench #7: Drawn looking north-northwest. The tapered veinlets branching off of the main vein contain vuggy and comb-textured quartz. Vein orientations are as shown.

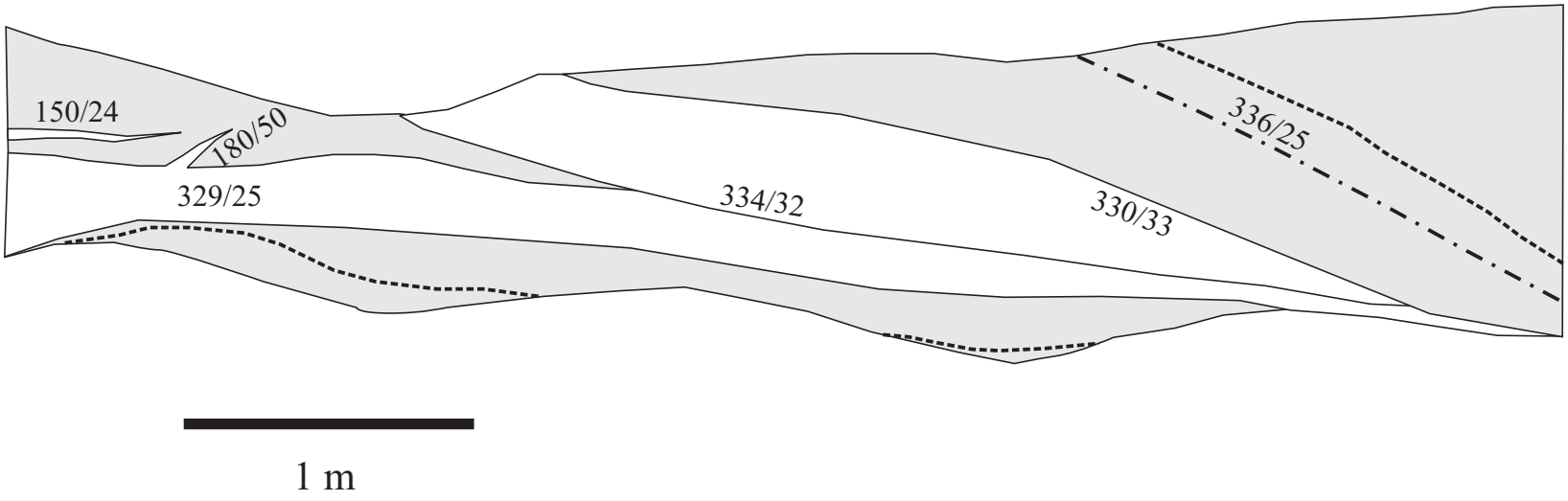

Figure 56 Trench #13: Drawn looking west-northwest. Vein orientations are as shown.

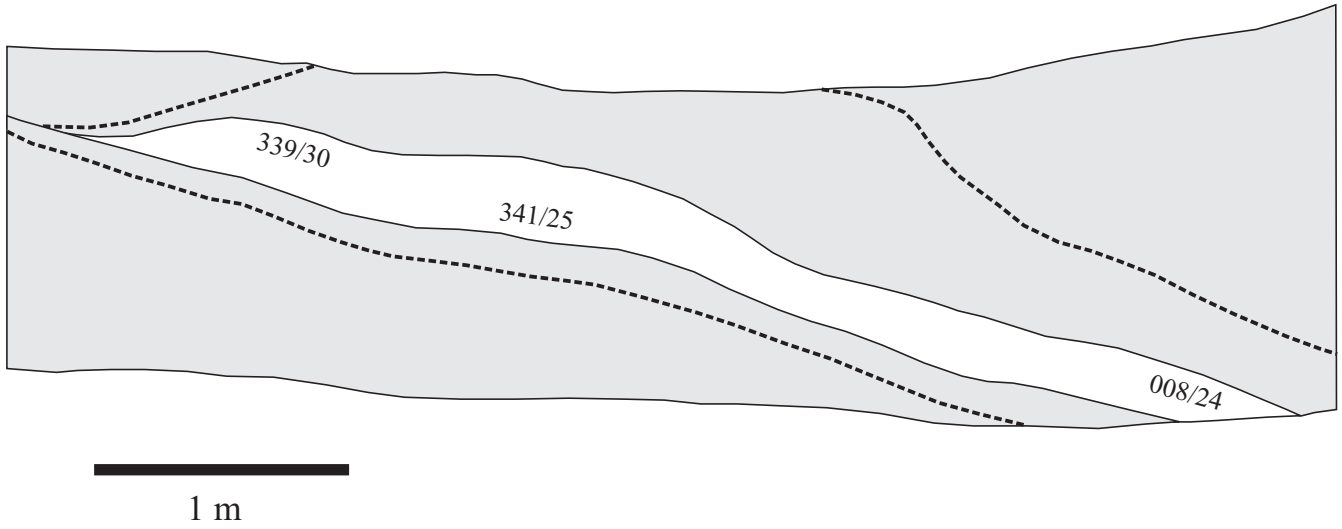

Figure 57 Trench #12: Drawn looking northwest. Vein orientations are as shown.

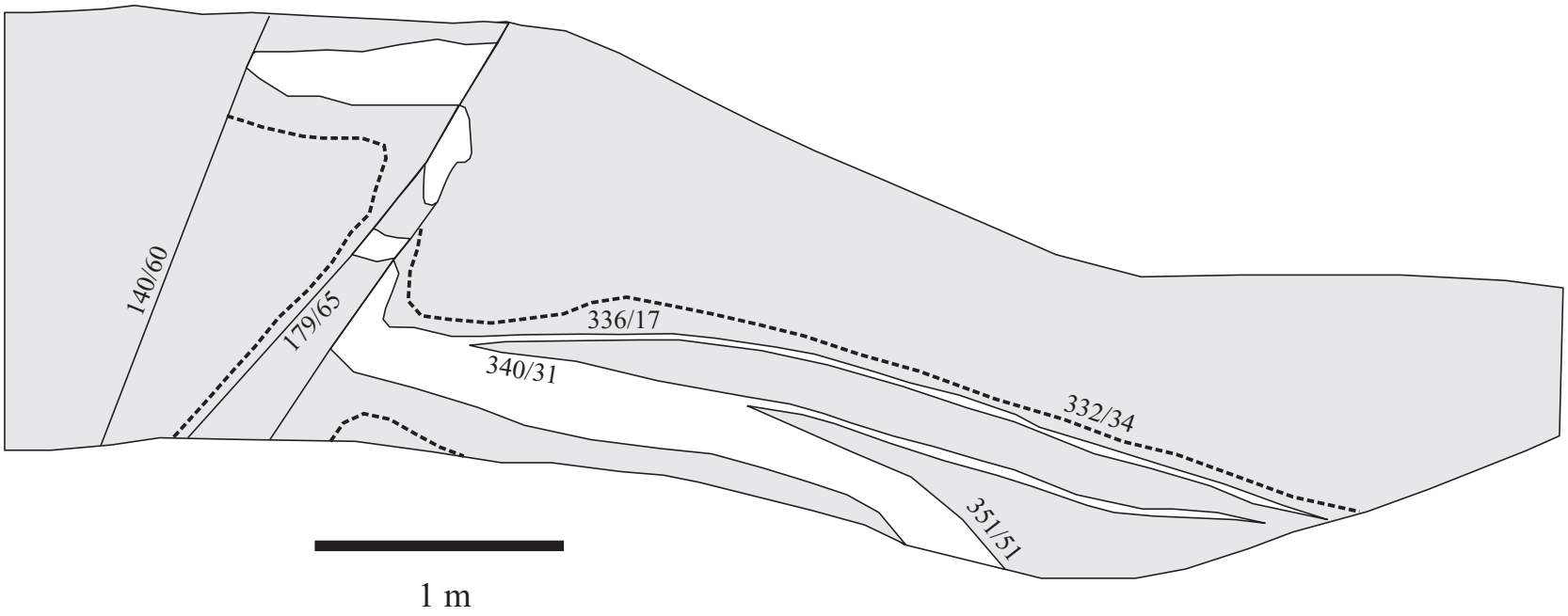

Figure 58 Trench #16: Drawn looking northwest. The quartz vein is slightly offset by a set of faults. The quartz in the fault zone has a floury or sugary texture from the brittle deformation. Vein orientations are as shown.

APPENDIX B

Selected Microprobe Data for Vein Sulphides and Sulphosalts

APPENDIX B Selected results of electron microprobe analyses of vein sulphide and sulphosalt phases (expressed in wt%)

Spot Analysis	S	Mn	Fe	Co	Ni	Cu	Zn	As	Ag	Cd	Sn	Sb	Pb	Bi	Total	Mineral
99N-4B-1	21.731	0.000	35.107	0.000	0.000	0.014	0.004	42.015	0.000	0.028	0.015	0.025	0.000	0.030	**98.970**	Arsenopyrite
99N-4B-2	21.901	0.000	35.233	0.000	0.000	0.015	0.014	41.935	0.000	0.000	0.009	0.009	0.000	0.057	**99.172**	Arsenopyrite
99N-4B-4	18.759	0.000	0.021	0.010	0.001	0.034	0.021	0.116	0.040	0.021	0.082	24.950	53.872	0.793	**98.719**	Boulangerite
99N-4B-5	0.040	0.026	0.015	0.008	0.022	0.030	0.000	0.051	21.949	0.073	0.007	0.008	0.000	0.047	**22.274**	?
99N-4B-6	18.625	0.021	0.000	0.015	0.001	0.016	0.004	0.159	0.023	0.018	0.090	24.879	54.313	0.666	**98.827**	Boulangerite
99N-4B-7	21.649	0.000	35.084	0.000	0.000	0.002	0.008	41.831	0.001	0.002	0.013	0.022	0.000	0.043	**98.657**	Arsenopyrite
99N-4B-9	18.442	0.014	0.058	0.008	0.000	0.014	0.000	0.165	0.017	0.048	0.057	25.213	53.613	0.631	**98.279**	Boulangerite
99N-4B-10	21.657	0.000	35.084	0.019	0.018	0.016	0.010	42.204	0.019	0.000	0.038	0.000	0.000	0.037	**99.104**	Arsenopyrite
99N-4B-11	17.899	0.000	0.073	0.032	0.000	0.007	0.008	0.217	0.029	0.017	0.070	23.543	54.325	0.637	**96.857**	Boulangerite
99N-4B-12	17.046	0.026	0.206	0.004	0.007	0.006	0.000	0.306	0.004	0.074	0.046	24.474	52.266	0.702	**95.168**	Boulangerite
99N-4B-14	20.924	0.000	35.072	0.000	0.006	0.025	0.033	42.871	0.000	0.005	0.021	0.006	0.000	0.033	**98.997**	Arsenopyrite
99N-4B-17	13.493	0.026	0.065	0.002	0.001	0.000	0.018	0.005	0.313	0.006	0.021	0.252	84.646	1.145	**99.992**	Galena
99N-3B-1	17.730	0.006	0.093	0.000	0.022	0.018	0.094	0.092	0.019	0.000	0.106	23.691	55.053	0.766	**97.690**	Boulangerite
99N-3B-2	32.759	0.011	2.975	0.000	0.009	0.027	60.488	0.000	0.000	1.594	0.010	0.000	0.000	0.123	**97.995**	Sphalerite
99N-3B-3	20.747	0.000	34.779	0.000	0.000	0.007	0.138	43.746	0.001	0.016	0.032	0.048	0.000	0.112	**99.626**	Arsenopyrite
99N-3B-4	32.284	0.013	3.220	0.007	0.003	0.094	60.041	0.007	0.009	1.576	0.003	0.000	0.000	0.115	**97.372**	Sphalerite
99N-3B-5	32.602	0.023	2.698	0.005	0.000	0.038	60.776	0.000	0.030	1.516	0.000	0.016	0.000	0.145	**97.850**	Sphalerite
99N-3B-6	22.736	0.001	2.852	0.000	0.012	23.933	3.462	0.736	18.971	0.375	0.104	25.436	0.000	0.148	**98.768**	Tetrahedrite
99N-3B-7	13.132	0.001	0.599	0.015	0.000	0.129	0.908	0.132	0.098	0.165	0.082	26.837	47.383	0.636	**90.117**	Boulangerite
99N-3B-8	18.585	0.001	0.015	0.002	0.001	0.011	0.015	0.097	0.022	0.000	0.158	25.198	54.359	0.593	**99.057**	Boulangerite

Samples 99N-4B and 99N-3B were collected near the "M-Vein" (Fig. 23) along the crest of the Moosehorn Range

APPENDIX C

Fluid Inclusion Microthermometric Data

APPENDIX C

Fluid Inclusion Data Summary

Aqueous Inclusions $H_2O_{(l)} + H_2O_{(v)}$

Sample	Degree of Fill		T_{eu} (°C)	T_{mIce} (°C)	T_h(°C)
	Liquid	Vapour			
99N-22C	0.90	0.10		-2.2	
	0.80	0.20			271.0
	0.70	0.30			248.3
	0.90	0.10			270.0
	0.90	0.10			240.0
	0.80	0.20			262.9
	0.85	0.15			272.9
	0.60	0.40			269.5
	0.70	0.30			262.8
	0.80	0.20	-18.4		204.6
	0.70	0.30		-5.1	
	0.80	0.20	-17.7	-3.3	
	0.75	0.25	-17.4	-4.2	
	0.90	0.10	-18.8	-4.3	256.8
	0.85	0.15			251.4
	0.90	0.10			258.3
	0.70	0.30			286.4
	0.90	0.10			239.4
	0.90	0.10			259.3
99N-22F	0.90	0.10		-2.2	
	0.90	0.10		-5.2	235.3
	0.90	0.10		-5.7	225.2
	0.90	0.10		-5.6	237.5
	0.90	0.10	-22.1	-6.2	231.2
	0.90	0.10	-20.0	-7.1	239.1
	0.90	0.10			237.5
	0.75	0.25	-24.6	-3.4	257.8
	0.70	0.30	-22.1	-3.1	
	0.90	0.10		-4.6	
	0.90	0.10	-23.6	-5.0	
	0.90	0.10	-22.5	-3.6	
	0.80	0.20			203.6
	0.70	0.30			208.3
	0.80	0.20			202.8
	0.60	0.40			208.9
	0.90	0.10			204.2
	0.70	0.30			210.1
	0.80	0.20			201.8
	0.90	0.10			244.9
	0.70	0.30			248.2
	0.70	0.30			247.1
	0.70	0.30			
	0.70	0.30	-23.1	-4.2	
	0.80	0.20		-12.0	
	0.70	0.30	-22.2	-4.9	
	0.70	0.30			340.1
	0.90	0.10	-21.2	-7.5	
	0.70	0.30	-22.2	-8.2	
	0.90	0.10	-24.0	-5.8	285.7
	0.90	0.10	-25.2	-6.7	
	0.85	0.15		-2.6	191.6
	0.90	0.10	-26.2	-4.2	234.6
	0.95	0.05	-26.6	-3.4	261.3
	0.80	0.20	-23.1	-4.5	
	0.80	0.20			221.7
	0.85	0.15			222.8
	0.90	0.10			231.2
	0.90	0.10			228.2
	0.90	0.10			237.0

Aqueous Inclusions $H_2O_{(l)}$ + $H_2O_{(v)}$ (continued)

	Degree of Fill				
Sample	**Liquid**	**Vapour**	**T_{eu} (°C)**	**T_{mIce} (°C)**	**T_h(°C)**
99N-4D	0.90	0.10		-3.7	
	0.90	0.10	-22.6	-3.6	
	0.90	0.10	-24.3	-3.7	
	0.95	0.05	-24.0	-3.8	
	0.90	0.10	-24.2	-6.2	223.2
	0.95	0.05	-23.8	-7.1	226.9
	0.90	0.10	-21.5	-3.9	227.9
	0.90	0.10		-3.7	224.7
	0.90	0.10		-4.1	232.0
	0.90	0.10	-24.3	-4.7	
	0.90	0.10	-22.5	-4.0	222.9
	0.90	0.10			221.8
	0.80	0.20			251.4
	0.90	0.10			230.4
	0.95	0.05			237.1
	0.90	0.10			237.8
	0.80	0.20			219.0
	0.90	0.10			228.5
	0.80	0.20			239.5
	0.65	0.35			231.9
	0.70	0.30			230.5
	0.90	0.10			216.6
	0.80	0.20		-3.1	
	0.90	0.10		-4.2	238.9
	0.95	0.05	-20.5	-6.2	203.2
	0.90	0.10	-24.9	-6.4	170.6
	0.90	0.10	-22.3	-4.0	
	0.90	0.10	-19.2	-4.8	248.4
	0.80	0.20	-20.8	-4.0	237.1
	0.80	0.20			210.1
	0.70	0.30			209.2
	0.70	0.30			218.8
	0.90	0.10			213.8
	0.90	0.10			212.1
	0.80	0.20			211.2
	0.90	0.10	-17.2	-3.1	
	0.90	0.10	-25.4	-5.0	
	0.75	0.25		-5.5	
	0.90	0.10			225.9
	0.90	0.10			296.2
	0.90	0.10			262.4
	0.90	0.10			267.1
	0.90	0.10	-23.2	-9.0	
	0.90	0.10	-21.6	-9.6	
	0.90	0.10	-25.8	-8.5	
	0.85	0.15	-23.1	-6.5	
	0.90	0.10	-22.1	-9.9	
	0.80	0.20	-24.3	-2.1	
	0.90	0.10	-21.3	-12.1	
	0.90	0.10	-23.8	-8.1	
	0.95	0.05	-26.0	-3.2	
	0.95	0.05	-23.2	-12.1	
	0.90	0.10	-21.8	-6.3	216.8
	0.90	0.10	-23.1	-5.7	
	0.90	0.10			240.7
	0.90	0.10			264.4
	0.85	0.15			222.5
	0.80	0.20			267.0
	0.75	0.25			231.5
	0.90	0.10			240.2
	0.90	0.10			230.0
	0.90	0.10			212.8
	0.90	0.10			242.6
AVERAGE	**0.85**	**0.15**	**-22.6**	**-5.4**	**236.3**
RANGE	**0.65-0.95**	**0.05-0.45**	**-17.2 to -26.6**	**-2.1 to -12.1**	**170.6 to 340.1**
			n=46	**n= 60**	**n=84**

Aqueous-Carbonic ($H_2O > CO_2$) Inclusions

	Degree of Fill				
Sample	**CO_2**	**H_2O**	**$CO_{2(l)}$**	**$CO_{2(v)}$**	**$T_{m(CO2)}$ (°C)**
99N-22C	0.40	0.60	0.65	0.35	-57.8
	0.50	0.50	0.60	0.40	-57.8
	0.40	0.60	0.60	0.40	
	0.40	0.60	0.60	0.40	
	0.40	0.60	0.50	0.50	-55.5
	0.40	0.60	0.60	0.40	-55.8
99N-22F	0.50	0.50	0.60	0.40	-56.2
	0.50	0.50	0.90	0.10	
	0.45	0.55	0.60	0.40	
	0.50	0.50	0.70	0.30	-56.1
99N-4D	0.20	0.80			-58.5
	0.40	0.60			-57.4
	0.40	0.60			-56.9
	0.40	0.60			-56.9
	0.30	0.70	0.60	0.40	-56.8
	0.30	0.70	0.50	0.50	-56.3
	0.40	0.60			-58.3
	0.30	0.70			-57.4
	0.30	0.70	0.50	0.50	-55.5
	0.45	0.55	0.65	0.35	-56.9
	0.45	0.55	0.60	0.40	
	0.45	0.55	0.80	0.20	
	0.25	0.75	0.60	0.40	-55.7
	0.25	0.75	0.50	0.50	-55.2
	0.45	0.55	0.55	0.45	
	0.50	0.50	0.60	0.40	
	0.50	0.50	0.86	0.14	-56.9
	0.50	0.50	0.80	0.20	-56.4
	0.50	0.50	0.90	0.10	
	0.50	0.50	0.90	0.10	
	0.50	0.50	0.90	0.10	
	0.45	0.55	0.65	0.35	-55.2
	0.45	0.55	0.65	0.35	
	0.45	0.55	0.65	0.35	
	0.50	0.50	0.90	0.10	
	0.50	0.50	0.80	0.20	
	0.50	0.50	0.90	0.10	
	0.50	0.50	0.80	0.20	
	0.50	0.50	0.80	0.20	
	0.50	0.50	0.90	0.10	
	0.45	0.55	0.65	0.35	
	0.45	0.55	0.65	0.35	
	0.40	0.60	0.85	0.15	
AVERAGE	**0.43**	**0.57**	**0.70**	**0.30**	**-56.6**
RANGE	**0.20 - 0.50**	**0.50 - 0.80**	**0.50 - 0.90**	**0.10 - 0.50**	**-58.5 to -55.2**
n =	**43**	**43**	**37**	**37**	**21**

Aqueous-Carbonic (H_2O > CO_2) Inclusions (continued)

Sample	T_{mClath} (°C)	T_{hCO2} (°C)	Homog. into	T_h(°C)	Homog. Into
99N-22C	7.4	27.5	(liquid) L		
	8.4	29.8	L	299.2	(water) H
		29.6	(vapour) V	259.8	H
		29.3	V	256.1	H
	-2.2				
	8.9				
99N-22F	4.0	30.0	L	293.2	H
		24.6	L	252.7	H
		28.5	L	265.0	H
	3.8		L	296.6	H
99N-4D					
	3.6				
	2.2				
	3.2	30.7	L	258.0	H
	2.5	28.3	L	300.6	H
		30.6	L	253.6	H
		28.5	L	286.6	H
	-0.2	28.7	L	259.4	H
	3.8	28.7	L	246.6	H
		30.4	L	228.8	H
		30.4	L	241.0	H
	1.4	26.4	L	292.8	H
	-0.3	26.5	L	294.1	H
		26.5	L	289.3	H
		25.9	L	308.0	H
		27.8	L	288.3	H
	6.3	30.5	L	257.8	H
		28.5	L	275.2	H
		28.3	L	254.2	H
		30.1	L	265.9	H
		29.4	L	231.1	H
		27.2	L	264.3	H
		29.1	L	303.7	H
		28.9	L	258.4	H
		27.7	L	258.9	H
		27.1	L	263.4	H
		26.9	L	278.3	H
		26.8	L	297.8	H
AVERAGE	**3.5**	**28.4**		**271.2**	
RANGE	**-2.2 to 8.9**	**24.6 - 30.7**		**228.8 - 308.0**	
n =	**15**	**32**		**32**	

Carbonic aqueous ($CO_2 > H_2O$) Inclusions

	Degree of Fill					
Sample	**CO_2**	**H_2O**	**$CO_{2(l)}$**	**$CO_{2(v)}$**	**$T_{m(CO2)}$ (°C)**	**T_{mClath} (°C)**
99N-22C	0.50	0.50	0.60	0.40	-58.0	7.4
	0.60	0.40	0.70	0.30	-57.8	6.7
	0.60	0.40	0.50	0.50	-57.5	7.2
	0.50	0.50	0.50	0.50	-56.6	3.8
	0.50	0.50	0.60	0.40	-55.9	3.0
	0.50	0.50	0.50	0.50	-59.9	6.1
	0.50	0.50	0.70	0.30	-58.1	5.6
	0.50	0.50	0.60	0.40	-59.3	5.9
	0.50	0.50	0.60	0.40	-58.1	8.0
	0.65	0.35	0.50	0.50		
	0.65	0.35	0.50	0.50		
	0.50	0.50	0.80	0.20		
	0.50	0.50	0.80	0.20		
	0.60	0.40	0.70	0.30		
	0.60	0.40	0.95	0.05		
	0.60	0.40	0.95	0.05		
	0.60	0.40	0.70	0.30		
	0.50	0.50	0.60	0.40		
	0.50	0.50	0.70	0.30		
	0.50	0.50	0.70	0.30		
	0.50	0.50	0.90	0.10		
	0.50	0.50	0.90	0.10		
	0.50	0.50	0.90	0.10		
	0.50	0.50	0.90	0.10		
	0.50	0.50	0.70	0.30		
	0.60	0.40	0.70	0.30		
	0.50	0.50	0.60	0.40		
	0.60	0.40	0.75	0.25		
	0.50	0.50	0.70	0.30		
	0.50	0.50	0.60	0.40		
	0.60	0.40	0.70	0.30		
	0.50	0.50	0.60	0.40		
	0.50	0.50	0.60	0.40		
	0.50	0.50	0.60	0.40		
	0.50	0.50	0.60	0.40		
	0.60	0.40	0.80	0.20		
	0.50	0.50	0.70	0.30		
	0.50	0.50	0.80	0.20		
	0.60	0.40	0.60	0.40		
	0.50	0.50	0.80	0.20		
	0.60	0.40	0.70	0.30		
	0.60	0.40	0.70	0.30		
	0.60	0.40	0.70	0.30		
	0.50	0.50	0.70	0.30		
	0.50	0.50	0.80	0.20		
	0.50	0.50	0.80	0.20		
	0.50	0.50	0.60	0.40		
	0.50	0.50	0.60	0.40		
	0.50	0.50	0.60	0.40		
	0.50	0.50	0.60	0.40		
	0.60	0.40	0.70	0.30		
	0.55	0.45	0.70	0.30		
	0.50	0.50	0.80	0.20		

Carbonic aqueous ($CO_2 > H_2O$) Inclusions (continued)

Sample	T_{hCO2} (°C)	Homog. into	T_h(°C)	Homog. into
99N-22C				
	29.1	L		
	28.6	L	313.6	C ($C0_2$)
	28.7	L	314.2	C
	27.8	L	312.2	C
	27.2	L	320.6	C
	27.9	L	312.2	C
	28.2	L	318.6	C
	28.0	L	315.3	C
	28.5	L	317.0	C
	29.1	L	317.1	C
	28.2	L	313.0	C
	29.3	V	299.3	C
	28.0	L	310.0	C
	28.1	L	302.3	C
	28.2	L	306.6	C
	28.2	L	300.8	C
	28.9	L	280.7	C
	28.8	L	284.7	C
	29.2	L	302.8	C
	28.8	L	292.8	C
	29.1	L	272.5	C
	29.3	L	302.1	C
	29.3	L	290.9	C
	28.6	L	285.6	C
	29.0	L	301.8	C
	29.1	L	296.4	C
	29.3	L	282.1	C
	29.3	L	288.9	C
	28.8	L	293.7	C
	29.2	L	286.4	C
	29.5	L	287.1	C
	29.4	L	261.2	C
	29.4	L	276.9	C
	29.5	L	283.8	C
	29.4	L	274.9	C
	29.0	L	267.7	C
	29.2	L	280.1	C
	29.1	L	283.6	C
	29.0	L	261.5	C
	28.4	L	291.1	C
	27.8	L	272.4	C
	28.3	L	294.8	C
	28.7	L	287.7	C
	28.5	L	269.4	C
	28.5	L	271.8	C

Carbonic aqueous ($CO_2 > H_2O$) Inclusions (continued)

Sample	Degree of Fill CO_2	H_2O	$CO_{2(l)}$	$CO_{2(v)}$	$T_{m(CO2)}$ (°C)	T_{mClath} (°C)
99N-22F	0.50	0.50	0.60	0.40	-57.0	5.3
	0.55	0.45	0.65	0.35	-57.3	5.1
	0.50	0.50	0.75	0.25	-56.1	4.4
	0.50	0.50	0.70	0.30	-56.2	2.9
	0.50	0.50	0.70	0.30	-56.2	3.1
	0.50	0.50	0.80	0.20	-56.8	2.4
	0.50	0.50	0.70	0.30	-55.8	1.3
	0.53	0.47	0.90	0.10	-55.8	3.5
	0.70	0.30	0.70	0.30	-55.3	-0.9
	0.50	0.50	0.80	0.20	-56.9	3.0
	0.50	0.50	0.70	0.30	-56.8	0.4
	0.50	0.50	0.80	0.20	-55.7	3.9
	0.55	0.45	0.65	0.35		3.9
	0.50	0.50	0.70	0.30	-56.3	5.2
	0.50	0.50	0.70	0.30	-55.8	2.9
	0.50	0.50	0.60	0.40		
	0.50	0.50	0.90	0.10		
	0.50	0.50	0.70	0.30	-55.3	0.2
	0.50	0.50	0.86	0.14		
	0.50	0.50	0.80	0.20		
	0.50	0.50	0.80	0.20	-55.7	2.9
	0.50	0.50	0.90	0.10		
	0.50	0.50	0.70	0.30		
99N-4D	0.50	0.50	0.90	0.10	-56.2	3.3
	0.50	0.50	0.80	0.20	-56.0	3.8
	0.50	0.50	0.80	0.20	-56.3	3.2
	0.50	0.50	0.90	0.10	-56.5	2.4
	0.50	0.50	0.90	0.10	-55.1	-3.4
	0.50	0.50	0.80	0.20	-54.7	-3.5
	0.50	0.50	0.70	0.30	-58.8	2.3
	0.50	0.50	0.80	0.20	-55.2	1.4
	0.60	0.40			-58.5	
	0.50	0.50	0.80	0.20		
	0.45	0.55	0.85	0.15		
	0.45	0.55	0.90	0.10		
AVERAGE	**0.52**	**0.48**	**0.72**	**0.28**	**-56.7**	**3.3**
RANGE	**0.45 - 0.65**	**0.35 - 0.55**	**0.50 - 0.90**	**0.05 - 0.50**	**-59.9 to -54.7**	**-3.5 to 8.0**
n =	**88**	**88**	**87**	**87**	**34**	**34**

Carbonic aqueous ($CO_2 > H_2O$) Inclusions (continued)

Sample	T_{hCO2} (°C)	Homog. into	T_h(°C)	Homog. into
99N-22F				
	26.7	L	294.8	C
	27.4	L	278.4	C
	29.2	L	276.9	C
	28.2	L	283.5	C
	27.3	L	289.8	C
	27.8	L	288.2	C
	26.4	L	268.8	C
	29.0	L	284.6	C
	28.6	L	290.3	C
	28.8	L	273.8	C
	29.5	L	293.3	C
	25.6	L	282.1	C
	26.9	L	295.5	C
AVERAGE	**28.5**		**291.2**	
RANGE	**25.6 - 29.5**		**261.2 - 320.6**	
n =	**58**		**57**	